# THEORY OF THE RAYLEIGH–TAYLOR INSTABILITY

**H.J. KULL**

*Institut für Angewandte Physik, Technische Hochschule Darmstadt, W-6100 Darmstadt, Fed. Rep. Germany*

NORTH-HOLLAND

PHYSICS REPORTS (Review Section of Physics Letters) 206, No. 5 (1991) 197–325. North-Holland

# THEORY OF THE RAYLEIGH–TAYLOR INSTABILITY

H.J. KULL

*Institut für Angewandte Physik, Technische Hochschule Darmstadt, W-6100 Darmstadt, Fed. Rep. Germany*

Editor: J. Eichler Received March 1991

*Contents*:



*Abstract*:

The theory of the Rayleigh–Taylor instability of accelerated fluid layers is systematically developed from basic fluid equations. Starting with the classical potential flow theory for moving contact surfaces, the discussion extends to various fluid systems describing inhomogeneous, viscous, compressible, and isobaric flows. Thereby an overview on the major stability issues under a broad variety of physical conditions can be given. In particular, the stability analysis is addressed to layered materials in plane and spherical geometries under various dynamical conditions, to inhomogeneous media with variable gradients and different boundary conditions, to viscous boundary layers, compressible atmospheres, and to stationary ablation fronts in laser-driven plasma experiments. The stability theory is further extended to the nonlinear stage of the Rayleigh–Taylor instability and to a discussion of bubble dynamics in two and three dimensions for closed and open bubble domains. For this purpose simple flow models are studied that can describe essential features of bubble rise and bubble growth in buoyancy-driven mixing layers.

## 1. Introduction

### 1.1. Rayleigh–Taylor phenomena

The instability of a heavy fluid layer supported by a light one is generally known as Rayleigh–Taylor (RT) instability. It can occur under gravity and, equivalently, under an acceleration of the fluid system in the direction toward the denser fluid. A simple example may illustrate typical evolution times for the overturn of ordinary liquids under the effect of the earth's gravity. Assuming an acceleration $a = 9.8\,\mathrm{m/s^2}$ and a perturbation wavelength $\lambda = 1\,\mathrm{cm}$, the classical e-folding time $\tau = \sqrt{\lambda}/\sqrt{2\pi a}$ of the free-surface RT instability would be 0.013 s. Even if an unstable equilibrium would be established, the instability evolution would be too fast for direct observation. However, the typical finger-like flow patterns can be nicely modeled, for instance, by Hele–Shaw cells consisting of thin sheets of viscous fluids inside the gap between two parallel glass plates.

Because of the transient nature of RT instabilities in common situations, its physical significance may have escaped attention for a long time. Experimental observations of RT instabilities have only started with the work of Taylor [1] and Lewis [2] about forty years ago, although Rayleigh's theoretical analysis [3] dates back to the end of the last century. At present, a number of laboratory experiments with accelerated liquids have been reported that illustrate the instability evolution under various circumstances. In the following, we describe some of these observations.

The first experiments by Lewis [2] have shown three subsequent stages in the evolution of an unstable air–water interface. The initial phase of exponential growth is followed, first, by a transition phase of bubble formation and then by an asymptotic stage of rising air columns. One should clearly distinguish between the instability problem, related to the initial phase, and the mixing problem, related to the asymptotic phase. In the instability problem, one is mainly concerned with the modification of instability growth rates by various physical effects. In contrast, the mixing problem is addressed to the penetration of perturbation fronts through the liquid.

Another series of experiments by Emmons et al. [4] has largely confirmed these findings. In addition, the effect of surface tension was investigated. Theoretically, it leads to stabilization of perturbations with wavenumbers larger than the cutoff $k_c = \sqrt{\rho a/T}$, where $\rho$ denotes the density and $T$ the surface tension. The experimental results have indicated the trend toward reduced growth rates close to the cutoff, although complete stabilization was not observed. This lack of agreement was explained in part with inaccuracies in the determination of the initial amplitude and in part with nonlinearities. The experiment was reconsidered by Cole and Tankin [5] with improved accuracy, but with about the same cutoff behavior.

The instability evolution between fluid layers of nearly the same density has been studied experimentally by Allred and Blount [6]*) and by Ratafia [7]. The density dependence can be expressed by the so-called Atwood number (section 3.1) leading to appreciably lower growth rates for fluids with nearly equal densities. Moreover, the nonlinear evolution of the interface appears more symmetric, showing mushroom-like flow patterns in both fluids.

The instability of shock-accelerated interfaces has been studied theoretically by Richtmyer [8] and experimentally by Meshkov [9]. It was found that the long-time evolution of Richtmyer–Meshkov instabilities can be well described by the model of an impulsive RT instability. It describes constant velocity growth of initial surface corrugations.

*) Some of Allred and Blount's results are discussed in ref. [4].

More advanced stages of intermixing have been observed by Read [10] and by Dikarev and Zatsepin [11] in the RT case. Similar experiments have been performed by Andronov et al. [12] in the Richtmyer–Meshkov case. Although a unique picture of mixing layers has not yet emerged, a trend toward larger bubble structures has been clearly observed. The experiments of Read have even indicated a simple similarity law for mixing layer growth in proportion to the acceleration distance of the fluid system.

An overview on characteristic flow patterns in the evolution of RT instabilities is given by the schematic drawings of fig. 1. In this figure, the heavy (light) fluid is represented by shaded (unshaded) regions and the kinematical acceleration is directed vertically upward in (a–h) or radially inward in (i). Normal mode perturbations of the horizontal equilibrium surface give rise to sinusoidal surface modulations [1] as represented in (a). The fluid interchange decreases the potential energy content of the system which is the cause of instability. The further upward motion of the lighter fluid assumes the form of rising gas bubbles with an approximately steady shape [2, 4] as illustrated in (b). For comparison, the evolution of a closed, initially spherical bubble is also shown in (c). These horseshoe-like deformations are based on incompressible inviscid fluid dynamics [13]. Experimental observations of underwater bubbles have also indicated the formation of a turbulent wake [14]. Typical features of the falling heavy fluid are represented in (d–g). In a low-density gas, the fluid particles can closely approach the stage of free fall. A corresponding contraction of the downward flow gives rise to needle-shaped spikes [15] as shown in (d). When the flow resistance of the lighter fluid becomes

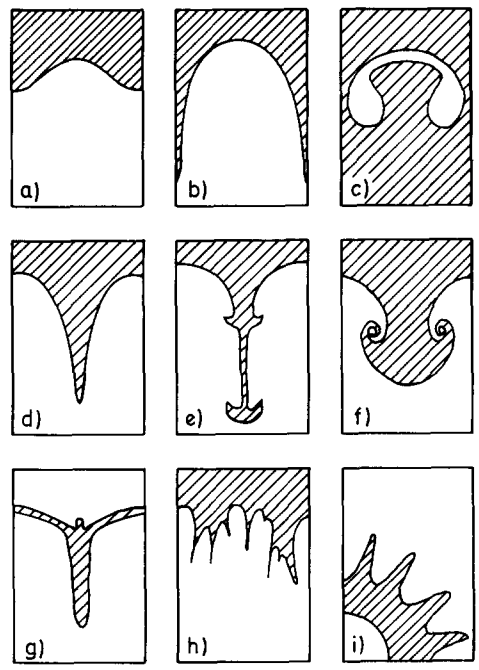


Fig. 1. Schematic flow patterns in the evolution of RT unstable two-dimensional flows. A light fluid (blank area) is penetrating a heavy fluid (dashed area) under the action of an acceleration directed vertically upward in (a–h) and radially inward in (i). (a) Normal mode perturbation, (b) free-surface bubble, (c) deformation of a spherical gas bubble, (d) falling spike in a medium with negligible density, (e) falling spike in a medium with finite density, (f) vortices between intermixing fluids with nearly equal densities, (g) anti-spike at the rear side of a thin foil, (h) advanced stage of intermixing, (i) RT instability of a spherical shell.

important, as in (e), broadening of the spike tips is observed along with the formation of mushroom-like vortex motions [16]. These additional structures are commonly attributed to secondary shear flow instabilities. The pronounced differences between bubbles and spikes disappear for fluids with nearly equal densities [17]. Corresponding bubble–spike pairs can be recognized in (f). Anti-spikes, of the form shown in (g), have been observed in fluid simulations [18] at the stable rear side of an accelerated thin foil. They have been explained theoretically as a result of colliding jets at a cusp point singularity in the surface equation of thin layers [19]. The advanced stage of intermixing [10] gives rise to much more complicated flow patterns as illustrated in (h). RT instabilities are also often encountered in spherical geometries (i). For instance, implosions of inertial confinement fusion pellets are subject to outside surface instabilities during acceleration and to inside cavity instabilities during deceleration.

Over the past decades, it also became obvious that RT instabilities would play an important role in many different fields. Their control is of vital interest for a number of technological applications, in particular in inertial confinement fusion (ICF) devices [18, 20–23]. A number of experiments have demonstrated the physical significance of these instabilities in ICF [24–33]. In some cases, reduced growth rates, mostly attributed to ablative modifications, have been found. Other examples have been reported in geophysics, where some ionospheric phenomena, known as equatorial spread F bubbles, have been explained in the RT context [34–36]. In astrophysics, certain chain-like globules (elephant trunks) in the interstellar medium show close resemblance with RT flow patterns [37]. It is therefore believed that RT instabilities can occur in accelerated gas clouds, driven for instance by new-born stars [38] or supernova events [39, 40]. Other astrophysical RT instabilities have been discussed for magnetic field-supported accretion disks in neutron stars [41] and for collapsing stellar cores [42, 43] due to an intense release of neutrinos.

### *1.2. Historical background*

Since we are not primarily concerned with historical developments, it may be of general interest to first mention some of the original works that have largely contributed to our present understanding of the subject.

More than 100 years ago, Lord Rayleigh (1883) has published his classical treatment [3] entitled "Investigation of the Character of the Equilibrium of an Incompressible Fluid of Variable Density". It was motivated as an illustration of the theory of cirrus clouds but it is not specific for this case. The work describes the linear stability eigenvalue problem for incompressible fluids under gravity. The general stability criterion for incompressible inviscid fluids is discussed and particular perturbation solutions for exponential density variations are derived. It is remarkable that even a transcendental dispersion relation, describing the stability of exponential transition profiles, was already fairly completely analysed in this original work.

Rayleigh was probably the first to pose the stability problem in a general manner and to recognize its principal significance for atmospheric stratifications. At his time, stable surface waves had already been well understood theoretically. The mathematical description of surface waves between superposed liquids of different densities may be largely due to Stokes (1847) [44]. Some early observation of the density dependence of the oscillation period was apparently made by Benjamin Franklin (1762) [44], who compared the behavior of oil–water and air–water interfaces.

In later works, some of the idealizations of the inviscid incompressible fluid model have been overcome. Schwarzschild (1905) [45] has established the basic criterion for stability against convection in compressible atmospheres. Harrison (1908) [46] included the effect of viscosity in the treatment of

superposed fluid layers and Rayleigh (1916) [47] could explain the onset of Boussinesq convection by including viscosity and thermal conductivity.

Apart from these and other early studies of gravitational instabilities, the modern developments have started with the work of Taylor (1950). In a companion work by Taylor [1] and Lewis [2], the basic physical importance of RT instabilities for accelerated fluid layers could first be demonstrated. The theoretically predicted instability growth rates proved in excellent agreement with laboratory experiments. Furthermore, the subsequent stage of rising upstanding gas columns could be observed. The rate of rise of these gas columns could be explained by similar laws as for underwater bubbles and for bubbles rising in cylindrical tubes [14]. These findings have been highly influential for the future developments.

In the succession of Taylor's work, the instability theory was rapidly developed in various directions to include, for instance, surface tension and viscosity [48], magnetic fields [49], spherical geometries [50–52], finite-amplitude perturbations [53], and bubble theories [54–56]. There exist already excellent reviews of parts of the instability theory, especially those by Chandrasekhar [57] and by Birkhoff [58]. Chandrasekhar's work gives an overview on the linear theory for incompressible continuous media. Birkhoff's report describes the principle instability problems in potential flow theory along with a discussion of possible solution methods for linear and nonlinear evolution. Unfortunately, the latter work has not been published and existing copies of the original manuscript are quite cumbersome for reading. The textbook of Drazin and Read [59] represents another valuable introduction to hydrodynamic instabilities. However, there is only little overlap with the present RT problem, since this work has been largely devoted to the topics of thermal instabilities and shear flow instabilities.

### *1.3. Synopsis*

Over the past years, growing interest in RT instability came, on the one side, from the rapid developments in computational fluid dynamics and, on the other side, from various important applications, especially in ICF. This may partly justify to reconsider a classical subject of hydrodynamic stability theory from the viewpoint of present knowledge and current interest. Clearly, there is a profound scientific motivation for a better understanding of the many physical, mathematical and computational problems in this field. We only mention the multi-dimensional nonstationary character of these instabilities, the statistical nature of buoyancy-driven intermixing, and the great complexity in the physics of real systems, including interstellar clouds, supernova remnants, solar atmospheres, fusion plasmas, and many others.

It would be virtually impossible to give a complete account on all present investigations. The interested reader is therefore referred to a number of articles which cover broader topics in this field. A review of the present research status with emphasis on nonlinear evolution and mixing has been given by Sharp [60]. Computational methods and their applicability to RT problems have been discussed by Glimm et al. [61] and by Buchwald [62]. Stability and symmetry issues in ICF have been summarized, for instance, by Gardner et al. [63] and by Holstein and Meyer [64]. Some simplified model calculations of ICF related instabilities have been presented by Jacobs [65] and by Gupta [66]. A number of important achievements will be missing in this review, especially those related to MHD stability theory, to magnetic confinement in axisymmetric toroidal systems, or to computational methods. However, most of these subjects require special expertise and are frequently beyond the scope of a first principles analysis.

This work is addressed to a self-contained systematic presentation of the elementary theory of RT

instabilities. The perspective is to introduce the basic physical phenomena from first principles with a minimum of physical, mathematical, and computational complications. The search for approximations, leading to representative soluble problems for otherwise complicated fluid motions, may be one of the guiding principles in this work. Often an accuracy of results is intended which would not be justified from purely practical considerations. The purpose is to help improve the evidence for the underlying physical laws and to provide some standards for testing general computational methods. Of course, such an approach will necessarily have some limitations. In a few cases, the uncertainties of the theoretical approximations may raise additional questions. Sometimes, the simplicity of the physical assumptions or the nature of particular solutions may be too specific. However, it is the hope that the present work can provide a useful introduction to the subject and some guidance for future research in this field.

A large part of the present review is based on potential flow theory. It may provide the most immediate approach to interfacial instabilities and to the subsequent stage of bubble evolution. The classical potential flow theory of surface waves is of course well known and one of the most complete presentations may have been given by Lamb [44]. However, classical treatments have been mostly limited to linear perturbations of plane layers. Except for Birkhoff's unpublished work [58], there seems to be no systematic review of the stability problems in different geometries and beyond the linear stage. In the present discussion the emphasis may also be somewhat different. It lies more on the physical aspects rather than on the mathematical theory of conformal mapping methods.

The basic potential flow equations for moving fluid boundaries will be introduced in section 2. The mathematical formulation of the boundary value problem for potential flows will be the basis for many stability results in later sections. It is therefore recommended as an introductory part to the nonspecialized reader.

The major topic of section 3 is a review of the RT instability theory for arbitrarily stratified media in plane geometry. The stratified fluid model provides an alternative to the more conventional inhomogeneous fluid descriptions and may be of particular interest for the design of multi-shell ICF pellets. It was first studied shortly after Rayleigh's work by Webb and Greenhill [67, sect. 15]*). However, only recently definite results have been obtained from this theory in the ICF context by Mikaelian [68]. In the present work, the equivalence of the stratified fluid problem with Rayleigh's eigenvalue equation is also demonstrated in the continuum limit. As special cases, the discussion includes Taylor's model for an accelerated foil of finite width and the extension to three superposed layers with arbitrary densities.

Another type of stability problem concerns the amplification of symmetry perturbations on spherically converging shells. The spherical shell problem is discussed in detail in section 4, based on some early work on cavity stability by Birkhoff [50, 51] and by Plesset [52], and on some recent treatment of finite thickness shells by Book and Bodner [69].

Section 5 addresses the dynamics of rising bubbles in RT mixing layers. The weakly nonlinear stage of bubble formation is described in terms of nonlinear perturbation theory. The further evolution of single coherent bubbles is studied for some representative cases. Some insight can be gained through simple modeling assumptions which appear to be rather accurate in many cases. If these approximations are accepted, then one can even derive scaling laws for mixing regions which appear well consistent with present observations.

In section 6, the more classical subject of RT instabilities in inhomogeneous fluids is described. As a general property of the eigenvalue problem, the inversion symmetry of the eigenvalue spectrum, first noticed by Mikaelian [68], will be proved in general. In addition, specific growth rate calculations for

*) The work of R.R. Webb (1884) is mentioned on page 82 of ref. [67].

exponential transition profiles are presented which can illustrate the relationship between surface and internal modes.

The influence of viscosity is examined in section 7. The stability problem for an accelerated viscous shear layer will be treated in the long-wavelength approximation. This discussion includes both viscous shear flow instabilities and viscous RT instabilities. Its purpose is to illustrate the effects of shear flow, buoyancy and viscosity within a single model. For a more detailed discussion of the viscous flow theory the textbook by Drazin and Reid [59] is particularly recommended.

In section 8, the effects of compressibility are treated for ideal fluids with a general equation of state. The stability criterion for convective instabilities is derived from an energy principle which can also explain both stabilization and destabilization by compressibility. In addition, the normal mode analysis for RT instabilities in ideal fluids is described and a general perturbative treatment of compressibility is given.

Section 9 is concerned with the stability behavior of accelerated ablation fronts. This subject is of considerable importance for RT-type instabilities in ICF. The possibilities of ablative stabilization of RT instabilities have been rather controversial for a long time, which excludes definite conclusions at present. However, to the extent of the physics described, a consistent picture of steady ablation in ideal plasmas has emerged. An isobaric flow model of this instability will be discussed, which has been found in good agreement with a number of previous works.

Table 1 gives a survey on the different kinds of fluid descriptions in the present study of RT-type instabilities. Potential flow theory provides the simplest framework being of considerable interest for the nonlinear stages of instability evolution. Incompressible inhomogeneous flows can account for internal rotational modes driven by noncolinear pressure and density gradients or by viscosity. Ideal fluid flow can model the behavior of RT instabilities in compressible media. The isobaric flow model applies to subsonic ablation fronts where mass and heat flow are essential features.

Finally, it is noted that major topics of this article are based on previous work by the present author. In parts, these results have already been published, presented at conferences, or summarized for review purposes [70–72]. In particular, contributions to the theory of bubble dynamics [73–75], to ablative RT instabilities [76, 77], and to the stability of spherical shells [78] are mentioned. In addition, many original results have been rederived, often by simpler approaches, to give a systematic presentation of the subject in this work.

Table 1
Fluid models and their major predictions for RT instabilities. ($\boldsymbol{v}$ is velocity, $\rho$ is mass density, $s$ is specific entropy, $w$ is specific enthalpy, $\boldsymbol{q}$ is heat flow, $\mathrm{d}/\mathrm{d}t$ is time derivative along fluid trajectories)

| Model | Basic assumptions | Predictions |
|---|---|---|
| Potential flow | $\nabla\cdot\boldsymbol{v}=\nabla\times\boldsymbol{v}=0$, $\rho=\text{const.}$ | Surface modes at plane and spherical boundaries, harmonics, bubbles, spikes |
| Incompressible flow | $\nabla\cdot\boldsymbol{v}=0$, $\nabla\times\boldsymbol{v}\neq 0$, $\mathrm{d}\rho/\mathrm{d}t=0$ | Internal rotational modes, damping by finite gradients and by viscosity |
| Ideal fluid flow | $\nabla\cdot\boldsymbol{v}\neq 0$, $\nabla\times\boldsymbol{v}\neq 0$, $\mathrm{d}s/\mathrm{d}t=0$ | Convective instabilities, destabilization by expansion, stabilization by compressional work |
| Isobaric flow | $\mathrm{d}s/\mathrm{d}t\approx(\partial s/\partial\rho\|_p)\,\mathrm{d}\rho/\mathrm{d}t\neq 0$, $\nabla\cdot(\rho w\boldsymbol{v}+\boldsymbol{q})=0$ | Ablative instabilities, stabilization by inhomogeneities, mass flow, and thermal diffusion |

## 2. Potential flow model

An elementary description of RT instability can be given in terms of potential flow theory. It provides a well-known framework for the study of surface modes and has been the basis of many classical stability results. Important aspects of this approach are that the most severe interfacial perturbations can be isolated by this model, giving usually an upper bound on instability growth. Furthermore, it pertains to nonlinear evolution in a relatively simple manner.

In this section, the basic equations governing potential flows with moving boundaries will be outlined. First, the boundary-value problem for an arbitrary contact discontinuity between two fluids is introduced. Then, the mathematical model is specialized to linear perturbations about plane and spherically symmetric boundaries. The common aspects of the different geometries are emphasized by first deriving the general linearized boundary conditions and then performing the specific mode expansions. These equations will be applied to the stability analysis of various fluid systems in the following sections.

### *2.1. Basic equations*

#### *2.1.1. Kinematics*

Let $\boldsymbol{v}(\boldsymbol{x}, t)$ denote the velocity field of a uniform inviscid fluid of constant density $\rho$. In the RT instability, fluid motions are considered to be two-dimensional and they arise from small initial perturbations of an equilibrium state where the fluid is at rest. Under these conditions, the flow can be assumed irrotational at least in the linear approximation. Inspection of the linearized vorticity equation (section 6.1) shows that the vorticity field is necessarily time-independent, $\partial_t(\boldsymbol{\nabla} \times \boldsymbol{v}) = 0$. Even if vorticity is present in the initial conditions, it can be neglected after a short initial period in comparison with the unstable irrotational flow. We remark that there is a basic difference to shear flow instabilities where vorticity can be driven by the velocity shear of the basic flow.

Incompressible irrotational motions are subject to the constraints

$$\boldsymbol{\nabla} \cdot \boldsymbol{v} = 0\,, \quad \boldsymbol{\nabla} \times \boldsymbol{v} = 0\,. \tag{2.1}$$

Alternatively, a scalar potential $\varphi$ can be introduced through the relations,

$$\boldsymbol{v} = \boldsymbol{\nabla}\varphi\,, \quad \Delta\varphi = 0\,. \tag{2.2}$$

The description of the motion of fluid boundaries is partly a kinematical problem. Let $S(\boldsymbol{x}, t) = 0$ denote the surface equation of a boundary moving with the fluid in a given flow field. Its evolution is then governed by the quasi-linear first-order partial differential equation,

$$\partial_t S + \boldsymbol{v} \cdot \boldsymbol{\nabla} S = 0\,. \tag{2.3}$$

Using the method of characteristics, solutions can be found by calculating the trajectories of surface particles. Here and in the following, it is understood without explicit notation that flow variables in surface equations are evaluated on the surface.

*2.1.2. Dynamics*

The dynamics of the flow can be described by the conventional momentum conservation law for fluid particles. If each fluid particle is subject to a conservative force field $-\nabla U$ and to a scalar pressure $p$, its motion is governed by the Euler equation,

$$\rho \frac{\mathrm{d}}{\mathrm{d}t} \boldsymbol{v} = -\nabla p - \rho \nabla U \,, \tag{2.4}$$

where $\mathrm{d}/\mathrm{d}t = \partial_t + \boldsymbol{v} \cdot \nabla$ denotes the time derivative along particle trajectories. We will be mostly interested in constant accelerations of fluid layers. If $a$ denotes the magnitude of the acceleration along the $y$ direction, one can set

$$U = ay \,. \tag{2.5}$$

Physically, eq. (2.5) can describe either a fluid layer accelerated toward the positive $y$ direction or a fluid layer subject to gravitational acceleration along the negative $y$ direction. One should notice, however, that the equivalence between gravity and inertial forces applies only under constant acceleration. For instance, the gravitational instability of a fluid sphere is different from the instability of a spherically converging shell. Inserting $\boldsymbol{v} = \nabla\varphi$ in eq. (2.4) there follows immediately the integrated form

$$\rho(\partial_t \varphi + \tfrac{1}{2} v^2 + U) + p = C(t) \,. \tag{2.6}$$

This is a version of Bernoulli's equation which defines the pressure variations inside the fluid. The function $C(t)$ can be chosen for convenience corresponding to a particular gauge of the velocity potential $\varphi$.

*2.2. Contact discontinuities*

*2.2.1. Continuity conditions*

The simplifying assumptions (2.1) apply only to the interior domain of a uniform inviscid fluid. Within the boundary layer between two potential flow regions one has to consider the complete conservation laws of fluid dynamics. It is well known that the theory of ideal fluid flow admits the existence of contact discontinuities [79], which are moving passively within the fluid. There is no mass flow across a contact discontinuity and, in the absence of surface tension, it exerts no forces on its surroundings. More precisely, contact discontinuities are defined by the continuity conditions,

$$[v_n] = 0 \,, \quad [p] = 0 \,, \tag{2.7}$$

for the normal component of the fluid velocity $v_n = \partial_n \varphi$ and the pressure, respectively. The square brackets represent the jump of the argument across the boundary. Using eqs. (2.3) and (2.6), these continuity conditions can be expressed as

$$\partial_t S + \boldsymbol{v} \cdot \nabla S = 0 \,, \tag{2.8a}$$

$$[\rho(\partial_t \varphi + \tfrac{1}{2} v^2 + U)] = [C(t)] = \tilde{C}(t) \,. \tag{2.8b}$$

These equations are often referred to as kinematical and dynamical boundary conditions, respectively. We remark that (2.8a) has to be satisfied at both sides of the boundary thus representing actually two constraints. These imply the continuity of $v_n$ since $\nabla S$ is directed along the surface normal and $S(\boldsymbol{x}, t)$ denotes the same function in both fluids. The time function $\tilde{C}$ in (2.8b) is usually chosen to be zero with possible exceptions for steady flow problems. The two potentials $\varphi$ of both fluids and the surface $S$ have to be determined in accordance with these three boundary constraints. They determine the evolution of an arbitrary contact discontinuity in potential flow theory.

The boundary value problem (2.8) is rather complex and, in general, solutions can only be found by numerical computations. Boundary integral techniques have proved particularly successful in dealing with a number of surface problems [13, 15, 18]. Only in few special cases, analytic results can be obtained. The main approaches for these theoretical investigations will be briefly summarized in the following.

*2.2.2. Initial-acceleration problem*

The initial acceleration of a fluid globule in an extended fluid can be treated by a linear boundary-value problem which is similar to the classical boundary-value problems for dielectrics. The initial-acceleration potential $\Phi = \partial_t \varphi$ satisfies the continuity conditions

$$[\rho\Phi] = -[\rho]U\,, \quad [\partial_n \Phi] = 0\,, \tag{2.9}$$

where $\partial_n$ is the derivative in the direction of the surface normal. These conditions follow from eqs. (2.8) if the fluid is considered at rest. This approach is limited to a short initial period. Nevertheless, some interesting conclusions have been drawn from this model by Birkhoff [58]. It was found that spherical and ellipsoidal surfaces are accelerated rigidly while this is not true for closed surfaces of other shapes. The initial-acceleration problem for spherical bubbles will be discussed to some extent in section 5.2.

*2.2.3. Free-surface problem*

Another important special case is represented by a surface separating a fluid from a gas of negligible density. Setting the density of the gas equal to zero, Bernoulli's equation (2.6) yields spatially constant pressure inside the gas region and the boundary conditions (2.8) become

$$\partial_t S + \boldsymbol{v} \cdot \nabla S = 0\,, \tag{2.10a}$$

$$\partial_t \varphi + \tfrac{1}{2} v^2 + U = 0\,. \tag{2.10b}$$

At each instant of time, eq. (2.10b) describes a linear boundary value problem for the potential $\partial_t \varphi$ on the instantaneous surface $S$. A continuous sequence of such problems has to be solved to determine the time evolution. The time-dependent free-surface model will be examined by the method of least-squares approximation in section 5.1.

As a special case of eqs. (2.10), the steady flow problem

$$\tfrac{1}{2} v^2 + U = 0\,, \quad \boldsymbol{v} \cdot \nabla S = 0\,, \tag{2.11}$$

describes the rise of open-ended bubbles in channels or tubes. Even this comparatively simple case leads to considerable mathematical difficulties. A discussion of the steady-state bubble theory is presented in section 5.3.

*2.2.4. Perturbation problem.*

Only few evolution problems can be solved generally by analytic methods. Therefore these problems are of considerable importance in gaining an understanding of more complicated flows. A general approach is given by perturbing a known solution of high symmetry and studying the growth of surface perturbations in the linear approximation. This method applies in particular to plane, cylindrical and spherical boundaries. The basic perturbation equations are summarized in the following. The major perturbation results will be discussed in detail in the subsequent sections 3 and 4. Extensions to nonlinear perturbation methods are demonstrated in section 5.1.

## *2.3. Perturbations*

### *2.3.1. Plane boundaries*

Let us illustrate the foregoing remarks in the simplest case of a plane contact discontinuity. The unperturbed flow consists of two superposed fluid layers with an interface at $y = 0$ (fig. 2). We assume an acceleration $a$ along the $y$ direction and a uniform flow velocity $v$ in the $x$ direction. Small departures from the steady-state configuration are described by a potential perturbation $\delta\varphi$ and a surface perturbation $S = \zeta(x, t) - y = 0$. The boundary conditions (2.8) are now expanded about $y = 0$ and linearized in the perturbations. This procedure yields

$$\partial_t \zeta + v\partial_x \zeta - \partial_y \delta\varphi = 0\,, \tag{2.12a}$$

$$[\rho(\partial_t \delta\varphi + v\partial_x \delta\varphi + a\zeta)] = 0\,, \tag{2.12b}$$

evaluated at the plane $y = 0$.

### *2.3.2. Spherical boundaries*

Although the extension to spherical symmetry is straightforward, a few basic differences should be noticed in advance. Firstly, the acceleration can no longer be simply expressed by an equivalent gravity. We therefore omit the gravitational potential $U$ and consider the acceleration problem explicitly. The treatment of the gravitational case is due to Kelvin and can be found in the textbook of Chandrasekhar [57]. Secondly, a tangential flow discontinuity, as shown in fig. 2, would be inconsistent with the basic assumption of irrotational flow. As a consequence, we restrict attention to purely radial motions in the basic flow. This excludes, for instance, the instabilities of Taylor–Couette flow between rotating cylinders, a subject which has also been extensively discussed elsewhere [57]. Finally, the incompres-

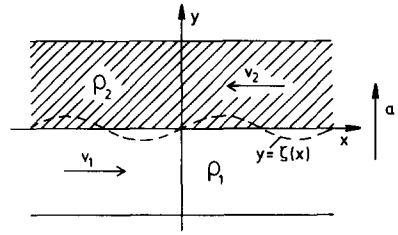


Fig. 2. Instability of a plane contact discontinuity. Surface perturbations $y = \zeta(x)$ can grow by the KH instability if $\boldsymbol{v}_1 \neq \boldsymbol{v}_2$ or by the RT instability if $\rho_2 > \rho_1$ and an acceleration $a$ is applied in the direction toward the denser fluid.

sibility assumption requires a void inside the sphere. We therefore consider only the free-surface problem. A generalization to finite densities has been given by Plesset [52], however, at the expense of assuming a flow singularity at the origin.

Let us now derive the free-surface conditions for the potential perturbations on spherically symmetric boundaries. The derivations can be given in complete analogy for plane ($\delta = 1$), cylindrical ($\delta = 2$), and spherical ($\delta = 3$) symmetry. More specifically, the unperturbed surface is the $\delta$-dimensional sphere $r = R(t)$, where $R(t)$ describes an arbitrary radial motion. For $\delta = 1$ the radius $r$ is identified with the $y$ coordinate. The perturbed flow is written in the form

$$\varphi = \varphi_0(r, t) + \delta\varphi\,, \quad S = R(t) + \zeta - r\,, \tag{2.13}$$

where $\varphi_0(r, t)$ represents the spherically symmetric basic flow, $\delta\varphi$ the perturbation, and $\zeta$ the corresponding surface displacement. We will also take into account a small nonuniformity in the applied pressure by writing $p = p_0(t) + \delta p$ for the surface pressure. The perturbation $\delta p$ may be produced in the surrounding gas and enters in this model as a prescribed function.

Firstly, we consider the dynamical boundary condition. At the perturbed surface, Bernoulli's equation (2.6) assumes the form

$$\rho(\partial_t\varphi + \tfrac{1}{2}v^2)|_{r=R+\zeta} + p_0 + \delta p = C(t)\,. \tag{2.14}$$

Expanding this equation up to first order in the perturbations and subtracting the radially symmetric part, one obtains the expression

$$\rho(\partial_t\delta\varphi + v_0\partial_r\delta\varphi) + \rho\partial_r(\partial_t\varphi_0 + \tfrac{1}{2}v_0^2)\zeta + \delta p = 0\,, \tag{2.15}$$

evaluated on the unperturbed sphere $r = R$ with $v_0 = \partial_r\varphi_0 = \dot{R}$. This equation can be further simplified by expressing the velocity potential in terms of the normalized coordinate $\eta = r/R$ and noting that

$$\partial_t|_\eta = \partial_t|_r + \dot{R}\eta\partial_r|_t\,. \tag{2.16}$$

As a result of this change of variables one obtains,

$$\begin{aligned}&(\partial_t\delta\varphi + v_0\,\partial_r\delta\varphi)|_{r=R} = \partial_t\,\delta\varphi|_{\eta=1}\,,\\ &\partial_r(\partial_t\varphi_0 + \tfrac{1}{2}v_0^2)|_{r=R} = \partial_t v_0|_{\eta=1} = \ddot{R}\,.\end{aligned} \tag{2.17}$$

Inserting eq. (2.17) into eq. (2.15) yields,

$$\partial_t\,\delta\varphi|_{\eta=1} + \ddot{R}\zeta + \delta p/\rho = 0\,. \tag{2.18a}$$

This equation has basically the same form as eq. (2.12b) for plane geometry. In the co-moving frame, defined by the coordinate $\eta = 1$, the shell acceleration appears as an effective gravity. Differences between the geometries will arise, however, because of different forms of the potential perturbations inside a half-plane, a circle, and a sphere. One should also notice that both the acceleration and the pressure nonuniformity can have an arbitrary time-dependence.

The second boundary condition is easily obtained by inserting the surface expression of eq. (2.13) into the kinematical boundary condition (2.10a). The linearized equation becomes

$$\partial_t \zeta - (\partial_r v_0)\zeta - \partial_r \delta\varphi = 0\,, \tag{2.18b}$$

on the sphere $r = R$. Comparing this equation with the corresponding equation (2.12a) in plane geometry, one can recognize an additional term for converging geometries. It arises from the radial variation of the unperturbed flow velocity. Such a variation is required to conserve the mass flux across the sphere with area $\sim R^{\delta-1}$. Equations (2.18a) and (2.18b) represent the basic perturbation equations for an accelerated interface that will be analyzed in the subsequent chapters.

*2.3.3. Flow potentials*

We now have to look for solutions of eq. (2.2) that satisfy boundary conditions on a plane, a circle, and on a sphere. The method of separation of variables provides well-known function systems that are known to be complete on these boundaries. We will only give a brief summary of the basic potentials to be used in this work and refer to the mathematical literature [80] for more detailed discussions.

The spherically symmetric flow depends only on the radial coordinate. The corresponding potentials are easily obtained from eq. (2.2),

$$\begin{aligned} \varphi_0 &= R\dot{R}\eta \qquad \text{for } \delta = 1\,, \\ \varphi_0 &= R\dot{R}\ln\eta \quad \text{for } \delta = 2\,, \\ \varphi_0 &= -R\dot{R}/\eta \quad \text{for } \delta = 3\,. \end{aligned} \tag{2.19}$$

They describe a uniform stream in one dimension and source flows in two and three dimensions. The flow velocity

$$v_0 = \partial_r \varphi_0 = \dot{R}\eta^{-(\delta-1)} \tag{2.20}$$

is directed radially and conserves the mass flux $\sim v_0 r^{(\delta-1)}$ through spherical shells.

The perturbations will be treated as being two-dimensional, depending on the Cartesian coordinates $x$, $y$ in the plane case and on the polar coordinates $r$, $\Theta$ in the cylindrical and spherical geometries. In the linear approximation, the assumption of two-dimensional flow represents only a restriction for the cylindrical geometry. Here, we neglect perturbations along the cylinder axis by restricting attention to simple flute modes. The symmetry of the plane and spherical geometries assures that normal mode growth will not depend on a second angle.

For a plane boundary, one may consider a Fourier expansion with respect to the $x$ coordinate. In the expansion of the complex velocity potential $W = \delta\varphi + \mathrm{i}\,\delta\psi$, each term has the general form

$$W(k) = (A\,\mathrm{e}^{-ky} + B\,\mathrm{e}^{ky})\,\mathrm{e}^{\mathrm{i}kx}\,, \tag{2.21}$$

with a constant wave number $k$ and time-dependent amplitudes $A$ and $B$. These potential perturbations will often be called surface modes, because they are exponentially damped toward the interior of the fluid. The boundary conditions at infinity are $A = 0$ for $y \to -\infty$ and $B = 0$ for $y \to \infty$.

A physical interpretation of surface modes may be given in terms of evanescent sound waves. Writing the sound wave dispersion relation in the familiar form,

$$\omega^2 = c^2(k_x^2 + k_y^2)\,, \tag{2.22}$$

and solving for the normal component of the wave number, there follows

$$k_y = \pm\sqrt{\omega^2/c^2 - k_x^2}\,. \tag{2.23}$$

For large sound velocities, $c^2 \to \infty$, wave propagation is no longer possible but instead evanescent modes can exist. Asymptotically, they approach the potential flow solutions.

In the cylindrical and spherical geometries analogous expansions exist, however, with the basic difference that the wave numbers are no longer constants. Actually, the arc length $r\Theta$ has to be identified with the $x$ coordinate, indicating wave numbers of the form $k(r) = j/r$. Assuming this dependence, the potential (2.21) may be generalized to the form

$$\delta\varphi = A(t)\exp\Big(-\int_R^r k(z)\,\mathrm{d}z\Big)g_l(\Theta) = A(t)\eta^{-l}g_l(\Theta)\,. \tag{2.24}$$

The angular parts $g_l(\Theta)$ and the corresponding powers $j$ can be found from the solution of the Laplace equation. There follows the familiar result,

$$g_l = \sin(l\Theta), \cos(l\Theta)\,, \quad \text{for } \delta = 2\,; \quad g_l = P_l(\Theta)\,, \quad \text{for } \delta = 3\,, \tag{2.25a}$$

where $P_l(\Theta)$ denotes the Legendre polynomials. The possible $j$ values are

$$j = l, -l\,, \quad \text{for } \delta = 2\,; \quad j = l+1, -l\,, \quad \text{for } \delta = 3\,, \tag{2.25b}$$

corresponding to radially decaying and growing solutions, respectively. These formulas complete our survey on the mathematical background of the potential flow model of RT instability.

## 3. Stability of plane boundaries

In this section, we are concerned with applications of potential flow theory to the stability of accelerated plane layers. Firstly, the stability of a single plane interface is outlined, leading to the classical growth formula for the combined RT and KH instabilities. The RT instability is further illustrated for a variety of different acceleration laws, including the impulsive acceleration model of the Richtmyer–Meshkov instability. The analysis of a single unstable interface is then extended to layers of finite width where Taylor's free-surface model is presented. Finally, the general stability eigenvalue problem for multi-layered fluid systems is reviewed. As an illustration of the theory a three-layer model, displaying essential features of accelerated foils and anti-mix-layers, is discussed.

### 3.1. Instability principles

Two of the most important principles of interfacial fluid instabilities can be inferred from the model of a single plane interface as shown in fig. 2. These are the Kelvin–Helmholtz (KH) instability of a tangential flow discontinuity and the Rayleigh–Taylor (RT) instability of a density discontinuity accelerated normally toward the denser fluid. Both principles arose from the classical studies of Stokes, Helmholtz, Kelvin, Rayleigh and others in the second half of the 19th century. Many results of this early period, concerning potential perturbations at a plane interface, have been summarized by Lamb [44].

Let us consider a simple normal mode analysis of the stability of a plane interface. Normal mode perturbations with frequency $\omega$ and wavenumber $k$ are taken proportional to the factor $\exp(-\mathrm{i}\omega t + \mathrm{i}kx)$. In linear systems, the frequency is subject to a dispersion relation $\omega = \omega(k)$. The system is linearly unstable, if there exists a positive growth rate $n = \mathrm{Im}(\omega)$ for at least one real value of $k$.

The potential perturbation (2.21) with $A = 0$ in the lower and $B = 0$ in the upper half-plane is assumed. With this choice, $k$ is restricted to positive values. Eliminating the surface displacement $\zeta$ from the boundary conditions (2.12), there follow the jump relations,

$$[\partial_y \delta\varphi/\tilde{\omega}] = 0\,, \quad [\tilde{\omega}\rho\,\delta\varphi] - [\rho]\, a\partial_y\, \delta\varphi/\tilde{\omega} = 0\,, \tag{3.1}$$

where $\tilde{\omega} = \omega - kv$. They form a linear system of equations for the potential amplitudes $A$ and $B$. Nonvanishing solutions can only exist if the frequency satisfies the dispersion relation

$$\omega = kv_s \pm \mathrm{i}\sqrt{\alpha ak + (\beta uk)^2}\,, \tag{3.2}$$

with

$$v_s = (\rho_1 v_1 + \rho_2 v_2)/(\rho_1 + \rho_2)\,, \quad u = \tfrac{1}{2}(v_2 - v_1)\,, \quad \alpha = (\rho_2 - \rho_1)/(\rho_2 + \rho_1)\,,$$

$$\beta = 2\sqrt{\rho_1\rho_2}/(\rho_2 + \rho_1)\,.$$

The interface is unstable if $\alpha ak + (\beta uk)^2 > 0$. Accordingly, instability can arise from an acceleration toward the denser fluid ($\alpha > 0$) or from a tangential flow discontinuity ($u \neq 0$). The special case of an unstable density discontinuity ($\alpha > 0$, $u = 0$) is called the RT instability. The instability of a tangential flow discontinuity ($u \neq 0$, $a = 0$) is called the KH instability. The corresponding growth rates are

$$n = \sqrt{\alpha ak}\,, \quad n = k|u|\,, \tag{3.3}$$

respectively. The dispersion relation (3.2) becomes particularly simple in a coordinate frame moving with the mean velocity $v_s$ of both layers. In this frame, a purely growing mode with $\mathrm{Re}(\omega) = 0$ is obtained. The density dependence is expressed by the coefficients $\alpha$ and $\beta$, where $\alpha$ is commonly called the Atwood number. Equal densities ($\alpha = 0$, $\beta = 1$) correspond to pure KH growth, while a free surface ($\alpha = 1$, $\beta = 0$) is only subject to RT instability. We also mention that the growth rate increases indefinitely with $k$, giving preference to the growth of short-wavelength perturbations. Growth saturation at large wavenumbers can result from a variety of physical effects such as surface tension, viscosity, finite density gradients, ablation, and nonlinearities. With the exception of surface tension, these effects will be treated in detail in the subsequent sections. Surface tension plays no role in present

ICF applications and has therefore been omitted for simplicity. Likewise, KH instabilities are not further examined in this review, because of the rather complete discussion in ref. [59]. Only in section 7 shear flow will again be included to demonstrate the close relationship between KH and RT instabilities in the viscous flow theory.

### 3.2. Accelerated interfaces

The stability of time-dependent accelerations can no longer be described by constant growth rates. Instead, the perturbation equations have to be solved for the underlying surface motions and initial data. This time-dependent stability problem will be addressed in this section. Although the surface equation of a single accelerated interface is quite simple, it can describe a number of physically important examples. These include constant, impulsive, transient, and nonuniform acceleration laws.

#### 3.2.1. Surface equation

The boundary conditions (2.18) will now be specialized for a plane boundary of an accelerated fluid layer in the half-space $r > R(t)$. The potential perturbation can then be assumed of the form (2.21) with $B = 0$ and $y = r$. Noting that $\eta = r/R$, the following relations hold:

$$W = A(t)\exp(-kr + \mathrm{i}\,kx) = A(t)\exp(-kR\eta + \mathrm{i}kx)\,,$$
$$\partial_r W = -kW\,, \qquad \partial_t[(\partial_r W)|_{r=R}] = -k\partial_t W|_{\eta=1}\,. \tag{3.4}$$

With the help of eq. (3.4), one can immediately eliminate the potential from the boundary conditions (2.18). Noting that $\partial_y v_0 = 0$, according to eq. (2.20), one obtains the surface equation,

$$\partial_t^2 \zeta - ak\zeta = \delta a\,. \tag{3.5}$$

It describes the growth of surface perturbations for a prescribed acceleration law $a(t) = \ddot{R}$. Nonuniform acceleration is described by the inhomogeneity $\delta a = k\,\delta p/\rho$. This term will be neglected until the discussion of nonuniformities in section 3.2.5.

#### 3.2.2. Constant acceleration

The RT instability of accelerated fluid layers has first been demonstrated by Taylor [1] and Lewis [2]. We will briefly summarize the classical instability results.

As already discussed in section 3.1, the growth of the free-surface RT instability under a constant acceleration $a$ can be expressed by the growth rate $n = \sqrt{ak}$. The unstable modes can arise from an initial surface displacement $\zeta_0$ or from an initial surface velocity $\partial_t \zeta_0$. The corresponding solution of eq. (3.5) is given by,

$$\zeta = \zeta_0 \cosh(nt) + n^{-1}\,\partial_t \zeta_0 \sinh(nt)\,. \tag{3.6}$$

The RT instability imposes principal limitations on the acceleration of foils by gas and ablation pressure. If a foil of thickness $d$ has been accelerated over a distance $s = at^2/2$, the growth increment becomes,

$$nt = \sqrt{2ks} = \sqrt{2kdQ}\,. \tag{3.7}$$

The inflight aspect ratio $Q = s/d$ is the basic dimensionless parameter governing foil stability. As a result of mixing theory (section 5), the typical failure modes can be expected in the wavenumber regime $kd \approx 1$–3. Choosing $kd = 1$ and $Q = 11$, eq. (3.7) predicts an amplification of the initial amplitude by a factor of $\approx 100$. Depending on the most critical wave numbers and the magnitude of the initial perturbations, the typical $Q$ values seem limited to $\approx 5$–15. This rather severe stability constraint may be considerably relaxed under more realistic conditions. For instance, numerical simulations of ablatively driven foils have indicated $Q \approx 30$ or more before foil break-up [18]. Possible stabilization mechanisms in these cases will be discussed in section 9.

Although the instability mechanism is only dependent on the acceleration distance, the kinetic energy of the foil depends explicitly on the acceleration. Using the hydrostatic pressure law, $p_0 = \rho a d$, the kinetic energy density of the foil is expressed in the form

$$E = \tfrac{1}{2}\rho v^2 = \rho a s = p_0 Q \,. \tag{3.8}$$

The potential advantage of large inflight aspect ratios lies in the better hydrodynamic efficiency for achieving high energy densities. In ICF applications, the attainable ablation pressures are much smaller than the required energy for fuel ignition. Therefore most present concepts are based on inflight aspect ratios in the range 30–100.

*3.2.3. Impulsive acceleration.*

Another interesting limiting case is given by an impulsive acceleration law: $a = \Delta v\, \delta(t)$, where $\delta(t)$ denotes the delta-function and $\Delta v$ the velocity increment imparted to the undisturbed foil. The solution of eq. (3.5) predicts a constant perturbation velocity and corresponding linear amplitude growth,

$$\zeta = \zeta_0 + (\partial_t \zeta_0 + k\, \Delta v\, \zeta_0) t \,. \tag{3.9}$$

The velocity increment of the perturbation depends on the initial amplitude and the wavenumber of the surface corrugations.

The impulsive approximation requires that the acceleration time is much shorter than the e-folding time of the unstable mode. This approximation applies mainly to long-wavelength modes with sufficiently small growth rates. Such modes can also reach large amplitudes $\zeta \sim k^{-1}$ before saturating nonlinearly.

The impulsive limit of the RT instability was applied to shock-accelerated interfaces by Richtmyer [8]. In numerical simulations of the shock problem, the linear evolution law (3.9) could be confirmed. However, there appears an ambiguity in the initial conditions, which are different immediately before and after the shock passage. For a shock moving toward the denser fluid, post-shock initial conditions have led to satisfactory agreement with the impulsive acceleration model. The prediction of a constant perturbation velocity has been observed experimentally by Meshkov [9]. Shock-induced interfacial instabilities are generally known as Richtmyer–Meshkov instabilities.

*3.2.4. Exponential acceleration law*

The finite duration of acceleration pulses limits the growth of long wavelength perturbations, having e-folding times longer than the acceleration time. A simple example of a transient pressure pulse is given by an exponential acceleration law [70],

$$a(t) = a \exp(bt) \,. \tag{3.10}$$

The constant $a$ denotes an initial acceleration at $t = 0$ and the constant $b$ can be positive for growing pulses or negative for decreasing pulses. In the latter case, a useful interpolation formula between the limiting cases of constant and impulsive acceleration can be gained. In particular, an analytic expression for the asymptotic perturbation velocity imparted to the perturbation during the passage of the pulse will be obtained.

The solutions of eq. (3.5) with an exponential acceleration law (3.10) can be found by a variable substitution. We define

$$\tau = \tau_0 \exp(bt/2), \qquad \tau_0 = 2\sqrt{ak}/|b|, \tag{3.11}$$

as a new independent variable with initial value $\tau_0$. It varies in the interval $0 < \tau < \tau_0$ for $b < 0$ and in the interval $\tau_0 < \tau < \infty$ for $b > 0$. Equation (3.5) becomes

$$\tau^2 \partial_\tau^2 \zeta + \tau \partial_\tau \zeta - \tau^2 \zeta = 0. \tag{3.12}$$

Two independent solutions of eq. (3.12) are given by the modified Bessel functions $I_0(\tau)$ and $K_0(\tau)$. Imposing initial conditions at $\tau = \tau_0$, we obtain

$$\zeta = \tau_0 \{[K_1(\tau_0) I_0(\tau) + I_1(\tau_0) K_0(\tau)]\zeta_0 + |[K_0(\tau_0) I_0(\tau) - I_0(\tau_0) K_0(\tau)]| \partial_t \zeta_0 / \sqrt{ak}\}. \tag{3.13}$$

The second bracket is positive for $\tau > \tau_0$ and negative for $\tau < \tau_0$. Its magnitude has to be taken because of a corresponding sign change of the constant $b$. In deriving eq. (3.13) we have also used the relations

$$I_1 = \partial_\tau I_0, \quad K_1 = -\partial_\tau K_0, \quad K_0 I_1 + K_1 I_0 = 1/\tau, \tag{3.14}$$

for the first derivatives and the Wronskian, respectively.

The asymptotic limits of large and small $\tau$ values can be analysed in more detail. Large $\tau$ values describe large growth rates and a corresponding slow time variation of the applied acceleration. Using for $\tau, \tau_0 \gg 1$ the asymptotic expressions

$$I_n \to \sqrt{1/2\pi\tau} \exp(\tau), \quad K_n \to \sqrt{\pi/2\tau} \exp(-\tau), \tag{3.15}$$

one obtains from eq. (3.13)

$$\zeta = \sqrt{\frac{\tau_0}{\tau}} \left( \zeta_0 \cosh(\tau_0 - \tau) + \frac{\partial_\tau \zeta_0}{\sqrt{ak}} \sinh(|\tau_0 - \tau|) \right). \tag{3.16}$$

This result represents the WKB generalization of the solution (3.6) for constant acceleration. The variable $\tau$ plays the role of the growth increment in the WKB solution.

The opposite limit, $\tau \to 0$, describes the time asymptotic response to a transient acceleration pulse with $b < 0$. Asymptotically, the perturbations grow with constant velocity whose magnitude depends on the pulse duration. Assuming small arguments, the modified Bessel functions can be approximated in the form,

$$I_0 \to 1, \quad I_1 \to \tau/2, \quad K_0 \to -\ln(\tau/2), \quad K_1 \to 1/\tau. \tag{3.17}$$

Neglecting $I_0$ in comparison with $K_0$ and noting that $\partial_t \ln \tau = b/2$, we obtain from eq. (3.13) the asymptotic perturbation velocity,

$$\partial_t \zeta = \sqrt{ak}\, I_1(\tau_0)\zeta_0 + I_0(\tau_0)\, \partial_t \zeta_0 \,. \tag{3.18}$$

It increases monotonically with the parameter $\tau_0$ that characterizes the pulse length in comparison with the e-folding time. Limiting forms for small and large parameter values are

$$\begin{aligned} &\partial_t \zeta = (ak/|b|)\zeta_0 + \partial_t \zeta_0 && \text{for } \tau_0 \ll 1 \,, \\ &\partial_t \zeta = (\sqrt{ak}\ \zeta_0 + \partial_t \zeta_0)\sqrt{1/2\pi\tau_0}\exp(\tau_0) && \text{for } \tau_0 \gg 1 \,, \end{aligned} \tag{3.19}$$

respectively. For short pulses or long wavelengths ($\tau_0 \ll 1$), we recover the result (3.9) for impulsive acceleration. The velocity increment $\Delta v = a/|b|$ is the time integral of $a(t)$ from $t = 0$ up to $t = \infty$. For long pulses or short wavelengths ($\tau_0 \gg 1$), the asymptotic velocity is substantially larger because of the exponential growth during the acceleration phase.

A specific example of the wavelength dependence of the solution (3.13) can be recognized in fig. 3. It shows the transition from exponential to linear amplitude growth for three different modes subject to the same acceleration pulse. The acceleration parameters are $a = 3.6 \times 10^{18}$ cm/s$^2$ and $b = -10^{11}$ s$^{-1}$, corresponding to a flight distance of $\approx 16$ μm in 55 ps. Similar conditions have been assumed for a 0.5 μm thick laser-driven ICF foil in ref. [18], although the present parameters may overestimate the time dependence of the acceleration. One can recognize an earlier saturation of exponential growth with increasing perturbation wavelength.

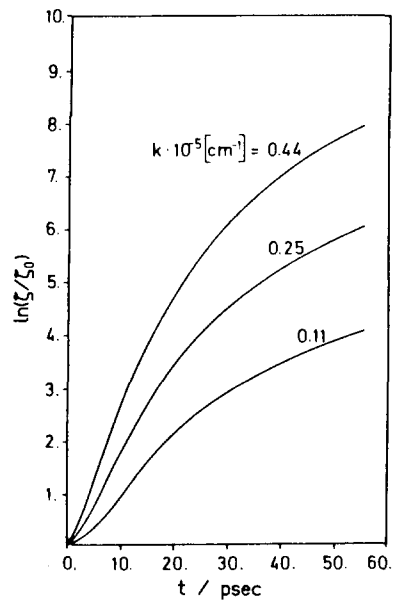


Fig. 3. Evolution of a sinusoidal surface perturbation $\zeta = \zeta_0 \cos(kx)$ under a time-dependent acceleration law, $a(t) = 3.6 \times 10^{18} \exp(-0.1t/\text{ps})$ cm/s$^2$. The amplitude growth is due to the RT instability (exponential growth) for large mode numbers and due to the Richtmyer–Meshkov instability (linear growth) for small wavenumbers. One can recognize the suppression of exponential growth with decreasing wavenumbers. (From ref. [70]).

*3.2.5. Nonuniform acceleration*

Finally, we wish to examine the role of pressure nonuniformities on the instability evolution. For this purpose, we assume a constant acceleration $a$ and solve eq. (3.5) with the inhomogeneity $\delta a$ that has been neglected until now.

In addition to the solution (3.6) of the homogeneous equation, satisfying the initial conditions at $t = 0$, one has to consider a solution of the inhomogeneous equation with vanishing initial values. Using the method of variation of constants, this solution is found to be,

$$\zeta = \frac{1}{2n}\left(\mathrm{e}^{nt}\int_0^t \mathrm{e}^{-nt}\,\delta a\,\mathrm{d}t - \mathrm{e}^{-nt}\int_0^t \mathrm{e}^{nt}\,\delta a\,\mathrm{d}t\right). \tag{3.20}$$

If the function $\delta a$ is bounded, $|\delta a| < M$, the second integral can be estimated as

$$\left|\mathrm{e}^{-nt}\int_0^t \mathrm{e}^{nt}\,\delta a\,\mathrm{d}t\right| < \frac{M}{n}\,. \tag{3.21}$$

Asymptotically, for $nt \gg 1$, its contribution can be neglected in the presence of unstable modes. Looking now at the first integral in eq. (3.20), we consider two limiting cases.

(i) If $\delta a$ is slowly varying over an e-folding time, it may be replaced by its initial value $\delta a_0$, yielding

$$\zeta \approx (\delta a_0/n^2)\,\mathrm{e}^{nt}/2\,. \tag{3.22}$$

(ii) If $\delta a$ is only nonzero over a small fraction of the e-folding time, it can be approximated by an impulse $\delta a = \delta v_0\,\delta(t - t_0)$. This leads to the amplitude

$$\zeta \approx (\delta v_0/n)\,\mathrm{e}^{n(t-t_0)}/2\,. \tag{3.23}$$

In both cases, the time asymptotic response is an unstable mode of the homogeneous equation. Comparing eqs. (3.22) and (3.23) with eq. (3.6), one can define effective initial surface perturbations by setting

$$\begin{aligned} &\text{(i)}\quad \zeta_0 = \delta a_0/n^2 = (\delta p/p_0)d\,,\\ &\text{(ii)}\quad \partial_t\zeta_0 = \delta v_0 = \frac{k}{\rho}\int \delta p\,\mathrm{d}t\,, \end{aligned} \tag{3.24}$$

where the relations $\delta a = k\,\delta p/\rho$ and $p_0 = \rho a d$ have been used. These formulas relate the pressure nonuniformities to equivalent surface perturbations of a uniformly driven foil. However, this result is likely to be limited by compressibility effects if the pressure fluctuates appreciably over the passage time of sound waves across the foil.

*3.3. Layers of finite width*

The model of a single free surface can readily be extended to fluid layers of finite width. A complete

solution of this problem has been given in the original work of Taylor [1]. Two important aspects of this treatment should be mentioned. First, the RT growth rate is found independent of the layer width. Second, there can be strong interference effects for thin layers between the two surface modes developing at the front and at the rear side of the foil. Both effects are dependent on the free-surface assumption and modifications will be discussed in the connection with inhomogeneity effects in sections 3.5 and 6.3. Nevertheless, the free-surface model is often adequate for gas-driven foils and its predictions are therefore of considerable interest for many applications.

A detailed discussion of Taylor's free-surface model will be given in the following. The notation is adopted from the spherical shell problem with the acceleration directed toward the origin. This will be convenient for comparing results in different geometries.

*3.3.1. Normal modes*

Consider a plane fluid layer, $0 < r < d$, under a constant acceleration $a$ toward the negative $r$ axis. In accordance with eq. (2.21), a potential perturbation

$$\delta\varphi = A_1 \mathrm{e}^{-kr} + A_2 \mathrm{e}^{k(r-d)} \tag{3.25}$$

will be assumed. We define a vector $\boldsymbol{A}$ with components $A_{1,2}$ and a vector $\boldsymbol{\zeta}$ whose components are the displacements $\zeta_{1,2}$ at the surfaces $r = 0$ and $r = d$, respectively. Setting again $\delta p = 0$, the boundary conditions (2.18), evaluated at both surfaces, become

$$\boldsymbol{M} \cdot \partial_t \boldsymbol{A} - a\boldsymbol{\zeta} = 0\,, \quad \partial_t \boldsymbol{\zeta} + k\boldsymbol{N} \cdot \boldsymbol{A} = 0\,, \tag{3.26}$$

where

$$\boldsymbol{M} = \begin{pmatrix} 1 & p \\ p & 1 \end{pmatrix}, \quad \boldsymbol{N} = \begin{pmatrix} 1 & -p \\ p & -1 \end{pmatrix}, \quad p = \mathrm{e}^{-kd}\,.$$

Eliminating now the displacement vector $\boldsymbol{\zeta}$ from these equations yields

$$\partial_t^2 \boldsymbol{A} = -ka\boldsymbol{M}^{-1} \cdot \boldsymbol{N} \cdot \boldsymbol{A} = -ka \begin{pmatrix} 1 & 0 \\ 0 & -1 \end{pmatrix} \cdot \boldsymbol{A}\,, \tag{3.27}$$

where

$$\boldsymbol{M}^{-1} = \Delta^{-1} \begin{pmatrix} 1 & -p \\ -p & 1 \end{pmatrix}$$

is the inverse and $\Delta = 1 - p^2$ the determinant of $\boldsymbol{M}$. The instability eigenvalue problem is already diagonal in the $\boldsymbol{A}$ representation. The normal mode solutions are

$$\boldsymbol{A} = A_1 \exp(\mp \mathrm{i}\sqrt{ak}\, t) \begin{pmatrix} 1 \\ 0 \end{pmatrix}, \quad \boldsymbol{A} = A_2 \exp(\mp \sqrt{ak}\, t) \begin{pmatrix} 0 \\ 1 \end{pmatrix}. \tag{3.28}$$

They correspond to a stable surface wave arising from the rear side and an unstable RT mode arising from the front side of the foil, respectively. As already mentioned, the growth rates are independent of the layer width in this model.

*3.3.2. Initial value problem*

The surface perturbations $\zeta_{1,2}$ are generally superpositions of both types of mode. Each surface is perturbed by the mode developing at the same surface and by an exponentially damped mode from the opposite surface. According to eq. (3.26), this superposition can be expressed in the form $\boldsymbol{\zeta} = \boldsymbol{M} \cdot \boldsymbol{X}$, where the components of $\boldsymbol{X}$ are proportional to those of $\boldsymbol{A}$. Choosing static initial corrugations $\boldsymbol{\zeta}_0$, $\boldsymbol{X}_0$ at $t = 0$, the evolution equations can be written as,

$$\boldsymbol{\zeta} = \boldsymbol{S} \cdot \boldsymbol{\zeta}_0 , \quad \boldsymbol{X} = \boldsymbol{T} \cdot \boldsymbol{X}_0 , \tag{3.29}$$

where

$$\boldsymbol{T} = \begin{pmatrix} c & 0 \\ 0 & C \end{pmatrix}, \quad c = \cos(\sqrt{ak}\, t) , \quad C = \cosh(\sqrt{ak}\, t) ,$$

$$\boldsymbol{S} = \boldsymbol{M} \cdot \boldsymbol{T} \cdot \boldsymbol{M}^{-1} = \Delta^{-1} \begin{pmatrix} c - p^2 C & -p(c - C) \\ -p(C - c) & C - p^2 c \end{pmatrix} .$$

At late times, when the unstable mode dominates, the surface amplitudes satisfy the relations,

$$\zeta_1 = p\zeta_2 , \quad \zeta_2 = \Delta^{-1}(\zeta_{20} - p\zeta_{10})C , \quad \zeta_2 - p\zeta_1 = (\zeta_{20} - p\zeta_{10})C . \tag{3.30}$$

At the unstable surface, the amplitude $\zeta_2$ is increased by the factor

$$\Delta^{-1}(1 - p\zeta_{10}/\zeta_{20}) = \frac{1 - \mathrm{e}^{-kd}\zeta_{10}/\zeta_{20}}{1 - \mathrm{e}^{-2kd}} \tag{3.31}$$

in comparison with the result for an infinitely thick layer. Especially for thin layers, this factor can describe an appreciable amplification of the initial amplitude $\zeta_{20}$. Only the relative perturbation $\zeta_2 - p\zeta_1$ evolves exactly according to the single mode RT instability. This behavior is an effect of mode interference in the initial state which will be discussed in more detail in the spherical shell problem.

*3.4. Stratified media*

We now discuss the stability eigenvalue problem for a stratified medium with an arbitrary number of interfaces. The characteristic equation for the possible normal mode frequencies and growth rates of multi-layered fluid systems was first derived by Webb and Greenhill [67, sect. 15]. The unstable roots are determined by a polynomial of arbitrarily high order and, in general, have to be calculated by numerical methods. This problem has been studied extensively by Mikaelian for RT instabilities [68], for Richtmyer–Meshkov instabilities [81], and for both of these instabilities with the inclusion of surface tension [82]. In the absence of surface tension, a hidden symmetry of the RT eigenvalue spectrum, corresponding to a specific inversion of the density profile, could be demonstrated. Furthermore, explicit growth rate calculations for various multi-layered fluid systems have been presented. The model can be applied to the design of surface coatings which optimize the surface stability against disruptive failure modes. Furthermore, it may serve as an approximation method for the investigation of continuous density profiles.

The instability theory for stratified fluid systems will now be considered. The discussion includes the stability eigenvalue problem of the RT instability, general properties of its eigenvalue spectrum, the

relationship with Rayleigh's eigenvalue problem for continuous media, and specific growth rate calculations for three layers with two coupled interfaces.

*3.4.1. Eigenvalue problem*

Let us consider an accelerated stratified medium consisting of $N+1$ superposed fluid layers. The equilibrium fluid configuration and the notation to be used are shown in fig. 4. The layer $i$ has the density $\rho_i$ and the thickness $d_i$. The normal mode perturbations are taken proportional to $\exp[i(kx - \omega t)]$ and are required to vanish at both boundaries $y_0$ and $y_{N+1}$ of the medium. In particular, these boundary conditions apply to the localized eigenmodes of an infinite medium if the limits $d_1 \to \infty$ and $d_{N+1} \to \infty$ are considered.

The boundary conditions, to be satisfied at each intermediate interface $i$, are those of eq. (3.1) with $v = 0$. The first jump condition in eq. (3.1) requires the continuity of the normal derivative $w = \partial_y \delta\varphi$. The potential (2.21) that has continuous normal derivatives $w_i = w(y_i)$ at $y_i$ is defined piecewise for each layer $y_{i-1} < y < y_i$ by the expression,

$$k\,\delta\varphi^{(i)} = \frac{1}{\sinh(kd_i)} \{w_i \cosh[k(y - y_{i-1})] - w_{i-1} \cosh[k(y - y_i)]\} . \tag{3.32}$$

This form can also be used for the first and the last layer by setting $w_0 = w_{N+1} = 0$. The boundary values $w_i$ are determined by $N$ continuity conditions,

$$[\rho k\,\delta\varphi]_i - (ak/\omega^2)[\rho]_i w_i = 0 , \tag{3.33}$$

following from eq. (3.1) for each interface $i$. We define an $N$-dimensional solution vector $\boldsymbol{w}$ with components $w_1, \ldots, w_i, \ldots, w_N$ and rewrite eqs. (3.32) and (3.33) as an eigenvalue problem of the form

$$Y\boldsymbol{A} \cdot \boldsymbol{w} = \boldsymbol{B} \cdot \boldsymbol{w} . \tag{3.34}$$

The nonvanishing matrix entries of $\boldsymbol{A}$ and $\boldsymbol{B}$ are given by the expressions

$$\begin{aligned} B_{ii} &= \rho_{i+1} - \rho_i , \\ A_{ii} &= \rho_{i+1} \coth(kd_{i+1}) + \rho_i \coth(kd_i) , \\ A_{i\,i-1} &= A_{i-1\,i} = -\rho_i / \sinh(kd_i) , \end{aligned} \tag{3.35}$$

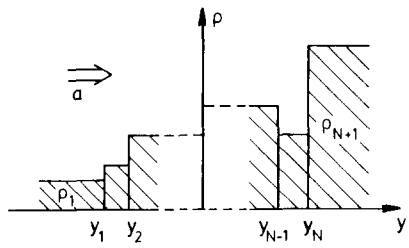


Fig. 4. Equilibrium fluid configuration of an accelerated stratified medium. The system consists of $N+1$ superposed fluid layers with $N$ internal interfaces. It can support $2N$ normal modes. The number of unstable modes is equal to the number of interfaces with adverse gradients, $\rho_{i+1} > \rho_i$.

where the matrix indices can assume values between 1 and $N$. The possible eigenvalues $Y = -\omega^2/ak$ are determined by the solubility condition,

$$\det|YA_{ij} - B_{ij}| = 0 . \tag{3.36}$$

The reason for using two matrices $\boldsymbol{A}$ and $\boldsymbol{B}$ instead of a single matrix $\boldsymbol{C} = \boldsymbol{B}^{-1} \cdot \boldsymbol{A}$ derives from the fact that both, $\boldsymbol{A}$ and $\boldsymbol{B}$ are symmetric while $\boldsymbol{C}$ generally is not. Equations (3.34)–(3.36) form the stability eigenvalue problem for a stratified medium with $N$ interfaces.

*3.4.2. Eigenvalue spectrum*

Some immediate conclusions concerning the eigenvalue spectrum will now be drawn:

(i) The spectrum consists of $N$ eigenvalues $Y$, corresponding to $2N$ eigenfrequencies $\omega$. We remark that $N$ is equal to the number of interfaces inside the medium and represents the degree of the characteristic polynomial (3.36).

(ii) All eigenvalues are real. This follows from the Hermitian form of eq. (3.34) after multiplication with the complex conjugate eigenvector $w^*$:

$$Y = \frac{w^* \cdot \boldsymbol{B} \cdot w}{w^* \cdot \boldsymbol{A} \cdot w} = \frac{w \cdot (\boldsymbol{B} \cdot w)^*}{w \cdot (\boldsymbol{A} \cdot w)^*} = \left( \frac{w^* \cdot \boldsymbol{B} \cdot w}{w^* \cdot \boldsymbol{A} \cdot w} \right)^* = Y^* . \tag{3.37}$$

For negative eigenvalues, the modes have real eigenfrequencies $\omega = \pm\sqrt{-Yak}$ and are therefore stable. For positive eigenvalues, unstable modes exist with positive growth rates $n = \sqrt{Yak}$.

(iii) Marginally stable modes with frequency $\omega \to 0$ can only exist at boundaries between two adjacent layers approaching the same density. The solutions of eq. (3.34) for $Y \to 0$ require

$$B_{jj} = \rho_{j+1} - \rho_j \to 0 , \quad w_i \to \delta_{ij} , \tag{3.38}$$

at one interface $j$, where $\delta_{ij}$ denotes the unit matrix. In the limit $\rho_{j+1} \to \rho_j$, the solution vector of the marginally stable mode has only a single component $j$, while all other interfaces can be treated as rigid. The corresponding eigenvalue near marginal stability can therefore be approximated in the form

$$Y = \frac{B_{jj}}{A_{jj}} = \frac{\rho_{j+1} - \rho_j}{\rho_{j+1} \coth(kd_{j+1}) + \rho_j \coth(kd_j)} . \tag{3.39}$$

(iv) The number of unstable modes is equal to the number of interfaces with a density inversion $\rho_{i+1} > \rho_i$. This assertion may be verified by induction in the following way. Suppose an additional interface is introduced inside a particular layer by slightly raising the density of the medium above that interface. This process will not change the number of the already existing unstable modes because an exchange of stability is only possible by passing through the state of marginal stability (3.38). At the additional interface, the eigenvalue is given by eq. (3.39). Consequently, the number of unstable modes increases by one if an interface with $\rho_{i+1} > \rho_i$ is added.

(v) The equilibrium is stable if and only if $\rho_{i+1} < \rho_i$ for all interfaces. In the short-wavelength limit each interface can be treated separately and the simple RT growth rate of eq. (3.3) becomes applicable. Therefore, the criterion $\rho_{i+1} < \rho_i$ is necessary for stability. According to the present conclusion (iv) the criterion is also sufficient. Long-wavelength modes, extending over several interfaces, do not provide a further destabilization of the system.

We remark that the self-adjoint form of the linear eigenvalue problem and the resulting conclusions (ii) and (v) are well known from the associated differential operators for continuous media [57]. However, the identification of stable, unstable, and marginally stable modes with discontinuities is specific for the stratified case.

In addition to these immediate conclusions, an interesting hidden symmetry of the eigenvalue spectrum was found by Mikaelian [68]. Setting $r_{ij} = \rho_i/\rho_j$, it can be expressed in the following form:

(vi) The eigenvalue spectrum is invariant with respect to an inversion of the density profile according to the rule:

$$r_{i1} \to 1/r_{N+2-i\,N+1}\,, \quad d_i \to d_{N+2-i}\,. \tag{3.40}$$

Mikaelian has shown that this transformation leaves the coefficients in the characteristic equation (3.36) invariant. Since the derivations become extensively long, the reader is referred to the original work for any details. However, a specific example of inversion symmetry will be given in section 3.5 and a general proof for continuous density profiles is presented in section 6.

*3.4.3. Continuum limit*

It may also be instructive to recover the eigenvalue problem for an inhomogeneous medium with a continuous density variation from the stratified fluid model. Although a positive answer can be found, it does not appear completely obvious. We remark that the flow inside each layer is irrotational potential flow, while the global eigenmode has a nonzero vorticity. In the stratified fluid model, this vorticity has to be generated across the discontinuities.

Consider now a sufficiently fine partition of a continuous density profile $\rho(y)$ into piecewise constant layers. The derivative of a function $f(y)$ at the layer $i$ can be defined as,

$$\partial_y f = (Df + [f]_i)/d_i\,. \tag{3.41}$$

This formula takes into account the continuous change $Df = (\partial_y f)_i d_i$ of $f$ inside the layer and its possible jump $[f]_i = f(y_{i^+}) - f(y_{i^-})$ across the interface $i$. Setting now $f = \rho\,\partial_y w$, the two contributions in eq. (3.41) become

$$\begin{aligned} Df &= \rho_i D(\partial_y w) = \rho_i(\partial_y^2 w_i)d_i = k^2\rho_i w_i d_i\,, \\ [f]_i &= k[\rho k\delta\varphi]_i = \frac{ak^2}{\omega^2}\,[\rho]_i w_i = \frac{ak^2}{\omega^2}\,(\partial_y\rho)_i d_i w_i\,, \end{aligned} \tag{3.42}$$

where eqs. (2.2) and (3.33) have been used. Combining eqs. (3.41) and (3.42) yields

$$\partial_y^2 w + \frac{\partial_y\rho}{\rho}\,\partial_y w - k^2\left(1 + \frac{a}{\omega^2}\,\frac{\partial_y\rho}{\rho}\right)w = 0\,. \tag{3.43}$$

This is the standard form of the RT eigenvalue problem for incompressible fluids with continuous density variations. It will be further discussed in section 6.

### 3.5. Three-layer model

To illustrate these remarks, we now specialize the results to the case of three layers with $N = 2$ interfaces. A discussion of the three-layer model can also be found in Mikaelian's work [68].

#### 3.5.1. Analytic evaluation

We assume a finite thickness $d_2 = d$ of the intermediate layer and half-infinite boundary regions, $d_{1,3} \to \infty$. In this case, the matrices (3.35) reduce to the form

$$A_{ij} = \frac{1}{S}\begin{pmatrix} \rho_1 S + \rho_2 C & -\rho_2 \\ -\rho_2 & \rho_2 C + \rho_3 S \end{pmatrix}, \qquad B_{ij} = \begin{pmatrix} \rho_2 - \rho_1 & 0 \\ 0 & \rho_3 - \rho_2 \end{pmatrix}, \tag{3.44}$$

where $S = \sinh(kd)$ and $C = \cosh(kd)$. The eigenvalues of eq. (3.36) are the roots

$$Y_{1,2} = (-g \pm \sqrt{g^2 - 4fh})/2f \tag{3.45}$$

of the quadratic $fY^2 + gY + h = 0$, with

$$f = (r_{21} + r_{32})S + (1 + r_{21}r_{32})C\,, \quad g = (1 - r_{21}r_{32})(S + C)\,, \quad h = (r_{21} - 1)(r_{32} - 1)S\,, \quad r_{ij} = \rho_i/\rho_j\,. \tag{3.46}$$

Already this simple example shows that the analysis becomes greatly complicated in the presence of a large number of boundary conditions. The result (3.45) can illustrate the general properties of the eigenvalues described above.

Noting that $f > 0$, the number of positive eigenvalues is found equal to the number of density inversions. If both density ratios $r_{21}$ and $r_{32}$ are smaller than one, both eigenvalues are negative ($g > 0, h > 0$). If only one ratio is larger than 1, the larger eigenvalue $Y_1$ becomes positive, while $Y_2$ is still negative ($h < 0$). Finally, if both ratios are larger than 1, both eigenvalues are positive ($g < 0, h > 0$).

One can also recognize that the eigenvalues (3.45) are invariant under an exchange of the density ratios at the two interfaces: $r_{21} \to r_{32}$ and $r_{32} \to r_{21}$. Although this symmetry is obvious for widely separated interfaces, it holds more generally for an arbitrary width of the intermediate layer. This conforms exactly to the inversion invariance (3.40) of the eigenvalue spectrum.

We now discuss the basic limits of thick and thin layers where simple growth rate expressions can be obtained. Assuming $kd \gg 1$, the eigenvalues (3.45) become

$$Y_1^{\infty} = \alpha_{21}\,, \quad Y_2^{\infty} = \alpha_{32}\,, \quad \alpha_{ij} = (r_{ij} - 1)/(r_{ij} + 1)\,. \tag{3.47}$$

They describe independent surface modes for the two separated interfaces. In the opposite limit, $kd \to 0$, the two eigenvalues can be approximated by the expressions,

$$Y_1^0 = -\frac{g}{f} = \alpha_{31}\,, \quad Y_2^0 = -\frac{h}{g} = \frac{(r_{21}-1)(r_{32}-1)}{r_{31}-1}\,kd\,. \tag{3.48}$$

The first root becomes independent of the layer width, describing the interface between the boundary layers in the absence of an intermediate layer. If this mode is stable, the stability of the intermediate layer can be governed by the second root. Here the growth is largely reduced by the finite layer width.

### 3.5.2. *Numerical evaluation.*

The three-layer model can demonstrate some important features of accelerated fluid systems. If the maximum density is assumed in the intermediate layer ($r_{21} > 1, r_{32} < 1$), the model describes an accelerated foil with an unstable front side and a stable rear side. In fig. 5, the growth rate of the

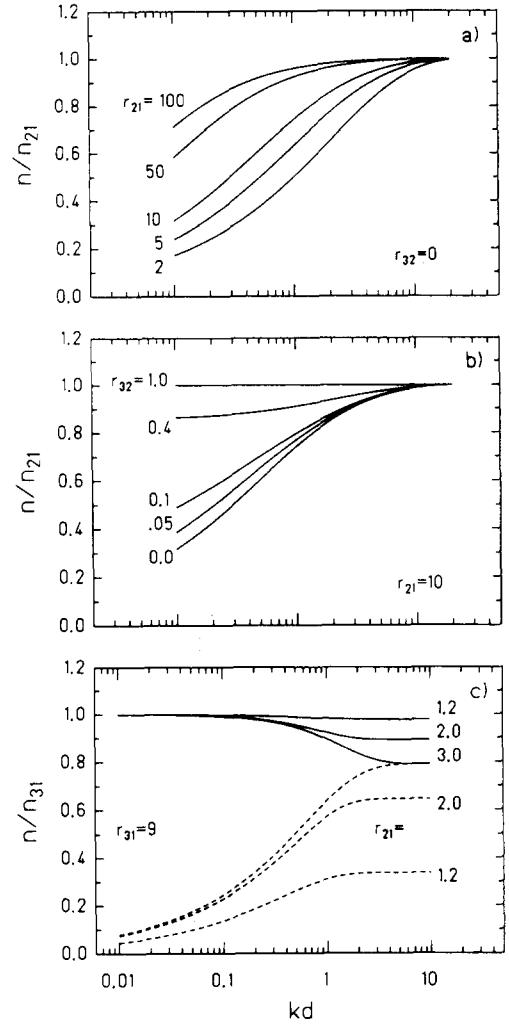


Fig. 5. Stability of a stratified medium with two interfaces separated by a distance $d$. The instability growth rate $n$ is compared with the growth rate $n_{ij}$ for a single interface with the density ratio $r_{ij} = \rho_i/\rho_j$. (a) Foil of density $\rho_2$ with a free backside ($r_{32} = 0$) and a finite density ratio $r_{21} > 1$ at the front side. (b) Same as in (a) but with a finite density ratio $r_{32} < 1$ at the backside of the foil. (c) Coating layer with two unstable surfaces, $r_{21} > 1$ and $r_{32} > 1$, between two boundary layers with a fixed density ratio $r_{31} = 9$. The two growth rates are represented by solid and dashed lines.

unstable mode is compared with the growth rate $n_{21} = \sqrt{\alpha_{21} ak}$ that would correspond to an infinitely thick layer.

In fig. 5a, the background density $\rho_3$ has been set equal to zero and the density ratio $r_{21}$ at the front side is varied. One can recognize significant growth reduction for thin layers, depending on the density of the accelerating medium. A pusher medium with a moderately high density may thus effectively prevent the growth of long-wavelength modes. The effect disappears for large density ratios, $r_{21} \to \infty$, in accordance with the predictions of the free-surface model (section 3.3).

In fig. 5b, the background density is varied. If $r_{31} = r_{21} r_{32} < 1$, the results are similar to those of fig. 5a. If $r_{31} > 1$, the asymptotic behavior becomes different for $kd \to 0$. Here, a finite growth rate is approached for thin layers, corresponding to an exchange of the unstable root from the branch $Y_2^0$ to the branch $Y_1^0$ in eq. (3.48). If the background density exceeds the pusher gas density, the growth reduction effects become reduced.

If both density ratios are larger than one ($r_{21} > 1$, $r_{32} > 1$), a surface coating in front of an unstable background surface can be modeled. Such coatings have been called anti-mix layers, preventing the intermixing at the interface between different media. The intermediate layer reduces the growth rate $n_{31} = \sqrt{\alpha_{31} ak}$ of the background surface, but at the expense of an additional unstable root.

The variation of the two unstable branches with the layer width is represented in fig. 5c by solid and dashed lines. As the width of the intermediate layer is increased, the larger growth rate becomes reduced until the asymptotic values (3.47) for separated interfaces are approached. This limit is reached to a good approximation when $kd \gtrsim 3$–5. To obtain the maximum possible growth reduction, the density ratios at both steps have to be equal, $r_{21} = r_{32} = \sqrt{r_{31}}$. The corresponding density of the intermediate anti-mix layer is $\rho_2 = \sqrt{\rho_1 \rho_3}$. This result was first obtained by Mikaelian [68].

The same conclusion can be drawn for an arbitrary number of intermediate layers. For a monotonic increasing step-profile function with $N$ interfaces, the maximum growth rate will be minimized in the short-wavelength limit, if all density ratios are chosen to be equal. The corresponding density of the layer $i + 1$ is then given by,

$$\rho_{i+1} = r\rho_i = r^i \rho_1 , \quad r = r_{N+11}^{1/N} . \tag{3.49}$$

## 4. Stability of spherical boundaries

Spherical geometries lead to a number of modifications in the analysis of surface instabilities. The stability criterion becomes much more restrictive in the presence of flow convergence, where even an unaccelerated surface is unstable. Time-dependence of the basic flow is a generic feature in these geometries. Conceptually, we no longer analyse the stability of an equilibrium or steady-state, but consider the evolution of symmetry perturbations for particular symmetric reference flows. In general, this stability problem can no longer be described by independent normal modes. Perturbation evolution is therefore much more dependent on particular initial data, shell motions and shell structures.

In this section an overview is given on the stability of spherical cavities and shells under various circumstances. The unperturbed dynamics of incompressible spherical shells is first summarized as a reference for the stability analysis. Then, a discussion of the perturbation equation for cavities is presented, including the major convergence effects, the amplification of cavity oscillations, and Birkhoff's stability criterion. The cavity model will be extended to account for spherical shells of finite thickness. Special attention will be devoted to thin shells, where a number of perturbation results can

be obtained analytically. The stability of shells of finite thickness is finally illustrated by numerical calculations for representative implosion models.

### 4.1. Symmetric shell motions

The motion of spherically symmetric cavities in an infinitely extended incompressible fluid plays an important role in the theory of cavitation bubbles. This problem has already been studied by Rayleigh [83]. An introduction to the theory of cavitation bubbles can be found in the textbook by Batchelor [84]. Generalizations of the cavity model to compressible flows have been discussed by Hickling and Plesset [85]. Further mass exchange processes have been considered by Prosperetti [86].

The following discussion is addressed to the dynamics of incompressible spherical shells of finite thickness. As in section 2.3.2, a $\delta$-dimensional surface is assumed, where plane ($\delta = 1$), cylindrical ($\delta = 2$), and spherical ($\delta = 3$) geometries are included. In this section, only the unperturbed spherically symmetric basic flows are considered. The shell parameters are indicated in fig. 6, consisting of the inner radius $R_1(t)$, the outer radius $R_2(t)$, the thickness $d(t) = R_2(t) - R_1(t)$, and a constant mass density $\rho$. For simplicity of notation, we will often use the abbreviations

$$R(t) = R_1(t)\,, \quad S(t) = R_1(t)/R_2(t)\,, \quad V(t) = \dot{R}_1(t)\,. \tag{4.1}$$

The shell is subject to an inside pressure $p_1(t)$ and an outside pressure $p_2(t)$. Its motion is therefore driven by the pressure difference $\Delta p = p_1 - p_2$. If $\Delta p = 0$, the motion is called ballistic [69].

The dynamics of incompressible spherical shells follows from simple conservation laws for its mass and its energy. Alternatively, dynamical equations for the shell boundaries subject to the applied pressure can be derived. Both approaches will be outlined and then illustrated by specific examples.

#### 4.1.1. Mass conservation

In the incompressible shell model, mass conservation governs the evolution of the shell thickness. One can therefore simply relate the motion of the outer surface to the motion of the inner surface. Using eq. (2.20), the velocity of the outer surface is found to be,

$$\dot{R}_2 = v_0(R_2) = VS^{\delta-1}\,. \tag{4.2}$$

The flux through the inner surface is equal to the flux through the outer surface and the mass integral

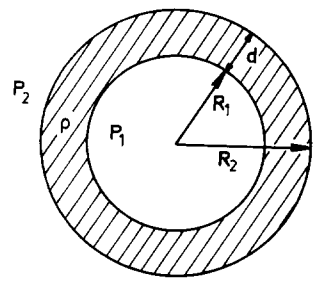


Fig. 6. Incompressible shell of density $\rho$ and thickness $d$. The dynamics of the shell boundaries $R_{1,2}(t)$ is determined by the pressure difference $\Delta p = p_1(t) - p_2(t)$ between the inner cavity and the outer surroundings. (From ref. [78]).

$$M = \rho \int_{R_1}^{R_2} \mathrm{d}r\, r^{\delta-1} = \frac{\rho}{\delta}\,(R_2^{\delta} - R_1^{\delta}) \tag{4.3}$$

is conserved. The outer radius can therefore be expressed by the inner radius and the corresponding initial values in the form,

$$R_2 = (R_{20}^{\delta} - R_{10}^{\delta} + R_1^{\delta})^{1/\delta}\,. \tag{4.4}$$

Noting eqs. (4.2) and (4.4), it is sufficient to examine the motion of one shell boundary, say $R_1$, only.

*4.1.2. Energy conservation*

The discussion of shell dynamics is considerably simplified by making use of the energy conservation law. In the following it is assumed that the surface pressure is prescribed as a function of the shell radius without having an explicit time-dependence. It is then possible to derive the dynamics from a simple potential energy expression.

Let us first define the kinetic energy of the shell by the integral

$$T = \int_{R_1}^{R_2} \mathrm{d}r\, \tfrac{1}{2}\rho v_0^2 r^{\delta-1}\,. \tag{4.5}$$

Inserting eq. (2.20), one obtains the expressions,

$$\begin{aligned} T &= \tfrac{1}{2}\rho V^2 (R_2 - R_1)\,, \quad \text{for } \delta = 1\,,\\ T &= -\tfrac{1}{2}\rho V^2 R^2 \ln S\,, \quad \text{for } \delta = 2\,,\\ T &= \tfrac{1}{2}\rho V^2 R^3 (1 - S)\,, \quad \text{for } \delta = 3\,. \end{aligned} \tag{4.6}$$

If the shell moves ballistically, the kinetic energy $T$ is conserved. More generally, one has to include a potential energy,

$$W = W_0 - \int_0^t \mathrm{d}t\,(\dot{R}_1 R_1^{\delta-1} p_1 - \dot{R}_2 R_2^{\delta-1} p_2)\,, \tag{4.7}$$

arising from the work that is delivered to the shell by pressure forces acting on its surface. Making use of eq. (4.2) and considering the pressure difference $\Delta p = p_1(R_1) - p_2(R_2) = \Delta p(R)$ as a known function of the inner radius, there follows

$$W = W_0 - \int_{R_0}^{R(t)} \mathrm{d}R\, R^{\delta-1}\, \Delta p(R)\,. \tag{4.8}$$

The total energy $E = T + W$ is conserved during the shell motion. From this energy integral one obtains immediately the surface velocity $V$ as a function of the shell radius $R$. Examples will be given below.

*4.1.3. Dynamics of shell boundaries*

A somewhat more systematic treatment of shell motions may be based directly on the dynamical equation (2.6). Inserting eqs. (2.19) and (2.20) into eq. (2.6) and taking the difference between the boundary conditions at the inside and the outside shell surface, one can derive an expression for the pressure difference $\Delta p = p_1 - p_2$. For plane geometry, this equation is simply Newton's law,

$$M\ddot{R} = \Delta p \,, \tag{4.9a}$$

applied to a fluid element with areal mass density $M = \rho d$. In cylindrical and spherical geometry, the corresponding equations are

$$(R\ddot{R} + V^2)\ln(1/S) - \tfrac{1}{2}V^2(1 - S^2) = \Delta p/\rho \,, \tag{4.9b}$$

$$(R\ddot{R} + \tfrac{3}{2}V^2)(1 - S) - \tfrac{1}{2}V^2 S(1 - S^3) = \Delta p/\rho \,, \tag{4.9c}$$

respectively. These equations determine the motion for an arbitrarily prescribed pressure law. One can convince oneself that their energy integrals are identical with the energy conservation law given by eqs. (4.6) and (4.8). Simplifications can be gained for either thin or thick shells. In the limit of thin shells, one can recover from eq. (4.9) the equation of motion for the mass element (4.3)

$$M\ddot{R} = R^{\delta-1}\,\Delta p \tag{4.10}$$

subject to the force $R^{\delta-1}\,\Delta p$. In the opposite limit of thick shells, eqs. (4.9b) and (4.9c) reduce to the cavity equations,

$$(R\ddot{R} + V^2)\ln(1/S) = \Delta p/\rho \quad (\delta = 2) \,, \tag{4.11a}$$

$$(R\ddot{R} + \tfrac{3}{2}V^2) = \Delta p/\rho \quad (\delta = 3) \,. \tag{4.11b}$$

We now discuss some specific shell motions being of particular interest for the stability analysis. Since the time does not appear explicitly, one can choose the radius $R$ as the independent variable. The perturbation evolution is then only dependent on the functions $V(R)$ and $\ddot{R}(R)$ that will be provided in the following. All these examples will be given for the three-dimensional case ($\delta = 3$) only.

*4.1.4. Ballistic motion*

The ballistic motion of an undriven shell ($\Delta p = 0$) is often realized after an initial acceleration phase when the applied pressure becomes negligibly small compared with the kinetic energy. It plays therefore an important role for the study of converging and diverging flows. Using eq. (4.6), the conservation law for the total energy $E$ becomes,

$$E = T = \tfrac{1}{2}\rho V^2 R^3(1 - S) \,. \tag{4.12}$$

To simplify the notation, we will always choose units of lengths and time such that $V = 1$ at $R = 1$. The corresponding value of $S$ at $R = 1$ will be denoted as $S_*$. With this convention, ballistic motion is governed by the relations,

$$E = \tfrac{1}{2}\rho(1 - S_*)\,, \tag{4.13a}$$

$$V = \pm\left(\frac{1 - S_*}{1 - S}\,\frac{1}{R^3}\right)^{1/2}\,, \tag{4.13b}$$

$$\ddot{R} = -\tfrac{3}{2}(V^2/R)[1 - \tfrac{1}{3}(S + S^2 + S^3)]\,, \tag{4.13c}$$

where eqs. (4.12) and (4.9c) have been used. One can recognize a strong divergence of the surface velocity for converging flows. The surface acceleration is always directed toward the cavity, indicating RT stability at the inner shell surface. Nevertheless, cavity oscillations can be amplified due to the converging geometry as will be discussed below.

For cavities ($S$, $S_* \ll 1$), the ballistic equation of motion can even be obtained explicitly as a function of time by integration of eq. (4.13b). Choosing the initial condition $R(0) = 0$, the solution is found to be,

$$R = (\tfrac{5}{2}|t|)^{2/5}\,, \quad V = \tfrac{2}{5}R/t\,, \quad \ddot{R} = -\tfrac{6}{25}R/t^2\,. \tag{4.14}$$

Negative times describe imploding and positive times expanding cavities.

*4.1.5. Acceleration*

Another important case concerns the acceleration of a thin shell from rest toward the shell center. According to eq. (4.10), constant acceleration of thin shells requires a pressure law,

$$\Delta p = -p_0(R_0/R)^2\,, \tag{4.15}$$

where $p_0$ denotes the initial pressure applied to the outside surface at $R = R_0$. The pressure increases as $R^{-2}$ to compensate for the decreasing surface area. Using eq. (4.15) in eq. (4.8), the potential energy becomes,

$$W = W_0 + p_0R_0^2(R - R_0)\,. \tag{4.16}$$

Assuming that the shell has been at rest, initially, the energy conservation law becomes $T + W - W_0 = 0$, yielding

$$\tfrac{1}{2}\rho V^2R^3(1 - S) - p_0R_0^2(R_0 - R) = 0\,. \tag{4.17}$$

We choose again the normalization convention $V = 1$, $S = S_*$ at $R = 1$ to obtain,

$$p_0 = \tfrac{1}{2}\,\rho(1 - S_*)/R_0^2(R_0 - 1)\,, \tag{4.18a}$$

$$V = -\left(\frac{1 - S_*}{(1 - S)R^3}\,\frac{R_0 - R}{R_0 - 1}\right)^{1/2}\,, \tag{4.18b}$$

$$\ddot{R} = -\,\frac{1 - S_*}{(1 - S)R^3}\,\frac{1}{2(R_0 - 1)} - \frac{3}{2}\,\frac{V^2}{R}\left(1 - \frac{S + S^2 + S^3}{3}\right). \tag{4.18c}$$

These equations determine the motion of an accelerated shell subject to the pressure law (4.15).

*4.1.6. Deceleration*

Converging shells will compress the internal cavity gas until the pressure has become sufficiently high to cause deceleration and ultimately stagnation of the inside surface motion. A simple deceleration model is given by a power law,

$$\Delta p = p_s (R_s/R)^\nu \,, \tag{4.19}$$

where $p_s$ denotes the cavity pressure at the stagnation point radius $R = R_s$. If the external pressure is negligible, the exponent $\nu$ may be related to an equation of state of the cavity gas. For a polytropic law, $p = \text{const.}\ \rho^\gamma$, one has $\nu = 3\gamma$. For instance, compression of a degenerate Fermi gas in ICF applications would correspond to the values $\gamma = 5/3$ and $\nu = 5$. However, various other choices of $\nu$ may be of interest, especially when the external pressure is not negligible during the compression phase.

Evaluating eq. (4.8) with eq. (4.19) leads to the potential energy,

$$\begin{aligned} W &= W_s + \frac{p_s R_s^\nu}{\nu - 3} (R^{-\nu+3} - R_s^{-\nu+3}) \,, \quad \text{for } \nu \neq 3 \\ W &= W_s - p_s R_s^\nu \ln(R/R_s) \,, \qquad\quad \text{for } \nu = 3 \,. \end{aligned} \tag{4.20}$$

The special case $\nu = 3$ corresponds to isothermal compression with $\gamma = 1$. It can be obtained from the general expression for $\nu \neq 3$ by taking the limit $\nu \to 3$. It will therefore not be treated explicitly in the following.

Proceeding as in the previous examples, we set $T + W - W_s = 0$ and $V = 1$, $S = S_*$ at $R = 1$. This yields,

$$p_s = \frac{\nu - 3}{2} \frac{\rho(1 - S_*)}{R_s^3 (1 - R_s^{\nu-3})} \,, \tag{4.21a}$$

$$V = -\left( \frac{1 - S_*}{1 - S} \frac{1}{R^\nu} \frac{R^{\nu-3} - R_s^{\nu-3}}{1 - R_s^{\nu-3}} \right)^{1/2} \,, \tag{4.21b}$$

$$\ddot{R} = \frac{1 - S_*}{1 - S} \frac{R_s^{\nu-3}}{1 - R_s^{\nu-3}} \frac{\nu - 3}{2R^{\nu+1}} - \frac{3}{2} \frac{V^2}{R} \left( 1 - \frac{S + S^2 + S^3}{3} \right) . \tag{4.21c}$$

The acceleration includes a positive repulsive contribution due to the cavity pressure and a negative ballistic contribution due to the converging geometry.

*4.1.7. Implosions*

The shell dynamics will now be illustrated for a particular implosion model that will form the basis of the stability analysis in section 4.4.3. Initially, a thin shell with inner radius $R_0 = 2$ and aspect ratio $\mathcal{A} = R_0/d_0$ is assumed. The shell is subject to the acceleration law (4.15) up to the intermediate radius $R = 1$. Subsequently, its kinetic energy is transformed into internal energy of an enclosed Fermi gas by assuming eq. (4.19) with $\nu = 5$. The inner radius stagnates at $R_s$, having achieved a radial convergence ratio of $\mathcal{C} = R_0/R_s$.

In fig. 7, we have represented the evolution of the shell boundaries for two different designs with parameters (a) $\mathcal{A} = 100$, $\mathcal{C} = 40$ and (b) $\mathcal{A} = \mathcal{C} = 30$. One can recognize an early stagnation of the outer

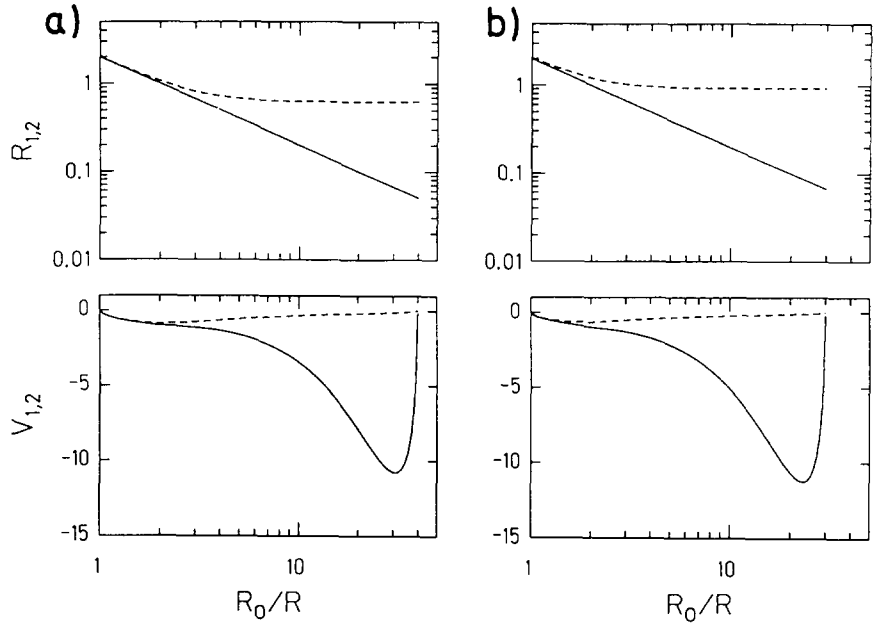


Fig. 7. Radius and velocity histories for spherically symmetric shell implosions. A shell with initial aspect ratio $\mathscr{A} = R_0/d_0$ is driven by an outside pressure $p_2 \sim R^{-2}$ from $R_0$ up to $R_0/R = 2$. Afterwards it implodes against an inside Fermi-gas pressure $p_1 \sim R^{-5}$ and stagnates at a final convergence ratio $\mathscr{C} = R_0/R_s$. Solid (dashed) lines refer to the inner (outer) surface and the variables are normalized by setting $R = V = 1$ at $R_0/R_s = 2$. (a) $\mathscr{A} = 100$, $\mathscr{C} = 40$, (b) $\mathscr{A} = \mathscr{C} = 30$. (From ref. [78].)

surface after acceleration. In contrast, the inner surface is further accelerated during a ballistic convergence phase and reaches a peak velocity around 12 prior to stagnation. The maximum velocity $V_m = \max|V|$, reached at radius $R_m$, follows from the condition $\ddot{R} = \dot{V} = (\partial_R V)V = 0$. Using eq. (4.21) and assuming $S \ll 1$ yields

$$R_m = (\nu/3)^{1/(\nu-3)} R_s ,$$

$$V_m = \left( (1 - S_*) \frac{R_s^{-3}}{1 - R_s^{\nu-3}} \frac{(\nu/3) - 1}{(\nu/3)^{1/(1-3/\nu)}} \right)^{1/2} = \left[ \frac{2}{3} \frac{p_s}{\rho} \left( \frac{R_s}{R_m} \right)^{\nu} \right]^{1/2} . \tag{4.22}$$

The ratio $R_m/R_s$ determines the deceleration distance of the shell and depends only on the pressure exponent $\nu$. Some numerical values are given in table 2. Large values of $\nu$ describe a sudden deceleration corresponding to a short deceleration distance. Conversely, small $\nu$ values can describe more gradual decelerations over longer distances. The maximum surface velocity $V_m$ increases with the convergence ratio but decreases with the initial aspect ratio. It is also simply related to the cavity pressure $p_s$ reached at the stagnation point.

Table 2
Deceleration distance of a stagnating incompressible shell. The cavity pressure is assumed as a power law $\sim R^{-\nu}$ of the inner shell radius. The exponent $\nu = 5$ corresponds to a degenerate Fermi gas. The radius $R_m$ marks the beginning and the radius $R_s$ the end-point of the deceleration phase. (From ref. [71])

| | $\nu = 0$ | $\nu = 0.1$ | $\nu = 0.5$ | $\nu = 1.0$ | $\nu = 3.0$ | $\nu = 5.0$ | $\nu = 10$ | $\nu = \infty$ |
|---|---|---|---|---|---|---|---|---|
| $R_m/R_s$ | $\infty$ | 3.2 | 2.0 | 1.7 | 1.4 | 1.3 | 1.2 | 1.0 |

## 4.2. Cavities

We will now discuss the stability of cylindrical and spherical cavities in an infinitely extended fluid. The cavity model can provide some insight into the stability of converging flows in the absence of shell effects. A discussion of the cavity stability problem is contained in two mathematical notes by Birkhoff [50, 51]. Apparently, the perturbation equations were first derived in an unpublished work by Penney and Price. A general stability criterion and an explicit solution for cavity oscillations was obtained by Birkhoff. Plesset [52] derived similar perturbation equations for spherical boundaries between two incompressible media of different densities. This model, however, requires a mass source or sink at the origin. One should also notice that the cavity problem is related, although not equivalent, to the gravitational perturbation problem for spherical bodies. Gravitational oscillations of a liquid globe are known as Kelvin modes. A detailed discussion of the latter problem has been given by Chandrasekhar [57].

### 4.2.1. Surface equation

The perturbation on a spherical cavity can be expanded into trigonometric functions ($\delta = 2$) or Legendre polynomials ($\delta = 3$) as described in section 2.3.3. We assume the single mode perturbations (2.24) with mode numbers $l = 1, 2, 3, \ldots$ and $j = l + \delta - 2$. Noting eq. (2.20) and using that

$$\partial_t[(R\partial_r \delta\varphi)|_{r=R}] = -j\, \partial_t \delta\varphi|_{\eta=1}\,, \tag{4.23}$$

the boundary condition (2.18b) can be written in the form

$$\partial_t(R\partial_t\zeta) + (\delta - 1)\, \partial_t(\dot{R}\zeta) + j\, \partial_t \delta\varphi|_{\eta=1} = 0\,. \tag{4.24}$$

Eliminating $\delta\varphi$ from eqs. (2.18a) and (4.24), there follows

$$\partial_t^2\zeta + \delta \frac{\dot{R}}{R}\, \partial_t\zeta - \frac{l-1}{R}\, \ddot{R}\zeta = \frac{j}{R}\, \frac{\delta p}{\rho}\,. \tag{4.25}$$

Equation (4.25) governs the evolution of the surface displacement $\zeta$ for arbitrary radial motions and mode numbers. One can recognize similarities with eq. (3.5), governing RT instability in plane geometry, but also major differences because of the variation of the radius with time.

We first attempt to give a more physical interpretation of the convergence effects described by eq. (4.25). Defining $k = j/R$ and $m = \rho R^{\delta-1}/k$, one can rewrite eq. (4.25) as an equation of motion,

$$\partial_t(m\, \partial_t\zeta) - \frac{l-1}{l+\delta-2}\, m\ddot{R}k\zeta = R^{\delta-1}\, \delta p\,, \tag{4.26}$$

with a time-dependent mass. Convergence effects are related to the variation of $m$ and $k$ with the radius. These variations correspond to the time-dependent periodicity length $L = 2\pi R$ and surface area $\sim R^{\delta-1}$ of the system. In addition, geometry effects are present for low $l$ modes. They slightly reduce the numerical coefficient of the buoyancy term and lead to its elimination for $l = 1$. This mode describes translations of the sphere without fluid interchange across the sphere. Being interested in the evolution of asymmetries, we will assume $l > 1$ in the following. Also, the external pressure force in eq. (4.26) will be omitted, in accordance with the discussion in section 3.2.5.

*4.2.2. Unaccelerated motion*

A new feature of converging flow consists in the possibility of amplification in the absence of acceleration. If a cavity implodes with a constant surface velocity $V$ and zero acceleration, $\ddot{R} = 0$, the perturbed momentum $m\,\partial_t \zeta$ is conserved. This conservation law implies that the normalized amplitude $A = \zeta/R$ grows as a function of the convergence ratio $q = R_0/R$ according to the formula

$$A = q\left(A_0 + \frac{1}{\delta - 1}(1 - q^{\delta - 1})B_0\right), \tag{4.27}$$

where $A_0 = \zeta_0/R_0$ and $B_0 = \partial_t \zeta_0/V$ denote initial values at $R = R_0$. For static initial corrugations ($B_0 = 0$), the displacement $\zeta$ remains constant but the relative amplitude $A$ still grows in proportion to the convergence ratio. If, on the other hand, $B_0 \neq 0$, the displacement itself diverges with the inverse of the surface area and $A$ grows as $q^{\delta}$. These convergence effects are independent of the mode number.

*4.2.3. Cavity oscillations*

If the surface is accelerated toward the cavity, surface oscillations can develop. Although the acceleration is stabilizing, it usually cannot prevent the amplification of the oscillation amplitudes. As an important example, we consider the ballistic equation of motion (4.14) for three-dimensional cavities. Inserting this solution into eq. (4.25) yields

$$\partial_t^2 \zeta + \tfrac{6}{5} t^{-1}\,\partial_t \zeta + \tfrac{6}{25}(l-1)t^{-2}\zeta = 0\,. \tag{4.28}$$

Choosing $s = \ln q$ as the independent variable, the solutions of eq. (4.28) can be expressed in the form

$$\zeta = \mathrm{e}^{s/4}(C_1\,\mathrm{e}^{\mathrm{i}\kappa s} + C_2\,\mathrm{e}^{-\mathrm{i}\kappa s})\,, \tag{4.29}$$

with constants $C_{1,2}$ and

$$\kappa = \tfrac{1}{4}\sqrt{25(l-1) - l} \approx 1.25\sqrt{l-1}\,.$$

Except for $l = 1$, the exponent $\kappa$ is real. Taking the initial conditions into account and choosing the same notation as in eq. (4.27), yields the result

$$A = q^{5/4}[A_0 \cos(\kappa s) - (A_0/4 + B_0)\kappa^{-1} \sin(\kappa s)]\,. \tag{4.30}$$

It describes cavity oscillations whose frequencies increase with the square root of the mode number. This behavior is in accordance with the dispersion relation (3.2) for stable gravity modes. In addition, eq. (4.30) leads to an amplification of the oscillation amplitudes with the convergence ratio. One should notice that the amplification factor is independent of the mode number and considerably weaker than for unaccelerated motion. Acceleration can therefore partly compensate the convergence effects that are expressed by eq. (4.27).

The evolution of some cavity modes with $l = 2, 4, 8, 16$ is represented in fig. 8. The figure shows the solution (4.30) for the initial amplitudes $A_0 = 0.01$, $B_0 = 0$ and for typical convergence ratios of $\approx$25–30. Oscillations can be recognized even for low $l$ modes and the amplitudes can reach critical values of $\approx$0.5–0.7. We remark that the normalized amplitude $A = \zeta/R$ indicates stability failure when $A$ approaches unity.

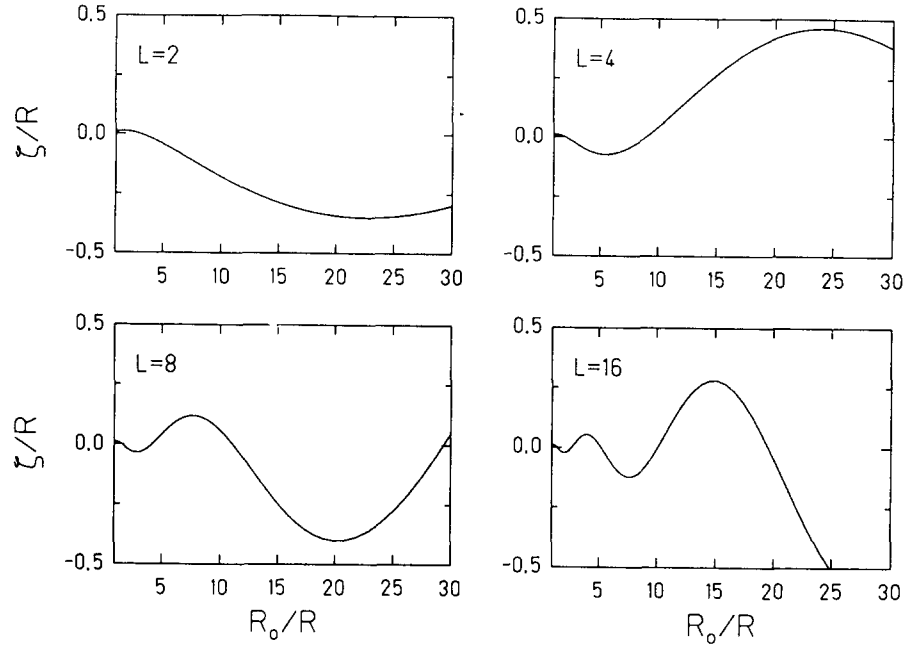


Fig. 8. Surface oscillations of a ballistically imploding spherical cavity in an infinitely extended fluid. The relative surface displacement amplitude $\zeta/R$ has been calculated from the solution (4.30) with an initial amplitude $\zeta_0/R_0 = 0.01$ for different mode numbers $l$. (From ref. [78].)

### 4.2.4. *Stability criterion*

A general stability criterion for the homogeneous part of the differential equation (4.25) has been proved by Birkhoff [50, 51]. It requires

$$\ddot{R} < 0\,, \quad R\dddot{R} + (2\delta - 1)\dot{R}\ddot{R} < 0\,, \tag{4.31}$$

for stability. According to the first condition the acceleration has to be directed toward the cavity, which avoids Rayleigh–Taylor instability. If the acceleration is assumed constant and negative, the second condition becomes $\dot{R} > 0$. Accordingly, there exist no stable converging flows in this case. The stability criterion is an immediate consequence of the identity

$$\partial_t(\zeta^2 + p^2/f) = -(p/f)^2\,\partial_t f\,, \tag{4.32}$$

derived from eq. (4.26) with

$$p = m\,\partial_t\zeta\,, \quad f = -\frac{l-1}{l+\delta-2}\,m^2 k\ddot{R}\,.$$

The displacement remains bounded if both $f > 0$ and $\partial_t f > 0$. These conditions are identical with those stated in eq. (4.31).

## 4.3. *Shell perturbations*

Incompressible shells represent a simple but physically instructive model for the stability and

symmetry issues in ICF implosions. The spherical shell model can describe mutual dependences in the evolution of outside and inside surface instabilities. The outside RT instability occurs during the acceleration phase. Its perturbations can penetrate the shell and cause cavity oscillations during the convergence phase. These are further amplified by an inside RT instability during the deceleration phase. The stability analysis is considerably more complicated than the analysis for plane layers of finite width as described in section 3.3. These complications arise from the time-dependent shell dynamics and require a careful analysis especially for the evolution of low $l$ modes.

The stability of incompressible shells has been examined in the ICF context by Book and Bodner [69]. In this work, the perturbation equations have been derived and explicit solutions for ballistic motions of thick and thin shells could be found. Furthermore, rapidly oscillating modes could be closely approximated by an adiabatic invariant. An extension of the analysis to more general types of shell motions, shell structures and initial data has been given in ref. [78] by the present author. This work includes a complete analytic solution of the thin shell problem for arbitrary radial motions and mode numbers. Some closely related results have also been reported in a recent work by Mikaelian [87] on incompressible multi-shell systems. Additional viscosity effects have been treated by Chandrasekhar [88] and by Iooss, Laure, and Rossi [89]. The neglect of compressibility is of course a considerable simplification for actual applications. However, the stability of compressible self-similar shell solutions was analysed by Hattori et al. [90] and no sensitive dependence on compressibility was found in this case. More specific calculations, based on linear perturbation codes of ICF implosions have been performed by Dufour et al. [91]. Some of the characteristic features of incompressible shell implosions, such as oscillatory amplification, seem to be present in these stability studies too. More recently, two-dimensional fluid simulations of the stagnation phase in cylindrical targets have been obtained by Sakagami and Nishihara [92].

*4.3.1. Perturbation equations*

For definiteness, we consider in the following a three-dimensional spherical shell whose boundaries $R_{1,2}$ are subject to displacements $\zeta_{1,2}$, respectively. The simpler notation of eq. (4.1) will also be used. Perturbations are chosen with angular part $P_l(\Theta)$ and the corresponding potential (2.24) is written in the form,

$$\delta\varphi = (R_1/r)^{l+1}A_1 + (r/R_2)^l A_2 \,. \tag{4.33}$$

Imposing the boundary conditions (2.18) on the potential solution (4.33) at both surfaces $r = R_{1,2}$, there follows the fourth-order system,

$$R_1\,\partial_t\zeta_1 + 2\dot{R}_1\zeta_1 + (l+1)A_1 - lS^l A_2 = 0\,, \tag{4.34a}$$

$$R_2\,\partial_t\zeta_2 + 2\dot{R}_2\zeta_2 + (l+1)S^{l+1}A_1 - lA_2 = 0\,, \tag{4.34b}$$

$$\partial_t(A_1 + S^l A_2) + \ddot{R}_1\zeta_1 = 0\,, \tag{4.34c}$$

$$\partial_t(A_2 + S^{l+1}A_1) + \ddot{R}_2\zeta_2 = 0\,. \tag{4.34d}$$

These equations govern the evolution of shell perturbations for arbitrary radial motions.

Some numerical results for typical shell implosions will be presented in section 4.4. In the numerical treatment, it is advantageous to choose the radius or the convergence ratio $q = R_0/R$ as the independent variable. The integration interval $1 < q < \mathscr{C}$ is then known in advance, if an implosion with initial radius $R_0$ and stagnation point radius $R_s = \mathscr{C}R_0$ is considered. The radial dependences of the unperturbed shell velocities and accelerations follow simply from energy and mass conservation, as discussed in section 4.1. It is therefore not necessary to solve for the explicit time-dependence of the motion. The transformation to the independent variable $q$ can easily be achieved by noting that

$$\frac{\mathrm{d}}{\mathrm{d}q} = \frac{\mathrm{d}t}{\mathrm{d}q}\frac{\mathrm{d}}{\mathrm{d}t} = -\frac{R^2}{R_0 V}\frac{\mathrm{d}}{\mathrm{d}t} = -\frac{R_0}{q^2 V}\frac{\mathrm{d}}{\mathrm{d}t}\,. \tag{4.35}$$

As a minor drawback of this transformation, the system becomes singular at $V = 0$. One has therefore to initialize and terminate the calculations with a small nonzero shell velocity. This can be done without appreciable deviations from the case where the shell is exactly at rest.

*4.3.2. Thin shell expansion*

Considerable simplification of the general shell problem can be gained in the limiting cases of thick ($S^l \ll 1$) and thin ($S^l \to 1$) shells. For thick shells, the outer surface can be considered at rest, while the inner surface is governed by the cavity equation (4.25). In the opposite limit of thin shells, the evolution of surface modes can be described by independent second-order equations for each shell boundary. The derivation of these equations by a systematic expansion procedure will be outlined in this section.

If the shell thickness approaches zero, the boundary conditions at the inner and the outer surface become identical. To obtain a closed system of equations in this case, one has to consider an expansion up to first order in the parameter $\varepsilon = (R_2 - R_1)/R_1$. The motion of the outer surface can be related to the motion of the inner surface by the following first-order relations,

$$\begin{aligned} &R_2 = (1+\varepsilon)R\,, \quad \zeta_{1,2} = C \pm \varepsilon D/2\,, \\ &\dot{R}_2 = S^2\dot{R} = (1-2\varepsilon)\dot{R}\,, \quad \ddot{R}_2 = (1-2\varepsilon)\ddot{R} + 6\varepsilon\dot{R}^2/R\,. \end{aligned} \tag{4.36}$$

Here, we have used eq. (4.2) for the spherically symmetric flow and we have introduced the mean and the relative displacements of the two surfaces,

$$C = (\zeta_1 + \zeta_2)/2\,, \quad D = (\zeta_1 - \zeta_2)/\varepsilon\,, \tag{4.37}$$

respectively. Both $C$ and $D$ are treated of order O(1). Expanding now eqs. (4.34) up to first order yields

$$R\dot{C} + 2\dot{R}C = -(l+1)A_1 + lA_2\,, \tag{4.38a}$$

$$\dot{A}_1 + \dot{A}_2 = -\ddot{R}C\,, \tag{4.38b}$$

$$R\dot{D} - \dot{R}D = -(l+1)(l+2)A_1 - l(l-1)A_2 - 6\dot{R}C\,, \tag{4.38c}$$

$$-(2l+1)\dot{A}_1 = \ddot{R}D + 3\dot{R}\dot{C} + (l+2)\ddot{R}C\,. \tag{4.38d}$$

Equations (4.38a, b) follow immediately from the leading order of eq. (4.34). Equations (4.38c, d) are obtained by taking the difference between the boundary conditions at the inner and the outer surfaces. Thereby the following expansions have been used

$$
\begin{aligned}
&R_1\,\partial_t\zeta_1 - R_2\,\partial_t\zeta_2 = \varepsilon(R\dot{D} - 3\dot{R}D - R\dot{C})\,, \quad \dot{R}_1\zeta_1 - \dot{R}_2\zeta_2 = \varepsilon(\dot{R}D + 2\dot{R}C)\,,\\
&\ddot{R}_1\zeta_1 - \ddot{R}_2\zeta_2 = \varepsilon[\ddot{R}D - (6\dot{R}^2/R - 2\ddot{R})C]\,,\\
&-(l+1)(1-S^{l+1})A_1 + l(S^l-1)A_2 = \varepsilon[-(l+1)^2A_1 - l^2A_2]\,,\\
&\partial_t[(1-S^{l+1})A_1 + (S^l-1)A_2] = \varepsilon[(2l+1)\dot{A}_1 + l\ddot{R}C + 3(\dot{R}\dot{C} + 2C\dot{R}^2/R)]\,.
\end{aligned}
\tag{4.39}
$$

Eliminating now the variables $A_{1,2}$ from eqs. (4.38), there follows a set of two coupled second-order equations of the form

$$
R\ddot{C} = \ddot{R}D\,, \quad R\ddot{D} = \ddot{R}[3D + (l+2)(l-1)C]\,. \tag{4.40}
$$

These equations can be decoupled by the variable transformation

$$
G = D + (l-1)C\,, \quad H = D - (l+2)C\,, \tag{4.41}
$$

yielding two independent second-order equations,

$$
R\ddot{G} - (l+2)\ddot{R}G = 0\,, \quad R\ddot{H} + (l-1)\ddot{R}H = 0\,, \tag{4.42}
$$

for the variables $G$ and $H$. The general structure of these equations is analogous to eq. (3.27). However, the present result is valid for arbitrary radial motions and mode numbers.

*4.3.3. Initial values*

To satisfy the initial conditions at the shell boundaries, we have to consider a superposition of the basic solutions. For definiteness, we define a system of fundamental solutions $G_1, G_2, H_1, H_2$ of eq. (4.42) by the canonical initial conditions,

$$
G_{10} = H_{10} = 1\,, \quad \dot{G}_{10} = \dot{H}_{10} = 0\,, \quad G_{20} = H_{20} = 0\,, \quad \dot{G}_{20} = \dot{H}_{20} = 1\,. \tag{4.43}
$$

Setting

$$
\boldsymbol{X} = \begin{pmatrix} G \\ H \end{pmatrix}, \quad \boldsymbol{T}_{1,2} = \begin{pmatrix} G_{1,2} & 0 \\ 0 & H_{1,2} \end{pmatrix}, \tag{4.44}
$$

the solutions of eq. (4.42) can be represented in the form

$$
\boldsymbol{X} = \boldsymbol{T}_1 \cdot \boldsymbol{X}_0 + \boldsymbol{T}_2 \cdot \dot{\boldsymbol{X}}_0\,. \tag{4.45}
$$

The displacement vector $\boldsymbol{\zeta}$, as defined in eq. (3.26), is related to the vector $\boldsymbol{X}$ by a linear but time-dependent transformation,

$$\boldsymbol{\zeta} = \boldsymbol{M} \cdot X\,, \quad X = \boldsymbol{M}^{-1} \cdot \boldsymbol{\zeta}\,, \quad \dot{X} = \boldsymbol{M}^{-1} \cdot \dot{\boldsymbol{\zeta}} + \dot{\boldsymbol{M}}^{-1} \cdot \boldsymbol{\zeta}\,. \tag{4.46}$$

Specifically, using eqs. (4.37) and (4.41), one finds

$$\begin{aligned} \boldsymbol{M} &= \frac{1}{2l+1}\begin{pmatrix} 1+b & -(1-a) \\ 1-b & -(1+a) \end{pmatrix}, \quad \boldsymbol{M}^{-1} = \frac{1}{\varepsilon}\begin{pmatrix} 1+a & -(1-a) \\ 1-b & -(1+b) \end{pmatrix}, \\ \dot{\boldsymbol{M}}^{-1} &= \frac{3}{\varepsilon}\frac{\dot{R}}{R}\begin{pmatrix} 1 & -1 \\ 1 & -1 \end{pmatrix}, \end{aligned} \tag{4.47}$$

with $a = \varepsilon(l-1)/2$ and $b = \varepsilon(l+2)/2$. The solution for $\boldsymbol{\zeta}$ can now be expressed in terms of the basic solutions (4.43). Using eqs. (4.45), (4.46), there follows

$$\boldsymbol{\zeta} = \boldsymbol{M} \cdot (\boldsymbol{T}_1 \cdot X_0 + \boldsymbol{T}_2 \cdot \dot{X}_0) = \boldsymbol{M} \cdot (\boldsymbol{T}_1 \cdot \boldsymbol{M}_0^{-1} + \boldsymbol{T}_2 \cdot \dot{\boldsymbol{M}}_0^{-1}) \cdot \boldsymbol{\zeta}_0 + \boldsymbol{M} \cdot \boldsymbol{T}_2 \cdot \boldsymbol{M}_0^{-1} \cdot \dot{\boldsymbol{\zeta}}_0\,. \tag{4.48}$$

To give a specific example, consider a shell, initially at rest, with a corrugated outer surface. Since $\dot{\boldsymbol{R}}_0 = \partial_t \boldsymbol{\zeta}_0 = 0$, there is no contribution from the solution matrix $\boldsymbol{T}_2$ in this case. The contribution from $\boldsymbol{T}_1$, with $\zeta_{10} = 0$, yields

$$\begin{aligned} \zeta_1 &= (\zeta_{20}/\Delta)[(1-a)(1+b_0)H_1 - (1+b)(1-a_0)G_1]\,, \\ \zeta_2 &= (\zeta_{20}/\Delta)[(1+a)(1+b_0)H_1 - (1-b)(1-a_0)G_1]\,, \end{aligned} \tag{4.49}$$

with $\Delta = (2l+1)\varepsilon_0$. The mode amplitudes are enhanced by the large factor $\Delta^{-1}$. It determines the value from which the Rayleigh–Taylor instability actually grows.

*4.3.4. Thin shell solutions*

The thin shell approximation has led to the basic evolution equations (4.42) and (4.48). We now examine their solutions for ballistic and accelerated shell motions.

The acceleration of a ballistically moving thin shell can be obtained from eq. (4.13c) as

$$\ddot{R} = -3\varepsilon \dot{R}^2/R\,. \tag{4.50}$$

Being of order $\varepsilon$ only, it can be neglected in the thin shell equations. With the help of eqs. (4.41) and (4.42), the ballistic motion can be described by the equations

$$\ddot{C} = \ddot{D} = 0\,, \quad \ddot{R} = 0\,. \tag{4.51}$$

Accordingly, the perturbations $C$ and $D$ grow with a constant velocity and vary linearly with the radius,

$$C = C_0 + \dot{C}_0(R - R_0)/\dot{R}\,, \tag{4.52a}$$

$$D = D_0 + \dot{D}_0(R - R_0)/\dot{R}\,. \tag{4.52b}$$

Using an analogous notation as in eqs. (4.27), (4.30), the normalized displacement amplitudes follow from eqs. (4.36) and (4.52) to be

$$A_{1,2} = q[(A_{10} + A_{20})/2 \pm (3q^2 - 2q^3)(A_{10} - A_{20})/2 - (1 - q^{-1})(B_{10} + B_{20})/2$$
$$\pm (q^2 - q^3)(B_{10} - B_{20})/2]\,. \tag{4.53}$$

Here, we have used the scaling $\varepsilon = q^3\varepsilon_0$ of the expansion parameter with the convergence ratio. One can recognize a sensitive dependence on the choice of initial conditions. Any perturbation of the shell thickness grows much faster than a mere distortion of the whole shell. One should also notice, that the result is limited due to the thin shell approximation ($\varepsilon \ll 1$) to moderate convergence ratios of the order $q^3 \lesssim 1/\varepsilon_0$. For larger convergence ratios the amplitude growth saturates and cavity oscillations, as described by eq. (4.30), will develop.

As a second example, the RT instability of an accelerated thin shell will now be considered. A constant acceleration $a$ in the direction toward the shell center is assumed and the implosion time $\tau = \sqrt{2R_0/a}$ is used to form a dimensionless time variable $x = t/\tau$. The convergence ratio is related to the variable $x$ by the expression $q = 1/(1 - x^2)$. Typical acceleration distances are given by the values $q = 2$ or alternatively $x = 1/\sqrt{2} \approx 0.71$. With $x$ as the independent variable, the thin shell equations (4.42) become

$$(1 - x^2)\ddot{G} + 2(l + 2)G = 0\,, \quad (1 - x^2)\ddot{H} - 2(l - 1)H = 0\,. \tag{4.54}$$

The different signs in the equations for $G$ and $H$ lead to qualitatively different solution behavior. While $G$ describes stable surface oscillations, $H$ has a purely growing solution branch. Physically, these two modes arise from the stable inner and from the RT unstable outer surface of the shell. We have calculated some of the basic solutions $G_1$ and $H_1$, as defined by the initial conditions (4.43). The results are represented in fig. 9. It can be seen, that the oscillation amplitudes of $G_1$ show no amplification and, actually, are even slightly decreasing with $x$. On the other hand, the solution $H_1$ is monotonically growing and can lead to strong amplifications for large mode numbers.

For completeness, it is mentioned that the solutions of eq. (4.54) can also be represented by Legendre functions $P_\nu(x)$, $Q_\nu(x)$ of degree $\nu$ [93]. This representation is obtained by noting that

$$Y_1 = (1 - x^2)\,\partial_x P_\nu(x)\,, \quad Y_2 = (1 - x^2)\,\partial_x Q_\nu(x) \tag{4.55}$$

are solutions of the differential equation [94]

$$(1 - x^2)\,\partial_x^2 Y + \nu(\nu + 1)Y = 0\,. \tag{4.56}$$

Solutions of eq. (4.54) can be obtained by choosing the appropriate degree $\nu$ in eq. (4.56). Unfortunately, the resulting degree is generally complex and the corresponding functions are not in common use.

It may also be of interest to compare the exact result with the simpler WKB approximation [95],

$$G_1 \approx (1 - x^2)^{1/4} \cos[\sqrt{2(l + 2)}\,\arcsin x]\,,$$
$$H_1 \approx (1 - x^2)^{1/4} \cosh[\sqrt{2(l - 1)}\,\arcsin x]\,. \tag{4.57}$$

The validity of these expressions is generally limited to slowly varying coefficients in eq. (4.54).

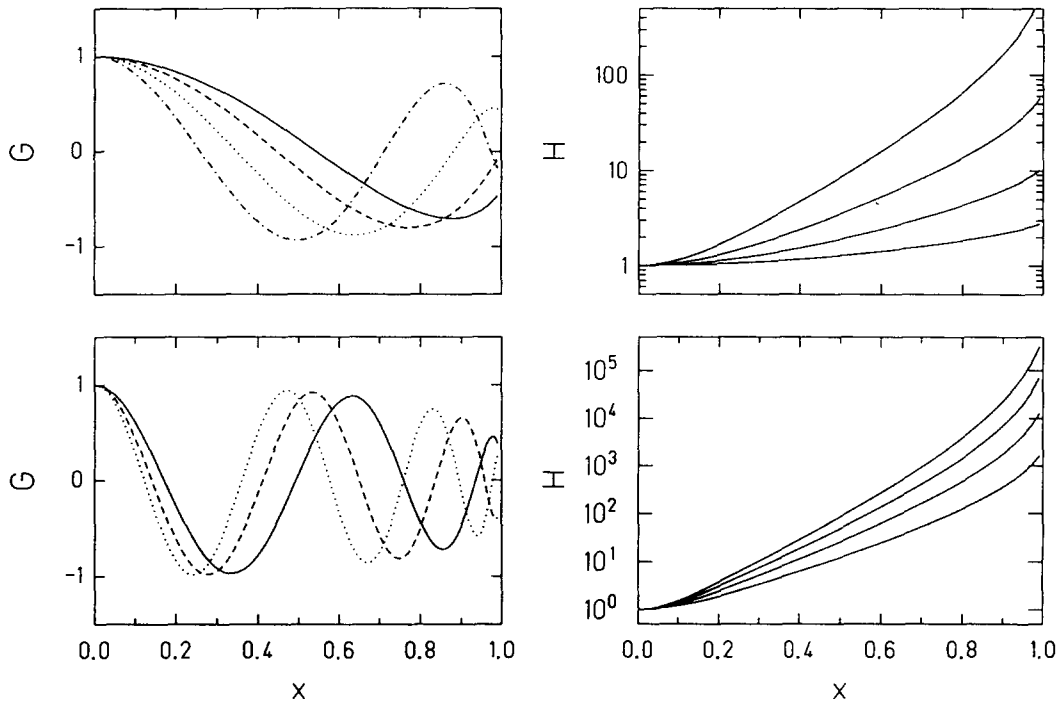


Fig. 9. Evolution of the surface modes $G$ and $H$ of an accelerated thin shell, according to eq. (4.54). The time coordinate is defined as $t = x\tau$, where $\tau = \sqrt{2R_0/a}$ is the implosion time under a constant acceleration $a$. With increasing frequencies, the solutions for $G$ correspond to the mode numbers $l = 2, 4, 8, 16, 40, 60, 80$. With increasing amplitudes, the solutions for $H$ correspond to the mode numbers $l = 2, 4, 8, 16, 20, 30, 40, 50$. (From ref. [78].)

Actually, the WKB approximation proves fairly accurate for $x \lesssim 0.8$. The accuracy of the approximation may be appreciated from the comparison of exact and approximated results presented in table 3.

### 4.4. *Stability results*

An overview on the evolution of incompressible shell perturbations under various circumstances is presented in the following. The computational results describe the full solution of the perturbation system (4.34) for different shell motions and initial data. We will discuss the stages of ballistic motion, of acceleration, and of deceleration in typical implosions. The initial aspect ratio of the shell is defined as $\mathcal{A} = R_0/d_0$, where $R_0$ denotes the initial radius of the inner shell boundary and $d_0$ the initial shell

Table 3
Comparison of the WKB approximation (4.57) with the numerical solution of eq. (4.54). Values of the growing mode $H_1$ at $x = 0.71$ for different mode numbers $l$

| | $H_1$ | | | |
|---|---|---|---|---|
| | $l = 2$ | $l = 4$ | $l = 8$ | $l = 16$ |
| eq. (4.57) | 1.4 | 2.9 | 8.0 | 31 |
| eq. (4.54) | 1.6 | 3.2 | 8.5 | 32 |

thickness. The final convergence ratio is denoted as $\mathscr{C} = R_0/R_s$, where $R_s$ represents the stagnation-point radius of the inner boundary.

*4.4.1. Ballistic motion*

First, consider a high aspect ratio shell moving with a constant kinetic energy toward the shell center. The initial shell parameters are: $R_0 = 1$, $V_0 = -1$, and $\mathscr{A} = 100$. This model describes the stability of converging shells of finite thickness in the absence of an external driver. With increasing convergence ratios, the shell becomes rapidly thick and reaches the stage of a collapsing cavity. The perturbation evolution will be described through this transition up to a convergence ratio of 30.

Perturbations have been initialized by imposing surface displacements to both shell boundaries. To gain some overview on possible evolutions, we discuss three different types of initial conditions:

$$\zeta_{10} = \zeta_{20} = 1\,, \tag{4.58a}$$

$$\zeta_{10} = -\zeta_{20} = 1\,, \tag{4.58b}$$

$$\zeta_{10} = 1\,, \quad \zeta_{20} = 0\,. \tag{4.58c}$$

The initial conditions (4.58a) will be called sphericity perturbations, describing deviations from the spherical shape with unperturbed shell thickness. In contrast, we will call the initial conditions (4.58b) uniformity perturbations, describing variations in the shell thickness with a fixed average shell radius. The perturbations of a single surface (4.58c) may be simply called surface corrugations.

The results of case (4.58a) are presented in fig. 10 for a number of different $l$ modes. Here and in the following, solid lines correspond to the inner and dashed lines to the outer surface. The amplitude evolution is represented as a function of the convergence ratio on a linear scale in fig. 10a and on a logarithmic scale in fig. 10b. We make this comparison to familiarize with the logarithmic representation that will be used in the following. Although the logarithmic scale gives only a poor picture of the oscillations, it seems to be the best way to display amplitude growth over several decades. Looking at the logarithmic representation fig. 10b, one should notice that the zeros of the oscillations appear as narrow spikes and that subsequent half-waves have actually different signs.

The present numerical solution can nicely illustrate the asymptotic results that have been obtained for thin and thick shells. For small convergence ratios the displacements remain constant, as predicted by eq. (4.52) for the present initial conditions. With increasing convergence ratios, the cavity approximation becomes valid and the inner surface starts to oscillate in accordance with the cavity solution (4.30). Since the perturbations remain static initially, the amplitude of the cavity oscillation is closely determined by the initial value at $R = R_0$. In particular, it is nearly independent of the mode number.

The thin shell solution (4.53) predicts major differences for the evolution of sphericity and uniformity perturbations. Actually, the initial conditions (4.58b) lead to a completely different picture of surface evolution. As shown in fig. 11, perturbation growth now starts immediately in the thin-shell regime and amplifications of the order of $1/\varepsilon_0 = \mathscr{A} = 100$ can be obtained. The saturation amplitude of the cavity oscillations depends considerably on the mode number. The largest amplifications are reached for low $l$ modes which saturate more slowly.

The evolution of inside surface corrugations, as described by eq. (4.58c), can be represented as a superposition of the previous results. As an immediate consequence, the asymptotic amplitudes will be

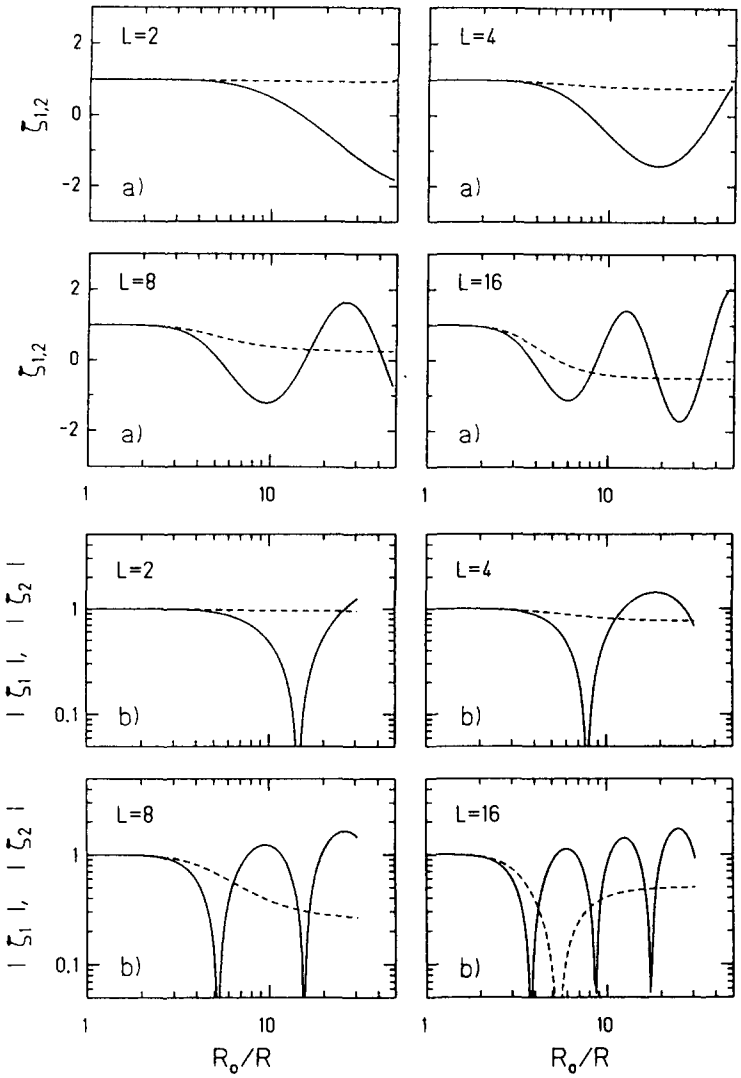


Fig. 10. Perturbation evolution for ballistic motion of a spherical shell with initial aspect ratio $\mathscr{A} = 100$. The initial conditions for the surface displacement amplitudes are $\zeta_{10} = \zeta_{20} = 1$. Solid (dashed) lines refer to the inner (outer) shell surface and the perturbation mode numbers are $l = 2$, 4, 8, 16. The displacement amplitudes are represented on (a) a linear scale and (b) a logarithmic scale. (From ref. [78].)

about one-half of those reached in the dominant case (4.58b). To show some additional features, we display in fig. 12a the evolution of the linear combinations $C = (\zeta_1 + \zeta_2)/2$ (solid line) and $\delta = (\zeta_1 - \zeta_2)/2$ (dashed line) and make comparison with the thin shell approximation (dotted and dot-dashed lines). The ballistic thin shell solution (4.53) stays approximately correct up to convergence ratios between 2 and 3. This corresponds to the shell thickness parameters $\varepsilon = q^3\varepsilon_0 \approx 0.08$–$0.27$ or $\Delta = (2l+1)\varepsilon \approx 0.4$–$1.4$.

We also show in fig. 12b the growth of the normalized amplitudes $A_{1,2} = \zeta_{1,2}/R_{1,2}$. The final amplifications are of the order $10^3$–$10^4$. For stable performance, these amplitudes should remain smaller than 1. The allowable initial amplitudes are therefore constrained to $\approx 1\%$ of the shell thickness: $\zeta_{10} < 10^{-4}R_0 = 10^{-2}d_0$. These requirements become most stringent for low mode numbers, which

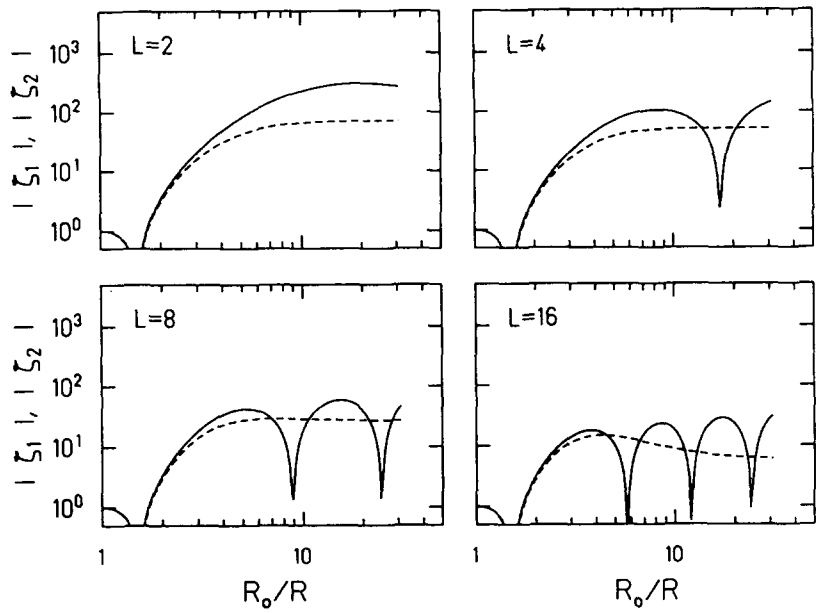


Fig. 11. Same motion as in fig. 10, with the initial conditions $\zeta_{10} = -\zeta_{20} = 1$. Note the large difference in the amplification of sphericity (fig. 10) and uniformity (fig. 11) perturbations. (From ref. [78].)

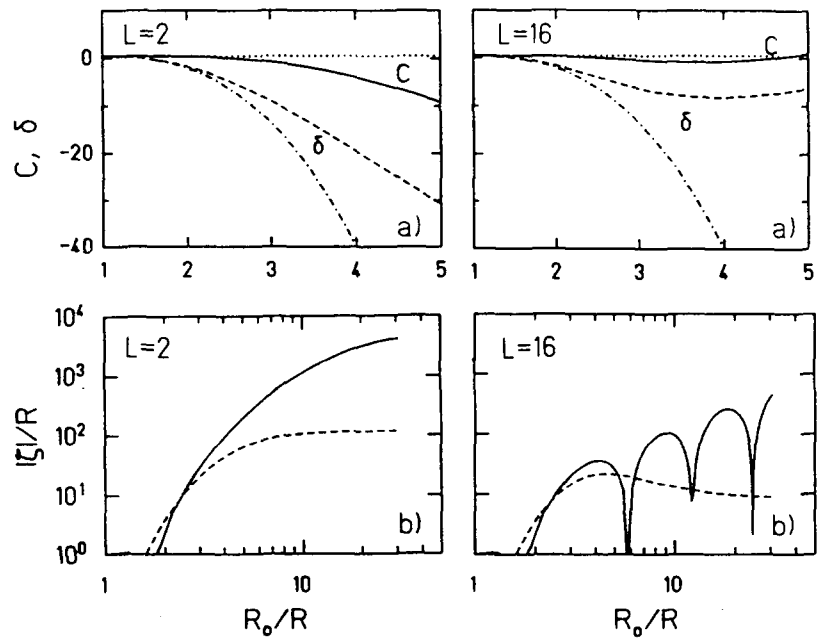


Fig. 12. Same motion as in fig. 10, with the initial conditions $\zeta_{10} = 1$ and $\zeta_{20} = 0$. (a) A comparison of the mean displacement $C = (\zeta_1 + \zeta_2)/2$ and the relative displacement $\delta = (\zeta_1 - \zeta_2)/2$ with the thin shell solution of eq. (4.53) (dotted and dot-dashed lines). (b) Evolution of the relative displacement amplitudes $\zeta_{1,2}/R$ for small ($l = 2$) and moderately large ($l = 16$) mode numbers.

saturate more slowly and therefore can reach larger oscillation amplitudes. If the shell is accelerated, this mode number dependence can be compensated by RT growth, affecting predominantly large mode numbers. The behavior of accelerated shells will be discussed in the following section.

*4.4.2. Acceleration*

Some perturbation results for accelerated high aspect ratio shells are now presented. They describe the RT instability of the outside surface and its penetration to the inside surface. The initial shell parameters are: $R_0 = 2$, $V_0 = 0$, and $\mathscr{A} = 100$. The acceleration law (4.15) is applied over a radial convergence ratio of 2.

As in the previous example, we will consider a set of different initial conditions,

$$\zeta_{10} = 1 + b_0\,, \quad \zeta_{20} = 1 - b_0\,, \tag{4.59a}$$

$$\zeta_{10} = 1 - a_0\,, \quad \zeta_{20} = 1 + a_0\,, \tag{4.59b}$$

$$\zeta_{10} = 0\,, \quad \zeta_{20} = d_0\,, \tag{4.59c}$$

to demonstrate the evolution of distinct modes and their possible interference. The initial conditions (4.59a) and (4.59b) impose basically sphericity perturbations, since the shell thickness variations are of order $\varepsilon_0$ only. The distinction between (4.59a) and (4.59b) is required to describe the evolution of the stable mode $G$ and the unstable mode $H$ independently. In the case (4.59c), sphericity and nonuniformity perturbations are of the same order. Here, the predominant response will come from the shell nonuniformities.

In the first calculation, the evolution of the stable surface mode $G$ is examined. As follows from eq. (4.46), the initial conditions (4.59a) correspond to the initial mode amplitudes $G_0 = 2l + 1$ and $H_0 = 0$. The computational results are presented in fig. 13a. Comparison is made with thin shell results (dotted and dot-dashed lines), following from eqs. (4.54) and (4.46). For low mode numbers ($l = 20$), one can recognize excellent agreement between the complete and the approximate solutions. In particular, no appreciable amplification is observed in both cases. For higher mode numbers ($l = 50$), the thin shell approximation becomes more restrictive and discrepancies can be observed at the outer boundary. The approximate solution remains still qualitatively correct at the inner boundary, however.

Corresponding results for the unstable surface mode $H$ are presented in fig. 13b. The initial conditions (4.59b) are equivalent to the mode amplitudes $G_0 = 0$ and $H_0 = -(2l + 1)$. The unstable outer surface is now well described by the thin shell approximation, while it becomes poor at the inner surface when surface oscillations develop. Nevertheless, the thin shell approximation can give a reasonably good estimate for the amplitude of the first cavity oscillation excited by the outside RT instability.

To discuss the amplification of shell nonuniformities we restrict our attention to the most severe mode $l = 2$. In fig. 13c, the evolution of the nonuniformity perturbation (4.59c) is compared with the evolution of the unstable sphericity perturbation (4.59b). As in the ballistic case (figs. 11, 12), one can observe strong nonuniformity growth in the thin shell regime, while there is only little amplification of the unstable RT mode. This surprising behavior is well described by the thin shell solution (4.49). Accordingly, the asymptotic growth of the average shell radius $C$ can be approximated in the form

$$C/d_0 = (H_1 - G_1)/(2l + 1)\varepsilon_0\,. \tag{4.60}$$

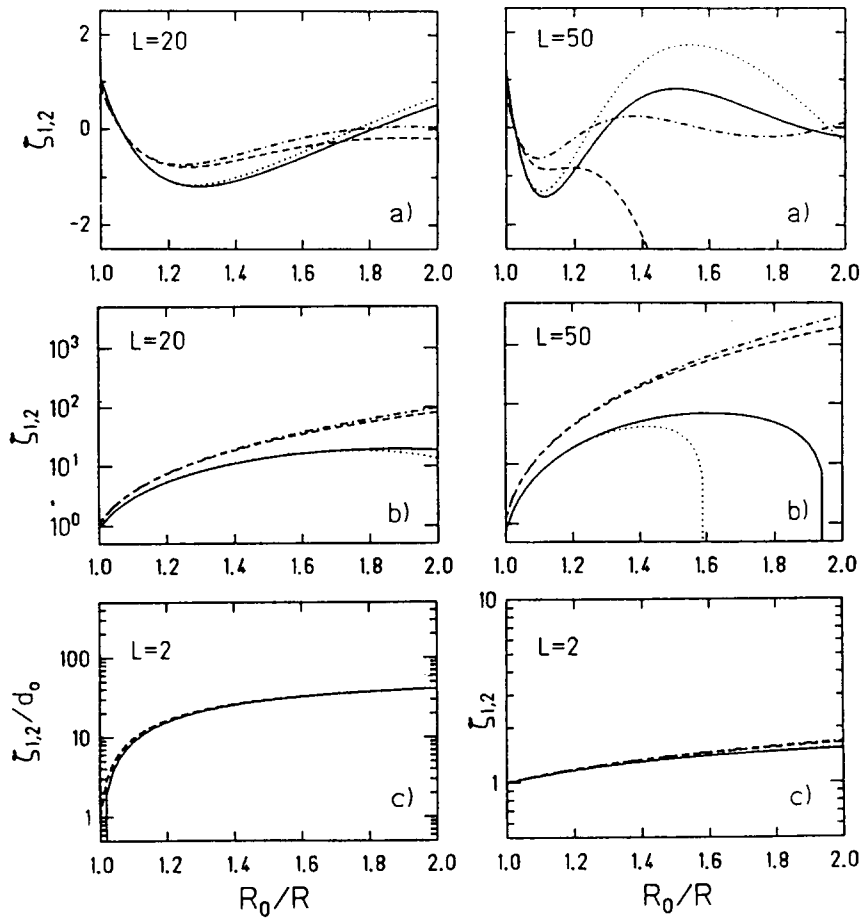


Fig. 13. Perturbation evolution for an accelerated shell with initial aspect ratio $\mathscr{A} = 100$. Solid and dashed lines are used as in fig. 10, dotted and dot-dashed lines refer to the thin shell approximation (4.54). (a) Initial conditions corresponding to the stable surface mode: $G_0 = 2l + 1$, $H_0 = 0$. (b) Initial conditions corresponding to the unstable surface mode: $G_0 = 0$, $H_0 = -(2l + 1)$. (c) Comparison of the amplifications by mode interference (left) and by RT growth (right) for the mode $l = 2$. Initial conditions are $\zeta_{10} = 0$, $\zeta_{20} = d_0$ (left) and $G = 0$, $H = -(2l + 1)$ (right). (From ref. [78].)

In excellent agreement with the numerical result, eq. (4.60) predicts an amplification of ≈40 at the end of the acceleration phase.

Physically, the effect is based on a destructive interference between the stable and unstable modes to satisfy the initial condition $\zeta_{10} = 0$ at the rear side of the shell. The initial perturbation at the front side is therefore much smaller than the individual mode amplitudes. In the course of time evolution, this interference is destroyed and the surface deformation is mainly due to the unstable mode amplitude $H$ (fig. 14).

### *4.4.3. Shell implosions*

Let us finally discuss some stability results for the implosion models described in section 4.1.7. They combine the different stages of acceleration, ballistic convergence, and deceleration as may be seen from fig. 7. The two implosion schemes correspond to the parameters (a) $\mathscr{A} = 100$, $\mathscr{C} = 40$ and (b) $\mathscr{A} = \mathscr{C} = 30$. Shell perturbations have been initialized at $R = R_0$ by assuming outside surface corrugations ($\zeta_{10} = 0$, $\zeta_{20} = d_0$).

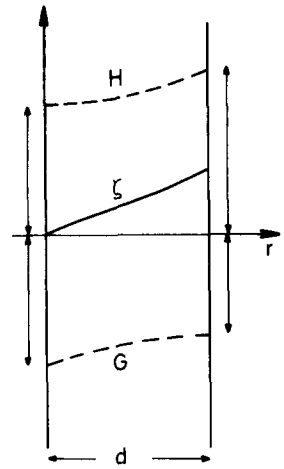


Fig. 14. Schematic representation of an initial shell perturbation $\zeta$ as a superposition of the two independent solutions $G$ and $H$. The left side is unperturbed because of destructive mode interference. At the right surface, the perturbation is nonzero but significantly smaller than the individual mode amplitudes. (From ref. [78].)

Results for scheme (a) are presented in fig. 15a, showing the development of both surface displacements for different mode numbers. At the outside surface, the growth is driven by RT instability and by mode interference in the acceleration phase. This growth saturates, when the outer surface is decelerated, and finally stagnates. However, one can recognize considerable overshooting of the value reached at the end-point of the acceleration phase ($q = 2$). The outside RT instability excites a cavity mode at the inner surface whose amplitude is further amplified in the final deceleration phase.

Corresponding results for scheme (b) are presented in fig. 15b. Comparing with (a), one can recognize considerably less amplification for the thicker shell. The design (b) seems more favorable for a number of reasons. The amplification factor is inversely proportional to the shell thickness, as described by the formula (4.60). This effect is important when both surface modes are excited. Furthermore, one can recognize from fig. 7 an earlier stagnation of the outside surface motion which also affects the saturation level of the outside surface amplitude. Finally, the thicker shell can more effectively suppress the excitation of cavity modes at the inner surface. The reduced oscillation amplitudes are particularly impressive for large mode numbers.

## 5. Bubble rise dynamics

RT instability marks only the onset of a complex interpenetration process, leading ultimately to the growth of mixing regions between neighboring fluids. On the other hand, the evolution of a free surface may be largely understood from first principles as an evolution of rising gas bubbles. The study of bubble dynamics, including various forms of bubble rise and bubble interactions, provides therefore a unique approach to a basic understanding of mixing-layer growth.

The theoretical description of free-surface flows leads to considerable mathematical difficulties which have probably not been satisfactorily solved in general. In this chapter, we therefore restrict attention to rather simple flow models suggested by physical considerations. First, the nonlinear perturbation theory of the RT instability is reviewed and the formation of bubbles is described. Then, a discussion of

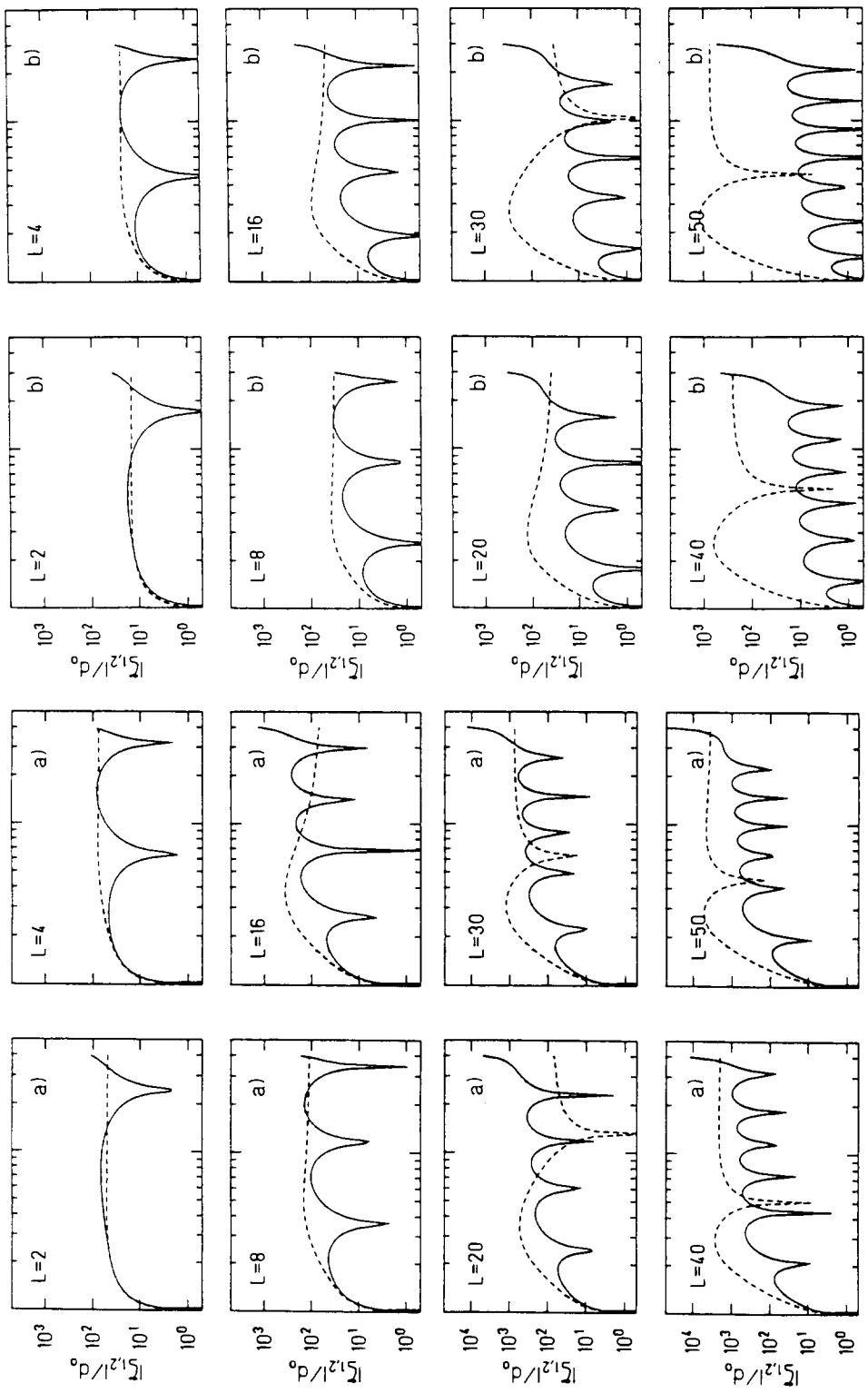


Fig. 15. Perturbation evolution for the shell implosions of fig. 7 with outside surface corrugations, $\zeta_{10} = 0$, $\zeta_{20} = d_0$. The initial aspect ratio $\mathscr{A}$ and the final convergence ratio $\mathscr{C}$ of the implosions are (a) $\mathscr{A} = 100$, $\mathscr{C} = 40$, (b) $\mathscr{A} = \mathscr{C} = 30$. (From ref. [78].)

bubble motions is presented, covering two- and three-dimensional flows around bounded and unbounded bubble domains. This analysis summarizes a number of bubble models that have proved particularly successful in the prediction of bubble parameters. These are the spherical-flow model of Taylor, the single-mode model first discussed by Layzer, and the source-row model introduced by the present author. Finally, applications of bubble theory to buoyancy-driven mixing layers are illustrated.

### *5.1. Nonlinear perturbation theory*

In this section, we consider the weakly nonlinear regime of the free-surface RT instability. The amplitude-to-wavelength ratio is still assumed small such that nonlinearities can be treated perturbatively. The initial-boundary-value problems for the first three perturbation orders are derived and subsequently solved for different initial conditions. The perturbation approach can explain the formation of bubble-spike asymmetry and gives some theoretical justification for nonlinear single-mode descriptions. Its limitations for larger amplitudes will be illustrated by a numerical calculation based on the method of least-squares approximation.

Nonlinear perturbation theories of the RT instability have been intensively studied in the presence of surface tension. The prediction of the stability boundary between RT instability and surface tension stabilization requires sophisticated perturbation methods. In a first treatment of this subject, a regular third-order expansion was given by Chang [4, 53]. Subsequently, singular perturbation methods have been introduced by Rajappa [96]. Thereby secular terms could be removed from the expansion for the stable modes above the instability cutoff. The problem was reconsidered by Kiang [97], and by Nayfeh [98]. As a major result, it was found that finite-amplitude waves can become nonlinearly unstable. While Rajappa's treatment apparently becomes invalid near the cutoff, Kiang and Nayfeh have obtained agreement in their nonlinear cutoff predictions. More recently, a different perturbation formula has been presented by Infeld and Rowlands [99], in making use of Witham's discussion [100] of nonlinear traveling surface waves. Although these authors may consider different initial and boundary conditions, their arguments should be taken with caution. As opposed to standing waves growing from rest, nonlinear traveling wave solutions become complex when the frequency is allowed to be complex.

Omitting the complications of surface tension, the present discussion is entirely based on regular perturbation theory. The purpose is to study the coupling to harmonics in an early stage of the instability evolution. In accordance with an earlier work by Leith [101], it is found that single-mode flow is exact up to third-order perturbation theory. This surprising result is rigorously valid if the evolution starts from an unperturbed initial surface and time-asymptotically for other initial conditions.

#### *5.1.1. Perturbation expansion*

The basic problem of the nonlinear free-surface instability consists in the determination of a potential $\varphi(x, y, t)$ satisfying the boundary conditions

$$(\partial_t \varphi + \tfrac{1}{2} v^2)\big|_{y=\zeta(x,t)} + \zeta(x, t) = 0\,, \tag{5.1a}$$

$$\partial_t \zeta + v_x(x, \zeta, t)\, \partial_x \zeta - v_y(x, \zeta, t) = 0\,, \tag{5.1b}$$

at the free surface $y = \zeta(x, t)$ at time $t$. Here, dimensionless variables normalized by the length unit $1/k$ and the time unit $1/\sqrt{ak}$ have been used. In the perturbation approach, the boundary conditions are expanded about the undisturbed interface, leading to a sequence of potential flow problems with

boundary conditions on $y = 0$. In principle, each perturbation order can then be solved by a superposition of normal modes, being complete on a plane surface.

The boundary condition (5.1a) can be rewritten in an alternative form, that is particularly well suited for the perturbation approach. For this purpose, we use the shorthand notation,

$$A(x, y, t)|_{y=\zeta} = 0\,, \quad A = \partial_t \varphi + \tfrac{1}{2} v^2 + y\,, \tag{5.2}$$

and differentiate eq. (5.1a) along the path of surface particles,

$$\frac{\mathrm{d}}{\mathrm{d}t}\,[A(x, y, t)|_{y=\zeta}] = (\partial_t A + v_x\,\partial_x A + v_y\,\partial_y A)|_{y=\zeta} = 0\,. \tag{5.3}$$

Substituting now $A$ back from eq. (5.2), there follows a homogeneous boundary condition for the potential $\varphi$,

$$F(x, y, t)|_{y=\zeta(x,\,t)} = 0\,, \tag{5.4}$$

with

$$F = \partial_t^2 \varphi + \partial_y \varphi + \partial_t v^2 + \boldsymbol{v} \cdot \boldsymbol{\nabla}(\tfrac{1}{2} v^2)\,.$$

We now expand $F(x, y, t)$ with respect to $y$ in a Taylor series about $y = 0$, and represent both $F$ and $\zeta$ by perturbation series,

$$\begin{aligned} &F = F|_{y=0} + \partial_y F|_{y=0}\zeta + \tfrac{1}{2}\partial_y^2 F|_{y=0}\zeta^2 + \cdots\,, \\ &F = \sum_{n=1} F_n \varepsilon^n\,, \quad \zeta = \sum_{n=1} \zeta_n \varepsilon^n\,. \end{aligned} \tag{5.5}$$

Ordering with respect to equal powers of $\varepsilon$ yields up to third-order

$$F|_{y=\zeta} = \varepsilon F_1|_{y=0} + \varepsilon^2[F_2 + (\partial_y F_1)\zeta_1]|_{y=0} + \varepsilon^3[F_3 + (\partial_y F_1)\zeta_2 + (\partial_y F_2)\zeta_1 + \tfrac{1}{2}(\partial_y^2 F_1)\zeta_1^2]|_{y=0}\,. \tag{5.6}$$

The advantage of the homogeneous boundary condition (5.6) derives from the fact that the linear part $F_1$ vanishes identically, if it is required to vanish on the surface. This would not be true for the corresponding part $A_1$ of the original inhomogeneous boundary condition (5.2). As a result, the partial derivatives of $F_1$ can be dropped in eq. (5.6), which greatly simplifies the evaluation of nonlinearities. Using eqs. (5.4) and (5.6), the boundary conditions at $y = 0$ for the first three orders of $\varphi$ follow to be

$$F_1 = \partial_t^2 \varphi_1 + \partial_y \varphi_1 = 0\,, \tag{5.7a}$$

$$F_2 = \partial_t^2 \varphi_2 + \partial_y \varphi_2 + \partial_t v_1^2 = 0\,, \tag{5.7b}$$

$$F_3 + (\partial_y F_2)\zeta_1 = \partial_t^2 \varphi_3 + \partial_y \varphi_3 + 2\partial_t(\boldsymbol{v}_1 \cdot \boldsymbol{v}_2) + \boldsymbol{v}_1 \cdot \boldsymbol{\nabla}(\tfrac{1}{2} v_1^2) + \partial_y(\partial_t^2 \varphi_2 + \partial_y \varphi_2 + \partial_t v_1^2)\zeta_1 = 0\,. \tag{5.7c}$$

In addition to these boundary conditions, initial conditions have to be specified for $\varphi_n$ and $\partial_t \varphi_n$. We will prescribe initial conditions on the first-order displacement $\zeta_1$ and its velocity $\partial_t \zeta_1$. The higher orders

are set equal to zero, initially: $\zeta_{n0} = \partial_t \zeta_{n0} = 0$ for $n > 1$. The surface displacement is defined by the original set of equations (5.1). The expansion of these equations up to third-order is given by,

$$\partial_t \varphi_1 + \zeta_1 = 0\,, \quad \partial_t \zeta_1 - \partial_y \varphi_1 = 0\,, \tag{5.8a}$$

$$\partial_t \varphi_2 + \zeta_2 + (\partial_t v_{y1})\zeta_1 + \tfrac{1}{2} v_1^2 = 0\,, \quad \partial_t \zeta_2 - \partial_y \varphi_2 + v_{x1}\,\partial_x \zeta_1 - (\partial_y v_{y1})\zeta_1 = 0\,, \tag{5.8b}$$

$$\begin{aligned} &\partial_t \varphi_3 + \zeta_3 + (\partial_t v_{y1})\zeta_2 + (\partial_t v_{y2})\zeta_1 + \tfrac{1}{2}(\partial_t \partial_y v_{y1})\zeta_1^2 + \boldsymbol{v}_1 \cdot \boldsymbol{v}_2 + \tfrac{1}{2}(\partial_y v_1^2)\zeta_1 = 0\,, \\ &\partial_t \zeta_3 - \partial_y \varphi_3 + v_{x2}\,\partial_x \zeta_1 + v_{x1}\partial_x \zeta_2 + (\partial_y v_{x1})(\partial_x \zeta_1)\zeta_1 \\ &\quad - [(\partial_y v_{y1})\zeta_2 + (\partial_y v_{y2})\zeta_1 + \tfrac{1}{2}(\partial_y^2 v_{y1})\zeta_1^2] = 0\,. \end{aligned} \tag{5.8c}$$

These equations have been commonly used in the perturbation approach. They determine both the potential and the displacement of each order simultaneously. In the present treatment, the potential is first determined from the simpler set of boundary conditions (5.7). The more complicated perturbation system (5.8) is only used when explicit displacement expressions are required.

*5.1.2. Harmonics*

In previous work, nonlinear perturbation results have been mostly derived for static initial corrugations of the surface. To discuss the dependence on initial conditions, we will consider general sinusoidal flow perturbations arising either from the displacement or from the velocity of the initial surface.

The first-order solution for the fundamental mode is written in the form

$$\varphi_1 = -[A \exp(t) + B \exp(-t)] \exp(-y) \cos(x)\,, \tag{5.9a}$$

$$\zeta_1 = [A \exp(t) - B \exp(-t)] \cos(x)\,, \tag{5.9b}$$

with arbitrary constants $A$ and $B$. Using these expressions, the boundary condition (5.7b) for the second-order potential becomes,

$$\partial_t^2 \varphi_2 + \partial_y \varphi_2 = -2[A^2 \exp(2t) - B^2 \exp(-2t)]\,. \tag{5.10}$$

With the help of eq. (5.8b), the initial conditions $\zeta_{20} = 0$ and $\partial_t \zeta_{20} = 0$ can be expressed as,

$$\partial_t \varphi_{20} = -[A^2 + B^2 + \tfrac{1}{2}(A - B)^2 \cos(2x)]\,, \quad \partial_y \varphi_{20} = (A^2 - B^2)\cos(2x)\,, \tag{5.11}$$

respectively. Solving these equations, yields the second-order result,

$$\begin{aligned} \varphi_2 = &-\tfrac{1}{2}[A^2 \exp(2t) - B^2 \exp(-2t)] \\ &-\tfrac{1}{2}[(A^2 - B^2)\cosh(\sqrt{2}\,t) + \sqrt{1/2}\,(A - B)^2 \sinh(\sqrt{2}\,t)] \exp(-2y)\cos(2x)\,, \end{aligned} \tag{5.12a}$$

$$\zeta_2 = -\tfrac{1}{2}\{[A \exp(t) - B \exp(-t)]^2 - \sqrt{2}(A^2 - B^2)\sinh(\sqrt{2}\,t) - (A - B)^2 \cosh(\sqrt{2}\,t)\}\cos(2x)\,. \tag{5.12b}$$

It is important to notice the difference between the different time-dependences in eq. (5.12). In each perturbation order, there is a driven response, arising from the nonlinearity in the evolution equation, and a reactive response, resulting merely from specific initial conditions. In $m$th order, the driven part will grow as $\exp(mt)$ but the reactive part only as $\exp(\sqrt{m}\,t)$. In this sense, the nonlinear evolution appears rather universal and stable against normal mode perturbations $\sim\exp(\sqrt{m}\,t)$. Neglecting reactive terms in the time-asymptotic limit, the dominant part of eq. (5.12) follows to be

$$\varphi_2 \to -\tfrac{1}{2}A^2 \exp(2t)\,, \tag{5.13a}$$

$$\zeta_2 \to -\tfrac{1}{2}A^2 \exp(2t)\cos(2x)\,. \tag{5.13b}$$

It is basically independent of the initial conditions, depending only on the unstable mode amplitude $A$. Furthermore, the asymptotic flow potential reduces to an unimportant time function, while the surface displacement becomes already modified by the first harmonic. Accordingly, single-mode flow is consistent with a nonlinear deformation of the surface. The negative sign of the first harmonic in eq. (5.13b) describes the onset of bubble–spike asymmetry. The total displacement of the rising fluid ($x = 0$) is reduced in comparison with the total displacement of the falling fluid ($x = \pi$).

We now discuss in more detail two important special cases. Choosing the initial conditions $A = B = V/2$, the evolution starts from a pure velocity perturbation. In this case, the first harmonic contribution to the velocity potential (5.12a) vanishes exactly. Up to second order, the corresponding solution is given by

$$\varphi = -\tfrac{1}{4}V^2 \sinh(2t) - V\cosh(t)\exp(-y)\cos(x)\,, \tag{5.14a}$$

$$\zeta = V\sinh(t)\cos(x) - \tfrac{1}{4}V^2[\cosh(2t) - 1]\cos(2x)\,. \tag{5.14b}$$

We now use this result to determine the third-order potential perturbation. Substituting eq. (5.14) into eq. (5.7c) there follows

$$\partial_t^2\varphi_3 + \partial_y\varphi_3 = -\boldsymbol{v}_1\cdot\boldsymbol{\nabla}(\tfrac{1}{2}v^2) - (\partial_y\partial_t v_1^2)\zeta_1 = \tfrac{1}{4}[5\cosh(3t) - \cosh(t)]V^3\cos(x)\,. \tag{5.15}$$

The third-order solution, corresponding to the initial conditions,

$$\zeta_{30} = -\partial_t\varphi_{30} = 0\,, \quad \partial_t\zeta_{30} = \partial_y\varphi_{30} = 0\,, \tag{5.16}$$

is found to be

$$\varphi_3 = \{\tfrac{5}{32}[\cosh(3t) - \cosh(t)] - \tfrac{1}{8}t\sinh(t)\}V^3\exp(-y)\cos(x)\,. \tag{5.17}$$

It should be noticed that the nonlinear evolution can be consistently described by the fundamental mode of the flow potential up to third-order. Actually, the third-order provides merely a feedback to the time dependence of the flow amplitude. Single-mode flows with time-dependent amplitudes will be further discussed in section 5.3.

To make comparison with previous work, we now specialize to the more usual initial conditions $A = -B = Z/2$, describing static initial corrugations of amplitude $Z$. Combining eqs. (5.9) and (5.12) yields

$$\varphi = -Z\sinh(t)\exp(-y)\cos(x) - \tfrac{1}{4}Z^2[\sinh(2t) + \sqrt{2}\sinh(\sqrt{2}t)\exp(-2y)\cos(2x)]\,, \tag{5.18a}$$

$$\zeta = Z\cosh(t)\cos(x) - \tfrac{1}{4}Z^2[\cosh(2t) - 2\cosh(\sqrt{2}\,t) + 1]\cos(2x)\,. \tag{5.18b}$$

These solutions agree up to second-order with the results of Chang [53] and Kiang [97], if surface tension is neglected there. Proceeding to third-order, the equations for the velocity potential become,

$$\begin{aligned} &\partial_t^2\varphi_3 + \partial_y\varphi_3 = \{-\sqrt{2}\,\partial_t[\sinh(t)\sinh(\sqrt{2}\,t)] + \tfrac{5}{4}\sinh(3t) + \tfrac{1}{4}\sinh(t)\}Z^3\cos(x)\,,\\ &\partial_y\varphi_{30} = 0\,, \quad \partial_t\varphi_{30} = -\tfrac{1}{8}Z^3[3\cos(3x) + \cos(x)]\,. \end{aligned} \tag{5.19}$$

Their solution includes a third-order contribution to the fundamental mode and an additional second harmonic,

$$\begin{aligned} \varphi_3 = {} & [\tfrac{1}{8}t\cosh(t) + \tfrac{9}{32}\sinh(t) + \tfrac{5}{32}\sinh(3t) - \tfrac{1}{2}\sqrt{2}\cosh(t)\sinh(\sqrt{2}\,t)]Z^3\exp(-y)\cos(x)\\ & - \tfrac{1}{8}\sqrt{3}\,Z^3\sinh(\sqrt{3}\,t)\exp(-3y)\cos(3x)\,. \end{aligned} \tag{5.20}$$

The appearance of secular terms, as represented by the first member in the bracket, is typical for higher-order perturbations. They can be removed by singular perturbation techniques, although this procedure has only basic justification for stable bounded solutions. For instance, the present term may be viewed as a nonlinear correction to the growth rate of the first-order solution,

$$\varphi_1 \to -Z\sinh[(1 - \tfrac{1}{8}Z^2)t]\exp(-y)\cos(x)\,. \tag{5.21}$$

This modification agrees with the more rigorous derivations in refs. [97, 98].

*5.1.3. Nonlinear mode interactions*

If the initial perturbation consists of a superposition of modes, beat waves can be excited by nonlinear mode couplings. The appearance of longer wavelengths in the evolution of multiple-mode problems is of considerable interest, since these modes can become dominant when the growth of the short-wavelength modes has reached nonlinear saturation. Unfortunately, the stage of saturation can no longer be described by the perturbation approach.

To demonstrate the principle possibility of nonlinear mode coupling, we allow for a superposition of two modes in the first-order solution,

$$\begin{aligned} &\varphi_1 = -m^{-1}F(t)\exp(-my)\cos(mx) - n^{-1}G(t)\exp(-ny)\cos(nx)\,,\\ &\zeta_1 = m^{-1}\partial_t F(t)\cos(mx) + n^{-1}\partial_t G(t)\cos(nx)\,. \end{aligned} \tag{5.22}$$

In the second-order, there appears an additional mode with the difference mode number $l = m - n$, where $m > n > l$ is assumed. Its potential has the general form

$$\varphi_2 = [b(t) + c_1\exp(\sqrt{l}\,t) + c_2\exp(-\sqrt{l}\,t)]\exp(-ly)\cos(lx)\,, \tag{5.23}$$

consisting of a driven solution $b(t)$ and the stable and unstable normal modes with amplitudes $c_{1,2}$. The boundary condition (5.7b) yields for $b$ the differential equation,

$$\partial_t^2 b - lb = -2\,\partial_t(FG)\,. \tag{5.24}$$

Noting that $\partial_t^2 F = mF$ and $\partial_t^2 G = nG$, the driven solution can be expressed in the form

$$b = -n^{-1} F\,\partial_t G\,. \tag{5.25}$$

From the initial conditions $\zeta_{20} = 0$ and $\partial_t \zeta_{20} = 0$ the constants $c_{1,2}$ are found,

$$c_{1,2} = \tfrac{1}{4}[\pm(\sqrt{l}/nm)\,\partial_t F\,\partial_t G + n^{-1} F\,\partial_t G + m^{-1} G\,\partial_t F]|_{t=0}\,, \tag{5.26}$$

where the upper sign refers to $c_1$ and the lower one to $c_2$. In this solution the freely evolving modes may be more important than the driven one because of the earlier saturation of short wavelength modes. This temptative interpretation suggests, that the long-time behavior is dominated by the unstable mode with amplitude $c_1$. We remark, that such a mode can only exist if the initial surface displacement is nonzero, $\partial_t F_0 \neq 0$ or $\partial_t G_0 \neq 0$.

*5.1.4. Least-squares approximation*

With increasing amplitudes, higher-order contributions can no longer be neglected in the perturbation series. The evolution of a larger number of harmonics can be studied numerically by the method of least-squares approximation. It was first applied to the free-surface problem by Pennington [102]. The method was reconsidered in ref. [75] with improved computational accuracy.

We first briefly outline the approximation method. According to the discussion in section 5.1.1, the $n$th order perturbation solution has the general form

$$\varphi(x, y, t) = \sum_{m=0}^{N} a_m(t) \exp(-my) \cos(mx)\,, \tag{5.27}$$

where the amplitudes $a_m(t)$ contain contributions from various perturbation orders. One should notice that this representation is not completely general. Even in the limit $N \to \infty$, it can fail to describe the full large-amplitude solution. The Fourier representation with respect to the $x$ coordinate will only converge if the potential has no singularities on each line $y = \text{const}$. It is therefore assumed, that the potential is analytic in the entire half-plane above the lowest surface point. However, this assumption becomes violated, if singularities appear in those regions of the half-plane that are not occupied by the fluid. Despite this principal limitation, it is of interest to see how far the nonlinear evolution can be described by the series (5.27) if higher-order terms are included.

The method of least-squares approximation determines the mode amplitudes by minimizing the mean square error on the surface for an expansion of given order. The set of basis functions

$$f_m(x, y) = \exp(-my) \cos(mx) \tag{5.28}$$

can be orthogonalized on the instantaneous surface $x = x(x_0, t)$, $y = y(x_0, t)$ by use of the Gram–Schmidt orthonormalization procedure. This yields a new function system $g_m(x, y, t)$, satisfying

$$\langle g_i, g_j \rangle = \frac{2}{\pi} \int_0^{\pi} \mathrm{d}x_0 \; g_i(x(x_0, t), y(x_0, t), t) g_j(x(x_0, t), y(x_0, t), t) = \delta_{ij} \,. \tag{5.29}$$

If the series (5.27) is rewritten in terms of the function set $\{g_m\}$ as

$$\varphi = \sum_{m=0}^{N} c_m(t) g_m(x, y, t) \,, \tag{5.30}$$

the boundary condition (5.1a) assumes the general form

$$\sum_{m=0}^{N} \dot{c}_m g_m = R(x_0, c_m, t) \,. \tag{5.31}$$

In this equation, the time-derivative $\dot{c}_m$ appears on the l.h.s. only and $R$ represents a known function at time $t$,

$$R(x_0, c_m, t) = -\left( \sum c_m \, \partial_t g_m + \tfrac{1}{2} v^2 + y \right) \Big|_{x = x(x_0, t), \; y = y(x_0, t)} \,. \tag{5.32}$$

Taking projections of eq. (5.31) on the basis functions and adding the equations of motions for the surface particles yields a closed system of ordinary differential equations,

$$\begin{aligned} &\dot{c}_m = \langle g_m, R \rangle \,, \quad c_m(0) = c_{m0} \,, \quad \dot{x}(x_0, t) = \partial_x \varphi \,, \quad x(x_0, 0) = x_0 \,, \quad \dot{y}(x_0, t) = \partial_y \varphi \,, \\ &y(x_0, 0) = \zeta_0(x_0) \,. \end{aligned} \tag{5.33}$$

Numerical solutions of the evolution equations (5.33) have been obtained in ref. [75]. An example is shown in fig. 16, corresponding to the initial values $c_m(0) = 0$, $\zeta_0(x) = 0.1 \cos x$. This calculation has been performed with $N = 11$ terms in the expansion (5.30) and with 100 particles distributed at equal distances over the initial surface. The normal mode spectrum at subsequent times is shown in fig. 16a. One can recognize that the rate of convergence of successive orders is quite fast at early times ($t = 0.6$ represented by square symbols) but it becomes increasingly worse in the course of time evolution. Note that the 10th harmonic amplitude grows from the order $10^{-11}$ up to the order $10^{-2}$ while the fundamental mode grows only by somewhat more than a factor of 10. The decrease in the slope of the mode spectrum is particularly pronounced after the time $t = 3.0$ and leads to computational failure after the time $t = 3.6$.

Corresponding results for the evolution of the fluid interface are represented in fig. 16b. The heavy fluid above the interface is pushed by the pressure of a gas below the interface. It can be recognized that the sinusoidal initial perturbation develops into a rising bubble centered around $x = 0$ and into a falling spike centered around $x = \pi$. The accuracy of the calculation is believed to be good up to the time $t = 3.6$ where the bubble and spike amplitudes have reached the values 1.01 and $-2.20$, respectively. For a comparison with the full numerical solution, a benchmark problem of refs. [15, 103], corresponding to a larger initial amplitude of 0.5, has also been studied. In this case, the full numerical solution approaches the asymptotic bubble velocity close to the time $t = 2$. The same prediction is made by the present perturbative treatment as can be seen from the data in fig. 22 below.

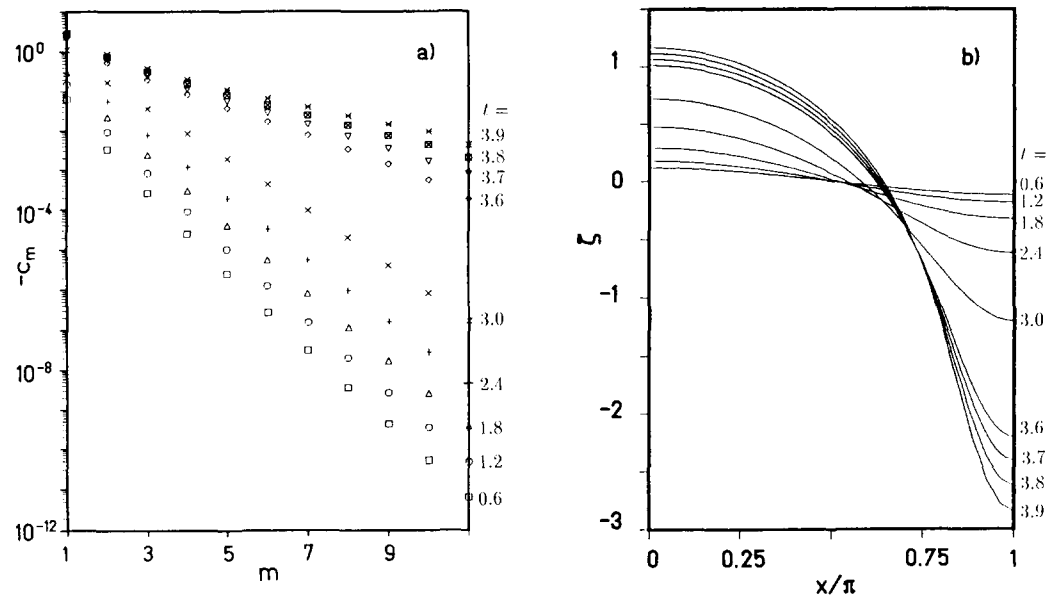


Fig. 16. Nonlinear evolution of a sinusoidal surface displacement $\zeta = 0.1 \cos x$ in the free-surface RT instability. The units are $k^{-1}$ for the length and $1/\sqrt{ak}$ for the time. (a) Spectrum of the mode amplitudes $c_m$ for the fundamental mode $m = 1$ and its first ten harmonics $m = 2$–11. Subsequent times are indicated by different marker symbols as defined at the right margin. (b) Surface displacements at corresponding times. The fluid occupies the region above the surface line and, for symmetry reasons, only one-half of a wavelength is shown. (From ref. [75].)

Despite the satisfactory explanation of bubble–spike asymmetry, it should be noticed that the perturbation method is faced with serious difficulties at larger amplitudes. In practice, calculations cannot be extended beyond a bubble–spike separation of at most half a wavelength. The main reason is an enormous increase of the exponentials $\exp(-my)$ when the spike amplitude exceeds $y = -1$. In addition, the series may fail to converge when singularities in the bubble region are encountered.

### 5.2. Closed bubbles

Free-surface bubbles may be classified according to their topology as open or closed and according to the number of relevant flow dimensions as two or three dimensional. Closed underwater bubbles have been studied experimentally by Davis and Taylor [14]. They have the shape of small caps with nearly spherical top and flat bottom. The top side seems nearly steady while the rear side is subject to rapid fluctuations caused by complicated wake currents. Open surface bubbles arise as an approximately periodic two-dimensional structure in the nonlinear RT instability. They approach the form of open-ended broad columns that are separated by narrow sheets of falling fluid. Experimental evidence of an asymptotic bubble stage was first gained by Lewis [2] and later confirmed by Emmons et al. [4]. Under more definite conditions, single open bubbles can be prepared and studied in rectangular channels or circular tubes.

Bubble experiments have indicated close analogies in the dynamics of these bubble structures. In all cases, an approximately constant rise velocity was observed. Its dependences can be expressed in the general form

$$u = F\sqrt{aL}\,, \tag{5.34}$$

where $L$ denotes a characteristic bubble length and $F$ is a dimensionless constant, known as the Froude number. Frequently, $L$ is chosen to be the radius of curvature, the channel width, the tube diameter, or the perturbation wavelength. The value of $F$ is the crucial parameter, which depends on the given circumstances. It can only be found by measurements or detailed calculations. We will derive Froude numbers for a variety of bubble flows. The underlying approximations will be discussed and the results are compared with a number of experimental and computational data. The discussion is divided into a description of closed bubbles, treated in this section, and of open bubbles, presented in section 5.3.

### *5.2.1. Spherical bubble model*

To explain the rate of rise of closed underwater bubbles, Taylor made comparison with the well-known potential flow around solid spheres [14]. Surprisingly good agreement with measured rise velocities could be found by assuming pressure equilibrium on the top side of the sphere. Unfortunately, the observed bubble shapes are quite different from a sphere on their rear sides.

This paradox may be resolved by considering an initial-value problem for spherical bubbles rather than a steady-state problem. An initially spherical bubble remains nearly spherical for a short time. Within this initial period, the evolution may be treated perturbatively. The expected evolution for spherical bubbles is shown schematically in fig. 17. If the sphere is assumed at rest, initially, one has to solve the initial acceleration problem and, subsequently, the approach toward an asymptotic steady-state at the top side of the sphere. Alternatively, one may consider an initially moving sphere. For a proper choice of the initial velocity, steady-state conditions could be maintained on the upper side from the very beginning. These two approaches will be illustrated in the following. A more complete computational treatment of the initial-value problem for spherical bubbles at rest has been described by Baker and Moore [13]. The calculations show a strong distortion of the bubble into a horseshoe-like shape due to the formation of an upward directed jet at the rear side of the sphere. In the initial phase, the results for the upper bubble amplitude are in close agreement with the present perturbation results. However, the asymptotic rise velocity is somewhat larger in these calculations, where it seems to be influenced by the rear side jet.

We will first discuss the initial acceleration of a spherical bubble at rest as a result of its buoyancy and its virtual mass. In accordance with Birkhoff's results, it is found that spherical bubbles experience the same initial acceleration as rigid spheres. Then, we analyse necessary conditions for steady-state flow at the top of an initially moving sphere and thereby derive Taylor's original result. Finally, the transient evolution from rest up to the final steady-state is described by a simple interpolation formula.

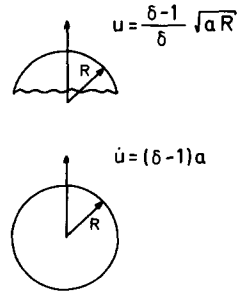


Fig. 17. Expected evolution of an initially spherical underwater bubble. A $\delta$-dimensional spherical bubble at rest experiences an initial acceleration $\alpha = (\delta - 1)a$ and approaches a final rise velocity $u = [(\delta - 1)/\delta]\sqrt{aR}$. Thereby its shape is flattened at the rear side by wake currents.

*5.2.2. Initial acceleration of spherical bubbles*

Consider a spherical bubble in an infinitely extended liquid subject to an acceleration $a$ along the $y$ direction. The bubble will experience an initial acceleration $\alpha$ with respect to the fluid. Choosing a reference frame moving with velocity $\alpha t$ along the $y$ direction, the boundary conditions at infinity and at the bubble surface $r = R(\Theta, t) = R_0 + \zeta(\Theta, t)$ become

$$\partial_y \varphi|_{|y|\to\infty} = -\alpha t\,, \tag{5.35a}$$

$$[\partial_t \varphi + \tfrac{1}{2}v^2 + (a+\alpha) r\cos\Theta]|_{r=R} = 0\,, \tag{5.35b}$$

$$(\partial_t \zeta + R^{-2}\,\partial_\Theta \varphi\,\partial_\Theta \zeta - \partial_r \varphi)|_{r=R} = 0\,. \tag{5.35c}$$

The first two boundary conditions can be somewhat simplified by setting $\varphi(r, \Theta, t) = \varphi_L(r, \Theta, t) - \alpha t r\cos\Theta$. In terms of $\varphi_L$, these boundary conditions are

$$\partial_y \varphi_L|_{|y|\to\infty} = 0\,, \quad (\partial_t \varphi_L + \tfrac{1}{2}v^2 + ar\cos\Theta)|_{r=R} = 0\,. \tag{5.36}$$

One should notice that $\varphi_L$ is the potential in the laboratory frame, but expressed in the coordinates of the moving frame, and the velocity is still defined in terms of $\varphi$.

During an initial stage, the bubble will stay approximately spherical and we can use a formal expansion about the initial surface $r = R_0$ that is similar to eq. (5.8). The first two perturbation orders yield

$$\begin{aligned} &\partial_t \varphi_{L1} + aR_0\cos\Theta = 0\,,\\ &\partial_t \zeta_1 - \partial_r \varphi_{L1} + \alpha t\cos\Theta = 0\,, \end{aligned} \tag{5.37a}$$

$$\begin{aligned} &\partial_t \varphi_{L2} + \tfrac{1}{2}v_1^2 + (\partial_r \partial_t \varphi_{L1} + a\cos\Theta)\zeta_1 = 0\,,\\ &\partial_t \zeta_2 - \partial_r \varphi_{L2} + R_0^{-2}\,\partial_\Theta \varphi_1\,\partial_\Theta \zeta_1 - \partial_r^2 \varphi_1 \zeta_1 = 0\,. \end{aligned} \tag{5.37b}$$

Using eqs. (2.24) and (2.25) for two- ($\delta = 2$) and three- ($\delta = 3$) dimensional flows, the first-order solution is given by

$$\varphi_{1L} = -\frac{\alpha t}{\delta - 1}\,\frac{R_0^\delta}{r^{\delta-1}}\cos\Theta\,, \quad \zeta_1 = 0\,, \quad \frac{1}{\delta - 1}\,\alpha = a\,. \tag{5.38}$$

In the first approximation, the induced acceleration field $\alpha$ is homogeneous and the sphere is accelerated rigidly. This acceleration may be viewed as arising from the buoyancy force $ma$, where $m$ is the mass of the fluid displaced by the sphere, and from a virtual inertial mass $\gamma m$ of the bubble inside the fluid. Setting $\gamma m\alpha = ma$, one finds from eq. (5.38) the inertial coefficient $\gamma = 1/(\delta - 1)$. The values $\gamma = 1$ for cylindrical geometry and $\gamma = \frac{1}{2}$ for a three-dimensional sphere are exactly those found for solid bodies with negligible masses [44].

Let us now extend the analysis to second-order. Using eq. (5.38) there follow the relations

$$v_1^2|_{r=R_0} = R_0^{-2}(\partial_\Theta \varphi_1)^2|_{r=R_0} = (\delta a t\sin\Theta)^2\,, \quad \sin^2\Theta = [(\delta - 1)/\delta]\,(g_0 - g_2)\,, \tag{5.39}$$

where the angular parts $g_l(\Theta)$ have been defined in eq. (2.25a). With these expressions, eqs. (5.37b) become

$$\partial_t \varphi_{L2} + \tfrac{1}{2}(\delta a t)^2[(\delta - 1)/\delta](g_0 - g_2) = 0\,, \tag{5.40a}$$

$$\partial_t \zeta_2 - \partial_r \varphi_{L2} = 0\,. \tag{5.40b}$$

Choosing the initial conditions $\zeta_2(0) = \partial_t \zeta_2(0) = 0$, the second-order solution is found to be

$$\varphi_{L2} = a_0 g_0 + a_2 (R_0^\delta / r^\delta) g_2\,, \quad \zeta_2 = b_2 g_2\,, \tag{5.41}$$

where

$$a_0 = -a_2 = -\tfrac{1}{6}(\delta - 1)\delta a^2 t^3\,, \quad b_2 = -\tfrac{1}{24}(\delta - 1)\delta^2 a^2 t^4 / R_0\,.$$

The total acceleration distance at the top side of the bubble then is

$$h = at^2(\tfrac{1}{2} - \tfrac{1}{6}\, at^2/R_0) \quad (\delta = 2)\,, \quad h = at^2(1 - \tfrac{3}{4}\, at^2/R_0) \quad (\delta = 3)\,. \tag{5.42}$$

The second-order corrections show the trend toward a reduction of the upward acceleration. To estimate the final steady-state rise velocity, we extrapolate the evolution law (5.42) up to the point where the acceleration becomes zero. Setting $\ddot{h} = 0$ in eq. (5.42) one finds,

$$\alpha t^2/2R_0 = \tfrac{1}{4}\,, \quad \dot{h} = \tfrac{1}{3}\sqrt{2}\sqrt{aR_0} \approx 0.47\sqrt{aR_0} \quad (\delta = 2)\,, \tag{5.43a}$$

$$\alpha t^2/2R_0 = \tfrac{2}{9}\,, \quad \dot{h} = \tfrac{4}{9}\sqrt{2}\sqrt{aR_0} \approx 0.94 \times \tfrac{2}{3}\sqrt{aR_0} \quad (\delta = 3)\,. \tag{5.43b}$$

In both cases, the acceleration distance is only a small fraction of the bubble radius. Despite our rough extrapolation, the velocities reached at the end of the acceleration phase are in close agreement with the steady-state rise velocities that will be derived below.

*5.2.3. Asymptotic rise velocity*

To analyse the steady flow conditions at the top of a moving sphere, we reconsider the initial-value problem by assuming an initial velocity $u$ along the $y$ direction. In the bubble rest frame, the initial flow is given by,

$$\varphi_0 = -[r + (\delta - 1)^{-1} R^\delta / r^{\delta - 1}] u \cos\Theta\,, \tag{5.44a}$$

$$v_{r0} = \partial_r \varphi_0 = -[1 - (R_0/r)^\delta] u \cos\Theta\,, \tag{5.44b}$$

$$v_{\Theta 0} = r^{-1}\, \partial_\Theta \varphi_0 = [1 + (\delta - 1)^{-1}(R_0/r)^\delta] u \sin\Theta\,, \tag{5.44c}$$

satisfying the required boundary conditions $v_{y0} = -u$ at infinity and $v_{r0} = 0$ on the sphere $r = R_0$. A schematic drawing of the streamlines of this flow is represented in fig. 18. The bubble surface is represented by a separatrix between the streamlines of the incident flow at infinity and those passing

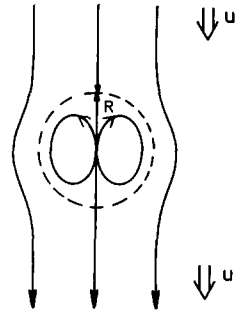


Fig. 18. Streamline pattern around a spherical bubble of radius $R$. The fluid has the same asymptotic velocity $u$ above and below the bubble. The flow has stagnation points at the top and bottom points of the sphere.

through the dipole source at the origin. On the surface there are two stagnations points at $\Theta = 0$ and $\Theta = \pi$. From a purely kinematical point of view, a steady-surface profile may be expected at the upper stagnation point, while it would be definitely unstable at the lower one.

For a sufficiently short time interval, the evolution of the potential can be treated perturbatively. Setting $\varphi = \varphi_0 + \varphi_1$ in the dynamical boundary condition (2.10b), there follows the first-order equation,

$$\partial_t \varphi_1 + \tfrac{1}{2} v_0^2 + aR_0 \cos\Theta = 0 . \tag{5.45}$$

In contrast to the initial acceleration problem (5.37a), the dynamical pressure and the effective gravitational potential are now treated in the same perturbation order. On the surface $r = R_0$, the solution for $\varphi_1$ can be written as a second-order polynomial in the variable $z = 1 - \cos\Theta$. This representation is convenient, being an expansion about the upper stagnation point. Setting $\varphi_1 = \alpha + \beta z + \gamma z^2$, we obtain from the different powers of $z$ in eq. (5.45),

$$\dot{\alpha} = -aR_0 , \quad \dot{\beta} = aR_0 - \left(\frac{\delta}{\delta - 1}\, u\right)^2 , \quad \dot{\gamma} = \frac{1}{2}\left(\frac{\delta}{\delta - 1}\, u\right)^2 . \tag{5.46}$$

The initial velocity $u$ is now chosen in such a manner, that the flow along the surface remains steady in a first-order neighborhood of the stagnation point. Setting $\beta = 0$, there follows

$$u = F\sqrt{aR_0} , \quad F = (\delta - 1)/\delta . \tag{5.47}$$

The Froude numbers are $F = \frac{2}{3}$ for the three-dimensional and $F = \frac{1}{2}$ for the two-dimensional case. The three-dimensional result has first been obtained by Davis and Taylor [14] and seems to be well confirmed by their experiments. We also mention the rather close agreement with the estimates given by eq. (5.43).

*5.2.4. Transient evolution*

With appropriate expressions for the velocity $u$, the potential (5.44a) can describe the initial acceleration phase and also the final steady-state. It is therefore a reasonable assumption to use this form at the bubble head throughout the entire evolution. Although this is not a completely rigorous procedure, it will lead to a useful closed interpolation formula between the initial and final stages of the evolution.

We now evaluate eq. (2.10b) on the sphere $r = R_0$ with the potential ansatz,

$$\varphi = b(t) - [r + (\delta - 1)^{-1} R_0 / r^{\delta - 1}] u(t) \cos \Theta \,, \tag{5.48}$$

and expand in the variable $z = 1 - \cos \Theta$. The boundary condition can be satisfied up to linear order in $z$ by setting,

$$\dot{b} = \frac{1}{\delta - 1} R_0 \dot{u} - a R_0 \,, \quad \frac{1}{\delta - 1} R_0 \dot{u} + \left( \frac{\delta}{\delta - 1} u \right)^2 = a R_0 \,. \tag{5.49}$$

While the first equation defines merely the time function $b(t)$ in the potential, the second equation determines the bubble rise velocity $u(t)$. Assuming for the bubble amplitude $h(t)$ the initial conditions $h(0) = \dot{h}(0) = 0$, the solution of eq. (5.49) becomes

$$u = \dot{h} = \frac{\delta - 1}{\delta} \sqrt{a R_0} \tanh(\delta \sqrt{a / R_0}\, t) \,, \tag{5.50a}$$

$$h = \frac{\delta - 1}{\delta^2} R_0 \ln[\cosh(\delta \sqrt{a / R_0}\, t)] \,. \tag{5.50b}$$

These interpolation formulas complete our discussion of closed free-surface bubbles in an extended fluid.

### *5.3. Open bubbles*

The treatment of closed underwater bubbles cannot be completely satisfactory until the fully developed flow has been described. Instead of analysing this obviously complicated flow, Davis and Taylor [14] have suggested the simpler problem of open bubbles rising under well-defined steady-flow conditions in circular tubes. Their ideas have stimulated in many ways the further developments in this field. In particular, the rise of two-dimensional bubbles in a vertical channel has been discussed extensively in the literature. We will describe a relatively simple analysis based on the model of periodic source flows. This approach has the advantage that it demonstrates the existence of exact solutions for certain acceleration fields. Moreover, a particular solution can be found that approximates closely presently accepted bubble parameters. The material of this section has first been presented in ref. [74] and was partly reviewed in ref. [75]. A summary of results from alternative approaches will be given in section 5.3.6.

#### *5.3.1. Steady-state model*

If a tube, filled with liquid, is opened at the bottom, a gas bubble will grow hemispherically from below and rise vertically in the tube. Asymptotically, a steady flow around an axially symmetric bubble will be established. We will discuss this steady-state problem in plane geometry, assuming a channel of width $D$ with parallel walls at $x = \pm D/2$. The bubble is rising in the $y$ direction with a constant velocity $u = F\sqrt{aD}$, where the Froude number $F$ has to be determined.

The mathematical problem can be easily formulated in the following way. We choose a reference frame moving with the bubble rise velocity $u$. The bubble surface is denoted as $y = \zeta(x)$. It extends below the top of the bubble $y_s = \zeta(0)$ on the axis of symmetry $x = 0$. Assuming constant pressure in the

bubble region, the boundary conditions for the velocity potential are

$$[\tfrac{1}{2}v^2 + a(y - y_s)]|_{y=\zeta(x)} = 0\,, \quad v_y|_{y=\infty} = -u\,, \quad v_x|_{x=0} = v_x|_{x=\pm D/2} = 0\,. \tag{5.51}$$

From the first condition, one can recognize the presence of a stagnation point at $y_s$. Below this point, the velocity of surface particles increases monotonically with the vertical distance $y_s - y$. This excludes the possibility of bubble closure at a second stagnation point as in fig. 18. Under steady-flow conditions, one can expect a contraction of the falling jets with increasing velocities. Asymptotically, the spike velocity will become nearly uniform and vertical over the spike cross-section. The limiting form of the spikes can be obtained by assuming mass conservation and free-fall according to the equations

$$(\tfrac{1}{2}D - x)v = \tfrac{1}{2}Du\,, \quad v^2 = -2ay\,. \tag{5.52}$$

Eliminating $v$, the surface equation of the falling jet is found to be,

$$\frac{y}{\frac{1}{2}D} = -\frac{F^2}{(1 - x/\frac{1}{2}D)^2}\,. \tag{5.53}$$

*5.3.2. Source rows*

We will proceed by modifying Taylor's spherical bubble model to account for the present boundary conditions. To avoid bubble closure, we replace the dipole source in Taylor's model by a single point source. To satisfy the boundary conditions at the walls of the channel, the model is further extended to a periodic row of equally spaced sources. We remark that periodic axially symmetric flows satisfy the rigid wall conditions automatically. If

$$v_x(x = -\tfrac{1}{2}D) = v_x(x = \tfrac{1}{2}D)\,, \quad v_x(-x) = -v_x(x)\,, \tag{5.54a}$$

then

$$v_x(x = -\tfrac{1}{2}D) = v_x(x = \tfrac{1}{2}D) = v_x(x = 0) = 0\,. \tag{5.54b}$$

We will first analyse the kinematics of the source flow and then discuss possible dynamical bubble solutions.

In plane geometry, the complex potential of a single source at the origin has the form,

$$W_s = \ln z\,, \tag{5.55}$$

where $z = x + \mathrm{i}y$. Now assume sources at the points $z = \pm mD$ of the real axis with integers $m = 0, 1, 2, \ldots$. The complex potential of the infinite source row can be evaluated in terms of the variable $t = \pi z/D$ as,

$$\begin{aligned} W_r &= \ln t + \sum_{m=1}^{\infty} [\ln(m\pi - t) + \ln(m\pi + t) - \ln(m^2\pi^2)] \\ &= \ln\Big(t \prod_{m=1}^{\infty} (1 - t^2/m^2\pi^2)\Big) = \ln(\sin t)\,. \end{aligned} \tag{5.56}$$

In the infinite sum, a constant has been subtracted that ensures convergence of the series for $t = 0$. In the last step, the product representation of $\sin t$ by its zeros [93] has been used. For convenience, we add the constant $c = (\ln 2 - i\pi)/2$ to eq. (5.56), set $k = 2\pi/D$, and define the velocity potential $\varphi_r$ and the stream function $\psi_r$ of the row as,

$$\varphi_r = \mathrm{Re}\{W_r + \tfrac{1}{2}\ln 2\} = \tfrac{1}{2}\ln[\cosh(ky) - \cos(kx)]\,, \tag{5.57a}$$

$$\psi_r = \mathrm{Im}\{W_r - \tfrac{1}{2}\pi\} = \arctan[\cot(\tfrac{1}{2}kx)\tanh(\tfrac{1}{2}ky)] - \tfrac{1}{2}\pi\,. \tag{5.57b}$$

The source flow (5.57) can be linearly combined with a uniform stream perpendicular to the row such that the incoming flow at $y \to \infty$ has a uniform velocity $u_1$ and the outgoing flow at $y \to -\infty$ another uniform velocity $u_2 > u_1$. Such a model will describe the acceleration of the incident fluid over a finite distance from the initial velocity $u_1$ up to the final velocity $u_2$. The asymptotic velocities $u_{1,2}$ are related by mass conservation $Du_1 = du_2$, where $d$ denotes the width of the asymptotic jet. The ratio $q = u_1/u_2 = d/D$ describes the contraction of the flow and may vary in the interval $0 < q < 1$. The velocity $u_s$ of the uniform stream and the velocity $u_r$ produced by the source row at $y \to -\infty$ can be expressed in terms of the asymptotic velocities $u_{1,2} = u_s \mp u_r$ as

$$u_s = \tfrac{1}{2}(u_2 + u_1)\,, \quad u_r = \tfrac{1}{2}(u_2 - u_1)\,. \tag{5.58}$$

With these expressions, the combined flow assumes the final form,

$$\varphi = -u_s y + 2u_r\varphi_r/k\,, \quad \psi = u_s x + 2u_r\psi_r/k\,. \tag{5.59}$$

The streamlines of the flow are illustrated schematically in fig. 19. The streamline $\psi = 0$ separates the flow domain of the incident fluid from the bubble region. A straightforward calculation yields the explicit surface equation,

$$y = \ln\left(\frac{\sin[kx/(1-q)]}{\sin[kxq/(1-q)]}\right). \tag{5.60}$$

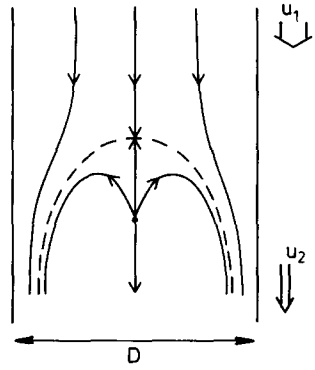


Fig. 19. Streamline pattern around an open bubble inside a channel of width $D$. In the source row model, the fluid has constant but different asymptotic velocities $u_1$ and $u_2$ above and below the sources, respectively. The flow has a stagnation point at the top of the bubble.

Expanding (5.60) about $x = 0$, one finds the local approximation,

$$y = y_s - \frac{1}{2R} x^2 , \quad \frac{y_s}{D} = -\frac{1}{2\pi} \ln q , \quad \frac{R}{D} = \frac{3}{2\pi} \frac{1-q}{1+q} . \tag{5.61}$$

*5.3.3. Dynamical bubble model*

Equation (5.60) describes a one-parameter family of possible bubble shapes. One cannot expect that these are already dynamically consistent solutions of the boundary-value problem (5.51). The following dynamical interpretation was therefore suggested [74]. Instead of assuming a uniform acceleration $a$, we consider the steady bubble flow in a general gravitational potential $U(y)$ with $a = \partial_y U(y_s)$ being the local acceleration at the top of the bubble. The form of $U(y)$ is not prescribed in advance, but it is determined self-consistently for the given flow. This procedure yields exact free-surface solutions for certain nonuniform acceleration fields. By comparing the resulting accelerations, we also obtain a criterion for choosing approximate solutions for uniform acceleration among the various bubble flows that may be constructed kinematically.

To make this interpretation precise, the self-consistent gravitational potential is defined as

$$U(y) = -\tfrac{1}{2} v^2 |_{x=\zeta^{-1}(y)} , \quad \partial_y U|_{y=y_s} = a . \tag{5.62}$$

This definition is an obvious generalization of the free-surface boundary condition in eq. (5.51). A unique surface function $x = \zeta^{-1}(y)$ exists, provided that the vertical distance from the stagnation point grows monotonically along the surface. This constraint, however, does not seem restrictive for steady-flow solutions.

Considering now the source flow (5.57)–(5.59), the condition $\partial_y U(y_s) = a$ can be satisfied by choosing the Froude number of the incident flow as

$$F = [(1 - q^2)/6\pi]^{1/2} . \tag{5.63}$$

The gravitational potentials (5.62) are zero at the stagnation point and drop to the constant value $-u_2^2/2$ in the asymptotic jet. Some corresponding bubble-potential pairs are shown in fig. 20.

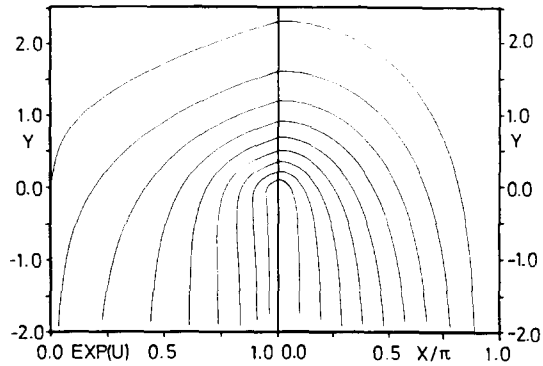


Fig. 20. Surface shapes of steady-state bubbles (right) and corresponding gravitational potentials (left). A source is located at $x = y = 0$ and the curves emanate from the stagnation point at $y = -\ln q$. The parameter $q$ is varied in steps of 0.1 from $q = 0.1$ up to $q = 0.9$. It denotes the ratio of the contracted spike width to the channel width, being 0.1 for the largest bubble and 0.9 for the smallest bubble of the figure. (From ref. [75].)

Comparing the potentials for different $q$ values, the best approximation for uniform acceleration is found by choosing $q \approx 0.2$ [74]. In this case, the acceleration is nearly uniform up to the asymptotic free-fall region. Assuming this value, the bubble parameters (5.61) and (5.63) become

$$F \approx 0.226\,, \quad R/D = 1/\pi \approx 0.318\,, \quad y_s/D \approx 0.256\,. \tag{5.64}$$

Both the Froude number $F$ and the radius of curvature $R$ are in excellent agreement with the results that have been obtained by other solution methods. One should also notice that the vertical distance of the source row from the bubble vertex is only one quarter of the channel width. This may explain the early failure of perturbation methods in the nonlinear RT instability.

*5.3.4. Normal mode expansions*

We now compare in more detail the present source solutions with normal mode expansions. Because of the singularities at $y = 0$, Fourier series will not converge in the entire plane. However, series representations can be found in the half-planes above and below the source row. In the region $y > 0$, the Fourier series of the potential (5.57a) is [75]

$$\varphi_r = -\tfrac{1}{2}\ln 2 + \tfrac{1}{2}k(y_s + y') - \sum_{m=1}^{\infty} \frac{q^m}{m} \exp(-mky') \cos(mkx)\,, \tag{5.65}$$

where $y' = y - y_s$ denotes the vertical distance from the bubble maximum. For sufficiently small $q$ values, the Fourier coefficients of subsequent harmonics decrease rapidly and the head of the bubble becomes well separated from the singularities at $y' = -y_s$. In this limit, the flow can be well approximated by a single mode or a few modes only. It was shown in ref. [73] that this approach leads also to acceptable estimates of bubble parameters.

The limit $q \to 0$ is of particular interest, corresponding to the single mode approximation. The bubble parameters of this flow can be found with the help of eqs. (5.61) and (5.63) as

$$F = 1/\sqrt{6\pi} \approx 0.230\,, \quad R/D = 3/2\pi \approx 0.477\,. \tag{5.66}$$

Comparing with eq. (5.64), it can be seen that the Froude number is well approximated by the single mode flow. However, the radius of curvature is much more sensitive to the flow model. The larger value in eq. (5.66) can be understood in terms of the different acceleration fields. In the case where $q = 0$, the effective gravitational potential (5.62) decreases exponentially and therefore gives rise to a much stronger contraction of the falling spike. A detailed comparison of the gravitational potentials near the bubble maximum can be recognized in fig. 21.

*5.3.5. Transient evolution*

The transition from the linear RT instability to the final steady-state flow can be described rather accurately by a single mode description. This model has been discussed before in refs. [73, 75] and was found independently in a former work by Layzer [54]. The single mode approximation is justified partially by perturbation theory (section 5.1.2) during the initial stage and partially by steady-state theory (section 5.3.4) in the asymptotic bubble stage. Moreover, its predictions for the bubble amplitude are in excellent agreement with complete computational solutions [15, 103].

In the following, we use the same dimensionless variables as in section 5.1 and a reference frame with the origin attached to the bubble vertex. The flow model is written in the form,

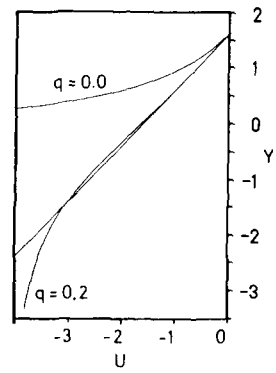


Fig. 21. Comparison of the gravitational potentials (5.62) for $q = 0$ and $q = 0.2$ with the gravitational potential for uniform acceleration (straight line). The value $q = 0$ corresponds to the single mode approximation. The value $q = 0.2$ provides an excellent approximation for a uniform acceleration field up to a depth where the spike is nearly freely falling.

$$\varphi = -u[-1 + y + \exp(-y)\cos(x)]\,, \tag{5.67a}$$

$$\psi = u[x - \exp(-y)\sin(x)]\,. \tag{5.67b}$$

The bubble velocity $u(t)$ can be an arbitrary time function that is not specified in advance. Despite this time dependence, the streamlines of the flow remain steady. They are coincident with particle trajectories and resemble those of fig. 19 with the source placed at $y = -\infty$. The streamline $\psi = 0$ represents the separatrix

$$y = \ln[(\sin x)/x]\,. \tag{5.68}$$

Initially, the fluid is confined to the half-space $y > \zeta_0(x)$. In the course of time evolution, the fluid is falling along the streamlines and the separatrix (5.68) becomes the asymptotic surface profile.

In the bubble reference frame, the boundary conditions are

$$[\partial_t\varphi + \tfrac{1}{2}v^2 + (1 + \dot{u})y]\big|_{y=\zeta(x)} = 0\,, \quad (\partial_t\zeta + v_x\,\partial_x\zeta - v_y)\big|_{y=\zeta(x)} = 0\,. \tag{5.69}$$

Inserting eqs. (5.67) in eqs. (5.69) yields

$$\begin{aligned} &\dot{u}(1 - \mathrm{e}^{-\zeta}\cos x) + \tfrac{1}{2}u^2(1 - 2\,\mathrm{e}^{-\zeta}\cos x + \mathrm{e}^{-2\zeta}) + \zeta = 0\,, \\ &\partial_t\zeta + u\,\mathrm{e}^{-\zeta}\sin x\,\partial_x\zeta - u(1 - \mathrm{e}^{-\zeta}\cos x) = 0\,. \end{aligned} \tag{5.70}$$

In accordance with the steady-state argument (5.62), it is sufficient to satisfy these conditions near the bubble vertex. Locally, the bubble surface can be expanded in the form $y = -\kappa x^2/2$ with a time-dependent curvature $\kappa(t)$. Expanding eq. (5.70) up to the order $O(x^2)$ yields, for the bubble amplitude $h(t)$, a system of evolution equations,

$$\dot{h} = u\,, \quad \dot{u} + \frac{u^2}{1-\kappa} - \frac{\kappa}{1-\kappa} = 0\,, \quad \dot{\kappa} = (1 - 3\kappa)u\,. \tag{5.71}$$

These equations may be integrated once. The result is

$$u^2 = \frac{\frac{2}{3}(1-g) - g[2f(h-h_0) - u_0^2(2+f)]}{2+fg}\,,$$
$$\kappa = \tfrac{1}{3}(1-fg)\,, \quad f = 1-3\kappa_0\,, \quad g = \exp[-3(h-h_0)]\,, \tag{5.72}$$

where the index 0 denotes initial values. In the linear approximation, one can easily recover from eq. (5.71) the amplitude equation $\ddot{h} - h = 0$ of the RT instability. For large amplitudes ($g \ll 1$), the steady-state values $\kappa = 1/3$ and $u = 1/\sqrt{3}$ are obtained from eq. (5.72). Noting that $F = u/\sqrt{2\pi}$ and $R/D = 1/2\pi\kappa$ with the present units, the steady-flow parameters of eq. (5.66) are reproduced.

The evolution of the amplitude $h$ and of the Froude number $F$ is shown in fig. 22 for a sinusoidal initial perturbation $\zeta_0 = h_0 \cos x$. The present predictions (solid lines) are compared with numerical calculations (symbols) based on the method of least-squares approximation as discussed in section 5.1. From this comparison one may conclude, that the single-mode approximation is excellent throughout the small-amplitude regime and, moreover, it can account accurately for nonlinear saturation of velocity growth.

### 5.3.6. *Comparison of results*

The analysis of bubble dynamics has received considerable attention mainly in the succession of the

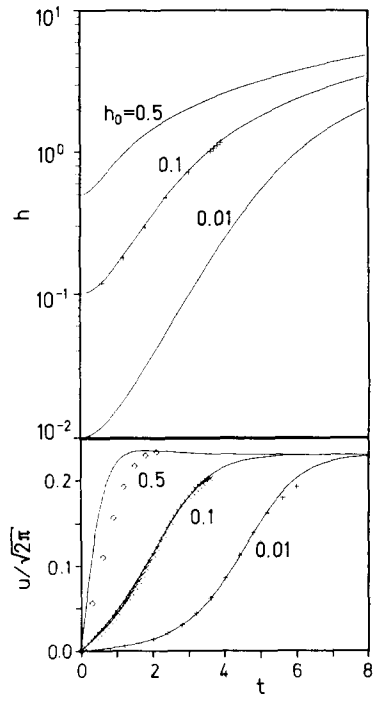


Fig. 22. Evolution of the bubble amplitude $h$ and velocity $u$ from an initial surface displacement $h_0 \cos x$. Solid lines refer to the solution of the nonlinear amplitude equation (5.71) and marker symbols show corresponding results from the least-squares approximation method (section 5.1.4). The units are $k^{-1}$ for the length and $1/\sqrt{ak}$ for the time. The complete numerical solution for $h_0 = 0.5$ [15, 103] is in close agreement with these results, showing growth saturation near the time $t = 2$. (From ref. [75].)

pioneering work of Taylor. We only mention some representative works. Experimental studies have been reported by Dumitrescu [104], Lewis [2], Davis and Taylor [14], Ratafia [7], and Read [10]. Theoretical bubble models have been developed by Davies and Taylor [14], Fermi [105], Layzer [54], and the present author [73–75]. Mathematical conformal mapping theories have been presented by Birkhoff and Carter [55], Garabedian [56], and Vanden-Broeck [106]. Various computational methods have been applied to the problem. These include particle-in-cell fluid simulations by Harlow and Welch [107] and by Daly [17], vortex simulations by Baker et al. [13, 15, 108] computations of conformal mappings by Menikoff et al. [103, 109], and front-tracking methods by Glimm et al. [61].

A number of works have been concerned with the rise of open-ended bubbles as observed in the RT instability. We first summarize some results for axially symmetric cylindrical bubbles and then discuss the more extensive literature on axially symmetric plane bubbles.

The cylindrical case has been studied experimentally by Davis and Taylor [14] as well as by Dumitrescu [104]. Davies and Taylor have measured Froude numbers $F = u/\sqrt{aD}$ in the range 0.33–0.35 using a cylindrical tube with diameter $D = 7.94$ cm. They could also verify the free-fall surface profile of the asymptotic jet below a depth of $\approx 0.75D$. However, the values of $F$ deduced from the jet equation (corresponding to eq. (5.53) in the cylindrical case) have been found too large. This discrepancy was explained by uncertainties in the measurement of thin sheets and by the possible existence of a boundary layer at the walls of the tube. Dumitrescu found the values $F = u/\sqrt{aD} = 0.35$ and $R/D = 0.375$ and therefore $u/\sqrt{aR} = 0.57$. The last value is only somewhat smaller than the coefficient 2/3 for spherical underwater bubbles. The experimental results may also be compared with the theoretical estimate $F = 0.36$ that has been derived by Layzer [54] from a single-mode description of the flow.

The rise of steady plane bubbles was investigated by conformal mapping methods by Birkhoff and Carter [55]. Their treatment is probably one of the most rigorous attempts to solve the free-surface boundary-value problem under gravity. The Froude number $F = 0.226$ was obtained for a particular numerical procedure but the result did depend slightly on the method of evaluation. It was therefore concluded that $F = 0.23 \pm 0.01$ within the numerical uncertainties. Unfortunately, consistent predictions of the curvature could not be obtained in this work. The problem was reconsidered by Garabedian [56] and more recently by Vanden-Broeck [106]. In these works it is found that steady-state solutions exist for any Froude number up to a critical value $F_c$. While Garabedian estimated $F_c = 0.24$, the calculations of Vanden-Broeck gave the critical value $F_c = 0.36$. However, it was also found that the classical values $F = 0.23$ and $R/D = 0.32$ are approached if an arbitrarily small surface tension is included in the algorithm.

In another series of papers, the RT initial-value problem has been studied numerically up to the bubble regime. In one of the first numerical treatments, Harlow and Welch [107] have applied particle-in-cell methods to the study of the free-surface instability. The bubble–spike structure was nicely reproduced in these calculations and the bubble parameters could be closely estimated as $F \approx 0.24$ and $R/D \approx 0.39$. The particle-in-cell approach has been extended by Daly [17] for the application to two-fluid calculations with surface tension. Their results show broadening and roll-up of the spike in fluids with finite densities. These calculations correspond closely to experimental observations by Ratafia [7]. The most accurate results could be obtained with vortex simulations by Baker et al. [15] and with conformal mapping methods by Menikoff et al. [103]. Starting with several small-amplitude perturbations, the first treatment gave asymptotic bubble values in the range $F = 0.225$–$0.226$ and $R/D = 0.322$–$0.318$. In the second treatment, the bubble results are similarly $F = 0.23$ and $R/D = 0.312$.

Table 4
Summary of bubble parameters for different geometries. ($u$ is rise velocity, $a$ is acceleration, $D$ is bubble diameter, $R$ is radius of curvature)

| | Geometry | Parameter | Method |
|---|---|---|---|
| Closed bubbles | cylindrical | $u = 0.5\sqrt{aR}$ | model: eq. (5.47) [58] |
| | spherical | $u = \frac{2}{3}\sqrt{aR}$ | model: eq. (5.47) [14]<br>experiment [14] |
| Open bubbles | plane | $u = 0.23\sqrt{aD} = 0.4\sqrt{aR}$,<br>$R = 0.32D$ | model: eq. (5.64) [74]<br>computation [15, 103] |
| | | $u = 0.23\sqrt{aD} = 0.33\sqrt{aR}$,<br>$R = 0.48D$ | model: eq. (5.66) [54, 73] |
| | | $u = 1.1\sqrt{aR}$ | experiment [2] |
| | | $u = (0.2\text{–}0.3)\sqrt{aD}$ | experiment [4] |
| | cylindrical | $u = (0.33\text{–}0.35)\sqrt{aD}$ | experiment [14] |
| | | $u = 0.35\sqrt{aD} = 0.57\sqrt{aR}$<br>$R = 0.375\,D$ | experiment [104] |
| | | $u = 0.36\sqrt{aD}$ | model [54] |

The typical bubble parameters are summarized in table 4. Although these results are only approximate, they should be indicative for two major trends. Firstly, one can recognize that 3D bubbles rise faster than 2D bubbles. It is therefore expected, that the late time evolution of the RT instability will be three-dimensional rather than two-dimensional. The three-dimensional bubble flow may have a more or less regular lattice structure, which, however, has not been investigated in detail so far. Some three-dimensional calculations have been reported by Davidov [110] and a three-dimensional model was discussed by Colombant et al. [111]. The latter one is based on a nonlinear solution for thin sheets that has been found before by Ott [19]. Secondly, it is important to note the increase of the rise velocity with the bubble dimensions. This dependence suggests a transition to larger bubbles by processes as competition, coalescence and expansion. This stage is the subject of the statistical mixing theory. Some basic models of bubble competition and bubble expansion will be described in the following.

### *5.4. Self-similar evolution*

While a rather complete understanding of the single-bubble problem has been gained, the more complex phenomena of bubble interactions are still under investigation. Mixing experiments by Read [10] have shown the growth of bubbles from small scales up to the dimension of the accelerated system. The experimental results could be basically confirmed with different experimental methods by Andrews and Spalding [112] and with ab initio calculations of the RT mixing problem by Youngs [113]. Theoretical modeling of mixing-layer growth is frequently based on a phenomenological diffusion approach. It was introduced by Belen'kii and Fradkin [114] and later modified by various authors [12, 115]. These diffusion models obtain consistency with experimental data by the use of one or more empirical constants. Another approach, the statistical bubble model, is based explicitly on bubble dynamics. It was first introduced by Sharp and Wheeler and received renewed attention in the works of Gardner et al. [16] and Glimm et al. [116]. Some variants of this model have been considered by Inogamov [117] and by Zufiria [118]. A novel criterion for nonlinear saturation in multi-mode problems

was introduced by Haan [119]. Other work has been concerned with turbulent energy estimates for the mixing regime [120, 121].

Self-similarity plays an important role in the evolution of RT mixing layers. In the absence of a prescribed bubble length-scale, the mixing layer is expected to grow in proportion to the acceleration distance. This similarity assumption suggests an evolution law $h(t) = cat^2$, where $h$ denotes the width of the mixing layer and $c$ an approximately universal similarity constant. According to the experimental studies [10], the constant $c$ is $\approx 0.058$–$0.065$ for two-dimensional and $\approx 0.073$–$0.077$ for three-dimensional flows. These values correspond to free-surface evolution, where $h$ is measured by the distance between the front of emerging bubbles and the undisturbed interface. Apparently, the mixing layer grows with a small fraction of the applied acceleration and with a weak dependence on the number of space dimensions.

In the following, we will describe three different attempts to derive self-similar evolution laws. These models may provide some background for future statistical theories. Making simplifying assumptions, we wish to discuss how predictions support each other and how they differ. First, mode competition in the linear RT instability is analysed as a particularly simple example. Then, a model of bubble competition between noninteracting bubbles of various sizes is presented. Finally, the dynamics of self-similarly expanding bubbles is studied.

*5.4.1. Mode competition*

A remarkable feature of the RT instability growth rate (3.3) is the absence of a finite wave number of maximum growth. This difficulty can be resolved by including damping effects as viscosity or surface tension [57]. However, when these effects are negligible, a different interpretation has to be found.

One way of specifying the dominant mode would be to evaluate the time-asymptotic response in the RT initial-value problem. Unfortunately, the Fourier-series method is generally not applicable to the surface evolution even in the linear theory. It leads to ill-defined expressions for the surface displacement after an arbitrarily small time interval if the initial data are not analytic [122]. To avoid this problem, the Fourier representation of the velocity potential may be applied to interior points ($y > 0$) of the fluid, only. The spatial damping of the modes inside the fluid provides the required convergence of the series. Boundary values have then to be defined by a limiting procedure. For the present purpose, it is sufficient to examine the propagation of perturbations inside the fluid. Because of the strong spatial damping of short-wavelength modes, longer wavelengths become more competitive in the course of time evolution. This mode competition leads to a self-similar evolution law.

Let us assume a fluid layer in the half-space $y > 0$ supported by gas pressure at the surface $y = 0$ under an acceleration $a$ along the $y$ direction. Choosing an interior point $x = 0$, $y > 0$, the growth amplitude of the velocity potential can be represented as a superposition of unstable modes,

$$\varphi(y, t) = \int_0^\infty \mathrm{d}k\, \varphi_k \exp(nt - ky)\,. \tag{5.73}$$

Each mode with wave number $k$ evolves with the classical growth rate $n = \sqrt{ak}$ and is spatially damped toward the interior of the fluid layer $y > 0$. The integral will converge for $t > 0$, provided that it is convergent initially. The wave number of maximum growth $k = k_\mathrm{m}$ and the corresponding growth rate $n_\mathrm{m} = \sqrt{ak_\mathrm{m}}$ may be defined by the saddle-point condition $\partial_k(nt - ky) = 0$. It leads to the relationship

$$k_\mathrm{m} y = \tfrac{1}{2} n_\mathrm{m} t = \tfrac{1}{4} a t^2 / y\,. \tag{5.74}$$

Accordingly, the dominant wavenumber increases with time and decreases with the vertical distance from the initial surface. For localized perturbations, the mode amplitudes $\varphi_k$ are slowly varying. In the time-asymptotic limit where $at^2/y \gg 1$, one can then evaluate the integral (5.73) by the saddle-point approximation, yielding

$$\varphi(y, t) \approx (1/y)(\pi at^2/y)^{1/2} \varphi_{k_m} \exp(at^2/4y) . \tag{5.75}$$

With these expressions, one can roughly estimate the growth of the mixing layer. Let us define the front $y = h$ of the mixing region by a fixed number of e-foldings $N = at^2/4h$. This leads to the self-similar scaling relation,

$$h \sim (1/4N)at^2 , \quad k_m h \sim N , \tag{5.76}$$

where $N$ will be a number of the order of 2–6. The precise value of the similarity constant $c = 1/4N$ cannot be derived from linear theory, although it may be expected much smaller than one. The following bubble models will lead to a similar scaling as in eq. (5.76) and there the constants will assume definite values.

The present arguments can also be applied to estimate the critical failure modes that will lead to breakup of an accelerated foil of thickness $d$. Using the break-up condition $h = d$, there follows from eq. (5.76) the estimate

$$k_m d = N , \quad Q = at/2d = 2N , \tag{5.77}$$

for the worst wavenumber $k_m$ and the maximum inflight aspect ratio $Q$, respectively. It is generally believed that the most critical wavelengths are those in the range $k_m d \sim 1$–3. The estimate of the inflight aspect ratio is probably too pessimistic. It will be improved by nonlinear theory and by the inclusion of a number of stabilizing effects discussed in section 9.

*5.4.2. Bubble competition*

The linear theory of noninteracting normal modes can easily be extended to a model of noninteracting bubbles. For this purpose we divide the fluid layer into a large number of vertical channels of different widths. In each channel, the fundamental mode is excited with a small amplitude at the initial time $t = 0$. It will first grow exponentially and finally saturate linearly. The problem is to determine the maximum amplitude in the whole ensemble at time $t$.

Let us now analyse this problem in detail. The amplitude evolution for the mode with wavenumber $k$ can be expressed in the general form $A(k, t) = \hat{A}(\tau)/k$, where $\tau = \sqrt{ak}t$ denotes the dimensionless time variable and $\hat{A}(\tau)$ the dimensionless amplitude. We will assume and ultimately verify that the maximum of $A(k, t)$ with respect to $k$ occurs in the asymptotic bubble stage. The amplitude evolution can therefore be approximated as

$$A(k, t) = k^{-1}(u\tau - \beta) , \tag{5.78}$$

where $u = 1/\sqrt{3}$ denotes the dimensionless bubble rise velocity (5.72). The constant $\beta$ depends only on the dimensionless initial amplitude $\hat{A}(0) = kA_0$. It can be calculated from the single-mode equations (5.71). Specifically, assuming $\hat{A}(0) = 0.01$, one finds $\beta = 2.7$. We will take this value for the whole

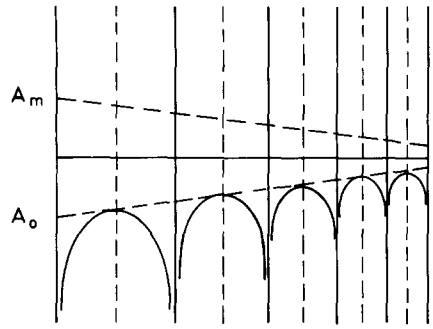


Fig. 23. Bubble ensemble in the competition model. The fluid is divided into channels of different widths $2\pi/k$ where bubbles start rising at $t = 0$ with different initial amplitudes $A_0 = -\beta/k$. A bubble reaches the perturbation front when its amplitude is equal to $A_m = \beta/k$. The constant $\beta$ can be related to the initial amplitude of sinusoidal surface perturbations and is found to be $\approx 2.7$. From this model, there follows a self-similar evolution law $h = 0.03at^2$ for the maximum amplitude in the bubble ensemble at time $t$.

ensemble. We remark that $\beta$ can also be viewed as defining a virtual initial bubble amplitude $A_0 = -\beta/k$ if the evolution law (5.78) is extrapolated back to the time $\tau = 0$. The distribution of these initial amplitudes in the bubble ensemble is illustrated in fig. 23. The largest bubbles rise from the deepest points but they will ultimately overtake the smaller bubbles because of their larger rise velocities.

The maximum of the amplitude (5.78) with respect to $k$ occurs when $\tau = 2\beta/u$. Defining the mixing layer width $h$ by the maximum bubble amplitude with wavenumber $k_m$, there follow the relations,

$$k_m = \left(\frac{2\beta}{u}\right)^2 \frac{1}{at^2} \approx 85.5 \frac{1}{at^2}, \tag{5.79a}$$

$$h = \frac{u^2}{4\beta} at^2 \approx 0.03at^2, \tag{5.79b}$$

$$k_m h = \beta \approx 2.7. \tag{5.79c}$$

The general form of this result agrees with eq. (5.76). The numerical constants should be quite accurate for the initial conditions considered. We remark that the amplitude $k_m h$ is found to be larger than one. The amplitude equation (5.78) is therefore well justified by our result. The constant $c = 0.03$ in the self-similar evolution law appears to be too small by about a factor of two. On the other hand, our analysis shows that a single-mode worst-wavelength analysis will not be completely wrong in the description of mixing regions.

As in section 5.4.1, the result can serve as a criterion for foil breakup by setting $h = d$. In the present case, we obtain the corresponding formulas,

$$k_m d = 2.7, \quad Q = 2\beta/u^2 \approx 16. \tag{5.80}$$

As an explicit example, we show in fig. 24 the nonlinear amplitude evolution for different modes as a function of the inflight aspect ratio $Q$. The amplitudes have been calculated from eq. (5.71) with initial value $kA_0 = 0.01$. The foil breaking amplitude $A_c$ is defined slightly different by requiring $A_c(1 - e^{-kd}) = d$. If this condition is satisfied, the thickness of the perturbed foil approaches zero. One can

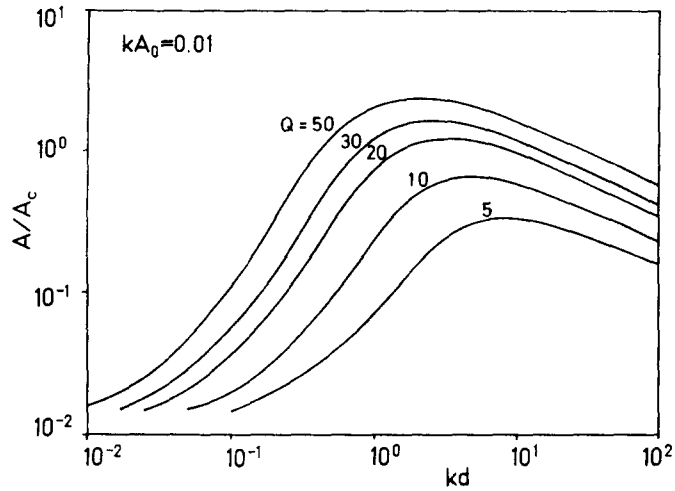


Fig. 24. Evolution of single mode perturbations as a function of the wave number $k$. The result is based on eq. (5.71) with an initial amplitude $kA_0 = 0.01$. The time is expressed in terms of the inflight aspect ratio $Q = at^2/2d$ for an accelerated foil of thickness $d$ and the amplitudes have been normalized by an estimate $A_c = d/(1 - e^{-kd})$ for foil breakup. The amplitude maximum follows closely the self-similar evolution law $A/d = 0.062Q$ and $kd = 43/Q$ of the bubble competition model (5.79). (From ref. [75].)

recognize the shift of the perturbation maximum toward smaller wavenumbers during the evolution. Foil breaking, $A = A_c$, occurs at about the same parameters as given by eq. (5.80). Minor differences are due to the different definitions of $A_c$. We have convinced ourselves that the criterion (5.80) is in excellent agreement with the numerical result.

### 5.4.3. Bubble expansion

In the preceding analysis we have neglected the influence of the increasing bubble size on the bubble rise dynamics. We now consider a number of well separated bubbles that can expand sideways over an appreciable distance before coalescing with neighboring bubbles. In this expansion model, a single dominant bubble can continuously adjust its size to the optimum value $kA \approx 2.7$ found in the preceding competition model. The question is how expansion affects bubble acceleration.

Now, consider a bubble rising in a vertical channel with a time-dependent width as illustrated in fig. 25. We will assume that the surface shape around the head of the bubble remains self-similar in the course of time evolution. Measuring lengths in units of the acceleration distance, the bubble wave number can be expressed in the form $k = 2\pi/D = 1/\varepsilon at^2$ with some constant $\varepsilon$. Further constants $u$, $c$, and $p$ may be defined through the relations,

$$u' = u\sqrt{a/k}\,, \quad h = cat^2\,, \quad kh = 1/p \tag{5.81}$$

for the rise velocity, the bubble amplitude, and the wavelength-to-amplitude ratio, respectively. These constants are simply related by

$$c = u\sqrt{\varepsilon}/2 = pu^2/4\,, \quad p = \varepsilon/c\,. \tag{5.82}$$

The expression for the similarity constant $c$ has again the same form as in eq. (5.79b). However, in the present theory, the rise velocity $u$ can be different from its steady-state value. In the following, we

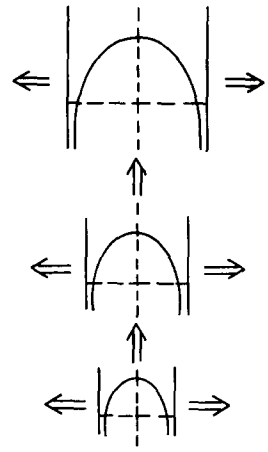

Fig. 25. Expansion model for accelerated bubble motion. The channel width and the bubble amplitude are assumed to grow in proportion to the acceleration distance. The bubble acceleration is estimated as a function of the amplitude-to-width ratio.

will estimate possible bubble accelerations as a function of the parameter $p$. For large amplitudes, $p \to 0$, the horizontal expansion rate $\mathrm{d}k^{-1}/\mathrm{d}t = pu$ becomes small in comparison with the vertical rise velocity. In this limit, the familiar steady-state theory becomes valid. For small amplitudes, $p \gg 1$, the instability is still in the linear stage where the bubble model is no longer meaningful. According to eq. (5.79c), we expect that values around $p = 1/\beta \approx 0.37$ will be a physically reasonable choice.

To determine these constants, one has to consider the free-surface boundary-value problem for the velocity potential $\varphi(x, y, t) = (u'/k)\Phi(\xi, \eta)$, where $\xi = kx$ and $\eta = ky$. In a comoving coordinate frame, with the origin attached to the bubble vertex, the boundary values $v_\xi = \partial_\xi \Phi(\eta = \zeta)$, $v_\eta = \partial_\eta \Phi(\eta = \zeta)$, and $\Phi = \Phi(\eta = \zeta)$ are found subject to the relations,

$$p(\zeta - \xi\, \mathrm{d}\zeta/\mathrm{d}\xi) + v_\xi\, \mathrm{d}\zeta/\mathrm{d}\xi - v_\eta = 0\,, \tag{5.83a}$$

$$p[3\Phi - 2(\xi v_\xi + \eta v_\eta)] + v_\xi^2 + v_\eta^2 + (2/u^2 + p)\zeta = 0\,. \tag{5.83b}$$

The first equation is the kinematical condition for the surface velocity and the second one the dynamical condition of constant surface pressure. We note that the terms proportional to $p$ arise from the unsteady motion and are therefore absent in the steady-state theory.

To satisfy the boundary conditions (5.83b) around the top of the bubbles, we follow the procedure described in section 5.3. Approximating the flow by a source at a distance $-\ln q$ below the vertex $\zeta = -\kappa\xi^2/2$, we find the bubble parameters,

$$\kappa = \frac{1+q}{1-q}\,\frac{1}{3-p(1-q)}\,, \quad u^2 = \frac{\kappa(1-q)^2}{1-(p/2)(1-q)[1+\kappa(1-q)]}\,. \tag{5.84}$$

The parameter $q$ can be closely determined by minimizing the error of the constant pressure condition between the stagnation point and the asymptotic free-fall region. For definiteness, this distance is taken as half a wavelength ($|\eta| = \pi$). We then obtain possible bubbles as a function of the remaining parameter $p$. For such adjusted parameter pairs, the similarity constant $c$ can be evaluated by use of eq.

Table 5
Similarity constant $c$ as a function of the parameter $p = 1/kh$ in the bubble expansion model

| | | | | | | |
|---|---|---|---|---|---|---|
| $p$ | 0.0 | 0.1 | 0.3 | 0.4 | 0.5 | 0.6 |
| $q$ | 0.2 | 0.22 | 0.24 | 0.26 | 0.28 | 0.30 |
| $c$ | 0.0 | 0.009 | 0.031 | 0.044 | 0.060 | 0.077 |

(5.82). Results of this procedure are given in table 5. One should notice, that the expected bubble accelerations are approximately reproduced in the parameter range $0.3 < p < 0.6$. This seems to be well consistent with our estimate $p \approx 0.37$ for non-expanding bubbles. The experimentally predicted value $c \approx 0.06$ can be obtained by choosing $p \approx 0.5$. The shape of some of these bubbles is represented in fig. 26. One can recognize a contraction of the steady-state profile with increasing acceleration.

The expansion model can also be applied to spherically closed bubbles. In this case, the expansion law can even be derived more rigorously by a first-order perturbation solution. For this purpose, we reconsider the initial acceleration problem for spherical bubbles of section 5.2. We now wish to discuss the influence of bubble expansion on the upward acceleration.

In section 4.2.1, we have already derived the first-order perturbation equation (4.26) for an arbitrary radially symmetric bubble motion $r = R(t)$. In this equation, the effect of an externally applied acceleration $g$ can be included by setting $\delta p = \rho g R \cos \Theta$. The applied acceleration induces the growth of an $l = 1$ mode with the surface displacement $\zeta = h(t) \cos \Theta$. Specializing eq. (4.26) to this case yields,

$$\frac{1}{\delta - 1} \frac{\mathrm{d}}{\mathrm{d}t} \left( m \frac{\mathrm{d}}{\mathrm{d}t} h \right) = mg , \quad m = \frac{\rho R^{\delta}}{\delta - 1} , \tag{5.85}$$

where $\delta = 2$ for two-dimensional and $\delta = 3$ for three-dimensional flow. For a rigid sphere, $R = \text{const.}$,

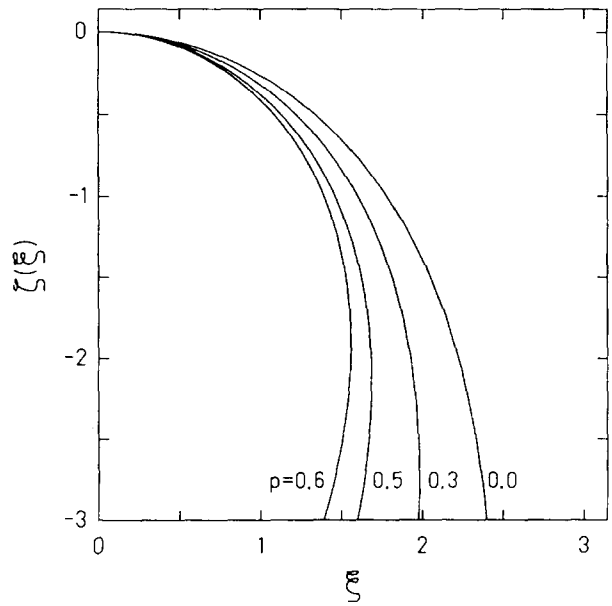


Fig. 26. Surface profiles $\eta = \zeta(\xi)$ of self-similarly expanding bubbles over one half-period $0 < \xi < \pi$ of the flow. The distances $\xi = kx$ and $\eta = ky$ are measured in units of $k^{-1} = ph$, where $h = cat^2$ denotes the bubble amplitude and $p = 1/kh$ a constant wavelength-to-amplitude ratio.

we recover from eq. (5.85) the inertial coefficient $\gamma = 1/(\delta - 1)$ as derived in eq. (5.38). Assuming now instead self-similar motion, $R \sim t^2$, $h \sim t^2$, we obtain from eq. (5.85)

$$\frac{1+2\delta}{\delta-1}\frac{\mathrm{d}^2}{\mathrm{d}t^2}h = g\,. \tag{5.86}$$

The inertia coefficients are now equal to 5 for $\delta = 2$ and equal to 7/2 for $\delta = 3$. Both values are significantly larger than for rigid motion because of the increase in bubble volume.

It is not completely obvious how the present simple result can be applied to the RT bubble problem. We suggest the following construction, which leads to satisfactory agreement with the observed behavior. We consider a bubble whose unperturbed diameter grows as $s = at^2/2$. In the laboratory frame, the bottom of the bubble is assumed at rest and the head of the bubble is viewed as the accelerated interface. In a coordinate frame where the bubble center is at rest, the effective gravity will be $g = a/2$. Using this relation in eq. (5.86) and writing its solution in the standard form $h = ct^2$, the similarity coefficients are found to be $c = 1/20 = 0.05$ for $\delta = 2$ and $c = 1/14 \approx 0.07$ for $\delta = 3$. We remark that both values are in surprisingly good accordance with the above cited experimental values for mixing-layer growth. In the present derivation, the decisive points are the increase of inertia by expansion and the redefinition of the effective gravity. Both aspects may be of general importance under the conditions of accelerated interface growth.

## 6. Stability of inhomogeneous fluids

The potential flow model, discussed so far, describes the motion of fluid layers with piecewise constant densities. In the following, we will consider incompressible fluids with continuous density variations. A basic difference arises from the possibility of vorticity generation in the presence of noncolinear pressure and density gradients. The evolution of these rotational modes and their relationship to the surface modes of potential flow theory is the main subject of this chapter.

We first introduce the nonlinear evolution equations for two-dimensional incompressible flow in an inhomogeneous medium. Rayleigh's classical eigenvalue problem for the stability of accelerated fluid layers is briefly reviewed and a general proof for the inversion invariance of its eigenvalue spectrum is presented. As an application, the stability of exponential density variations subject to various boundary conditions is discussed.

### *6.1. Incompressible flow model*

Incompressible motions of an inhomogeneous fluid in an external gravitational potential $U(\boldsymbol{x})$ are governed by the set of basic equations

$$\mathrm{d}\rho/\mathrm{d}t = 0\,, \quad \boldsymbol{\nabla}\cdot\boldsymbol{v} = 0\,, \tag{6.1a}$$

$$\mathrm{d}\boldsymbol{v}/\mathrm{d}t = -\rho^{-1}\boldsymbol{\nabla}p - \boldsymbol{\nabla}U\,, \tag{6.1b}$$

$$\mathrm{d}/\mathrm{d}t = \partial_t + \boldsymbol{v}\cdot\boldsymbol{\nabla}\,. \tag{6.1c}$$

In this model, the density is assumed constant along particle trajectories, but it can be different for different fluid particles.

*6.1.1. Hydrostatic equilibrium*

We first briefly discuss the equilibrium states in this model. Any steady incompressible flow is subject to the condition $\boldsymbol{v} \cdot \boldsymbol{\nabla} p = 0$. It excludes the possibility of mass flow along the density gradient. We will therefore restrict attention to the hydrostatic equilibrium,

$$\boldsymbol{v} = 0\,, \quad \partial_t \rho = 0\,, \quad \boldsymbol{\nabla} p = -\rho\, \boldsymbol{\nabla} U\,. \tag{6.2}$$

Both the pressure and the density have to be constant on equipotential surfaces. In fact, their gradients are directed along the surface normal direction $\boldsymbol{\nabla} U$ according to the relations,

$$\boldsymbol{\nabla} U \times \boldsymbol{\nabla} p = 0\,, \quad \boldsymbol{\nabla} \times \boldsymbol{\nabla} p = \boldsymbol{\nabla} U \times \boldsymbol{\nabla} \rho = 0\,. \tag{6.3}$$

The condition of hydrostatic equilibrium assumes therefore the form,

$$p(U) = -\int \mathrm{d}U\, \rho(U)\,, \tag{6.4}$$

where the function $\rho(U)$ can be prescribed arbitrarily.

*6.1.2. Two-dimensional flow*

The incompressible fluid equations can be further simplified in the case of two-dimensional flow. To satisfy the incompressibility condition $\boldsymbol{\nabla} \cdot \boldsymbol{v} = 0$, the velocity field is first expressed by the curl of a vector potential $\boldsymbol{\psi}$,

$$\boldsymbol{v} = \boldsymbol{\nabla} \times \boldsymbol{\psi}\,. \tag{6.5}$$

If the flow is uniform along a particular direction specified by the unit vector $\boldsymbol{n}$, it can be described by the single component $\psi = \boldsymbol{n} \cdot \boldsymbol{\psi}$ according to the relations

$$\boldsymbol{n} \cdot \boldsymbol{\nabla} \equiv 0\,, \quad \boldsymbol{n} \times \boldsymbol{v} = \boldsymbol{n} \times (\boldsymbol{\nabla} \times \boldsymbol{\psi}) = \boldsymbol{\nabla} \psi\,, \quad \boldsymbol{v} = \boldsymbol{\nabla} \psi \times \boldsymbol{n}\,. \tag{6.6}$$

The function $\psi$ is known as the stream function because it is constant along steady streamlines. This property follows from the identity

$$\boldsymbol{v} \cdot \boldsymbol{\nabla} \psi = (\boldsymbol{\nabla} \psi \times \boldsymbol{n}) \cdot \boldsymbol{\nabla} \psi = \boldsymbol{n} \cdot (\boldsymbol{\nabla} \psi \times \boldsymbol{\nabla} \psi) = 0\,. \tag{6.7}$$

The curl of the velocity field is generally non-zero,

$$\boldsymbol{\nabla} \times \boldsymbol{v} = -\Delta \psi\, \boldsymbol{n}\,. \tag{6.8}$$

According to eq. (6.1b), its evolution is governed by the vorticity equation,

$$\frac{\mathrm{d}}{\mathrm{d}t}\, \Delta \psi = \partial_t \Delta \psi + \{\Delta \psi, \psi\} = \rho^{-2} \{p, \rho\}\,. \tag{6.9}$$

Here we have used the bracket notation,

$$\{f, g\} = \boldsymbol{n} \cdot (\boldsymbol{\nabla} f \times \boldsymbol{\nabla} g) = \partial_x f \, \partial_y g - \partial_y g \, \partial_x f \,,$$

with $\boldsymbol{n}$ being normal to the $x$, $y$ plane. It can be seen that noncolinear pressure and density gradients are responsible for vorticity generation in inhomogeneous media. Irrotational potential flow is basically limited to homogeneous conditions. In this spectral context, the stream function $\psi$ is harmonic ($\Delta\psi = 0$) and it is related to the velocity potential $\varphi$ by the Cauchy–Riemann differential equations,

$$\boldsymbol{v} = \boldsymbol{\nabla}\varphi = \boldsymbol{\nabla}\psi \times \boldsymbol{n} \,. \tag{6.10}$$

To describe the fluid motion in terms of the variables $\rho$ and $\psi$ only, it is necessary to eliminate the pressure. Using eqs. (6.1) and (6.9) yields

$$\rho(\partial_t \Delta\psi + \{\Delta\psi, \psi\}) + \boldsymbol{\nabla}\rho \cdot (\partial_t \boldsymbol{\nabla}\psi + \{\boldsymbol{\nabla}\psi, \psi\}) = \{\rho, U\} \,, \tag{6.11a}$$

$$\partial_t \rho + \{\rho, \psi\} = 0 \,. \tag{6.11b}$$

These equations still describe the full nonlinear evolution of two-dimensional incompressible flow.

*6.1.3. Flow perturbations*

Consider now an arbitrary hydrostatic equilibrium. Small perturbations can be described by linearizing eq. (6.11) with respect to $\psi$. This yields

$$\boldsymbol{\nabla} \cdot (\rho \, \boldsymbol{\nabla} \partial_t^2 \psi) + \{\{\rho, \psi\}, U\} = 0 \,, \tag{6.12}$$

where $\rho$ denotes the unperturbed equilibrium density. The double bracket is proportional to the applied gravitational acceleration $\boldsymbol{g} = -\boldsymbol{\nabla} U$. More explicitly, it can be written as,

$$\{\{\rho, \psi\}, U\} = \boldsymbol{g} \cdot [\boldsymbol{\nabla} \times (\boldsymbol{\nabla}\rho \times \boldsymbol{\nabla}\psi)] \,. \tag{6.13}$$

*6.2. Stability eigenvalue problem*

The gravitational instability of fluid layers with variable density was first analysed by Rayleigh [3]. The classical eigenvalue problem and various extensions have been reviewed in great detail by Chandrasekhar [57]. The present discussion is mainly concerned with more recent developments. These include the inversion symmetry of the eigenvalue spectrum [68, 123] and explicit growth rate calculations for exponential transition layers [68, 124–127].

*6.2.1. Normal mode equation*

While eq. (6.12) is valid for arbitrary potentials $U = U(x, y)$, we now specialize to the physically important case $U = ay$, describing constant acceleration along the $y$ direction. Assuming normal mode perturbations, $\psi \sim \exp[\mathrm{i}(kx - \omega t)]$, eq. (6.12) becomes

$$\partial_\eta^2 \psi + \beta \, \partial_\eta \psi - (1 + \lambda\beta)\psi = 0 \,, \tag{6.14}$$

where $\eta = ky$, $\beta = \partial_\eta \rho/\rho$, and $\lambda = ak/\omega^2$. This is Rayleigh's famous eigenvalue equation for the normal mode growth rates and frequencies of accelerated fluid layers.

*6.2.2. Boundary conditions*

For a given density profile, the possible eigenvalues $\lambda$ are determined by boundary conditions imposed on the solution $\psi$. The most common boundary conditions are

$$\lim_{|\eta|\to\infty} \psi(\eta) = 0\,, \tag{6.15a}$$

$$\psi|_{\eta=\eta_i} = 0\,, \tag{6.15b}$$

$$(\partial_\eta \psi - \lambda\psi)|_{\eta=\eta_i} = 0\,. \tag{6.15c}$$

They apply to (a) infinite systems with stable boundary regions and to bounded systems with (b) rigid walls or (c) free surfaces, respectively. In addition, internal interfaces with discontinuous density variations may be present. Multiplying eq. (6.14) by $\rho$ and integrating across the interface layer, one finds the continuity conditions,

$$[\psi] = 0\,, \quad [\rho(\partial_\eta \psi - \lambda\psi)] = 0\,, \tag{6.16}$$

with the same notation as in section 2.2.

To illustrate the relationship between the different sets of boundary conditions, we consider an arbitrary fluid layer $0 < \eta < h$ and a boundary medium with constant densities $\rho_1$ for $\eta < 0$ and $\rho_2$ for $\eta > h$. According to the infinite medium boundary conditions (a), the solution inside the boundary regions becomes,

$$\begin{aligned} &\psi = \psi(0)\exp(\eta), && \text{for } \eta < 0\,, \\ &\psi = \psi(h)\exp(h-\eta)\,, && \text{for } \eta > h\,. \end{aligned} \tag{6.17}$$

The rigid- and free-surface problems can now be recovered by the following limiting procedures:

*High-density limit*: We apply the continuity conditions (6.16) to the interfaces at $\eta = 0$ and $\eta = h$ and perform the limit $\rho_{1,2} \to \infty$. Using eq. (6.17) for the solutions inside the boundary medium, one is left with the constraints

$$(1-\lambda)\psi(0) = 0\,, \quad (1+\lambda)\psi(h) = 0 \tag{6.18}$$

on the boundary values of the solution inside the fluid layer. These constraints can be satisfied in three different ways by setting

$$\psi(0) = \psi(h) = 0\,, \tag{6.19a}$$

$$\psi(0) = 0 \quad \text{and} \quad \lambda = -1\,, \tag{6.19b}$$

$$\psi(h) = 0 \quad \text{and} \quad \lambda = 1\,, \tag{6.19c}$$

respectively. The first case recovers the rigid wall condition (6.15b). The other cases yield two further modes with eigenvalues $\lambda = \pm 1$. The vanishing of the solution at one boundary only can always be satisfied, by taking an appropriate linear combination of the two independent solutions of eq. (6.14). These additional modes correspond to the free-surfaces of the boundary medium at $\eta = 0$ and $\eta = h$ with respect to the low density fluid layer.

*Low-density limit*: Taking now the opposite limit $\rho_{1,2} \to 0$, the second continuity condition of eq. (6.16) reduces simply to the free-surface condition (6.15c). In contrast to the previous case, the low-density limit is equivalent to the free-surface problem. Here, one can also find free-surface modes with eigenvalues $\lambda = \pm 1$. The corresponding solutions are simply $\psi \sim \exp(\pm 1)$, satisfying both the differential equation (6.14) and the boundary conditions (6.15c). We remark that these free-surface modes exist for any density profile of the fluid layer. This confirms and extends the potential flow result of section 3.3 that free-surface growth rates are independent of the layer width. Apparently, growth reductions by inhomogeneity effects require partial stabilization of these modes.

We have seen that the free-surface eigenvalues $\lambda = \pm 1$ occur both, for high and low density boundaries. The remaining eigenvalues are in general different. However, there exists a particular class of density profiles, called inversion invariant profiles, for which the spectrum of all eigenvalues is exactly the same for high and low density boundaries. This is a consequence of the inversion symmetry of the eigenvalue problem, which will be discussed in the following.

### 6.2.3. *Inversion symmetry*

The inversion theorem was first proposed by Mikaelian [68] for multi-layered fluid systems. A generalization of this symmetry to continuous density profiles was suggested by Inogamov [123] and could be verified for a particular class of power-law density profiles. In the following, we will outline a general proof of the inversion theorem for arbitrary density variation [128].

In analogy to the symmetry transformation (3.40), one expects invariance of the eigenvalues under an exchange between $\rho(\eta)$ and its inversion $R(\eta) = 1/\rho(-\eta)$. However, this symmetry is not explicitly manifest in the standard form of the differential operator. Substituting in eq. (6.14) $\rho(\eta)$ by $R(\eta)$ and transforming to the new variables $x = -\eta$ and $W(x) = w(\eta)$, one finds

$$\partial_x^2 W - \frac{\partial_x \rho(x)}{\rho(x)}\, \partial_x W - \left(1 + \lambda \frac{\partial_x \rho(x)}{\rho(x)}\right) W = 0 . \tag{6.20}$$

Since the logarithmic derivative of the density remains invariant under inversion, the first derivative term of the differential operator has changed its sign.

The eigenvalue operator allows a more symmetric representation as a first-order system in the variables $y_{1,2} = w \pm \partial_\eta w$. The first subscript refers to the upper and the second one to the lower sign. Setting $B = \partial_\eta \rho / 2\rho$ and $\lambda_{1,2} = \lambda \mp 1$, one finds

$$\partial_\eta y_{1,2} = \pm y_{1,2} \pm B(\lambda_1 y_1 + \lambda_2 y_2) . \tag{6.21}$$

The idea is now to compensate the sign change of the first derivative by an exchange of the dependent variables under inversion. For this purpose, a further transformation $z_{1,2} = \sqrt{\rho}\, y_{1,2}$ is convenient, because it leads to the same diagonal element $A = 1 + \lambda B$ in both equations. Substituting in eq. (6.21) yields

$$\partial_\eta z_{1,2} = \pm A z_{1,2} \pm \lambda_{2,1} B z_{2,1} . \tag{6.22}$$

One can easily verify that this system remains form-invariant under the following inversion operation,

$$\rho(\eta)\to R(\eta)\,,\quad x=-\eta\,,\quad u_1=\lambda_2 z_2\,,\quad u_2=\lambda_1 z_1\,. \tag{6.23}$$

Specifically, substituting $\rho(\eta)$ by $R(\eta)$ in eq. (6.22) and performing the given variable transformations, one obtains the original equations for $u_{1,2}(x)$. Consequently, for any solution of the original problem there is a corresponding solution of the inverted problem with the same eigenvalue.

If the original eigenfunction satisfies the infinite medium boundary conditions (6.15a), they will also be satisfied by the transformed eigenfunction. However, some care is required for rigid and free boundaries. Free boundaries can be replaced by a low-density medium, extending toward infinity. The same eigenvalue spectrum will be found for the inverted profile with high-density boundary regions. If these boundary regions are replaced by rigid walls, the free-surface eigenvalues (6.19b) and (6.19c) are omitted. As an immediate conclusion, there follows the eigenvalue theorem for inversion invariant profiles: If the density profile is inversion invariant, the eigenvalue spectrum for free boundaries consists of the free-surface eigenvalues $\lambda=\pm 1$ combined with the eigenvalue spectrum for rigid boundaries.

In addition to the invariance of the eigenvalues, the present treatment shows also how the eigenfunctions are transformed. We will denote the solutions for $\rho(\eta)$ by small and the corresponding solutions for $R(\eta)$ by capital letters. Taking the inverse of the two variable substitutions, we obtain for the solution of the inverted problem,

$$\begin{pmatrix} W(x) \\ \partial_x W(x)\end{pmatrix}=\frac{1}{2\sqrt{R(\eta)}}\begin{pmatrix}1 & 1\\ 1 & -1\end{pmatrix}\begin{pmatrix}Z_1(x)\\ Z_2(x)\end{pmatrix}=\frac{\sqrt{\rho(x)}}{2\lambda_1\lambda_2}\begin{pmatrix}\lambda_1 & \lambda_2\\ -\lambda_1 & \lambda_2\end{pmatrix}\begin{pmatrix}U_1(x)\\ U_2(x)\end{pmatrix}. \tag{6.24}$$

Up to an arbitrary constant factor, the solution $U_{1,2}(x)$ can be identified with the solution

$$\begin{pmatrix}z_1(x)\\ z_2(x)\end{pmatrix}=\sqrt{\rho(x)}\begin{pmatrix}1 & 1\\ 1 & -1\end{pmatrix}\begin{pmatrix}w(x)\\ \partial_x w(x)\end{pmatrix} \tag{6.25}$$

of the original problem, that satisfies the same equations. Here the variable $x$ is merely a renaming of the variable $\eta$ used before. Inserting eq. (6.25) into eq. (6.24) there follows

$$\begin{pmatrix} W(x) \\ \partial_x W(x)\end{pmatrix}=\text{const.}\,\frac{\rho(x)}{\lambda_1\lambda_2}\begin{pmatrix}\lambda & -1\\ 1 & -\lambda\end{pmatrix}\begin{pmatrix}w(x)\\ \partial_x w(x)\end{pmatrix}. \tag{6.26}$$

This transformation law includes the first derivatives of the eigenfunctions. Inversion invariance appears therefore naturally in phase space rather than configuration space.

### *6.3. Exponential density variations*

As an explicit example, we now discuss the stability of fluid layers with exponential density variations. This profile model permits explicit solutions for the evolution of internal modes and demonstrates their connection with the surface modes of potential flow theory. Particular attention is devoted to the discussion of density transition layers in an infinitely extended fluid and to its basic limits of short- and long-wavelength perturbations.

The model of exponential density variations has been considered in the past by various authors. The transcendental equation for the growth rates of exponential transition profiles is already part of Rayleigh's original work [3]. Explicit evaluations of the model have been discussed by Mikaelian [68, 124] by Jacobs [125], and by the present author [126]. Discussions of the initial value problem for diffuse layers have been given by Ott and Russel [127]. Other analytic solutions for finite density gradients have been obtained, based on moment equations, by Mikaelian [129] and, based on variational principles, by Munro [130].

*6.3.1. Model equations*

Inside the layer $0 < \eta < h$, the density profile is assumed of the form, $\rho = \rho_1 \exp(\beta\eta)$, with a constant gradient $\beta > 0$. The general solution of eq. (6.14) becomes,

$$\psi = A \exp(q_1 \eta) + B \exp(q_2 \eta) , \tag{6.27}$$

with

$$q_{1,2} = -\beta/2 \pm z , \quad z = u + \mathrm{i}v = \sqrt{1 + \lambda\beta + \beta^2/4} .$$

Since the eigenvalues $\lambda$ are real, the branch of the square root is chosen on the positive real axis ($u > 0, v = 0$) or on the positive imaginary axis ($u = 0, v > 0$), depending on the sign of the discriminant. The point $z = 0$ is excluded, because the solution (6.27) would be incomplete in this case. The boundary conditions restrict the possible $z$ values. The corresponding growth rates $n = \mathrm{Im}(\omega)$ can then be obtained as

$$\frac{n^2}{ak} = -\frac{1}{\lambda} = \frac{\beta}{1 + \beta^2/4 - z^2} . \tag{6.28}$$

In the following, we will discuss in succession the normal mode solutions corresponding to the boundary conditions (6.15).

*6.3.2. Rigid boundaries*

Using eqs. (6.15b) and (6.27), one finds the linear system

$$A + B = 0 , \quad \exp(q_1 h) A + \exp(q_2 h) B = 0 . \tag{6.29}$$

The allowable solutions are given by $B = -A$ and $z = \mathrm{i}v_m$, where $v_m = m\pi/h$ and $m = 1, 2, 3, \ldots$ denotes a positive integer. The corresponding growth rates and eigenfunctions follow to be

$$\frac{n^2}{ak} = \frac{\beta}{1 + \beta^2/4 + v_m^2} , \quad \psi = \exp(-\beta\eta/2) \sin(v_m \eta) . \tag{6.30}$$

To discuss the physical dependences of this result, we introduce the gradient scale length $L$, the layer thickness $d$, a density increment $C$, and a parameter $p$ by the relations

$$\beta = 1/kL , \quad h = kd , \quad C = \tfrac{1}{2}\beta h = \tfrac{1}{2} \ln[\rho(h)/\rho(0)] , \quad p = \tfrac{1}{2}\sqrt{1 + (\pi m/C)^2} . \tag{6.31}$$

The growth rate, given by eq. (6.30), can then be expressed in the form

$$\frac{n^2}{ak} = \frac{kL}{(kL)^2 + p^2}, \quad \frac{n}{\sqrt{a/L}} = \frac{kL}{\sqrt{(kL)^2 + p^2}}. \tag{6.32}$$

We remark that $n$ increases linearly for $kL \to 0$ and approaches the constant value $\sqrt{a/L}$ for $kL \to \infty$. In both limits, it stays below the free-surface value. This reduced growth is due to the effect of finite gradients for short-wavelength modes and due to the stabilizing influence of rigid boundaries for long-wavelength modes. In the intermediate range of $k$ values the ratio $f = n^2/ak$ reaches a maximum given by

$$k_m L = p, \quad k_m d = 2pC, \quad f_m = 1/2p. \tag{6.33}$$

We note that $f_m$ cannot be larger than 1 and frequently will be smaller. For instance, choosing the lowest mode number $m = 1$ and a fairly large density ratio $\exp(\beta h) = 50$, the above parameters are given by $k_m L = 0.95$, $k_m d = 3.7$, $f_m = 0.53$. In the presence of surface modes, these internal modes will be negligible for most applications.

*6.3.3. Free boundaries*

Using eq. (6.15c) together with eq. (6.27), there follows

$$\begin{aligned} &(q_1 - \lambda)A + (q_2 - \lambda)B = 0, \\ &(q_1 - \lambda)\exp(q_1 h)A + (q_2 - \lambda)\exp(q_2 h)B = 0. \end{aligned} \tag{6.34}$$

The possible solutions of eq. (6.34) are restricted by

$$(q_1 - \lambda)(q_2 - \lambda)[\exp(q_1 h) - \exp(q_2 h)] = 0. \tag{6.35}$$

From the vanishing of the first two factors, the free-surface modes

$$\lambda = \pm 1, \quad \psi = \exp(\pm\eta), \tag{6.36}$$

are obtained. The vanishing of the third factor leads again to the eigenvalues (6.30) of the rigid-boundary case. However, the eigenfunctions are now shifted in phase,

$$\psi_m = \exp(-\beta\eta/2)[\beta v_m \cos(v_m \eta) - (1 + v_m^2 - \beta^2/4)\sin(v_m \eta)]. \tag{6.37}$$

We remark that the exponential profile is inversion invariant, satisfying $\rho(\eta) = 1/\rho(-\eta)$. It provides therefore an example for the rigid free eigenvalue theorem, discussed at the end of section 6.2.

*6.3.4. Transition layers*

We now assume homogeneous boundary regions with densities $\rho_1$ for $\eta < 0$ and $\rho_2 = \rho_1 \exp(\beta h)$ for $\eta > h$. In contrast to the previous cases, this model can demonstrate the transition from the surface modes in the long-wavelength limit to the internal modes in the short-wavelength limit.

Using eqs. (6.17) and (6.27), the continuity conditions (6.16) at the interfaces $\eta = 0$ and $\eta = h$ yield

$$(1 - q_1)A + (1 - q_2)B = 0\,, \quad (1 + q_1)\exp(q_1 h)A + (1 + q_2)\exp(q_2 h)B = 0\,. \tag{6.38}$$

Setting the determinant of the coefficient matrix equal to zero, the variable $z$ is found restricted by

$$\tanh(zh) = \frac{2z}{\beta^2/4 - (1 + z^2)}\,. \tag{6.39}$$

For each solution of eq. (6.39), the eigenfunctions can be expressed in the form

$$\psi = \exp(-\beta\eta/2)[z\cosh(z\eta) + (1 + \beta/2)\sinh(z\eta)]\,. \tag{6.40}$$

To discuss the possible growth rates, we will first analyse the short-and long-wavelength limits analytically and then present a numerical evaluation over the whole parameter space.

For short wavelengths, one has the scaling $\beta \to 0$, $z = \mathrm{O}(\beta)$, $h = \mathrm{O}(\beta^{-1})$. In this limit, eq. (6.39) reduces to the form $\tan(vh) = 0$. We therefore recover the growth rates of the internal modes (6.30). Since the wavelengths are assumed short, the result becomes independent of the boundary conditions used.

*6.3.5. Step-profile approximation*

The long-wavelength limit requires a more careful treatment. We define the small expansion parameter $\varepsilon = 2/\beta$ and set $x = \varepsilon z$, $C = \beta h/2 = h/\varepsilon$. Using this scaling, eqs. (6.28) and (6.39) become

$$\frac{n^2}{ak} = \frac{2\varepsilon}{1 - x^2 + \varepsilon^2}\,, \tag{6.41a}$$

$$2\varepsilon x = (1 - x^2 - \varepsilon^2)\tanh(Cx)\,. \tag{6.41b}$$

Expanding the solution $x$ of eqs. (6.41) in powers of $\varepsilon$ one obtains

$$x = 1 - a\varepsilon\,, \quad 1 - x^2 = 2a\varepsilon + b\varepsilon^2\,, \quad \tanh(Cx) = \alpha - \delta C a\varepsilon\,, \tag{6.42}$$

with

$$\alpha = \tanh(C) = \frac{\exp(\beta h) - 1}{\exp(\beta h) + 1} = \frac{\rho_2 - \rho_1}{\rho_2 + \rho_1}\,,$$

$$\delta = \partial_C \tanh(C) = \cosh^{-2}(C) = 1 - \alpha^2\,.$$

Comparing equal powers of $\varepsilon$ in eq. (6.41b) yields

$$\alpha a = 1\,, \quad \alpha b = \alpha - 2/\alpha + 2\delta C/\alpha^2\,. \tag{6.43}$$

Inserting these expansion coefficients in eq. (6.41a), there follows the growth rate expression,

$$\frac{n^2}{ak} = \alpha - \frac{2}{\beta}\left(\frac{1}{\alpha} - \alpha\right)(C - \alpha)\,. \tag{6.44}$$

It determines the maximum growth rate of the diffuse boundary model in the long-wavelength limit. The leading order represents the well-known step-profile result (3.3) for surface modes. In addition, we have obtained a finite gradient correction to this formula. These corrections become small both, for small ($\alpha \to 0$) and large ($\alpha \to 1$) density ratios. For a moderate density ratio of $\rho_2/\rho_1 = 20$, we have $\alpha = 0.90$, $C = 1.5$. Choosing for instance $\beta = 3$, the approximate expression (6.44) yields $n^2/ak = 0.826$. This value is in close agreement with the exact numerical solution, $n^2/ak = 0.814$, for the same parameters.

The real solutions of the variable $z$ determine the largest values of the growth rate (6.28). Such a solution exists when $(\beta^2/4 - 1)h > 2$. This condition is obtained by considering the limit $z \to 0$ in eq. (6.39). If this condition is not satisfied, for instance when $\beta < 2$, the growth rates will be significantly reduced in comparison with the step-profile values.

We have calculated numerically the maximum growth rates for different values of $\beta$ and $\beta h = \ln(\rho_2/$

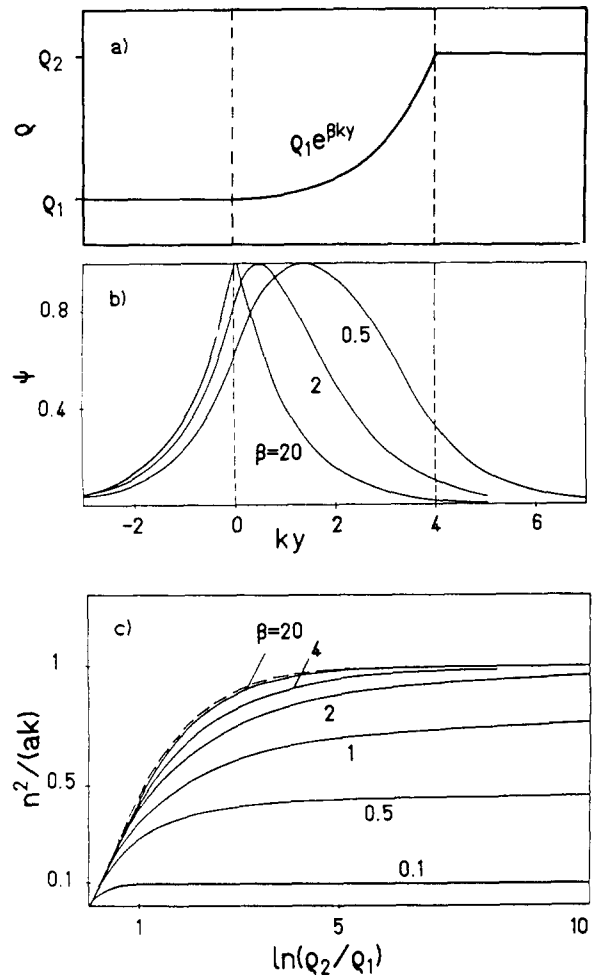


Fig. 27. RT instability of superposed fluids separated by a transition layer with an exponential density variation. (a) Density profile, (b) typical eigenfunctions of the most unstable mode for different gradients $\beta$, (c) maximum instability growth rate $n$ for different density ratios $\rho_2/\rho_1$ and density gradients $\beta$. Comparison is made with the step-profile growth rate (dashed curve) which is approached in the long-wavelength approximation. (From ref. [70].)

$\rho_1$). The results are represented in fig. 27, showing (a) the density profile, (b) typical eigenfunctions, and (c) maximum instability growth rates. The growth rates are found limited above by the step-profile result (dashed line). For $\beta < 2$, the growth rates remain below this limit, demonstrating the growth reduction effects by finite gradients. The eigenfunctions have a maximum whose position varies with the density gradient. The eigenfunctions are peaked near the lower boundary for large $\beta$, but they become shifted toward the middle of the layer for small $\beta$. This behavior explains the strong dependence of the surface modes on the choice of boundary conditions in comparison with the internal modes, being always present.

### 6.4. *Single-mode model*

We finally give a simple illustration of mixing motions in the RT instability. We consider the passive motion of fluid particles in the field of a single internal mode. Although the model gives no consistent dynamical description of nonlinear evolution, it is based on exact particle trajectories and conservation of both the mass and the total energy of the system.

The passive motion of particles in a single internal RT mode can be described by the system,

$$\psi = \psi_0(t)\cos(px)\sin(qy)\,. \quad v_x = \partial_y\psi\,, \quad v_y = -\partial_x\psi\,. \tag{6.45}$$

The stream function follows from eq. (6.30) in the limit of weak density gradients. The time dependence of the amplitude $\psi_0$ is arbitrary. To calculate the particle motions in this flow field, it is convenient to transform to the variables,

$$\xi = px\,, \quad \eta = qy + \pi/2\,, \quad \tau = pq\int_0^t \psi_0\,\mathrm{d}t\,. \tag{6.46}$$

Denoting the derivative with respect to $\tau$ by a dot, the transformed equations become,

$$\psi = -\psi_0\cos(\xi)\cos(\eta)\,, \quad \dot{\xi} = \cos(\xi)\sin(\eta)\,, \quad \dot{\eta} = -\sin(\xi)\cos(\eta)\,. \tag{6.47}$$

The streamline $\psi(\xi,\eta) = \psi(\xi_0,\eta_0)$ through some reference point $\xi_0, \eta_0$ is given by the equation,

$$\cos(\xi)\cos(\eta) = \cos(\xi_0)\cos(\eta_0) = C\,. \tag{6.48}$$

Some streamlines, obtained for different values of $C$, are represented in fig. 28. They are periodic and form closed orbits inside the vorticity cell: $-\pi/2 < \xi < \pi/2$, $-\pi/2 < \eta < \pi/2$.

The motion of fluid particles along these streamlines can now be described by the equations

$$\dot{\xi} = \pm\mathrm{sgn}(\eta)\sqrt{\cos^2\xi - C^2}\,, \quad \dot{\eta} = \mp\mathrm{sgn}(\xi)\sqrt{\cos^2\eta - C^2}\,, \tag{6.49}$$

where the upper sign corresponds to clockwise and the lower to counterclockwise rotation. According to eq. (6.47), these signs alternate for subsequent cells both in the $\xi$ and in the $\eta$ direction. Since $\xi$ is related to $\eta$ by the streamline equation (6.48), it is sufficient to solve the equation for $\eta$. The solution can be expressed in the form

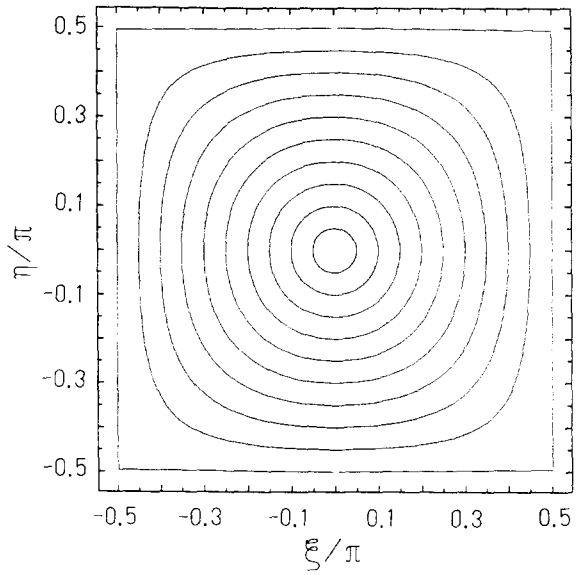


Fig. 28. Streamlines of the stream function (6.47) expressed in terms of the coordinates $\xi = px$, $\eta = qy + \pi/2$ where $p$ and $q$ represent horizontal and vertical wavenumbers, respectively. The flow pattern corresponds to the eigenmode (6.30) for an exponential density profile with a sufficiently weak gradient. (From ref. [70].)

$$\sin\eta = \sqrt{\mu}\,\mathrm{sn}(\tau + \tau_0, \mu)\,, \quad \sin\eta_0 = \sqrt{\mu}\,\mathrm{sn}(\tau_0, \mu)\,, \tag{6.50}$$

where $\mu = 1 - C^2$ and sn denotes the elliptic Jacobi function [93].

To visualize these mixing motions, we have calculated particle trajectories for a number of particles with different initial conditions. The results can be recognized in fig. 29. The lines correspond to the position of particles at time $\tau$, having the same initial coordinate $\eta_0$. Since the density is constant along particle trajectories, these lines can also be viewed as iso-density contour lines. Initially, the lines deform sinusoidally, as predicted by the linear stability theory. At later times, however, strong intermixing occurs. The contours of two neighboring cells evolve into a mushroom-like flow pattern. Such vortex motions are characteristic for mixing processes and have been observed both in experiments and in fluid simulations.

In the present model, mixing is basically a result of the different periods of revolution for particles on different streamlines. In the variable $\tau$, the period of particles on the streamline $\mu$ is given by

$$T = 4\int_0^{\pi/2} \frac{\mathrm{d}u}{\sqrt{1 - \mu\sin^2 u}}\,. \tag{6.51}$$

It approaches $2\pi$ for the innermost ($\mu = 0$) and $\infty$ for the outermost streamline ($\mu = 1$) of the cell.

The time dependence of the flow amplitude has not yet been specified. In principle, it can be chosen in such a way that global energy conservation results. The increase of kinetic energy is then limited by the available potential energy of the fluid layer. We illustrate this procedure for the initial small amplitude regime. Setting $\psi_0 = \exp(\int n\,\mathrm{d}t)$, the variations of the kinetic and potential energies are given by

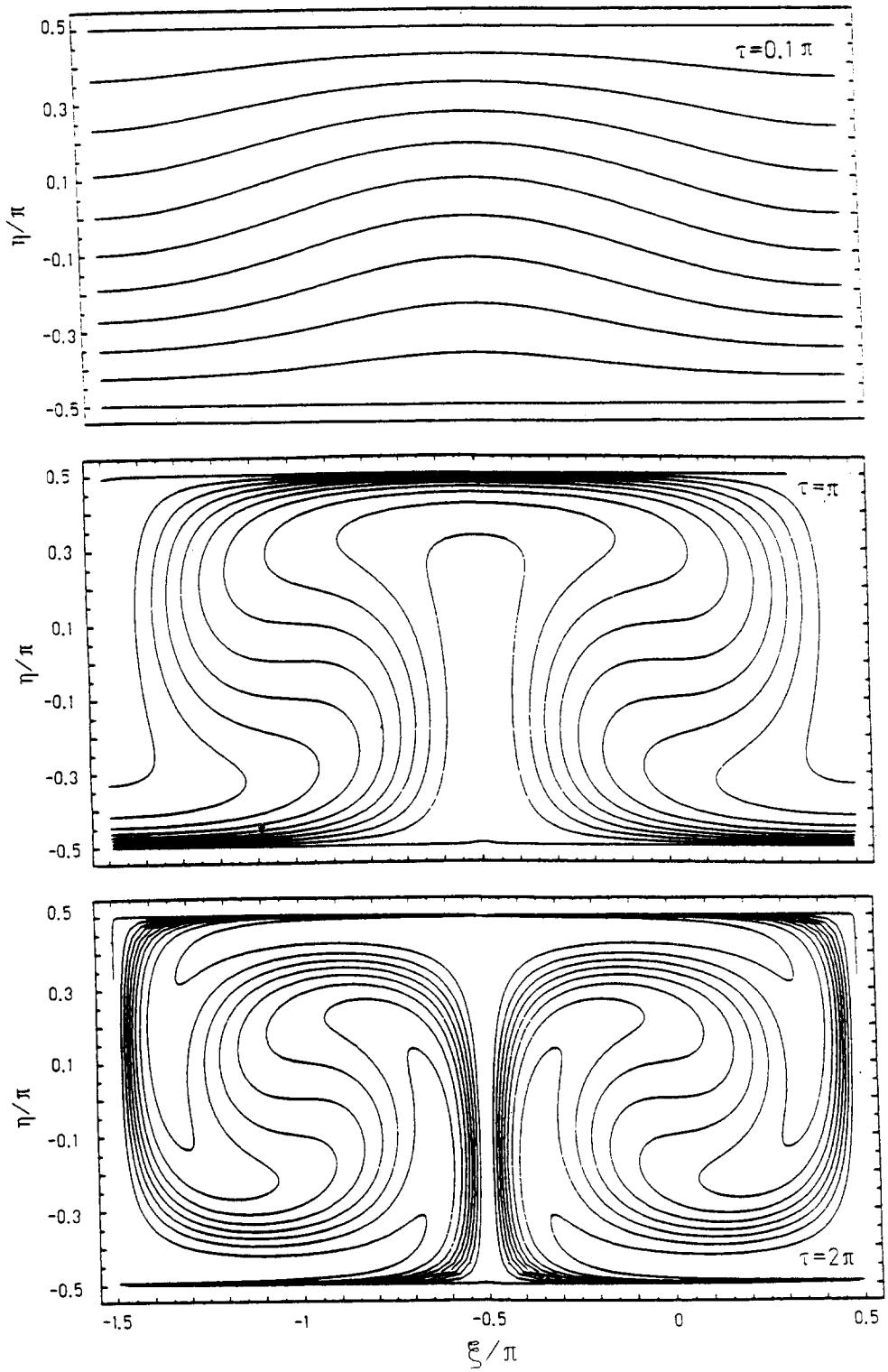


Fig. 29. Evolution of iso-density contour lines for passive motion in the flow field of fig. 28. Initially, the contour lines have been assumed horizontal and a complete spatial period of the flow, consisting of two neighboring vorticity cells with opposed circulations, is presented. The time $\tau = 2\pi$ corresponds to the period of revolution of a fluid particle on the innermost streamline of the cell.

$$\frac{\mathrm{d}T}{\mathrm{d}t} = \int \mathrm{d}x \int \mathrm{d}y \, (\tfrac{1}{2} v^2 \partial_t \rho + n \rho v^2) \,,$$
$$\frac{\mathrm{d}U}{\mathrm{d}t} = \int \mathrm{d}x \int \mathrm{d}y \, ay \, \partial_t \rho = \int \mathrm{d}x \int \mathrm{d}y \, ay [-\partial_y (\rho v_y)] = \int \mathrm{d}x \int \mathrm{d}y \, a \rho v_y \,. \tag{6.52}$$

In linear theory the following relations hold,

$$\int \mathrm{d}x \, \rho v_y = -\frac{1}{n} \partial_y \rho_0 \int \mathrm{d}x \, v_y^2 \,, \quad \int \mathrm{d}x \, v^2 \, \partial_t \rho = \mathrm{O}(v^3) \,. \tag{6.53}$$

The requirement of energy conservation,

$$\frac{\mathrm{d}}{\mathrm{d}t} (T + U) = n \rho_0 \int \mathrm{d}x \int \mathrm{d}y \, (v_x^2 + v_y^2) - \frac{a}{n} \partial_y \rho_0 \int \mathrm{d}x \int \mathrm{d}y \, v_y^2 = 0 \,, \tag{6.54}$$

yields, together with eq. (6.45), the linear growth rate expression

$$n^2 = a \frac{\partial_y \rho_0}{\rho_0} \frac{p^2}{p^2 + q^2} \,. \tag{6.55}$$

It agrees with the weak gradient limit of the result (6.30) of the normal mode analysis.

## 7. Stability of viscous fluids

Viscosity presents another source for vorticity generation in incompressible fluids. In contrast to the rotational modes in inviscid fluids, viscosity acts already in homogeneous fluids and it is responsible for the dissipation of kinetic energy on small spatial scales. This property is particularly important in boundary layer flows, in the evolution of homogeneous fluid turbulence, and in the present context, as a damping mechanism for fluid instabilities.

In the following, the surface instabilities between two uniform fluid layers are examined in the presence of shear flow, buoyancy and viscosity. A general characteristic equation can be obtained in the long-wavelength approximation that combines KH-like instabilities of viscous shear flows on the one side with RT instabilities of accelerated viscous fluids on the other side. These limiting cases are analysed in more detail and explicit growth rate expressions for these instabilities are discussed.

### *7.1. Viscous flow model*

The growth rates (3.3) for the basic surface instabilities in inviscid fluids are increasing indefinitely with the wavenumber. This lack of a finite maximum growth rate in the inviscid fluid description can be overcome by the inclusion of viscosity. As far as RT instability is concerned, the first treatment of viscosity effects has been given by Harrison [46]. Although this early work has been addressed to stable gravity waves, the general eigenvalue relation for the surface modes in superposed viscous fluids has been derived and the limit of small viscosities has been evaluated perturbatively. Later work by Bellman and Pennington [48] and by Chandrasekhar [57] has led to a rather complete understanding of

RT instabilities in incompressible viscous fluids, including effects of surface tension and of variable fluid densities. For superposed fluid layers, explicit growth rate curves have been obtained that could demonstrate the existence of a maximum growth rate. This case was further studied by Menikoff et al. [131] over the whole parameter range of densities and viscosities. These authors arrived at a particularly simple representation of the dispersion relation and thereby they have been able to identify the Atwood number and a density-weighted average viscosity as the main dependences of the instability growth rate. In addition to the normal mode analysis, initial value problems for RT instabilities in viscous fluids have also been studied occasionally [132, 133].

Viscosity in the KH instability has to be regarded under a broader perspective. The simple model of a contact discontinuity between adjacent fluid layers no longer applies and, instead, parallel shear flows with continuous velocity profiles have to be considered. There is extensive mathematical literature on this topic, being largely based on the famous Orr–Sommerfeld equation. An excellent account to the theory of both, inviscid and viscous flow instabilities can be found in the textbook by Drazin and Read [59]. It also includes many references to the pertinent literature.

After a brief introduction to the viscous flow equations, the present discussion is mainly concerned with surface instabilities in the long-wavelength approximation. Under this assumption, the interface between two uniform viscous fluid layers can be idealized as a discontinuity much in the same way as for inviscid fluid layers. This approach appears therefore particularly instructive for a comparison with inviscid flow theory presented in section 3.1. As a further application of this model, the possibility of convective amplification of surface instabilities in moving fluid layers is discussed.

*7.1.1. Viscous shear flows*

Viscous stresses can often be related linearly to the spatial derivatives of the velocity field. Within this framework, the stress tensor of an incompressible viscous fluid can be assumed of the form [134]

$$\sigma_{ij} = -p\delta_{ij} + \eta(\partial_{x_j} v_i + \partial_{x_i} v_j)\,, \tag{7.1a}$$

where $\delta_{ij}$ denotes the unit tensor and $\eta$ the coefficient of viscosity. The corresponding fluid equations for incompressible motions of a nonuniform viscous fluid are given by,

$$\nabla\cdot\boldsymbol{v} = 0\,, \quad \mathrm{d}\rho/\mathrm{d}t = 0\,, \quad \mathrm{d}\boldsymbol{v}/\mathrm{d}t = \rho^{-1}\,\nabla\cdot\boldsymbol{\sigma} - \nabla U\,. \tag{7.1b}$$

They replace the system (6.1) in the presence of viscosity. In the special case of a homogeneous fluid layer with the kinematic viscosity $\nu = \eta/\rho$, the equation of motion simplifies to the well-known Navier–Stokes equation

$$\mathrm{d}\boldsymbol{v}/\mathrm{d}t = -\nabla(p/\rho + U) + \nu\,\Delta\boldsymbol{v}\,. \tag{7.1c}$$

We only remark its basic role for the theory of homogeneous fluid turbulence [135].

As an immediate consequence of viscous stresses, tangential flow discontinuities do no longer exist. Instead, one has to deal with viscous boundary layers where the flow velocity changes suddenly but in a continuous manner. Normally accelerated viscous shear layers can be represented in the form,

$$\begin{aligned} &\nabla U = (0, a, 0)\,, \quad \boldsymbol{v} = (v_0(y), 0, 0)\,, \\ &\rho = \rho_0(y)\,, \quad p = p_0(y) + cx\,. \end{aligned} \tag{7.2a}$$

While the density profile $\rho_0(y)$ is arbitrary, the velocity and pressure profiles are given by

$$v_0(y) = -\int \mathrm{d}y \, \frac{cy + d}{\eta} \,, \quad p_0(y) = -a \int \mathrm{d}y \, \rho_0 \,. \tag{7.2b}$$

These are strictly parallel steady-state flows of the system (7.1) with arbitrary integration constants $c$ and $d$. In the absence of flow ($v_0 = 0$), one recovers the hydrostatic equilibrium state of the inviscid theory as presented in section 6.1. In the presence of flow ($v_0 \neq 0$), viscosity imposes a constraint on the velocity profile according to eq. (7.2b). In the past, particular attention has been devoted to KH-type instabilities of unaccelerated shear flows. These are known as plane Couette flow ($c = 0, a = 0$) in the absence of an applied pressure and otherwise as plane Poiseuille flow ($c \neq 0, a = 0$).

*7.1.2. Perturbations*

If each steady flow variable $X_0$ is subject to a two-dimensional perturbation $\delta X = \delta X(y) \exp(-\mathrm{i}\omega t + \mathrm{i}kx)$ in the $x$, $y$ plane, eq. (7.1) yields the linear perturbation system

$$\delta v_y' + \mathrm{i}k \, \delta v_x = 0 \,, \tag{7.3a}$$

$$-\mathrm{i}\tilde{\omega} \, \delta\rho + \rho_0' \, \delta v_y = 0 \,, \tag{7.3b}$$

$$\begin{aligned} &\rho_0(-\mathrm{i}\tilde{\omega} \, \delta v_x + v_0' \, \delta v_y) = \mathrm{i}k(-\delta p + 2\mathrm{i}k\eta \, \delta v_x) + \{\eta(\delta v_x' + \mathrm{i}k \, \delta v_y)\}' \,, \\ &\rho_0(-\mathrm{i}\tilde{\omega}) \, \delta v_y = -a \, \delta\rho - \delta p' + \mathrm{i}k\eta(\mathrm{i}k \, \delta v_y + \delta v_x') + 2(\eta \, \delta v_y')' \,, \end{aligned} \tag{7.3c}$$

where $\tilde{\omega} = \omega - kv_0$ and the prime denotes differentiation with respect to the $y$ coordinate.

In deriving eq. (7.3), it was assumed that viscosity perturbations are negligibly small. If $\Delta$ denotes the shear layer width and $q$ a characteristic perturbation wavenumber, this approximation requires,

$$\delta\eta/\eta \ll \delta v'/v_0' \sim q\Delta \, \delta v/v_0 \,. \tag{7.4}$$

It applies to so-called Boussinesq fluids, having negligible variations in their thermodynamic properties, and also to pure hydrostatic equilibria with $v_0 = 0$. In general, however, the condition (7.4) appears rather restrictive. If it is not satisfied strong viscous heating $\sim\delta\eta(v_0')^2$ and corresponding mass diffusion will ensue. These effects could probably only be reconciled with each other in a more advanced compressible theory and they are therefore neglected for the present purposes.

The perturbations of homogeneous steady-state flows with constant densities and velocities can be obtained most easily from the vorticity equation,

$$[-\mathrm{i}\tilde{\omega} + \nu(k^2 - \partial_y^2)]\nabla \times \delta\boldsymbol{v} = 0 \,. \tag{7.5}$$

It follows immediately from the curl of the linearized Navier–Stokes equation (7.1c) by noting that $\delta\rho = 0$ for $\tilde{\omega} \neq 0$ according to eq. (7.3b). For unstable modes with complex frequencies, the condition $\tilde{\omega} \neq 0$ can be assumed without restriction. Looking at eq. (7.5), it can be seen that vorticity perturbations are generated by viscosity. In addition, irrotational potential flow perturbations can exist as in the absence of viscosity. The corresponding wavenumbers along the $y$ direction are given by

$$\pm\sqrt{k^2 - \mathrm{i}\tilde{\omega}/\nu}\,, \quad \text{for } \nabla\times\delta\boldsymbol{v}\neq 0\,; \quad \pm k\,, \quad \text{for } \nabla\times\delta\boldsymbol{v}=0\,. \tag{7.6}$$

Now, consider two superposed homogeneous fluid layers 1 and 2 in the half-spaces $y<0$ and $y>\Delta$, respectively, separated by an inhomogeneous shear layer of width $\Delta$. In the upper and lower half-spaces, the perturbations that converge at infinity ($|y|\to\infty$) can be written in the form

$$\delta v_x = A\,\mathrm{e}^{-ky} + B\,\mathrm{e}^{-q_2 y}\,, \quad \delta v_y = \mathrm{i}A\,\mathrm{e}^{-ky} + \mathrm{i}(k/q_2)B\,\mathrm{e}^{-q_2 y}\,,$$
$$\delta p/\rho_2 = (\tilde{\omega}_2/k)A\,\mathrm{e}^{-ky} \quad (y>\Delta)\,; \tag{7.7a}$$

$$\delta v_x = C\,\mathrm{e}^{ky} + D\,\mathrm{e}^{q_1 y}\,, \quad \delta v_y = -\mathrm{i}C\,\mathrm{e}^{+ky} - \mathrm{i}(k/q_1)D\,\mathrm{e}^{q_1 y}\,,$$
$$\delta p/\rho_1 = (\tilde{\omega}_1/k)C\,\mathrm{e}^{ky} \quad (y<0)\,, \tag{7.7b}$$

where the subscripts refer to the flow regions. In eqs. (7.7) the wavenumber of the vorticity perturbation is defined to be $q=(k^2-\mathrm{i}\tilde{\omega}/\nu)^{1/2}$ and the branch of the square root is chosen such that $\mathrm{Re}(q)>0$ to ensure convergence at infinity.

*7.1.3. Jump conditions*

In the inviscid instability theory, the unstable interface between different fluid layers can be simply idealized as a co-moving contact surface where the continuity conditions (2.7) are known to be satisfied. The jump conditions (3.1) are then found to hold for inviscid surface modes in the linear approximation. Unfortunately, a viscous boundary layer cannot be treated in an analogous way as a contact surface between two viscous fluids. The corresponding continuity conditions would be

$$[\boldsymbol{v}]=0\,, \quad [\boldsymbol{\sigma}\cdot\boldsymbol{n}]=0\,, \tag{7.8}$$

where the brackets denote jumps across the contact surface and $\boldsymbol{n}$ is the surface normal unit vector of the surface element. These conditions cannot be satisfied in general by the basic flow (7.2) if the jumps are evaluated between the boundaries $y=0$ and $y=\Delta$ of the shear layer. Similar arguments apply to the perturbations. Vortex motion will lead to nonuniformities in the shear layer width and viscous stresses will contribute to the momentum balance between both fluids. It should therefore be clearly recognized that the viscous boundary layer plays an active role in the evolution of perturbations in the neighboring fluids.

The matching relations between the outer solutions (7.7) have to be derived from the viscous flow equations. This can be accomplished most easily in the long-wavelength approximation where the layer width $\Delta$ is assumed much smaller than the width of the perturbed flow. In the limit of a vanishing layer thickness, $\Delta\to 0$, the steady flow gradients $\rho_0'$ and $v_0'$ diverge. These terms have to be balanced by the highest derivatives $\delta\rho, \delta p', \delta v_x''$, and $\delta v_y''$ of each flow variable in the perturbation system (7.3). The variation of the lower derivatives $\delta p, \delta v_x', \delta v_y'$ will remain bounded and that of the functions $\delta v_x, \delta v_y$ will even be continuous across the layer. Using these properties and integrating eq. (7.3) across an infinitely thin layer $0<y<\Delta$, the following jump conditions are obtained,

$$[\delta v_x]=0\,, \tag{7.9a}$$

$$[\delta v_y]=0\,, \tag{7.9b}$$

$$[\eta(\delta v_x' + \mathrm{i}k\,\delta v_y)] = J_1\,\delta v_y\,, \tag{7.9c}$$

$$[2\eta\,\delta v_y' - \delta p] = J_2\,\delta v_y\,, \tag{7.9d}$$

where

$$J_1 = \lim_{\Delta\to 0}\int_0^{\Delta} \mathrm{d}y\;\rho_0 v_0'\,, \quad J_2 = \lim_{\Delta\to 0} a\int_0^{\Delta} \mathrm{d}y\;\frac{\rho_0'}{\mathrm{i}\tilde{\omega}}\,.$$

The first two conditions require the continuity of the perturbed flow at the unperturbed interface. The displacement $\zeta = \delta v_y/(-\mathrm{i}\tilde{\omega})$ of the shear layer boundaries is therefore no longer continuous as in eq. (3.1). Instead one has the relationship $v_{01}\zeta_1 = v_{02}\zeta_2$. For symmetric shear layers with $v_{01} = -v_{02}$ it leads to opposite displacements of equal magnitudes, $\zeta_1 = -\zeta_2$.

The last two conditions include the source terms $J_{1,2}$ for surface instabilities. In particular, the viscous RT instability is obtained from a density discontinuity with $v_0 = 0$, $J_1 = 0$, and $J_2 = a[\rho]/\mathrm{i}\omega$. The viscous KH instability follows from a flow discontinuity with $\rho_0 = \text{const.}$, $J_1 = \rho_0[v_0]$, and $J_2 = 0$.

### *7.2. Viscous surface instabilities*

#### *7.2.1. Stability eigenvalue problem*

The normal mode frequencies and growth rates of the combined KH and RT instabilities in a viscous fluid can be obtained from the linear set of equations (7.7) and (7.9). In explicit form these equations become

$$\begin{aligned}
&A + B = C + D\,, \quad \mathrm{i}A + \mathrm{i}(k/q_2)B = -\mathrm{i}C - \mathrm{i}(k/q_1)D\,,\\
&\eta_2(-kA - q_2B) - \eta_1(kC + q_1D) - \{(\eta_2 - \eta_1)k + \mathrm{i}J_1\}\{A + (k/q_2)B\} = 0\,,\\
&2k(\eta_2 - \eta_1)(A + B) + J_2(A + (k/q_2)B) - (\mathrm{i}\tilde{\omega}_2\rho_2/k)A + (\mathrm{i}\tilde{\omega}_1\rho_1/k)C = 0\,.
\end{aligned} \tag{7.10}$$

Solving the first equation for $D$ and the second one for $B$, one can rewrite eq. (7.10) in the form

$$\begin{aligned}
&D = A + B - C\,, \quad B = d_1A + d_2C\,,\\
&(a_{1,2} + d_1b_{1,2})A + (c_{1,2} + d_2b_{1,2})C = 0\,,
\end{aligned} \tag{7.11}$$

where the coefficients are defined by the expressions

$$a_1 = -2k\eta_2 - (q_1 - k)\eta_1 - \mathrm{i}J_1\,, \quad a_2 = 2k(\eta_2 - \eta_1) - \mathrm{i}\tilde{\omega}_2\rho_2/k + J_2\,,$$

$$b_1 = -\eta_2q_2 - \eta_1q_1 - (k^2/q_2)(\eta_2 - \eta_1) - \mathrm{i}(k/q_2)J_1\,, \quad b_2 = 2(\eta_2 - \eta_1)k + (k/q_2)J_2\,,$$

$$c_1 = \eta_1(q_1 - k)\,, \quad c_2 = \mathrm{i}\tilde{\omega}_1\rho_1/k\,, \quad d_1 = -(q_2/k)(q_1 + k)/(q_1 + q_2)\,,$$

$$d_2 = -(q_2/k)(q_1 - k)/(q_1 + q_2)\,.$$

The last member in eq. (7.11) represents two separate equations, one for the first and one for the second subscript. The solubility condition for these equations assumes the form

$$(a_1 + b_1 d_1)c_2 - (a_2 + b_2 d_1)c_1 + (a_1 b_2 - a_2 b_1)d_2 = 0 . \tag{7.12}$$

It determines the possible complex eigenfrequencies $\omega = \omega(k)$ of normal mode perturbations. Since the general expression (7.12) is still rather complex, we will now restrict attention to velocity and density discontinuities.

*7.2.2. Viscous KH instability*

Consider first the KH instability of a shear layer in an incompressible fluid of constant density and viscosity. Setting $\rho_1 = \rho_2 = \rho$, $\eta_1 = \eta_2 = \eta$ and defining

$$\begin{aligned} &v_s = \tfrac{1}{2}(v_1 + v_2) , \quad u = \tfrac{1}{2}(v_2 - v_1) , \quad N = -\mathrm{i}(\omega - k v_s)/ku , \\ &K = \nu k/u = \eta k/\rho u , \quad p_{2,1} = q_{2,1}/k = \sqrt{1 + (N \pm \mathrm{i})/K} , \end{aligned} \tag{7.13}$$

the coefficients of eq. (7.11) become,

$$\begin{aligned} &a_1 = -k\eta(2 + p_1 - 1 + 2\mathrm{i}/K) , \quad a_2 = \rho u(N + \mathrm{i}) , \\ &b_1 = -k\eta(p_2 + p_1 + 2\mathrm{i}/p_2 K) , \quad b_2 = 0 , \\ &c_1 = k\eta(p_1 - 1) , \quad c_2 = \rho u(-N + \mathrm{i}) , \\ &d_1 = -p_2(p_1 + 1)/(p_1 + p_2) , \quad d_2 = -p_2(p_1 - 1)/(p_1 + p_2) . \end{aligned} \tag{7.14}$$

The dimensionless eigenvalue $N$ can now be obtained explicitly as a function of the dimensionless parameter $K$ in the following way. Inserting eqs. (7.14) into eq. (7.12) yields

$$p_2 - p_1 - \mathrm{i}/K + 2\mathrm{i}/K(p_1 + p_2) + N[\mathrm{i}p_1 p_2 - \mathrm{i} - 2p_1/K(p_1 + p_2) + 1/K] = 0 . \tag{7.15}$$

If this equation is multiplied by $p_1 + p_2$ and eq. (7.13) is used for $p_{1,2}^2$ one arrives at the simpler form

$$(1 + \mathrm{i}N)^2 p_2 + (1 - \mathrm{i}N)^2 p_1 = 4 . \tag{7.16}$$

To eliminate the square roots $p_{1,2}$ with the help of the defining equation (7.13), one may take the square on both sides of eq. (7.16). The resulting equation can be divided by the factor $1 + N^2$ to yield

$$p_1 p_2 (1 + N^2) = 7 - N^2 + (N/K)(3 - N^2) . \tag{7.17}$$

Squaring eq. (7.17) again leads to the polynomial

$$16(3 - N^2)K^2 + 8(5 - 3N^2)NK - (1 - 3N^2)^2 = 0 . \tag{7.18}$$

If eq. (7.18) is regarded as quadratic in $K$, one arrives at the two roots

$$K_1 = (\sqrt{3}\,N - 1)^2/4(\sqrt{3} - N)\,, \quad K_2 = -(\sqrt{3}\,N + 1)^2/4(\sqrt{3} + N)\,. \tag{7.19}$$

Finally, solving the equations $K = K_1$ and $K = K_2$ for the eigenvalue $N$, the four possible solutions of the polynomial (7.18) are found to be

$$N_{1,2} = 1/\sqrt{3} - \tfrac{2}{3}\{K \pm (K^2 + 2\sqrt{3}\,K)^{1/2}\}\,, \quad N_{3,4} = -1/\sqrt{3} - \tfrac{2}{3}\{K \pm (K^2 - 2\sqrt{3}\,K)^{1/2}\}\,. \tag{7.20}$$

One should notice that in the process of squaring equations additional roots have been introduced that will not satisfy the original equation (7.16). These solutions have to be discarded from eq. (7.20) and then only one unstable branch is found.

To choose the correct unstable branch, one can restrict attention to the case where $u > 0$ and therefore also $K > 0$. In accordance with eq. (7.13), a sign change $u \to -u$ is accompanied by a sign change $K \to -K$ and $N \to -N$ of both, $K$ and $N$. This inversion will only lead to an interchange between the two solutions in eq. (7.20). Assuming now $K > 0$, the unstable branch is given by the solution $N_1$. The branch $N_2$ has to be discarded, as will be shown below, and the remaining branches $N_{3,4}$ have no positive real parts that could lead to instability.

For real values of $N$, eq. (7.16) can be further simplified to the form

$$\mathrm{Re}\{(1 + \mathrm{i}N)^2(X + \mathrm{i}Y)\} = XZ = 2\,, \tag{7.21}$$

where $p_{2,1} = X \pm \mathrm{i}Y$ are complex conjugate expressions with

$$X = (1/\sqrt{2K})\{K + N + \sqrt{1 + (K + N)^2}\}^{1/2}\,, \quad Y/X = \{K + N + \sqrt{1 + (K + N)^2}\}^{-1}\,,$$
$$Z = 1 - N^2 - 2NY/X\,. \tag{7.22}$$

The real part $X$ of $p_{2,1}$ has been chosen positive in accordance with the constraint for evanescent solutions in eq. (7.7). Solutions of eq. (7.21) are distinguished by the requirement $Z > 0$. Along the two branches $N_{1,2}$, a sign change of $Z$ can only occur at the branch-point $K = 0$, $N = 1/\sqrt{3}$, where $X$ becomes infinite. Near this point, eqs. (7.19) and (7.22) yield the expansion

$$N = (1 + \varepsilon)/\sqrt{3}\,, \quad K = \mathrm{O}(\varepsilon^2)\,, \quad Y/X = (1 - \tfrac{1}{2}\varepsilon)/\sqrt{3}\,, \quad Z = -\varepsilon\,. \tag{7.23}$$

It follows that the condition $Z > 0$ is only satisfied for $\varepsilon < 0$, corresponding to the lower branch $N = N_1 < 1/\sqrt{3}$.

In summary, the KH instability of a viscous shear layer can be described in the long-wavelength approximation by a complex eigenfrequency $\omega = \omega_r + \mathrm{i}\omega_i$ whose real and imaginary parts are given by

$$\omega_r = k(v_1 + v_2)/2\,, \quad \omega_i = Nk|v_1 - v_2|/2\,. \tag{7.24}$$

The effects of viscosity are expressed by the factor

$$N = 1/\sqrt{3} - \tfrac{2}{3}\{K + (K^2 + 2\sqrt{3}\,K)^{1/2}\} \tag{7.25}$$

and its dependence on the dimensionless parameter $K = 2\nu k/|v_1 - v_2|$.

A peculiarity of this result can be recognized in the limit of vanishing viscosity where $K = 0$ and $N = 1/\sqrt{3}$. Remarkably, the same growth rate applies to thin inviscid shear layers with a linear velocity profile and free boundaries, which has been treated by Mjolsness [136]. For this free-surface mode, the uniform flow regions are not actively involved in the evolution of the intermediate shear layer. On the other hand, the factor $1/\sqrt{3}$ is absent if the usual KH instability [eq. (3.3)] of a contact discontinuity between counterstreaming inviscid fluids is considered.

The discrepancy with the conventional KH instability for inviscid fluids seems to be due to different parameter regimes for the Reynold number $R = u\Delta/\nu$ and the normalized wavenumber $\kappa = k\Delta$. The present long-wavelength approximation corresponds to the parameter range $\kappa R \sim (q\Delta)^2 \ll 1$. In contrast, the inviscid theory applies to the opposite range $\kappa R \gg 1$, since $\kappa$ may be taken small but finite while $R$ becomes arbitrarily large.

The instability growth rate (7.24) reaches a maximum that can be readily determined. It is assumed for $K = 0.0667$, which is the positive root of the quadratic equation,

$$8\sqrt{3}\,K^2 + 51K - 2\sqrt{3} = 0\,. \tag{7.26}$$

The corresponding mode of maximum instability is given by the values

$$k_m = 0.0667u/\nu\,, \quad \omega_{i,m} = 0.014u^2/\nu\,, \tag{7.27}$$

where the growth rate $\omega_{i,m}$ is reduced by the factor $N = 0.209$ in comparison with the growth rate (3.3) for inviscid fluids.

Another important feature of the present result is the stabilization of the flow for large wavenumbers. According to eq. (7.19), marginal stability ($N = 0$) is obtained at the cut-off $K = K_c = 1/4\sqrt{3} \approx 0.144$. The presence of a cut-off is also a well-known feature of the inviscid theory. Specifically, the KH instability for an inviscid shear layer with a linear velocity profile cuts off at $\kappa = 1.2785$. In the past, the wavenumber of marginal stability has been studied intensively for linear shear layers as a function of the parameter $\kappa R$. The present result, $\kappa = \sqrt{K_c \kappa R} \approx 0.38\sqrt{\kappa R}$, becomes valid as an asymptote to the curve of marginal stability for $\kappa R \lesssim 1$. The cut-off $\kappa = 1.2785$ of the inviscid theory is approached for $\kappa R \gg 1$. A more complete discussion of these issues can be found in the book by Drazin and Read [59]. The long-wavelength asymptote to the shear layer instability was also derived by these authors.

*7.2.3. Viscous RT instability*

In the following, the RT instability of viscous fluids will be illustrated for the simplest case of an accelerated free surface. Assuming $v_1 = \rho_1 = \eta_1 = 0$ for the lower fluid and omitting the subscript 2 for the upper fluid, the general dispersion relation (7.12) reduces to the simpler form,

$$a_1 b_2 - a_2 b_1 = 0\,, \tag{7.28}$$

where the coefficients are given by,

$$a_1 = -2k\eta\,, \quad a_2 = 2k\eta - \mathrm{i}\rho\tilde{\omega}/k + J_2\,, \quad J_2 = -\mathrm{i}a\rho/\tilde{\omega}\,,$$

$$b_1 = -\eta(q + k^2/q)\,, \quad b_2 = 2k\eta + J_2 k/q\,.$$

From eq. (7.28) there follows

$$J_2\eta(q^2-k^2)-4qk^2\eta^2+\eta(q^2+k^2)(2k\eta-\mathrm{i}\rho\tilde{\omega}/k)=0\,. \tag{7.29}$$

Eliminating $q$ with the help of eq. (7.6) yields,

$$4\sqrt{1-\mathrm{i}\tilde{\omega}/\nu k^2}=(2-\mathrm{i}\tilde{\omega}/\nu k^2)^2-a/\nu^2k^3\,. \tag{7.30}$$

To determine the instability growth rate, eq. (7.30) has to be solved for $\tilde{\omega}$ together with the constraint $\mathrm{Re}(q)>0$ for bounded solutions. Without proof, it is noted that only a single unstable branch exists which has a real growth rate $n=-\mathrm{i}\tilde{\omega}$. For a further discussion of this solution, it is convenient to define dimensionless variables by setting

$$\sigma=(\nu/a^2)^{1/3}n\,,\quad \kappa=(\nu^2/a)^{1/3}k\,,\quad Q=\kappa^{-3}\,,\quad s=\sigma/\kappa^2\,,\quad y=\sqrt{1+s}\,. \tag{7.31}$$

In terms of $\sigma$ and $\kappa$, eq. (7.30) becomes

$$\Lambda(\sigma,\kappa)=4\sqrt{1+\sigma/\kappa^2}-(2+\sigma/\kappa^2)^2+\kappa^{-3}=0\,. \tag{7.32}$$

In the limits of small and large wavenumbers, one can readily obtain the asymptotic expressions,

$$\begin{aligned}&\kappa\lesssim 0.1\text{:}\quad \sigma=\sqrt{\kappa}-2\kappa^2\,,\quad n=\sqrt{ak}-2\nu k^2\,;\\ &\kappa\gtrsim 2.5\text{:}\quad \sigma=1/2\kappa\,,\quad n=a/2\nu k\,,\end{aligned} \tag{7.33}$$

for the instability growth rate, respectively. They are in excellent agreement with the exact numerical solution within the given wavenumber limits [57]. At small wavenumbers, viscosity becomes negligible and the inviscid growth rate (3.3) is approached. At large wavenumbers, the RT instability is strongly damped by viscosity but, in contrast to the KH instability, no complete stabilization is possible.

In the range of intermediate wavenumbers, the growth rate curve assumes a maximum where

$$\mathrm{d}\sigma/\mathrm{d}\kappa=-\partial_\kappa\Lambda/\partial_\sigma\Lambda=0\,. \tag{7.34}$$

Using eqs. (7.31) and (7.32), the condition for the maximum growth rate can be written as

$$\begin{aligned}&\Lambda=Q-(y-1)(y^3+y^2+3y-1)=0\,,\\ &\kappa^{-1}\,\partial_x\Lambda=-3Q+4(y-1)(y^3+y^2+y-1/y)=0\,.\end{aligned} \tag{7.35}$$

These equations specify the maximum in terms of the variables $Q$ and $y$. Eliminating $Q$ from eq. (7.35), yields a single equation for $y$,

$$y^4+y^3-5y^2+3y=y(y+3)(y-1)^2=4\,. \tag{7.36}$$

It has only one real solution for $y>1$. Numerically, one finds

$$y_m = 1.7059\,, \quad Q_m = 8.4652\,, \quad \kappa_m = 0.4907\,, \quad \sigma_m = 0.4599\,, \tag{7.37}$$

where eqs. (7.36), (7.35) and (7.31) have been used and m refers to the growth rate maximum. The maximum viscous growth rate is about 2/3 of the corresponding inviscid growth rate, $\sigma_m = 0.657\sqrt{\kappa_m}$.

The free-surface model of the viscous RT instability can be extended in an analogous way to two fluids with arbitrary densities and viscosities. Using appropriately scaled variables, the growth rate has been found remarkably insensitive to variations in the densities and viscosities of both fluids [131]. Specifically, defining dimensionless variables $\sigma = (\bar{\nu}/\alpha^2 a^2)^{1/3} n$ and $\kappa = (\bar{\nu}^2/\alpha a)^{1/3} k$ in terms of the Atwood ratio $\alpha = (\rho_2 - \rho_1)/(\rho_2 + \rho_1)$ and the average viscosity $\bar{\nu} = (\rho_1 \nu_1 + \rho_2 \nu_2)/(\rho_1 + \rho_2)$, the variation of the growth rate maximum (7.37) with density and viscosity has been found limited to

$$0.478 \le \kappa_m \le 0.526\,, \quad 0.448 \le \sigma_m \le 0.5\,. \tag{7.38}$$

Corresponding results with the inclusion of surface tension have also been reported in ref. [131].

*7.2.4. Spatial amplification*

If a fluid layer moves parallel to its surface, RT instabilities can become convectively unstable. This situation may arise for steady-state flow around free-surface bubbles as described in section 5.3. Perturbations that become excited at the top side of the bubbles will be carried with the flow along the bubble surface, eventually reaching large amplitudes in the region of the falling spikes. In this section, the possibility of convective amplification of RT instabilities is examined. A moving plane layer with a free surface is considered and both inviscid and viscous amplification factors are derived. The present criteria for convective instabilities arose from studies in plasma physics and have been reviewed in a comprehensive form by Bers [137].

Let us first illustrate the role of convective amplification in the inviscid instability theory. If the fluid layer moves along the $x$ direction with a constant velocity $v$, the dispersion relation of the free-surface RT instability becomes

$$\omega = kv + \mathrm{i}\sqrt{ak}\,. \tag{7.39}$$

The frequency is simply Doppler shifted with respect to the familiar imaginary part, being valid in the rest frame of the fluid. Because of the horizontal motion of the fluid layer, a local surface perturbation will only be present for a transient time at each fixed position in the laboratory frame. Mathematically, this behaviour is expressed by the fact that the dispersion relation (7.39) has no branch-points with $\partial\omega/\partial k = 0$ in the physical complex half-plane $\mathrm{Re}(k) > 0$. Such instabilities are commonly called convective.

It is customary to describe convective instabilities by complex wavenumbers and real frequencies. Solving therefore eq. (7.39) for $k$ yields

$$k = (a/v^2)\{\omega v/a - \tfrac{1}{2} \mp \mathrm{i}(\omega v/a - \tfrac{1}{4})^{1/2}\}\,. \tag{7.40}$$

Complex wavenumbers are indicative for convective instability if the additional constraints

$$\mathrm{Re}(k) > 0\,, \quad \mathrm{Im}(k) > 0 \quad \text{for } \mathrm{Im}(\omega) \to +\infty\,, \quad \mathrm{Im}(k) < 0 \quad \text{for } \mathrm{Im}(\omega) = 0 \tag{7.41}$$

are satisfied. The first condition defines the physical half-plane where the potential perturbations (2.21) are spatially damped inside the fluid. Comparing with eq. (7.40), one obtains a lower cut-off frequency

$$\omega > a/2v \tag{7.42}$$

for convective amplification. Above the cut-off (7.42), the wavenumbers (7.40) are complex and the upper sign corresponds to a spatially growing mode in the $x$ direction.

A convectively unstable system can be distinguished from a merely impenetrable medium by the second condition in eq. (7.41). If $\mathrm{Im}(k)$ changes its sign as $\mathrm{Im}(\omega)$ varies from $+\infty$ to 0, spatially bounded initial perturbations can evolve into unbounded spatially growing modes. This criterion holds only for the upper sign in eq. (7.40), showing that amplification occurs only in the flow direction.

The spatial growth increment of the inviscid theory, $\mathrm{Im}(k)x$, increases indefinitely with the frequency. Actually, however, high-frequency oscillations will become strongly damped by viscosity. This can be shown most easily in the limit of high viscosities where eq. (7.33) yields the asymptotic result

$$\omega = kv + \mathrm{i}\, a/2\nu k\,, \quad k = \omega/v - \mathrm{i}a/2\nu\omega\,. \tag{7.43}$$

The complex wavenumber describes a convectively unstable mode, but its imaginary part now decreases with increasing oscillation frequencies.

For a rough estimate of the frequency of maximum amplification, one may look for the crossing point of the asymptotic growth increments. Equating the amplification factors of eqs. (7.40) and (7.43), one finds

$$\omega_{\mathrm{m}} \sim v\, a^{1/3}/\nu^{2/3}\,, \quad k_{\mathrm{m}} \sim (1/v)a^{2/3}/\nu^{1/3}\,. \tag{7.44}$$

A more complete description of the viscosity effects on the convectively unstable mode could be based on the general dispersion relation (7.30). It would require an analysis of the complex $k$ roots of this equation when $\tilde{\omega} = \omega - kv$ is substituted and $\omega$ is taken real. We will not further pursue this case since the polynomial form is of degree seven and an overview can only be gained by numerical means.

## 8. Stability of ideal fluids

The ideal fluid model provides a means for the investigation of the stability of compressible dissipationless fluids. Compressibility affects in an essential way the instability threshold, leading to Schwarzschild's stability criterion for convective instabilities. On the other hand, its influence on free-surface modes with constant surface pressure is by definition small.

The stability of ideal fluid systems has been intensively studied in MHD plasma theory. Based on these methods, the stability criterion for convective instabilities will be derived from an energy principle for static equilibria with arbitrary thermodynamic properties. The role of compressibility is shown to be either stabilizing or destabilizing, depending on the precise definition of the class of comparison profiles. Finally, the normal mode analysis of RT instabilities is extended to compressible fluids and thereby a general perturbative treatment of compressibility effects is given.

### 8.1. Ideal fluid model

While the incompressibility assumption is often adequate for surface instabilities, it cannot be applied to equilibria whose variations are governed by the gravitational scale height of the system. This is typically the case for convective instabilities in compressible atmospheres. Here, a much better description is given by the ideal fluid equations, being based on adiabatic instead of incompressible motion of fluid particles.

The ideal fluid model of RT-type instabilities concerns also several issues of more theoretical interest. These include for instance (i) the stability criterion for convective instabilities, (ii) its relationship to the energy principle for ideal fluids, (iii) dependences on special material equations (ideal gas approximation), and (iv) the role of compressibility for instability growth. In the following, we attempt a careful analysis of these basic aspects. The present discussion is largely based on a previous stability study [126] whose results have been published in part in [70].

The energy principle analysis of ideal fluid equilibria has been developed in the context of hydromagnetic stability theory [138]. The present analysis is based on this general framework. Magnetic fields will not be considered although more general equations of state are permitted. The stability criterion to be derived was first introduced by Schwarzschild [45] and is well known from the classical theory of convection [134]. The influence of compressibility on RT instability seems controversial, some authors claiming stabilization, destabilization or both. A general argument is due to Newcomb [139], proving destabilization for density profiles in polytrope gases. However, other interpretations seem possible if the class of comparison states is chosen differently. In particular, it will be shown that compressibility leads to stabilization if equilibria with a unique functional for the gravitational energy are compared.

A number of works have been concerned with normal mode analysis of RT unstable compressible systems. These may be distinguished according to the basic states considered. In an early work, Skumanich [140] has treated the stability problem for a polytropic atmosphere. Several authors have investigated the stability of temperature step-profiles including Baker [141], Bernstein and Book [142], and Kull [126]. The corresponding problem of an entropy step was analysed by Lezzi and Prosperetti [143]. To the understanding of this author, the isentropic approximation was also implicit in an earlier treatment by Plesset and Prosperetti [144]. Continuum modes have been treated in the short-wavelength approximation by Scannapieco [145]. Considerable effort was also spent in stability analyses of self-similar flows which will not be covered by this article. The interested reader is referred to work by Book [146], by Book and Bernstein [147], and by Han [148].

#### 8.1.1. Thermodynamic relations

An ideal fluid can be defined by the conservation law for the specific entropy $s$ of fluid particles,

$$\mathrm{d}s/\mathrm{d}t = 0\,. \tag{8.1}$$

This condition neglects dissipation by viscosity and heat conduction but it fully accounts for the finite compressibility and the inhomogeneity of the medium. Together with the continuity equation for mass conservation,

$$\mathrm{d}\rho/\mathrm{d}t = -\rho\,\boldsymbol{\nabla}\cdot\boldsymbol{v}\,, \tag{8.2}$$

it replaces eq. (6.1a) in the incompressible fluid description.

Many features of convective instabilities in ideal fluids can be established without reference to particular material properties. To emphasize this general nature of the stability problem, the reader is first reminded of a few basic thermodynamic relations. These are

$$
\begin{aligned}
&c_p = T\left.\frac{\partial s}{\partial T}\right|_p\,, \quad c^2 = \left.\frac{\partial p}{\partial \rho}\right|_s\,, \quad \alpha = \frac{1}{V}\left.\frac{\partial V}{\partial T}\right|_p = -\frac{1}{\rho}\left.\frac{\partial \rho}{\partial T}\right|_p = -\frac{1}{V}\left.\frac{\partial s}{\partial p}\right|_T\,,\\
&\kappa = -\frac{1}{V}\left.\frac{\partial V}{\partial p}\right|_s = \frac{1}{\rho}\left.\frac{\partial \rho}{\partial p}\right|_s = \frac{1}{\rho c^2}\,, \quad \left.\frac{\partial s}{\partial \rho}\right|_p = \left.\frac{\partial s}{\partial T}\right|_p \left.\frac{\partial T}{\partial \rho}\right|_p = -\frac{c_p}{\rho \alpha T}\,,\\
&\frac{\partial s/\partial p|_\rho}{\partial s/\partial \rho|_p} = -\frac{1}{c^2}\,,
\end{aligned}
\tag{8.3}
$$

with $c_p$ representing the specific heat at constant pressure, $c$ the speed of sound, $\alpha$ the coefficient of thermal expansion, $\kappa$ the adiabatic compressibility, $V = 1/\rho$ the specific volume, and $T$ the temperature. With these definitions, entropy changes can be expressed as,

$$
\begin{aligned}
&\mathrm{d}s = \left.\frac{\partial s}{\partial \rho}\right|_p \mathrm{d}\rho + \left.\frac{\partial s}{\partial p}\right|_\rho \mathrm{d}p = -\frac{c_p}{\alpha T}\left(\frac{\mathrm{d}\rho}{\rho} - \kappa\,\mathrm{d}p\right),\\
&\mathrm{d}s = \left.\frac{\partial s}{\partial T}\right|_p \mathrm{d}T + \left.\frac{\partial s}{\partial p}\right|_T \mathrm{d}p = c_p\frac{\mathrm{d}T}{T} - \alpha\frac{\mathrm{d}p}{\rho}\,.
\end{aligned}
\tag{8.4}
$$

Previous work on compressible RT instabilities has been mostly limited to the ideal gas approximation. It is based on the well-known relations,

$$
\begin{aligned}
&s - s_0 = c_V \ln[(p/p_0)(\rho_0/\rho)^\gamma]\,, \quad p = \rho T/m\,, \quad mc_V = 1/(\gamma - 1)\,,\\
&mc_p = \gamma/(\gamma - 1)\,, \quad \alpha = 1/T\,, \quad \kappa = 1/\gamma p\,, \quad c^2 = \gamma\, p/\rho\,,
\end{aligned}
\tag{8.5}
$$

for an ideal gas with the adiabatic index $\gamma$ and particles of mass $m$. In the following, these formulas will be used to establish the stability properties for entropy, density and temperature gradients from the ideal fluid equations.

*8.1.2. Stability eigenvalue equation*

Perturbations of a hydrostatic equilibrium state, are conveniently described by a displacement vector $\boldsymbol{\xi}(\boldsymbol{x}, t)$ of the fluid particles from their equilibrium position $\boldsymbol{x}$. If a harmonic time-dependence with $\boldsymbol{\xi} \sim \exp(-\mathrm{i}\omega t)$ is assumed, the corresponding velocity, density and pressure perturbations are given by

$$
\begin{aligned}
&\delta \boldsymbol{v} = -\mathrm{i}\omega\boldsymbol{\xi}\,, \quad \delta\rho = -\boldsymbol{\nabla}\cdot(\rho_0\boldsymbol{\xi})\,,\\
&\delta p = -\boldsymbol{\xi}\cdot\boldsymbol{\nabla}p_0 - c^2\rho_0\,\boldsymbol{\nabla}\cdot\boldsymbol{\xi} = c^2\,\delta\rho + c^2\,\boldsymbol{\xi}\cdot(\boldsymbol{\nabla}\rho_0 - c^{-2}\,\boldsymbol{\nabla}p_0)\,,
\end{aligned}
\tag{8.6}
$$

respectively. The pressure perturbation can be obtained most easily from

$$
\mathrm{d}p/\mathrm{d}t = c^2\,\mathrm{d}\rho/\mathrm{d}t = -c^2\rho\,\boldsymbol{\nabla}\cdot\boldsymbol{v}\,,
\tag{8.7}
$$

using eqs. (8.1), (8.2), and (8.4). The simpler relation, $\delta p = c^2\,\delta\rho$, applies only to isentropic fluids ($s_0 = \text{const.}$). It will therefore not be used in the following. If eq. (8.6) is inserted into the linearized Euler equation,

$$\rho_0\,\partial_t\,\delta\boldsymbol{v} = -\boldsymbol{\nabla}\,\delta p - \delta\rho\,\boldsymbol{\nabla}U\,, \tag{8.8}$$

there follows the eigenvalue equation

$$\boldsymbol{L}\cdot\boldsymbol{\xi} + \rho_0\omega^2\boldsymbol{\xi} = 0\,, \tag{8.9}$$

with the linear differential operator

$$\begin{aligned}\boldsymbol{L}\cdot\boldsymbol{\xi} &= \boldsymbol{\nabla}(c^2\rho_0\,\boldsymbol{\nabla}\cdot\boldsymbol{\xi} + \boldsymbol{\xi}\cdot\boldsymbol{\nabla}p_0) + (\boldsymbol{\nabla}U)\boldsymbol{\nabla}\cdot(\rho_0\boldsymbol{\xi})\\ &= \rho_0[c^2\boldsymbol{\nabla}(\boldsymbol{\nabla}\cdot\boldsymbol{\xi}) - \boldsymbol{\nabla}(\boldsymbol{\xi}\cdot\boldsymbol{\nabla}U)] + [\boldsymbol{\nabla}(c^2\rho_0 - p_0)]\boldsymbol{\nabla}\cdot\boldsymbol{\xi}\,.\end{aligned} \tag{8.10}$$

The last representation follows with the help of the equilibrium relations (6.2) and (6.3). Before specializing this equation further to the uniform acceleration case, a few general properties of the present eigenvalue operator will be briefly mentioned.

*8.1.3. Lagrange–Green identity*

An important symmetry property of the differential operator $\boldsymbol{L}$ is expressed by the Lagrange–Green identity,

$$\int_V \mathrm{d}V\,[\boldsymbol{v}\cdot(\boldsymbol{L}\cdot\boldsymbol{u}) - \boldsymbol{u}\cdot(\boldsymbol{L}\cdot\boldsymbol{v})] = \int_{\partial V}\mathrm{d}\boldsymbol{S}\cdot[c^2\rho_0(\boldsymbol{v}\,\boldsymbol{\nabla}\cdot\boldsymbol{u} - \boldsymbol{u}\,\boldsymbol{\nabla}\cdot\boldsymbol{v}) + (\boldsymbol{u}\times\boldsymbol{v})\times\boldsymbol{\nabla}p_0]\,, \tag{8.11}$$

being valid for arbitrary vector fields $\boldsymbol{u}(\boldsymbol{x})$, $\boldsymbol{v}(\boldsymbol{x})$ and for an arbitrary integration volume $V$ with the surface $\partial V$. If the boundary term on the r.h.s. of eq. (8.11) vanishes, on account of specific boundary conditions, the operator $\boldsymbol{L}$ is called Hermitian. In particular, $\boldsymbol{L}$ is Hermitian for rigid boundaries where the normal component of the displacement vector is required to be zero. It is also Hermitian for two-dimensional flows with free boundaries. In this case, the constancy of the surface pressure leads to the vanishing of the flow divergence, according to eq. (8.7), while the remaining cross-product term in eq. (8.11) is zero in two dimensions. For any medium with sufficiently extended stable boundary regions, the choice of rigid boundaries does not seem to be particularly restrictive. Hermiticity of $\boldsymbol{L}$ will therefore be assumed throughout the following discussion. This property ensures that all eigenvalues $\omega^2$ are real, corresponding either to stable oscillations ($\omega^2 > 0$) or to exponential instability growth ($\omega^2 < 0$).

For definiteness, it is also mentioned that Hermitian operators are not necessarily self-adjoint. According to modern mathematical terminology, self-adjointness of a Hermitian operator requires a suitable choice of its domain, imposing important constraints on the allowable boundary conditions [149]. Only if the more stringent requirement of self-adjointness is met, the completeness of the set of eigenvectors will be guaranteed.

The above identity (8.11) can be readily derived by the following partial integrations,

$$\begin{aligned}
\int_V \mathrm{d}V\, \boldsymbol{v}\cdot(\boldsymbol{L}\cdot\boldsymbol{u}) &= \int \mathrm{d}V\, \boldsymbol{v}\cdot[\boldsymbol{\nabla}(\boldsymbol{u}\cdot\boldsymbol{\nabla}p_0 + c^2\rho_0\,\boldsymbol{\nabla}\cdot\boldsymbol{u}) + (\boldsymbol{\nabla}U)\boldsymbol{\nabla}\cdot\rho_0\boldsymbol{u}] \\
&= -\int \mathrm{d}V\,[(\boldsymbol{u}\cdot\boldsymbol{\nabla}p_0 + c^2\rho_0\,\boldsymbol{\nabla}\cdot\boldsymbol{u})\boldsymbol{\nabla}\cdot\boldsymbol{v} + \rho_0\,\boldsymbol{u}\cdot\boldsymbol{\nabla}(\boldsymbol{v}\cdot\boldsymbol{\nabla}U)] \\
&\quad + \int \mathrm{d}\boldsymbol{S}\cdot[\boldsymbol{v}(\boldsymbol{u}\cdot\boldsymbol{\nabla}p_0 + c^2\rho_0\,\boldsymbol{\nabla}\cdot\boldsymbol{u}) + \rho_0\boldsymbol{u}\,\boldsymbol{v}\cdot\boldsymbol{\nabla}U] \qquad (8.12) \\
&= \int \mathrm{d}V\,\boldsymbol{u}\cdot[\boldsymbol{\nabla}(c^2\rho_0\,\boldsymbol{\nabla}\cdot\boldsymbol{v}) - (\boldsymbol{\nabla}p_0)\boldsymbol{\nabla}\cdot\boldsymbol{v} - \rho_0\,\boldsymbol{\nabla}(\boldsymbol{v}\cdot\boldsymbol{\nabla}U)] \\
&\quad + \int \mathrm{d}\boldsymbol{S}\cdot[c^2\rho_0(\boldsymbol{v}\,\boldsymbol{\nabla}\cdot\boldsymbol{u} - \boldsymbol{u}\,\boldsymbol{\nabla}\cdot\boldsymbol{v}) + \boldsymbol{v}\,\boldsymbol{u}\cdot\boldsymbol{\nabla}p_0 - \boldsymbol{u}\boldsymbol{v}\cdot\boldsymbol{\nabla}p_0]\,,
\end{aligned}$$

and by further noting that

$$\begin{aligned}
-\rho_0\,\boldsymbol{\nabla}(\boldsymbol{v}\cdot\boldsymbol{\nabla}U) - (\boldsymbol{\nabla}p_0)\boldsymbol{\nabla}\cdot\boldsymbol{v} &= \boldsymbol{\nabla}(\boldsymbol{v}\cdot\boldsymbol{\nabla}p_0) + (\boldsymbol{v}\cdot\boldsymbol{\nabla}U)\,\boldsymbol{\nabla}\rho_0 - (\boldsymbol{\nabla}p_0)\,\boldsymbol{\nabla}\cdot\boldsymbol{v} \\
&= \boldsymbol{\nabla}(\boldsymbol{v}\cdot\boldsymbol{\nabla}p_0) + \boldsymbol{\nabla}U(\boldsymbol{v}\cdot\boldsymbol{\nabla}\rho_0) - (\boldsymbol{\nabla}p_0)\boldsymbol{\nabla}\cdot\boldsymbol{v} \\
&= \boldsymbol{\nabla}(\boldsymbol{v}\cdot\boldsymbol{\nabla}p_0) + \boldsymbol{\nabla}U[(\boldsymbol{v}\cdot\boldsymbol{\nabla}\rho_0) + \rho_0\,\boldsymbol{\nabla}\cdot\boldsymbol{v}] \qquad (8.13) \\
&= \boldsymbol{\nabla}(\boldsymbol{v}\cdot\boldsymbol{\nabla}p_0) + \boldsymbol{\nabla}U\,\boldsymbol{\nabla}\cdot\rho_0\boldsymbol{v}\,.
\end{aligned}$$

In eq. (8.13), use has been made of the identity

$$(\boldsymbol{v}\cdot\boldsymbol{\nabla}U)\boldsymbol{\nabla}\rho_0 - \boldsymbol{\nabla}U(\boldsymbol{v}\cdot\boldsymbol{\nabla}\rho_0) = \boldsymbol{v}\times(\boldsymbol{\nabla}\rho_0\times\boldsymbol{\nabla}U) = 0\,. \qquad (8.14)$$

*8.1.4. Energy principle*

The stability of the equilibrium state depends on the sign of the lowest eigenvalue $\omega_0^2$. It is therefore convenient to express the eigenvalue problem by an equivalent variational problem,

$$\omega_0^2 = \min_{\xi}(W/K)\,. \qquad (8.15)$$

The potential energy functional $W$ and the normalization integral $K$ are defined by the expressions,

$$W = -\frac{1}{2}\int \mathrm{d}V\,\boldsymbol{\xi}^*\cdot\boldsymbol{L}\cdot\boldsymbol{\xi}\,,\quad K = \frac{1}{2}\int \mathrm{d}V\,\rho_0\,\boldsymbol{\xi}^*\cdot\boldsymbol{\xi}\,. \qquad (8.16)$$

Considering variations of the displacement field and using the Hermiticity property of $\boldsymbol{L}$, one can readily recover from eq. (8.15) the original eigenvalue equation (8.9). Since $K$ is always positive, the equilibrium will be unstable if $W$ can be made negative for some displacement field. The criterion $W>0$ is both necessary and sufficient for stability in the linear theory. This has been proved in the framework of MHD theory without the present restriction to harmonic perturbations [138].

To indicate the physical relevance of the energy principle for convective instabilities, the potential

energy will now be transformed to a different representation. If eq. (8.8) is inserted into eq. (8.16), there follows

$$2W = \int \mathrm{d}V\, \boldsymbol{\xi}^* \cdot (\boldsymbol{\nabla}\, \delta p + \delta\rho\, \boldsymbol{\nabla} U) = \int \mathrm{d}V\, (\delta\rho\, \boldsymbol{\xi}^* \cdot \boldsymbol{\nabla} U - \delta p\, \boldsymbol{\nabla} \cdot \boldsymbol{\xi}^*) + \int \mathrm{d}\boldsymbol{S} \cdot \boldsymbol{\xi}^*\, \delta p\,. \tag{8.17}$$

The first term represents the gravitational potential energy associated with the displacement in the potential $U$. The remaining two terms are due to pressure perturbations in a compressible medium. One can attribute a definite sign to these energies if both $\delta\rho$ and $\boldsymbol{\nabla} \cdot \boldsymbol{\xi}^*$ are eliminated from eq. (8.17) with the help of eq. (8.6). This yields

$$W = W_{\mathrm{g}} + W_{\mathrm{p}} + W_{\mathrm{b}}\,, \tag{8.18}$$

with

$$W_{\mathrm{g}} = -\frac{1}{2} \int \mathrm{d}V\, \frac{\alpha T}{c_p}\, (\boldsymbol{\xi}^* \cdot \boldsymbol{\nabla} p_0)(\boldsymbol{\xi} \cdot \boldsymbol{\nabla} s_0)\,,$$

$$W_{\mathrm{p}} = \frac{1}{2} \int \mathrm{d}V\, \kappa |\delta p|^2\,, \quad W_{\mathrm{b}} = \frac{1}{2} \int \mathrm{d}\boldsymbol{S} \cdot \boldsymbol{\xi}^*\, \delta p\,.$$

Here the definitions of eq. (8.3) for the adiabatic compressibility $\kappa$ and of eq. (8.4) for the entropy gradient $\boldsymbol{\nabla} s_0$ have also been used. Neglecting again the boundary term $W_{\mathrm{b}}$, the finite compressibility of the medium gives only rise to a positive energy $W_{\mathrm{p}}$. This energy agrees with the well-known expression for the compressional energy of sound waves. Instability can only result from the gravitational potential energy $W_{\mathrm{g}}$. Noting that the coefficient of thermal expansion is mostly positive, $\alpha > 0$, instability requires parallel pressure and entropy gradients. In this case, a two-dimensional perturbation can be found that makes $W$ negative. Firstly, the displacement parallel to the gradient is chosen such that $W_{\mathrm{g}}$ becomes negative. Then, the perpendicular component is chosen such that $W_{\mathrm{p}} = 0$ by making use of eq. (8.6). Although this test field may not correspond to the actual minimum, it shows that the minimum has to be negative.

In conclusion, a hydrostatic equilibrium state will be stable if $\alpha > 0$ and the entropy gradient is everywhere opposed to the pressure gradient. This criterion plays an important role in atmospheric and astrophysical applications, where it is generally known as Schwarzschild's criterion. We remark that the criterion is in perfect agreement with the energy principle analysis and does not depend on the ideal gas approximation to the equation of state.

The relationship of Schwarzschild's stability criterion to the RT instability can be recognized from eq. (8.4). If the medium is assumed incompressible ($\kappa \to 0$), the entropy gradient becomes antiparallel to the density gradient. Consequently, stability of an incompressible medium requires parallel pressure and density gradients.

In problems of thermal convection, it is often the temperature gradient that is externally controlled. Using eqs. (8.4) and (6.2), adverse temperature gradients in the direction of the pressure gradient are found to be stable, if they do not exceed the instability threshold:

$$|\boldsymbol{\nabla} T| < (\alpha T / c_p) |\boldsymbol{\nabla} U|\,. \tag{8.19}$$

The onset of thermal convection is also often influenced by viscosity and heat conduction. For more details on thermal instabilities the reader is referred to refs. [57, 59].

### 8.1.5. Compressibility effects

The energy principle can help to clarify the somewhat controversial role of compressibility in the RT instability. One should notice that the question whether compressibility can stabilize or destabilize the equilibrium state is ill defined, because a unique equilibrium state does not exist. The answer is therefore partly a matter of definition.

One way of making a meaningful comparison between the stability properties of different media is to require a unique expression for the gravitational energy $W_g$. This constraint avoids discrepancies due to different choices of unstable gradients. The corresponding equilibria are defined by the relationship

$$-(\alpha T\rho_0/c_p)\,\nabla s_0 = \nabla\rho_0 + (\rho_0/c^2)\,\nabla U = (\nabla\rho_0)_\infty\,, \tag{8.20}$$

where $(\nabla\rho_0)_\infty$ is a prescribed density gradient of the incompressible comparison medium.

Within the chosen class of equilibrium states (8.20), the incompressible one has obviously the largest instability growth rate. Since $W_g$ is independent of $\kappa$, by definition, and $W_p$ increases with $\kappa$, the minimum of eq. (8.15) will also increase with $\kappa$. This result conforms to the physical intuition that compressional work should have a stabilizing influence on instability growth.

However, this interpretation is not the only possible one and an apparently contrary conclusion may be drawn from a comparison of equilibrium states with equal density gradients, $\nabla\rho_0 = (\nabla\rho_0)_\infty$. In this case, compressibility can lower the gravitational energy $W_g$ due to the expansion of fluid elements when displaced against the pressure gradient. If one eliminates $\delta p$ instead of $\nabla\cdot\boldsymbol{\xi}$ from eq. (8.17), one arrives at the alternative form,

$$W = W_\kappa + W_0 + W_b\,, \tag{8.21}$$

with

$$W_\kappa = \frac{1}{2}\int \mathrm{d}V\,|\nabla\cdot\boldsymbol{\xi}|^2/\kappa_s\,,$$

$$W_0 = \frac{1}{2}\int \mathrm{d}V\,\nabla p_0\cdot[\boldsymbol{\xi}^*(\boldsymbol{\xi}\cdot\nabla\rho_0/\rho_0) + \boldsymbol{\xi}(\nabla\cdot\boldsymbol{\xi}^*) + \boldsymbol{\xi}^*(\nabla\cdot\boldsymbol{\xi})]\,.$$

Comparing now equilibrium states with equal density profiles, the energy $W_0$ is found independent of compressibility while the positive energy $W_\kappa$ is a decreasing function of compressibility. It then follows that the minimum eigenvalue (8.15) is also decreasing with compressibility. In this case, the compressible system is found less stable. Again, these conclusions remain valid for arbitrary thermodynamic systems. The destabilizing role of compressibility for polytrope gases has been emphasized by Book and Newcomb. The energy principle argument in the form of eq. (8.21) is due to Newcomb [139]. Other authors may have contributed to the subject as well, but precise criteria are often lacking.

## 8.2. Uniform accelerations

### 8.2.1. Normal mode equation

To describe RT instabilities in compressible fluids, one may consider the standard equilibrium state, $\nabla p_0 = -\rho_0\,\nabla U = -\rho_0 a\,\nabla y$, corresponding to a uniform gravitational acceleration $a$ in the direction of

the negative $y$ axis. The evolution of normal mode perturbations, $\boldsymbol{\xi} \sim \exp(\mathrm{i}kx - \mathrm{i}\omega t)$, is conveniently described in terms of the following set of variables,

$$\eta = ky\,, \quad \lambda = ak/\omega^2\,, \quad \beta = \partial_\eta \rho_0/\rho_0\,, \quad \varepsilon = a/c^2k = -\kappa\,\partial_\eta p_0\,,$$
$$\Pi = \rho_0 c^2 k^{-1}\,\boldsymbol{\nabla}\cdot\boldsymbol{\xi} = \kappa^{-1}(\mathrm{i}\xi_x + \partial_\eta \xi_y)\,. \tag{8.22}$$

The quantities $\eta$, $\lambda$, and $\beta$ have already been introduced for incompressible fluids in section 6.2.1 and the compressibility $\kappa$ has been defined in eq. (8.3). The variable $\Pi$ represents the pressure perturbation at the position of a displaced fluid particle, according to eq. (8.6). Being continuous across a discontinuity surface, it is particularly useful as a dependent variable. Finally, the parameter $\varepsilon$ can be regarded as a dimensionless measure for compressibility effects.

In the present case, the eigenvalue equation (8.9) assumes the simpler form

$$\rho_0 \omega^2 \boldsymbol{\xi} - a\rho_0\,\boldsymbol{\nabla}\xi_y + k\,\boldsymbol{\nabla}\Pi + (ak/c^2)\Pi\,\boldsymbol{\nabla}y = 0\,. \tag{8.23}$$

Separating the $x$ and $y$ components of eq. (8.23) yields,

$$\lambda\xi_y - \partial_\eta \xi_y + (\kappa - \lambda\, k/a\rho_0)\Pi = 0\,, \quad \lambda^{-1}\xi_y - \partial_\eta \xi_y + (k/a\rho_0)\partial_\eta \Pi + \kappa\Pi = 0\,, \tag{8.24}$$

where $\xi_x$ has been eliminated with the help of eq. (8.22). Taking the linear combinations,

$$(\lambda^{-1} - \lambda)\xi_y + (k/a\rho_0)(\partial_\eta \Pi + \lambda\Pi) = 0\,,$$
$$(\lambda^{-1} - \lambda)\partial_\eta \xi_y + (k/a\rho_0)(\lambda\,\partial_\eta \Pi + \Pi) + (\lambda - 1/\lambda)\kappa\Pi = 0\,, \tag{8.25}$$

of eq. (8.24) and differentiating the upper equation in (8.25) once, there follows a single second-order equation for the variable $\Pi$,

$$\partial_\eta^2 \Pi - \beta\,\partial_\eta \Pi - [1 + \lambda\beta + (\lambda - 1/\lambda)\varepsilon]\Pi = 0\,. \tag{8.26}$$

It represents the desired generalization of Rayleigh's equation (6.14) to compressible fluids. In the limit where $\varepsilon \to 0$, the operator (8.26) becomes identical to the operator (6.20) and it has therefore the same eigenvalue spectrum as (6.14).

The effects of compressibility are described by the last term in eq. (8.26), which is proportional to $\varepsilon$. Near the instability threshold, where $\lambda \to \infty$, the dominant contribution is a gradient correction,

$$\beta + \varepsilon = \partial_\eta \rho_0/\rho_0 - \kappa_0\,\partial_\eta p_0 = -(\alpha_0 T_0/c_{p0})\,\partial_\eta s_0\,. \tag{8.27}$$

It confirms the significance of the entropy gradient (8.4) for the stability of compressible media. In the absence of acceleration, where $\lambda \to 0$, eq. (8.26) becomes the wave equation for monochromatic sound waves. The factor $\varepsilon/\lambda = \omega^2/(ck)^2$ then gives rise to the familiar sound wave dispersion relation.

Both compressibility effects cancel for the free-surface eigenvalues $\lambda = \pm 1$. Accordingly, a free surface of a compressible fluid will basically evolve in an incompressible manner. This justifies the incompressible fluid description for many applications.

The operator (8.26) can also be written in an explicitly Hermitian representation,

$$L\Pi = F\Pi \tag{8.28}$$

by defining

$$L = \partial_\eta \rho_0^{-1} \partial_\eta - [1 + \lambda\beta]\rho_0^{-1}, \quad F = (\lambda - 1/\lambda)\varepsilon\rho_0^{-1}.$$

Integrating eq. (8.28) across a discontinuity surface, the continuity conditions follow,

$$[\Pi] = 0, \quad [\rho_0^{-1}(\partial_\eta \Pi + \lambda\Pi)] = 0. \tag{8.29}$$

The first condition describes the continuity of the surface pressure while the second one corresponds to the continuity of $\xi_y$ as given by eq. (8.25).

*8.2.2. Growth rate shift in compressible media*

Compressibility effects present often only a small correction to the instability growth rates of RT instabilities. These corrections can be simply evaluated by perturbation theory. The following treatment was first described in refs. [126, 70].

Let us compare the instability growth rates of a compressible medium ($\varepsilon \neq 0$) to those of an incompressible medium ($\varepsilon = 0$) with the same equilibrium density. For sufficiently small values of $\varepsilon$, one may consider the perturbation ansatz, $\Pi = \Pi_0 + \Pi_1$, $\lambda = \lambda_0 + \lambda_1$, $L = L_0 - \beta\rho^{-1}\lambda_1$, where the index 0 refers to a nondegenerate unperturbed solution ($\varepsilon = 0$) and the index 1 to first-order quantities in $\varepsilon$. The corresponding perturbation system,

$$L_0\Pi_0 = 0, \quad L_0\Pi_1 = (\beta\rho^{-1}\lambda_1 + F)\Pi_0, \tag{8.30}$$

will be supplemented by infinite medium boundary conditions, $\lim_{\eta\to\infty} \Pi_{0,1} = 0$. The eigenvalue shift $\lambda_1$ is obtained by multiplying the first-order equation with $\Pi_0$, integrating over the flow region $-\infty < \eta < \infty$ and making use of the Hermiticity of $L_0$. This yields,

$$\frac{\lambda_1}{\lambda_0} = -(1 - \lambda_0^{-2})\mu, \quad \mu = \left(\int_{-\infty}^{\infty} \mathrm{d}\eta\, \varepsilon\rho^{-1}\Pi_0^2\right) \Big/ \left(\int_{-\infty}^{\infty} \mathrm{d}\eta\, \beta\rho^{-1}\Pi_0^2\right). \tag{8.31}$$

The corresponding instability growth rate is given by,

$$n^2 = -ak/\lambda = n_0^2(1 - \lambda_1/\lambda_0) = n_0^2\{1 + [1 - (n_0^2/ak)^2]\mu\}. \tag{8.32}$$

It shows again the absence of compressibility effects for the free-surface growth rate $n_0 = \sqrt{ak}$. For all growth rates below this value, the shift $n_1$ is positive, in agreement with the destabilizing role of thermal expansion as discussed in section 8.1.5. The condition $\mu > 0$ for $\lambda_0 < 0$ can be easily verified by looking at the quadratic form associated with the unperturbed operator $L_0$. For an assumed growth rate above the free-surface value, eq. (8.32) would predict a growth rate reduction. This is a clear contradiction to the energy principle (8.21), and it may therefore be taken as an indirect proof that $n_0 = \sqrt{ak}$ is the maximum possible growth rate of the incompressible RT instability.

*8.2.3. Density step-profile*

The perturbation treatment can be readily applied to a density step-profile with constant densities $\rho_1$ for $\eta<0$ and $\rho_2$ for $\eta>0$. The unperturbed incompressible solution,

$$n_0^2=[(\rho_2-\rho_1)/(\rho_2+\rho_1)]ak\,,\quad \Pi_0=\exp(-|\eta|)\,, \tag{8.33}$$

has been derived in section 3.1. For a compressible medium with the same density profile, the integrals in eq. (8.31) can be evaluated as

$$\begin{aligned}&\int_{-\infty}^{\infty} d\eta\,\varepsilon\rho^{-1}\Pi_0^2=(a/k)(\bar{\kappa}_1+\bar{\kappa}_2)/2\,,\\ &\int_{-\infty}^{\infty} d\eta\,\beta\rho^{-1}\Pi_0^2=\int_{0-}^{0+} d\rho_0\,\rho_0^{-2}=(\rho_2-\rho_1)/\rho_1\rho_2\,,\end{aligned} \tag{8.34}$$

with the compressibility averages

$$\bar{\kappa}_1=2\int_{-\infty}^{0} d\eta\,\kappa_1\exp(2\eta)\,,\quad \bar{\kappa}_2=2\int_{0}^{\infty} d\eta\,\kappa_2\exp(-2\eta)\,,$$

of the two regions. Inserting eqs. (8.33) and (8.34) into eq. (8.32) yields

$$n^2=n_0^2[1+2(a/k)(\bar{\kappa}_1+\bar{\kappa}_2)(\rho_1\rho_2)^2/(\rho_2+\rho_1)^2(\rho_2-\rho_1)]\,. \tag{8.35}$$

It describes compressibility effects to first order in $\kappa$. A qualitatively similar formula has been derived by Plesset and Prosperetti from a simplified model equation [144]. However, the present result does not confirm their finding that compressibility effects will disappear for equal sound velocities in both fluids.

*8.2.4. Temperature step-profile*

An exact solution of eq. (8.26) can be obtained for the interface between two isothermal atmospheres. Making use of the ideal gas relations (8.5), the equilibrium density at constant temperature is given by the Boltzmann distribution,

$$\rho_0(\eta)=\rho_i\exp(-b_i\eta)\,,\quad b_i=am/kT_i\,, \tag{8.36}$$

where $i=1$ refers to the lower half-space, $\eta<0$, and $i=2$ to the upper half-space, $\eta>0$. The density jump at the interface $\eta=0$ occurs at constant pressure, which determines the ratio

$$\rho_2/\rho_1=T_1/T_2=b_2/b_1\,. \tag{8.37}$$

Both isothermal regions are in thermodynamic equilibrium, but instability can result from an interface with $T_1>T_2$.

The coefficients of the differential equation (8.26), $\beta=-b$ and $\varepsilon=b/\gamma$, are constants. Assuming

convergence at infinity, the solutions for both half-spaces are found to be

$$\Pi_i = \Pi_0 \exp(q_i \eta) , \tag{8.38}$$

with

$$q_1 = -\tfrac{1}{2} b_1 + \sqrt{D_1} , \quad q_2 = -\tfrac{1}{2} b_2 - \sqrt{D_2} ,$$

$$D_i = \tfrac{1}{4} b_i^2 + 1 - \lambda b_i + (\lambda - 1/\lambda) b_i / \gamma .$$

Inserting eq. (8.38) into the continuity condition (8.29), there follows

$$\rho_2 (q_1 + \lambda) = \rho_1 (q_2 + \lambda) . \tag{8.39}$$

Noting eqs. (8.37) and (8.38), one obtains the simpler form

$$-1/\lambda = (b_2 - b_1)/(b_1 \sqrt{D_2} + b_2 \sqrt{D_1}) , \tag{8.40}$$

which implicitly determines the eigenvalue $\lambda$. In the limit of weak gradients, where $b_i \to 0$ and $D_i \to 1$, the r.h.s. reduces to the Atwood number, in agreement with eq. (8.33). Compressibility effects are most important in the limit of small growth rates. For $\lambda \to -\infty$ and $\gamma > 1$ one obtains the approximate result

$$D_i = -\lambda (1 - \gamma^{-1}) b_i , \quad \frac{n}{\sqrt{ak}} = \frac{1}{\sqrt{1 - \gamma^{-1}}} \frac{b_2 - b_1}{b_1 \sqrt{b_2} + b_2 \sqrt{b_1}} . \tag{8.41}$$

From eq. (8.41) one can recognize the decrease of the growth rate with increasing values of $\gamma$.

According to eq. (8.40), the normalized growth rate $n/\sqrt{ak}$ can be viewed as a function of the density ratio (8.37), the gradient $b_1$ of the lower medium, and of the adiabatic index $\gamma$. These dependences are illustrated in fig. 30. If $\gamma$ is kept fixed (fig. 30a), variation of $b_1$ shows a reduction of the growth rates with increasing gradients. The classical result for a density-step profile becomes valid for weak gradients ($b_1 \to 0$). These density gradient effects have to be clearly distinguished from

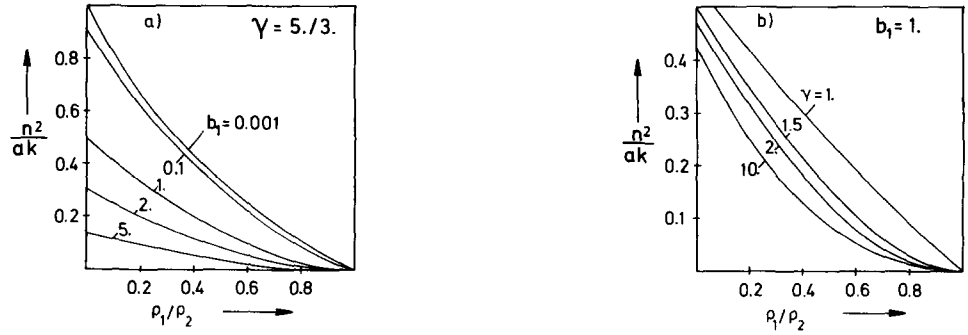


Fig. 30. Instability growth rate $n$ for a temperature step-profile in a compressible fluid with adiabatic index $\gamma$. The density of each layer is given by a Boltzmann distribution. The density jump across the temperature step is given by the ratio $\rho_1/\rho_2$. (a) Variation of the density gradient $b_1$ inside the lower fluid for a fixed adiabatic index $\gamma = 5/3$. (b) Variation of the adiabatic index $\gamma$ for a fixed gradient $b_1$.

compressibility effects. If $\gamma$ is varied (fig. 30b) for a fixed gradient $b_1$, the growth rates become a decreasing function of $\gamma$. This behavior confirms the destabilizing role of compressibility on the density profile.

## 9. Stability of ablation fronts

In terms of an isobaric flow model, we describe steady ablation fronts and their stability under acceleration. The RT instability of ablatively accelerated foils is strongly influenced by mass ablation, heat flow, and inhomogeneities. These effects can significantly reduce the classicial instability growth rates and lead to stabilization of short-wavelength modes.

### *9.1. Isobaric flow model*

The stability analysis of inhomogeneous static states is now extended to inhomogeneous steady states. Such flows arise typically as a result of mass ablation if the surface of an accelerated body is heated up to temperatures that allow the formation of a plasma state. A typical ablation profile is represented in fig. 31. The slab is heated by an incoming heat flow from the left-hand side up to the ablation front $y_1$. The front advances inside the slab with a constant velocity $v_1$. In the reference frame moving with the ablation front, steady-state flow is established. The slab of thickness $d$ is accelerated by the ablation pressure $p_a \approx \rho_1 ad$.

For most applications, the ablation front can be regarded as a subsonic, approximately isobaric flow region. Within this region the instability evolution may be well described by an isobaric flow model. A detailed discussion of the isobaric approximation and the resulting stability analysis has been given in refs. [76, 77]. These works include also detailed comparisons with a number of previous treatments of laser ablation. In the following, we will only describe the main physical features of the model, omitting the derivations given in the original work.

#### *9.1.1. Steady ablation*

The general framework for the present description of an ablating plasma are the conventional one-component fluid equations,

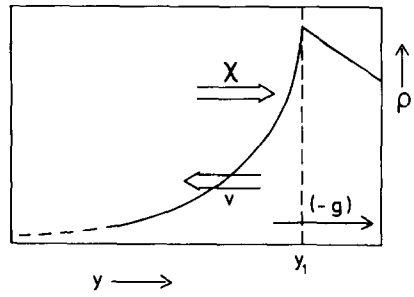


Fig. 31. Schematic representation of the ablation front. A steady-state density profile $\rho(y)$ is established by an incoming heat flow ($\chi$) and an ablated mass flow ($v$). The acceleration ($a = -g$) of the slab is RT unstable. (From ref. [77].)

$$\partial_t \rho + \boldsymbol{\nabla}\cdot \rho \boldsymbol{v} = 0\,, \tag{9.1a}$$

$$\rho(\partial_t \boldsymbol{v} + \boldsymbol{v}\cdot\boldsymbol{\nabla})\boldsymbol{v} = -\boldsymbol{\nabla} p - \rho \boldsymbol{a}\,, \tag{9.1b}$$

$$\partial_t[\rho(\varepsilon + \tfrac{1}{2}v^2)] + \boldsymbol{\nabla}\cdot[(w + \tfrac{1}{2}\boldsymbol{v}^2)\rho\boldsymbol{v} + \boldsymbol{q}] + \rho\, \boldsymbol{a}\cdot\boldsymbol{v} = 0\,, \tag{9.1c}$$

for the density $\rho$, velocity $\boldsymbol{v}$, pressure $p$, temperature $T$, specific internal energy $\varepsilon = c_V T$, specific enthalpy $w = c_p T = \varepsilon + p/\rho$, and the heat flow $\boldsymbol{q}$. The plasma is subject to a constant acceleration $\boldsymbol{a} = (0, a, 0)$. The thermodynamic relations are those of an ideal gas with adiabatic index $\gamma = 5/3$,

$$p = \rho T/m\,, \quad mc_V = 1/(\gamma - 1)\,, \quad mc_p = \gamma/(\gamma - 1)\,, \tag{9.1d}$$

where $m = m_p A/(1 + Z)$, and $m_p$ denotes the proton mass, $A$ the atomic number, and $Z$ the charge state of the ion species. Under the conditions of local thermodynamic equilibrium, the heat flow has the form $\boldsymbol{q} = -\kappa\, \boldsymbol{\nabla} T$ with thermal conductivity $\kappa$. Specifically, for electronic heat conduction the thermal diffusivity $\chi = \kappa/\rho c_p$ is given by the expression [150],

$$\chi = 1.0 \times 10^{-3} \gamma_0 \frac{\gamma - 1}{\gamma} \frac{A}{Z(1+Z)} \frac{T_{\mathrm{eV}}^{5/2}}{\Lambda \rho} \quad \mathrm{cm}^2/\mathrm{s}\,, \tag{9.1e}$$

where $\Lambda$ denotes the Coulomb logarithm, $\gamma_0$ a $Z$-dependent numerical constant and the temperature is taken in electronvolt. For instance, $\gamma_0 = 8$ for a fully ionized carbon foil with $Z = 6$ and $\Lambda \approx 5$ for typical ablation fronts.

The one-dimensional steady-state equations can be written in the dimensionless form,

$$\frac{\tilde{v}^2 - \tilde{T}}{\tilde{v}} \frac{\mathrm{d}}{\mathrm{d}\tilde{y}} \tilde{v} + \frac{\mathrm{d}}{\mathrm{d}\tilde{y}} \tilde{T} + 1 = 0\,, \tag{9.2a}$$

$$\mu \tilde{T}^{5/2} \frac{\mathrm{d}}{\mathrm{d}\tilde{y}} \tilde{T} + \tilde{T} + \frac{\gamma - 1}{\gamma} (\tfrac{1}{2}\tilde{v}^2 + \tilde{y}) = C\,, \tag{9.2b}$$

where $\tilde{T} = T/T_s$, $\tilde{v} = -v_y/v_s$, $\tilde{y} = ya/v_s^2$, $\mu = \chi_s a/v_s^3$ and $C$ denotes an integration constant. The subscript s refers to the isothermal sonic point ($v_s^2 = T_s/m$), which is a singular point of the steady-state system. We will choose the origin $\tilde{y} = 0$ at the ablation front, where the maximum density is obtained. The requirement of a continuous subsonic–transonic solution leads to the constraint

$$\mu = 1 + [(\gamma - 1)/\gamma](\tfrac{1}{2} + \tilde{y}_s) - C \tag{9.3}$$

between the parameters $C$ and $\mu$. As a result, these solutions form a one-parameter family, distinguished, for instance, by different ablation front densities $\tilde{\rho}_1$. For all cases of potential interest, the parameter $\mu$ is $\approx 1$, the distance to the sonic point varies between $|y_s| = 0.4$ and 0.5, and $C$ is approximately equal to the ablation front temperature $\tilde{T}_1 \ll 1$.

A typical result corresponding to an ablation front density of $\tilde{\rho}_1 = 50$ is shown in fig. 32. One can recognize in fig. 32a the variation of the density, the pressure, the temperature, and the Mach number $M = v/\sqrt{T/m}$ across the entire ablation region. For typical failure modes, the width of the instability

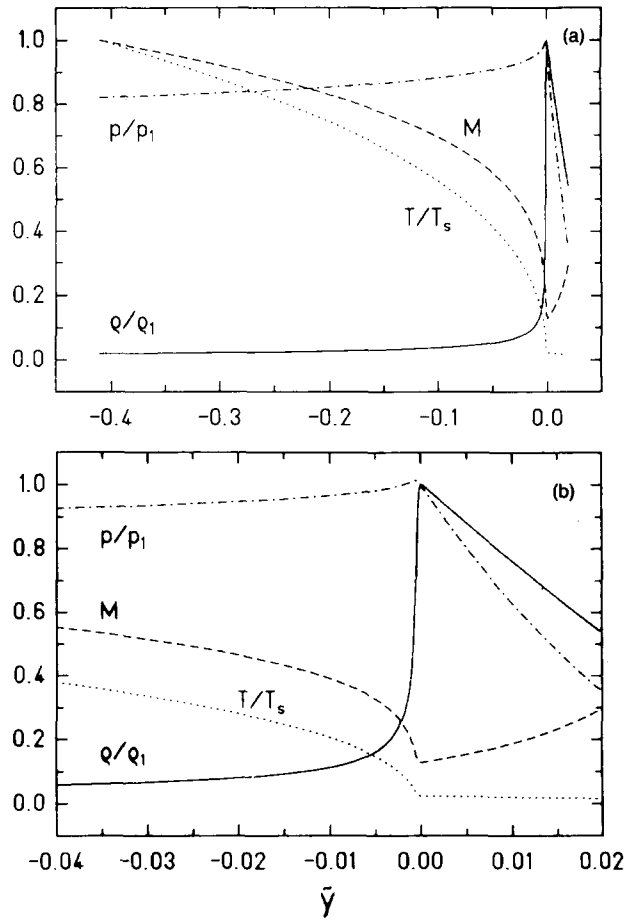


Fig. 32. One-dimensional solution of the steady ablation model (9.2) with the ablation front density $\rho_1 = 50\rho_s$. The index s refers to the isothermal sonic point ($M = 1$) and the index 1 to the ablation front (maximum density). The profiles of the pressure $p$, the Mach number $M$, the temperature $T$, and the density $\rho$ are represented versus the coordinate $\tilde{y} = yam/T_s$. (a) Flow region up to the sonic point, (b) subsonic flow region near the ablation front. (From ref. [77].)

zone is comparable with the slab thickness. A corresponding section of the ablation front is shown in fig. 32b. Here, the flow is well subsonic and the pressure varies only weakly in comparison with the density.

### *9.1.2. Isobaric approximation*

Prior to performing the stability analysis, it is advantageous to introduce a reduced isobaric fluid description. The main purpose is to avoid the compressibility effects that are known to be negligible in the classical free-surface RT instability. In addition, the restriction to subsonic fronts offers the opportunity to study actually a much wider class of steady flow solutions. In the subsonic flow domain, the sonic-point constraint (9.3) is unimportant, which extends the parameter space of allowable ablation fronts to arbitrary values of $\mu$.

The isobaric approximation consists in the neglect of all pressure variations in the energy equation (9.1c). On the other hand, the pressure gradient is retained in the momentum equation (9.1b). This

procedure is admissible, since the leading terms in the energy equation are due to density variations, while all terms of the momentum equation are of the same smallness. The isobaric approximation to the energy equation can be written in various equivalent forms. Some instructive representations are given by

$$\nabla\cdot(\rho w\boldsymbol{v} - \kappa\nabla T) = 0\,, \tag{9.4a}$$

$$\nabla\cdot(\boldsymbol{v} + \chi\nabla\rho/\rho) = 0\,, \tag{9.4b}$$

$$(1/\rho)\,\mathrm{d}\rho/\mathrm{d}t = \nabla\cdot(\chi\nabla\rho/\rho)\,, \tag{9.4c}$$

$$c_p\rho\,\mathrm{d}T/\mathrm{d}t = \nabla\cdot(\kappa\nabla T)\,. \tag{9.4d}$$

The first expression follows immediately from eqs. (9.1b) and (9.1c), if pressure variations are negligible. Accordingly, the sum of heat and enthalpy flow forms a conserved energy current in this model. The second expression can be obtained by dividing by the approximate constant $\rho w = mc_p p$ and noting that $\mathrm{d}\rho/\rho + \mathrm{d}T/T = \mathrm{d}p/p \approx 0$. It shows that the isobaric flow is no longer divergence-free because of the thermal expansion of the fluid. Combining this relation with the continuity equation (9.1a), there follows the diffusion equation (9.4c) for the density. The thermal diffusion is coupled to the fluid motion by the total derivative (6.1c) along the particle trajectories. Substituting the density by the temperature, there follows the heat diffusion equation (9.4d).

Well-known special cases, included in the isobaric model, are the classical incompressible fluid model ($\chi = 0$) and the Boussinesq model ($T \approx$ const.) of thermal convection [57],

$$\nabla\cdot\boldsymbol{v} = 0\,,\quad \mathrm{d}\rho/\mathrm{d}t = 0\,, \tag{9.5a}$$

$$\nabla\cdot\boldsymbol{v} = 0\,,\quad c_p\rho\,\mathrm{d}T/\mathrm{d}t = \kappa\,\Delta T\,, \tag{9.5b}$$

respectively. However, in general neither of these special cases is applicable to the ablation layer instability.

### *9.1.3. Isobaric steady-state*

The isobaric steady-flow equations can be obtained from eqs. (9.1) and (9.4) in the form

$$\rho v_y = \rho_1 v_{y1}\,,\quad \rho T = \rho_1 T_1\,,\quad \kappa\,\mathrm{d}T/\mathrm{d}y = c_p\rho_1 v_{y1}(T - T_1)\,. \tag{9.6}$$

The index 1 refers again to the maximum of the density profile, which now will be assumed at $y \to \infty$. We set $v_y = -v$ for the flow velocity and $\kappa = \text{const.} \times T^{\nu}$, for the thermal conductivity at constant pressure. Defining the length unit $L_1 = \chi_1/v_1$ and using dimensionless variables of the form $\bar{X} = X/X_1$ and $\xi = y/L_1$, the steady-state equations become,

$$\bar{v} = \bar{T} = \bar{\rho}^{-1}\,,\quad \mathrm{d}\bar{\rho}/\mathrm{d}\xi = \bar{\rho}^{\nu+1}(1 - \bar{\rho})\,. \tag{9.7}$$

Density profiles obtained from eq. (9.7) with the initial condition $\bar{\rho}(0) = 0.99$ are presented in fig. 33 for various values of $\nu$. The electronic conduction law (9.1e) corresponds to $\nu = 2.5$. The densities increase

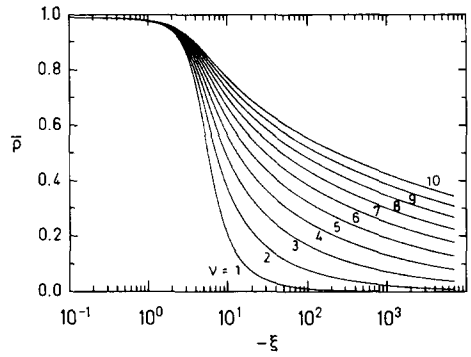


Fig. 33. Steady ablation profiles of the density $\bar{\rho} = \rho/\rho_1$ versus the coordinate $\xi = yv_1/\chi_1$ in the isobaric approximation (9.7). The parameter $\nu$ describes the temperature exponent of the thermal conductivity at constant pressure; $\nu = 2.5$ for classical electronic conduction. (From ref. [77].)

monotonically toward the cold slab, approaching there the asymptotic value $\bar{\rho} = 1$. The instability of these profiles against acceleration will be localized around the maximum density gradient. If the gradient scale length is defined as $L = \bar{\rho}/(\mathrm{d}\bar{\rho}/\mathrm{d}y)$, its minimum is given by

$$L = [(1+\nu)^{1+\nu}/\nu^{\nu}]L_1\,, \quad \bar{\rho} = \nu/(1+\nu)\,. \tag{9.8}$$

Especially, $L \approx 8.12L_1$ and $\bar{\rho} \approx 0.71$ for $\nu = 2.5$. One can readily convince oneself that these values are in close agreement with the exact ablation profiles. Using the length units of eq. (9.2) and the parameters of fig. 32, one finds $\tilde{L} = 8.12L_1 a/v_s^2 = 8.12\mu\tilde{T}^{\nu} \approx 7 \times 10^{-4}$.

*9.1.4. Homogeneous flow perturbations*

In the boundary regions $\xi \to \pm\infty$, the steady flow variables vary only weakly in comparison with the eigenmodes of the stability analysis. We therefore firstly describe the basic types of isobaric flow perturbations inside a homogeneous medium with constant density $\rho$, velocity $v_y = -v$, and thermal diffusivity $\chi$.

Perturbations of a variable $X$ are denoted as $\delta X$ and they are taken proportional to $\exp(nt + qy + \mathrm{i}kx)$. The isobaric flow equations admit five independent perturbation solutions, which differ in their longitudinal wavenumbers $q$. The linearized form of eq. (9.4c) becomes

$$[(n - vq) - \chi(q^2 - k^2)]\,\delta\rho = 0\,. \tag{9.9}$$

It governs the variation of density perturbations, $\delta\rho \neq 0$, with the possible roots

$$q_{1,2} = -v/2\chi \pm [(v/2\chi)^2 + k^2 + n/\chi]^{1/2}\,. \tag{9.10}$$

In the absence of flow, $v \to 0$, the perturbations are smoothed by thermal diffusion. The approximate decay constants,

$$q_{1,2} = \pm(k^2 + n/\chi)^{1/2}\,, \tag{9.11}$$

have the same magnitude in both directions and are usually of the order of $k$. Conversely, assuming the

limit $\chi \to 0$, one finds from eq. (9.10) the expressions

$$q_1 = n/v\,, \quad q_2 = -v/\chi\,. \tag{9.12}$$

The first solution arises from the corresponding density transport equation $(\mathrm{d}/\mathrm{d}t)\,\delta\rho = 0$. It describes familiar entropy convection modes in the isobaric approximation. Typically, the mode number $q_1$ is also of the order of $k$. The second root may be called an ablation mode, describing thermal diffusion toward $y \to \infty$ against the counterstreaming flow. Its presence leads to a sharp decrease of density perturbations inside the cold slab. One should notice that the ablation mode varies basically over the minimum steady-state gradient scale length, $q_2 L \sim 1$, and is therefore typically much larger than the transverse perturbation wavenumber $k$. This discrepancy in length scales presents one of the major difficulties of the instability analysis. It puts severe limitations on the validity of discontinuity models and imposes high demands on the computational resolution of the ablation layer.

Apart from the density perturbations described by eq. (9.9), there can exist additional solutions with $\delta\rho = 0$. For constant density, we obtain from eqs. (9.1a) and (9.1b) the two relations

$$\boldsymbol{\nabla}\cdot\delta\boldsymbol{v} = 0\,, \quad (n - vq)\,\boldsymbol{\nabla}\times\delta\boldsymbol{v} = 0 \tag{9.13}$$

for the velocity perturbations $\delta\boldsymbol{v}$. They describe a vorticity convection mode,

$$q_3 = n/v\,, \tag{9.14}$$

and the familiar surface modes,

$$q_{4,5} = \pm k\,, \tag{9.15}$$

of potential flow theory. In summary, the isobaric flow model supports five distinct perturbations, two associated with the density, one with the vorticity, and two with potential flow. All these perturbations become linearly coupled across the inhomogeneous ablation region. The problem is to determine the eigenmodes that are evanescent on both sides of the ablation front.

*9.1.5. Stability boundary-value problem*

We will only briefly indicate how the eigenmodes and the corresponding growth rates can be calculated. A rather complete discussion can be found in refs. [76, 77]. The isobaric fluid equations (9.1a), (9.1b), and (9.4b) have been linearized about the steady state (9.7). This leads to a linear vector system,

$$\mathrm{d}\boldsymbol{Y}/\mathrm{d}\xi = \boldsymbol{M}\cdot\boldsymbol{Y}\,, \tag{9.16}$$

with the definitions

$$\boldsymbol{Y} = \begin{pmatrix} \bar{\rho}\,\delta\bar{v}_y - \delta\bar{\rho}/\bar{\rho} \\ \mathrm{i}\,\delta\bar{v}_x \\ \delta\bar{\rho}/\bar{\rho}^2 - 2\,\delta\bar{v}_y + \delta\bar{p} \\ \delta\bar{\rho}/\bar{\rho}^{\nu+2} \\ \delta\bar{v}_y + (\mathrm{d}/\mathrm{d}\xi)(\delta\bar{\rho}/\bar{\rho}^{\nu+2}) \end{pmatrix},$$

$$\boldsymbol{M} = \begin{pmatrix} 0 & -\kappa\bar{\rho} & 0 & -\sigma\bar{\rho}^{\nu+2} & 0 \\ -2\kappa/\bar{\rho} & \sigma\bar{\rho} & -\kappa & -\kappa\bar{\rho}^{\nu} & 0 \\ -\sigma & \kappa & 0 & -\Gamma\bar{\rho}^{\nu+2} & 0 \\ -1/\bar{\rho} & 0 & 0 & -\bar{\rho}^{\nu} & 1 \\ 0 & -\kappa & 0 & \kappa^2 & 0 \end{pmatrix}, \tag{9.17}$$

$$\delta\bar{\rho} = \delta\rho/\rho_1 , \quad \delta\bar{v}_{x,y} = \delta v_{x,y}/v_1 , \quad \delta\bar{p} = \delta p/(\rho_1 v_1^2) ,$$

$$\sigma = n\,\chi_1/v_1^2 , \quad \kappa = k\,\chi_1/v_1 , \quad \Gamma = a\,\chi_1/v_1^3 .$$

One should notice that the components $Y_i$ of the solution vector $\boldsymbol{Y}$ represent the perturbed fluxes of the system. These variables are advantageous, since they are only slowly varying even if the density profile becomes discontinuous. Actually, the matrix $\boldsymbol{M}$ contains no gradient terms, which would diverge in the steep-profile limit. It can also be recognized that the general instability dispersion relation will be of the form

$$\sigma = \sigma(\kappa, \Gamma, \nu) . \tag{9.18}$$

The dimensionless growth rate $\sigma$ depends on the dimensionless wavenumber $\kappa$ and the parameters $\Gamma$ and $\nu$. These dependences will be addressed in the subsequent discussion.

We consider localized solutions of eq. (9.16), becoming evanescent at infinity $\xi \to \pm\infty$. These boundary conditions can be imposed by use of the perturbation solutions discussed in section 9.1.4. Asymptotically for $\xi \to +\infty$, the eigenmodes can be represented as a superposition of an ablation mode ($q_2$) and a surface mode ($q_5$). Asymptotically for $\xi \to -\infty$, a representation by an entropy convection mode ($q_1$), a vorticity convection mode ($q_3$), and a surface mode ($q_4$) can be chosen. The eigenvalues $\sigma$ are determined by the requirement that the eigenmodes approach these asymptotes.

### *9.2. Stability results*

The ablative modifications of the classical RT instability will first be illustrated by analytic solutions for a flow discontinuity. Subsequently, self-consistent results from the numerical stability analysis of steady ablation profiles are presented. This section concludes with a brief discussion of the literature on ablative stabilization and growth reduction.

#### *9.2.1. Discontinuity model*

We first discuss a simple mathematical model of the ablation front, replacing the steady-state profile in eq. (9.16) by a flow discontinuity. A detailed analysis of this model has been described in ref. [76]. In certain limiting cases, simple analytic results can be derived. They describe physically instructive examples of the ablative stabilization of RT instabilities. Furthermore, these special solutions are extremely helpful in testing the general numerical eigenvalue analysis. One should notice, that the present results are rigorous weak solutions of the perturbation system (9.16). Of course, they do not necessarily describe the stability behavior of the original steady ablation flow. Nevertheless, it may be expected that the solutions for step-profiles and for self-consistent steady-flow profiles are at least qualitatively similar. This conclusion will be basically confirmed by our numerical analysis.

The discontinuity model assumes constant flow variables $\rho_1, v_1, \chi_1$ in the half-space $\xi > 0$ and

$\rho_2, v_2, \chi_2$ in the half-space $\xi < 0$. These are related across the discontinuity $\xi = 0$ by the continuity requirements (9.6) for pressure and mass flow. The only profile parameter is therefore the density ratio $R = \rho_1/\rho_2$.

The perturbation solutions in both half-spaces can be matched by the continuity condition,

$$[Y] = 0\,, \tag{9.19}$$

for the flux vector (9.17). This condition applies for any transition profile, centered around $\xi = 0$, provided its width $\Delta$ is only a small fraction of the penetration depth $q^{-1}$ of the perturbations. Because of the presence of the steep ablation mode $q_2 \approx -v_1/\chi_1 = -1/L_1$ inside the cold slab region, the discontinuity approximation assumes the rather restrictive form $\Delta \ll L_1$.

Instability dispersion relations, derived from this model, can be recognized in fig. 34. They show the variation of the growth rate $N = n/k_1 v_1$ as a function of the wavenumber $K = k/k_1$, where $k_1 = \alpha a/v_1^2$ and $\alpha$ denotes the Atwood number as defined in eq. (3.2). The different curves correspond to different profile-steps $R$ and different parameters $S = \alpha\Gamma$, while $\nu = 2.5$ is kept fixed. In all cases, the instability

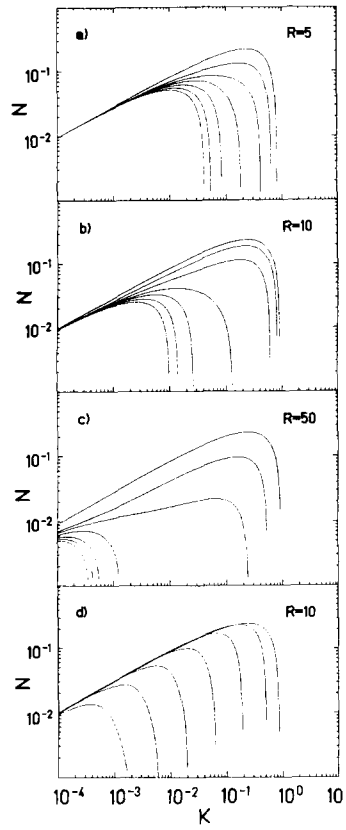


Fig. 34. Instability growth rate $N = n/k_1 v_1$ versus wavenumber $K = k/k_1$ for a flow discontinuity with density ratio $R = \rho_1/\rho_2$. The wavenumber $k_1 = \alpha a/v_1^2$ represents the largest cutoff in this model. The different curves correspond to different values of the instability parameter $S = \alpha\Gamma$. They increase with $S$ in the convection regime $S \lesssim 1$, and decrease in the diffusion regime $S \gg 1$. (a) $S = 10^{-3}$, $5\times10^{-3}$, 0.01, 0.015, 0.02, 0.03, 0.1; (b) $S = 10^{-4}$, $10^{-3}$, $2\times10^{-3}$, $3\times10^{-3}$, $5\times10^{-3}$, 0.01, 0.05; (c) $10^{-6}$, $10^{-5}$, $2\times10^{-5}$, $4\times10^{-5}$, $6\times10^{-5}$, $8\times10^{-5}$, $5\times10^{-4}$; (d) $S = 0.1$, 1, 10, 100, 1000, $10^4$, $10^5$. (From ref. [76].)

growth rates reach a maximum and stabilization is found for sufficiently large $K$ values. The following limiting cases have been evaluated analytically.

(i) If $k\chi_2/v_2 \ll 1$, the thermal diffusion rate is negligible in comparison with the flow convection rate. This limit leads to the simple dispersion relation

$$n = -kv_2 + \sqrt{\alpha a k}\,, \tag{9.20}$$

which describes the lower asymptotes ($S \to 0$) in figs. 34a–34c. Here, the RT instability is stabilized by the downstream flow $v_2$. The growth rate (9.20) becomes zero at the cutoff wavenumber

$$k_2 = \alpha a / v_2^2\,. \tag{9.21}$$

The corresponding cutoff $K_2 = k_2/k_1 = R^{-2}$ can be clearly recognized in fig. 34.

(ii) If $k\chi_2/v_2 \gg 1$ and $k\chi_1/v_1 \ll 1$, the discontinuity model describes thermal diffusion in the hot ablation region, but still flow convection in the cold slab region. Taking this limit, the dispersion relation can be written as

$$n = -kv_1 + \sqrt{\alpha a k}\,. \tag{9.22}$$

It has the same form as eq. (9.20), however, stabilization is now due to the upstream flow $v_1$. This gives rise to the larger cutoff $k = k_1$ or equivalently $K_1 = 1$. Actually, all the cutoff values in figs. 34a–34c are seen to fall in the interval between the lower boundary $K_2$ and the upper boundary $K_1$.

(iii) If $k\chi_1/v_1 \gg 1$, thermal diffusion is dominant on both sides of the ablation front. Without further approximations, the dispersion relation of this special case is still a complicated expression. However, assuming $\alpha \gg 1$ the corresponding cutoff can be expressed in the simple form

$$k_3 = \sqrt{3a/8v_1\chi_1} = \sqrt{\tfrac{3}{8}}\,\frac{\sqrt{a/L_1}}{v_1}\,, \quad K_3 = \sqrt{3/8\Gamma}\,. \tag{9.23}$$

It describes the decreasing sequence of growth rate curves in fig. 34d.

One should notice that the discontinuity model describes an increase of the stability boundary with $\Gamma$ in the convection regime $\Gamma \ll 1$, a maximum around $\Gamma \sim 1$, and a decrease in the diffusive regime $\Gamma \gg 1$. This stability behavior will be essentially confirmed by the numerical calculations for self-consistent ablation profiles.

*9.2.2. Self-consistent ablation model*

Next, the stability of the self-consistent isobaric steady state (9.7) is discussed, based on the results of ref. [77]. We consider the dependence of the growth rate curves (9.18) on the parameter $\Gamma$ for classical conduction, $\nu = 2.5$. Corresponding results are presented in fig. 35. The growth rate curves in fig. 35a are similar to those of the discontinuity model in fig. 34. The growth is approximately classical at small wavenumbers and approaches the ablative cutoff at large wavenumbers. The monotonic increase with the parameter $\Gamma$ in fig. 35 is due to the different normalizations of the wavenumbers.

The major result of this treatment is the stability boundary $K = K(\Gamma)$ of the cutoff wavenumbers $K = kv_1^2/a$ as a function of $\Gamma$. It can be recognized in fig. 35b as obtained from the present calculations (solid curve) and from the discontinuity model of the ablation front (dotted curve). In the latter case a

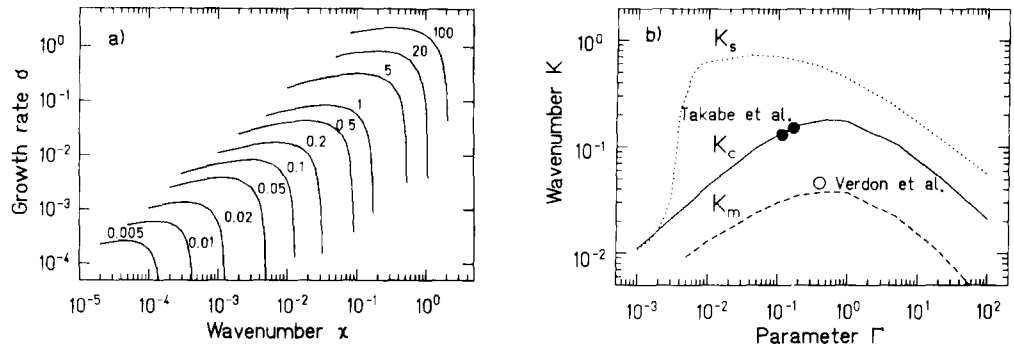


Fig. 35. Stability results from the isobaric ablation model with self-consistent steady-flow profiles. (a) Instability dispersion relations $\sigma = \sigma(\kappa)$ for $\nu = 2.5$ with $\Gamma$ varying between 0.005 and 100. (b) Instability boundary $K_c$ and wavenumber of maximum growth $K_m$. Comparison is made with the sharp-boundary result $K_s$ for $R = 10$, the cutoff predictions from ref. [151], and the maximum growth rate from ref. [18]. (From ref. [77].)

step-ratio of $R = 10$ has been chosen. The wavenumber region $K > K(\Gamma)$ is stabilized by ablation. We have also indicated the wavenumbers $K_m(\Gamma)$ of maximum growth (dashed curve). For $K < K_m$, the growth is approximately classical. Comparison is also made with a previous stability analysis of steady ablation flows by Takabe et al. [151] and with a fluid simulation of laser ablation by Verdon et al. [18]. One can recognize rather close agreement of these data with the present isobaric instability description. However, this consistency of results is only obtained when the proper ablation profile is used. The step-profile predictions are qualitatively similar, but they can be quantitatively inaccurate.

To illustrate potential applications of these results, one has to relate the wavenumbers to the thickness $d = p_1/\rho_1 a$ of the accelerated foil, yielding $K = M_1^2 kd$. Stabilization of the critical failure modes $kd \sim 1$ is limited by the Mach numbers at the ablation surface, leading to the restrictive constraint $K < M_1^2$ for the instability cutoff. For a specific example one may assume the typical values $kd \approx 2$–$3$, $M_1 \approx 0.1$, $K \approx 0.02$–$0.03$. Ablative stabilization will be most efficient if these $K$ values lie above the maximum growth rate $K_m$ in fig. 35b. In principle, this is possible for both small and large $\Gamma$ values, although the predictions for small $\Gamma$ may depend on extremely steep gradients. Radiatively driven ICF shells will possibly allow large inhomogeneity scale lengths of the order of $L/d = M_1^2 \Gamma \approx 0.5$. Choosing again $M_1 \approx 0.1$, there follows the estimate $\Gamma = 50$ for the instability parameter. In this parameter regime, the critical failure modes $K \approx 0.02$–$0.03$ could be close to the ablative cutoff. Of course, this simple model calculation requires confirmation by more complete fluid simulations and by experiments.

### *9.2.3. Bibliographical notes*

The stability of accelerated ablation fronts plays an important role in various applications. Although we are mainly concerned with ablation in the ICF context, it may be of general interest that similar phenomena in the interstellar medium, in star envelopes, and on the surface of meteorites and re-entry bodies in the earth's atmosphere have been discussed. There is also a close relationship in the physics of ablation layers, flame fronts [152], and thermal convection cells [153].

The interest into ablative stabilization of RT instabilities goes back to the beginnings of laser fusion research and, since then, has been extensively studied by many groups for more than 15 years. Some major approaches to this problem have been concerned with (i) physical modeling, (ii) linear stability calculations, (iii) two-dimensional fluid simulations, and (iv) experiments. In the following, we attempt

to give an overview on some representative works in each of these categories. At present, such an overview is necessarily incomplete and the conclusions can only be preliminary.

(i) A number of ablative stabilization mechanisms have been proposed in the past. Although a clear distinction may not always be possible, the principle physical concepts seem to be based on one of the following effects: (1) reversed pressure gradients, (2) sonic flow, (3) thermal smoothing, (4) fire-polishing, (5) flow convection, (6) inhomogeneities. We will briefly discuss these points in turn and thereby refer to some of the original works.

(1) It has often been argued that ablative instability growth is small, being restricted to a narrow region of opposed pressure and density gradients. Typically, the maximum pressure is assumed somewhat in front of the maximum density and only inside the region between these maxima opposed pressure and density gradients exist. However, this argument is based on the stability criterion for a hydrostatic equilibrium and it is therefore not necessarily valid in the presence of flow. It seems much more reasonable to assume that the driving source of the instability is the release of effective gravitational energy under an interchange of the steady-flow density. According to this criterion, instability would result if the acceleration is directed along the density gradient irrespective of the direction of the pressure gradient. Looking, for instance, at the pressure and density profiles in fig. 32, it seems not very likely that the observed instability growth for long-wavelength modes can be caused by the extremely narrow intermediate layer of opposed pressure and density gradients.

(2) Potential stabilization of RT instabilities by ablation was already recognized in an early programatic paper on laser fusion by Nuckolls et al. [154]. In the absence of detailed calculations, a dispersion relation of the general form

$$\omega^2 = s^2k^2 - ak\,, \quad s = \sqrt{p/\rho}\,, \tag{9.24}$$

was postulated. It describes sonic modifications of the incompressible instability growth rate and predicts stabilization for all wavenumbers $kd \gtrsim 1$, where $d = p/\rho a$ denotes the shell thickness. For most present designs, this criterion appears to be too optimistic. It is also doubtful whether RT modes can effectively couple their energy into sound waves. In the absence of flow, compressibility effects can be shown to vanish for the most important case of free-surface modes. However, there may be applications of eq. (9.24) in the case of supersonic ablation. For instance, it is known that KH instabilities can be stabilized by supersonic flow.

(3) Transverse temperature perturbations decay by thermal diffusion at a rate of the order of $\chi k^2$. Physically, the transverse heat flow is directed from the areas of increased temperature to the areas of decreased temperature. Thermal smoothing by transverse conduction is considered highly efficient in producing the required illumination uniformity on the pellet surface, especially for radiatively driven shells. On the other hand, the effect on acceleration nonuniformities in the RT instability is less well understood. In the nonlinear stage of the RT instability, this effect may lead to partial ablation of the colder spikes. In the absence of flow, the linear conduction effect was analysed by Catto [155] and by Takabe and Mima [156]. It was found that the RT mode cannot be completely stabilized by this mechanism, although reduced growth rates of the order of

$$n \approx a\,\frac{\partial_y \ln(\rho/p^{1/\gamma})}{\chi k^2} \tag{9.25}$$

are obtained at sufficiently large wavenumbers. In the isobaric model discussed above, the diffusive

regime corresponds to large $\Gamma$ values. Stabilization results from the combined effects of diffusion and convection, as expressed by the cutoff (9.23).

(4) A related, although somewhat different idea, is the fire-polishing effect. While thermal smoothing is based on transverse heat flow, the fire-polishing effect assumes modifications of the longitudinal heat flow. The temperature gradients will be steepened at the tip of the spikes in comparison with the unperturbed steady-state gradient. Consequently, the spikes are expected to be subject to stronger ablation. This would result in higher ablation pressures and stronger acceleration. To our knowledge, the fire-polishing mechanism was not analysed in detail in the published literature. It is discussed qualitatively in the work by Bodner [21] and was apparently suggested in an early work by Leith. Fluid simulations of laser ablation indicate some saturation of spike growth, but it does not seem to modify the evolution of bubbles in a significant manner [18].

(5) If the typical ablation velocity $v$ is larger than the typical penetration velocity $\sqrt{a/k}$ of RT modes, the instability can be stabilized by flow convection. The requirement $v = \sqrt{a/k}$ leads to the typical cutoff wavenumber $k = a/v^2$. It seems well consistent with most present stability results, if the velocity $v$ is chosen to be $v \approx 3v_1$, where $v_1$ denotes the velocity at the ablation front. The convective stabilization mechanism was first discussed by Bodner [21], based on a discontinuity model of the ablation surface. Similar treatments have been discussed later by various authors [157–159]. An overview on the different modeling assumptions in these works has been given by Manheimer and Colombant [159]. While Bodner's model describes convective stabilization with the upstream velocity $v = v_1$, the isobaric discontinuity model, described in section 9.2.1, can also account for larger velocities up to the maximum ablation velocity $v = v_2$.

(6) The effect of density inhomogeneities can be described by the classical instability theory as discussed in section 6. To stabilize the typical failure modes ($kd \sim 1$) by density gradient effects, large inhomogeneity scale lengths of the order of $L \sim d$ are required. This could be promising for future indirect-drive pellet designs with large inhomogeneity scale lengths. To stabilize the growth of long-wavelength nonuniformities ($kd \gg 1$), a low but finite density corona surrounding the pellet could be advantageous to make use of the thin-shell effects described by the three-layer model in section 3.5. Instability growth rates for typical shell structures have been calculated by Mikaelian [68] and by Colombant and Manheimer [160]. The maximum possible reduction effects in inhomogeneous media have been examined by Munro [130].

(ii) Although the simplifying descriptions of the ablative RT instability have greatly improved the physical understanding, it also became apparent that only self-consistent stability treatments of representative ablation flows could lead to definite answers.

Some of the first computational perturbation results have been reported in the year 1974. A linear stability analysis of a laser-driven spherical implosion by Shiau et al. [161] showed significant growth for small mode numbers ($l \approx 1$–$10$), while growth reduction could be observed for higher mode numbers ($l \approx 100$). No attempt was made to correlate the observed amplification with RT growth rates, but it appears much too large to be explained by classical growth increments. The stability of another design has been studied by Henderson et al. [162], where no appreciable amplification could be found for low $l$ modes. In a third analysis, the steady-state ablation model was introduced as the basis of the stability analysis by Brueckner et al. [163]. In a first attempt, stability was found over a wide range of wavenumbers, but later these calculations have been found in error. Some corrected results showed RT growth but with significantly reduced growth rates.

The stability of the steady ablation model was analysed more completely by Takabe et al. [151]. In this work, the relationship between classical and ablative growth rates may have first been demon-

strated in a convincing manner. At small wavenumbers, the classical RT instability was recovered but at large wavenumbers an ablative cutoff was obtained. The maximum growth rate was found to be about one-half of the classical free-surface growth rate. The isobaric ablation model, discussed in section 9.2.2, is an extension of this work to the larger class of ablation fronts distinguished by the parameter $\Gamma$. Thereby a number of previous results could be explained and represented more systematically.

(iii) Most of the controversial conclusions in the early perturbation treatments could be clarified by Lindl and Mead [20]. Their work describes the first complete fluid simulation of two-dimensional instabilities in laser-fusion pellets. It discusses the conflicting requirements between pellet stability and high gain. The basic stability limitations imposed by the most critical failure modes on the shell aspect ratio and the pulse shape have been described. No evidence could be found for ablative stabilization in typical low-adiabat implosions. The stability of the implosion studied before by Henderson et al. [162] was attributed to a different pulse shape, leading to shock acceleration rather than optimized isentropic acceleration.

A number of simulation studies of laser ablation has since confirmed the importance of RT-type instabilities during the acceleration phase. In three independent calculations by McCrory et al. [18], Emery et al. [22], and Evans et al. [23] ablatively reduced growth rates by a factor of $\approx 2$ have been consistently reported. These results appear also in reasonable agreement with the eigenvalue analysis of the steady ablation model. Some more strongly inhibited growth rates have been reported for shorter laser wavelengths (0.25 μm) but these findings could not be confirmed in later investigations [164]. More recent calculations by Tabak et al. [165] and Mikaelian [166] have given additional confirmation for reduced ablative growth rates. Over a wide range of parameters, the calculated growth rates could be fitted to eq. (9.20) with the values $v_2 = 3v_1$ and $\sqrt{\alpha} = 0.9$. Furthermore, it was demonstrated that the ablation velocity $v_1$ can be varied to some extent by controlled radiation preheat. At higher preheat levels ablation becomes stronger which correlates well with larger growth reduction effects. The comparison with the steady-flow results should nevertheless be taken with caution. Steady flow conditions have not been established convincingly in these calculations and the decisive steady flow parameters can often not be determined unambiguously with the desired precision. We also mention a computational study by Atzeni et al. [167], which shows interesting results on bubble evolution in a nonuniformly driven compressible sphere.

(iv) In the past years, some experiments with laser-driven foils have confirmed the growth of RT modes under various conditions. Although the diagnostic of the unstable evolution is difficult, much progress has been made with X-ray backlighting methods. In experiments by Grun et al. [28], 10–11 μm thick polystyrene foils have been ablatively driven at a relatively low irradiance of $(2\text{–}6) \times 10^{12}$ W/cm$^2$ with 1.053 μm laser light. The initial perturbation was imposed as a square wave profile at the rear side of the foil with periods of 50, 100, and 150 μm. The longer-wavelength modes grew at their predicted rates. No growth was observed at 50 μm. This unexpected feature has been partly attributed to incoherent illumination (ISI) but its significance for ICF is still under investigation [166].

Similar experiments at higher irradiances have been performed by Desselberger et al. [33]. A 16 μm thick plastic foil was irradiated with 0.53 μm laser light at an intensity of $1.5 \times 10^{14}$ W/cm$^2$. The growth rates of sinusoidal perturbations with periods of 30, 50, 70, and 100 μm have been measured. RT growth was clearly exhibited in all cases, including the 50 μm perturbation. However, the growth rates have been found surprisingly small, being only a fraction between 0.2 and 0.6 of the free-surface value. No explanation of this strong growth inhibition could be given by the present computational modeling of the experiment.

Another experiment was performed with the Nova laser system by Kilkenny et al. [32]. Using 15 kJ

of 0.35 μm light, foils have been accelerated indirectly by pressures exceeding 1 Mbar. The spatial resolution was high enough to exhibit some nonlinear features for 50 and 100 μm perturbations. Bubble–spike asymmetry and second harmonic growth was observed. The growth rates could not be related to simple scaling laws but they have been found in excellent agreement with computer simulations including the effects of inhomogeneities and ablation.

At present there seems to be general agreement between theory, computations, and experiments on a significant reduction of the classical RT growth rate in ablatively accelerated targets. To make further use of the advantages of gradient and flow stabilization, indirect-drive designs with large density gradient scale lengths and with a tolerable amount of radiation preheat seem promising for achieving the goal of high gain in future ICF compression experiments [168].

## Acknowledgements

I am grateful to P. Mulser who has suggested to me the subject of Rayleigh–Taylor instability and who has constantly supported this research in his group for Quantum Electronics at the Technische Hochschule, Darmstadt. I wish to acknowledge fruitful discussions with many colleagues, especially H.L. Berk, S.I. Anisimov, S.E. Bodner, C.E. Leith, and K.O. Mikaelian on different aspects of the theory. Finally, I wish to thank S. Grossmann for helpful suggestions for improvements of the manuscript.

Parts of this work have been supported by the Bundesministerium für Forschung und Technologie and by the Deutsche Forschungsgemeinschaft.

## References

[1] G. Taylor, Proc. R. Soc. A 201 (1950) 192.
[2] D.J. Lewis, Proc. R. Soc. A 202 (1950) 81.
[3] Lord Rayleigh, Proc. London Math. Soc. 14 (1883) 170.
[4] H.W. Emmons, C.T. Chang and B.C. Watson, Fluid Mech. 7 (1960) 177.
[5] R.L. Cole and R.S. Tankin, Phys. Fluids 16 (1973) 1810.
[6] J. Allred and G. Blount (1953), unpublished.
[7] M. Ratafia, Phys. Fluids 16 (1973) 1207.
[8] R.D. Richtmyer, Commun. Pure Appl. Math. 13 (1960) 297.
[9] E.E. Meshkov, Izv. Akad. Nauk SSSR Mekh. Zhidk. Gaza 5 (1969) 151.
[10] K.I. Read, Physica D 12 (1984) 45.
[11] S.N. Dikarev and A.G. Zatsepin, Oceanology 23 (1983) 711.
[12] V.A. Andronov, S.M. Bakhrakh, E.E. Meshkov, V.N. Moshkov, V.V. Nikiforov, A.V. Pevnitskii and A.I. Tolshmyakhov, Soviet Phys. JETP 44 (1976) 424.
[13] G.R. Baker and D.W. Moore, Phys. Fluids A 1 (1989) 1451.
[14] R.M. Davies and G. Taylor, Proc. R. Soc. A 200 (1950) 375.
[15] G.R. Baker, D.I. Meiron and S.A. Orszag, Phys. Fluids 23 (1980) 1485.
[16] C.L. Gardner, J. Glimm, O. McBryan, R. Menikoff, D.H. Sharp and Q. Zhang, Phys. Fluids 31 (1988) 447.
[17] B.J. Daly, Phys. Fluids 10 (1967) 297; 12 (1969) 1340.
[18] R.L. McCrory, L. Montierth, R.L. Morse and C.P. Verdon, Phys. Rev. Lett. 46 (1981) 336;
C.P. Verdon, R.L. McCrory, R.L. Morse, G.R. Baker, D.I. Meiron and S.A. Orszag, Phys. Fluids 25 (1982) 1653.
[19] E. Ott, Phys. Rev. Lett. 29 (1972) 1429.
[20] J.D. Lindl and W.C. Mead, Phys. Rev. Lett. 34 (1975) 1273.
[21] S.E. Bodner, Phys. Rev. Lett. 33 (1974) 761.
[22] M.H. Emery, J.H. Gardner and J.P. Boris, Phys. Rev. Lett. 48 (1982) 677.
[23] R.G. Evans, A.J. Bennet and G.J. Pert, Phys. Rev. Lett. 49 (1982) 1639.

[24] M.A. Sweeney and F.C. Perry, J. Appl. Phys. 52 (1981) 4487.
[25] R.R. Whitlock, M.H. Emery, J.A. Stamper, E.A. McLean, S.P. Obenschain and M.C. Peckerar, Phys. Rev. Lett. 52 (1984) 819.
[26] J. Grun and S. Kacenjar, Appl. Phys. Lett. 44 (1984) 497.
[27] J. Grun, M.H. Emery, S. Kacenjar, C.B. Opal, E.A. McLean, S.P. Obenschain, B.H. Ripin and A. Schmitt, Phys. Rev. Lett. 53 (1984) 1352.
[28] J. Grun, M.H. Emery, C.K. Manka, T.N. Lee, E.A. McLean, A. Mostovych, J. Stamper, S. Bodner, S.P. Obenschain and B.H. Ripin, Phys. Rev. Lett. 58 (1987) 2672.
[29] J.S. Wark, J.D. Kilkeny, A.J. Cole, P.T. Rumsby and M.H. Key, Appl. Phys. Lett. 48 (1986) 969.
[30] H. Nishimura, H. Takabe, K. Mima, F. Hattori, H. Hasegawa, H. Azechi, M. Nakai, K. Kondo, T. Norimatsu, Y. Izawa, C. Yamanaka and S. Nakai, Phys. Fluids 31 (1988) 2875.
[31] P.A. Holstein. B. Meyer, M. Rostaing, D. Galmiche and N. Wilke, Comput. Rend. Acad. Sci. Paris 307 (1988) ser. II, 211.
[32] J.D. Kilkenny, Phys. Fluids B 2 (1990) 1400.
[33] M. Desselberger, O. Willi, M. Savage and M.J. Lamb, Phys. Rev. Lett. 65 (1990) 2997.
[34] S.L. Ossakov and P.K. Chaturvedi, J. Geophys. Res. 83 (1978) 2085.
[35] S. Zargham and C.E. Seyler, J. Geophys. Res. 92 (1987) 10073.
[36] M.C. Kelly, C.E. Seyler and S. Zargham, J. Geophys. Res. 92 (1987) 10089.
[37] M.H. Schneps, P.T.P. Ho and A.H. Barret, Ap. J. 240 (1980) 84.
[38] R. Weaver, R. McCray, J. Castor, P. Shapiro and R. Moore, Ap. J. 218 (1977) 377, 390.
[39] R.A. Chevalier, Ann. Rev. Astron. Astrophys. 1977.15 (1977) 175.
[40] E.M. Jones, B.W. Smith and W.C. Straka, Space Sci. Rev. 27 (1980) 579.
[41] Y.-M. Wang and M. Nepveu, Astron. Astrophys. 118 (1983) 267.
[42] J.R. Buchler, M. Livio and S.A. Colgate, Space Sci. Rev. 27 (1980) 571.
[43] L. Smarr, J.R. Wilson, R.T. Barton and R.L. Bowers, Ap. J. 246 (1981) 515.
[44] H. Lamb, Hydrodynamics, 6th Ed. (Dover, New York, 1932).
[45] K. Schwarzschild, Göttinger Nachr. 1906 (1905) 41;
A. Unsöld, Physik der Sternatmosphären, 2. Auflage (Springer, Berlin, 1968) p. 215.
[46] W.J. Harrison, Proc. London Math. Soc. Second Ser. 6 (1908) 396.
[47] Lord Rayleigh, Phil. Mag. 32 (1916) 529.
[48] R. Bellman and R.H. Pennington, Quart. Appl. Math. 12 (1954) 151.
[49] M. Kruskal and M. Schwarzschild, Proc. Roy. Soc. London A 223 (1954) 348.
[50] G. Birkhoff, Quart. Appl. Math. 12 (1954) 306.
[51] G. Birkhoff, Quart. Appl. Math. 13 (1955) 451.
[52] M.S. Plesset, J. Appl. Phys. 25 (1954) 96.
[53] C.T. Chang, Phys. Fluids 2 (1959) 656.
[54] D. Layzer, Ap. J. 122 (1955) 1.
[55] G. Birkhoff and D. Carter, J. Math. Mech. 6 (1957) 769.
[56] P.R. Garabedian, Proc. Roy. Soc. A 241 (1957) 423.
[57] S. Chandrasekhar, Hydrodynamic and Hydromagnetic Stability (Oxford Univ. Press, Oxford, 1961).
[58] G. Birkhoff, Taylor Instability and Laminar Mixing, Report LA-1862, Los Alamos, 1954); Appendices, Report LA-1927, Los Alamos, 1955, unpublished.
[59] P.G. Drazin and W.H. Reid, Hydrodynamic stability (Cambridge Univ. Press, Cambridge, 1981).
[60] D.H. Sharp, Physica D 12 (1984) 3.
[61] J. Glimm, O. McBryan, R. Menikoff and D.H. Sharp, SIAM J. Sci. Stat. Comput. 7 (1986) 230.
[62] G. Buchwald, Untersuchung von Stabilitätsproblemen bei Fusion durch schwerioneninduzierten Trägheitseinschluß, Thesis, Goethe Universität, Franfurt am Main (1984).
[63] J.H. Gardner, S.E. Bodner, J.P. Boris, M.H. Emery, M.J. Fritts and M.J. Herbst, Analysis of stability and symmetry implications for ICF, in: Laser Interaction and Related Plasma Phenomena, Vol. 6, eds H. Hora and G.H. Miley (Plenum Press, New York, 1984) p. 673.
[64] P.A. Holstein and B. Meyer, Implosion symmetry and stability, in: Inertial Confinement Fusion, Proc. of the Course and Workshop held at Varenna, Italy, 1988, eds A. Caruso and E. Sindoni (Società Italiana di Fisica, Editrice Compositori, Bologna, Italy, 1989) p. 251.
[65] H. Jacobs, Nucl. Techn. 71 (1985) 131.
[66] N.K. Gupta, Rayleigh–Taylor Instability in Inertial Confinement Fusion, Report B.A.R.C.-1372, Bombay (1987).
[67] A.G. Greenhill, Am. J. Math. IX (1887) 62.
[68] K.O. Mikaelian, Phys. Rev. Lett. 48 (1982) 1365; Phys. Rev. A 26 (1982) 2140.
[69] D.L. Book and S.E. Bodner, Phys. Fluids 30 (1987) 367.
[70] H.J. Kull, Laser Particle Beams 4 (1986) 473.
[71] H.J. Kull, Scaling relations of ICF related Rayleigh–Taylor instabilities, in: Inertial Confinement Fusion, Proc. of the Course and Workshop held at Varenna, Italy, 1988, eds A. Caruso and E. Sindoni (Società Italiana di Fisica, Editrice Compositori, Bologna, Italy, 1989) p. 5.
[72] H.J. Kull, Rayleigh–Taylor instability in ICF, Intern. Conf. on Plasma Physics, New Delhi, India (1989).
[73] H.J. Kull, Phys. Rev. Lett. 51 (1983) 1434.
[74] H.J. Kull, Phys. Rev. A 31 (1985) 540.

[75] H.J. Kull, Phys. Rev. A 33 (1986) 1957.
[76] H.J. Kull and S.I. Anisimov, Phys. Fluids 29 (1986) 2067.
[77] H.J. Kull, Phys. Fluids B 1 (1989) 170.
[78] H.J. Kull, Phys. Rev. A 41 (1990) 4312.
[79] R. Courant and K.O. Friedrichs, Supersonic Flow and Shock Waves (Springer, Berlin, 1976) p. 119.
[80] P.M. Morse and H. Feshbach, Methods of Theoretical Physics (McGraw-Hill, New York, 1953).
[81] K.O. Mikaelian, Phys. Rev. A 31 (1985) 410.
[82] K.O. Mikaelian, Phys. Rev. A 42 (1990) 7211.
[83] Lord Rayleigh, Phil. Mag. 34 (1917) 94.
[84] G.K. Batchelor, An Introduction to Fluid Dynamics (Cambridge University Press, Cambridge, 1967) p. 481.
[85] R. Hickling and M.S. Plesset, Phys. Fluids 7 (1964) 7.
[86] A. Prosperetti, Phys. Fluids 25 (1982) 409.
[87] K.O. Mikaelian, Phys. Rev. Lett. 65 (1990) 992; Phys. Rev. A 42 (1990) 3400.
[88] S. Chandrasekhar, Quart. J. Mech. Appl. Math. 8 (1955) 1.
[89] G. Iooss, P. Laure and M. Rossi, Phys. Fluids A 1 (1989) 915.
[90] F. Hattori, H. Takabe and K. Mima, Phys. Fluids 29 (1986) 1719.
[91] J.M. Dufour, D. Galmiche and B. Sitt, Investigation of hydrodynamic stability of high-aspect ratio targets in laser implosion experiments, in: Laser Interaction and Related Plasma Phenomena, Vol. 6, eds H. Hora and G.H. Miley (Plenum Press, New York, 1984) p. 709.
[92] H. Sakagami and K. Nishihara, Phys. Fluids B 2 (1990) 2715.
[93] M. Abramowitz and I.A. Stegun, Handbook of Mathematical Functions (Dover, New York, 1965).
[94] E. Kamke: Differentialgleichungen (Akademische Verlagsgesellschaft, Leipzig, 1967).
[95] J. Heading: An Introduction to Phase Integral Methods (Wiley, New York, 1962).
[96] N.R. Rajappa, J. Phys. Soc. Japan 28 (1970) 219; Acta Mech. 10 (1970) 193; Quart. J. Mech. Appl. Math. 30 (1977) 131.
[97] R.L. Kiang, Phys. Fluids 12 (1969) 1333.
[98] A.H. Nayfeh, J. Fluid Mech. 38 (1969) 619.
[99] E. Infeld and G. Rowlands, Phys. Rev. Lett. 60 (1988) 2273.
[100] G.B. Witham: Linear and Nonlinear Waves (Wiley, New York, 1974) section 13.13.
[101] C.E. Leith, private communication.
[102] R. Pennington: Machine Calculation of the Growth of Taylor Instability in an Incompressible Fluid, Report PNJ-LA-11 (undated).
[103] R. Menikoff and C. Zemach, J. Comp. Phys. 51 (1983) 28.
[104] D.T. Dumitrescu, Z. Angew. Math. Mech. 23 (1943) 139.
[105] E. Fermi, in: G. Birkhoff: Taylor instability, Appendices to report LA-1862, Report LA-1927, Los Alamos, 1955, Appendix G, unpublished.
[106] J.M. Vanden-Broeck, Phys. Fluids 27 (1984) 1090, 2604.
[107] F.H. Harlow and J.E. Welch, Phys. Fluids 9 (1966) 842.
[108] G.R. Baker, D.I. Meiron and S.A. Orszag, Physica D 12 (1984) 19.
[109] R. Menikoff and C. Zemach, J. Comp. Phys. 36 (1980) 366.
[110] Yu.M. Davidov, J. Appl. Mech. 22 (1981) 97.
[111] D. Colombant, W. Manheimer and E. Ott, Phys. Rev. Lett. 53 (1984) 446; Phys. Fluids 27 (1984) 2164.
[112] M.J. Andrews and D.B. Spalding, Phys. Fluids 12 (1990) 922.
[113] D.L. Youngs, Physica D 12 (1984) 32.
[114] S.Z. Belen'ki and E.S. Fradkin, Theory of turbulent intermixing, in: Quantum Field Theory and Hydrodynamics, Proc. of the Lebedev Physics Institute, Vol. 29, ed. D.V. Skobel'tsyn (Consultants Bureau, New York, 1967).
[115] R.L. McCrory and R.L. Morse, Phys. Fluids 19 (1976) 175.
[116] J. Glimm, X.L. Li, R. Menikoff, D.H. Sharp and Q. Zhang, Phys. Fluids A 2 (1990) 2046.
[117] N.A. Inogamov, Soviet Tech. Phys. Lett. 4 (1978) 299.
[118] J.A. Zufiria, Phys. Fluids 31 (1988) 440.
[119] S.W. Haan, Phys. Rev. A 39 (1989) 5812.
[120] K.O. Mikaelian, Physica D 36 (1989) 343; J. Appl. Phys. 65 (1989) 964.
[121] P.G. Saffman and D.I. Meiron, Phys. Fluids A 1 (1989) 1767.
[122] R.D. Richtmyer, Principles of Advanced Mathematical Physics, Vol. 1 (Springer, Berlin, 1978) p. 390.
[123] N.A. Inogamov, Hidden Symmetry in the Problem of Internal Waves in a Stratified Fluid, Landau Institute Preprint 1984-9 (1984).
[124] K.O. Mikaelian, Phys. Rev. A 40 (1989) 4801.
[125] H. Jacobs, Influence of Gradual Density Transition and Nonlinear Saturation on Rayleigh–Taylor Instability Growth, Report KfK 3756, Karlsruhe (1984). [partly published in: H. Jacobs, Nucl. Technol. 71 (1985) 131].
[126] H.J. Kull, Perfect Fluid Model of Rayleigh–Taylor Instability, Report IAP 102/82, TH Darmstadt (1982).
[127] E. Ott and D.A. Russell, Phys. Rev. Lett. 41 (1978) 1048.
[128] H.J. Kull, Inversion Symmetry of the Rayleigh–Taylor Eigenvalue Problem for Continuous Density Profiles, Report IAP 122/89, TH Darmstadt, (1989).
[129] K.O. Mikaelian, Phys. Rev. A 33 (1986) 1216.

[130] D.H. Munro, Phys. Rev. A 38 (1988) 1433.
[131] R. Menikoff, R.C. Mjolsness, D.H. Sharp and C. Zemach, Phys. Fluids 20 (1977) 2000.
[132] G.F. Carrier and C.T. Chang, Quart. J. Appl. Math. 16 (1959) 436.
[133] R. Menikoff, R.C. Mjolsness, D.H. Sharp, C. Zemach and B.J. Doyle, Phys. Fluids 21 (1978) 1674.
[134] L.D. Landau and E.M. Lifshitz, Fluid Mechanics, Course of Theoretical Physics, Vol. 6 (Pergamon Press, Oxford, 1959) pp. 47–53.
[135] G.K. Batchelor, The Theory of Homogeneous Turbulence (Cambridge Univ. Press, Cambridge, 1953).
[136] R.C. Mjolsness, Phys. Fluids 22 (1979) 1213.
[137] A. Bers, Space-time evolution of plasma instabilities – absolute and convective, in: Handbook of Plasma Physics, Vol. 1, eds M.N. Rosenbluth and R.Z. Sagdeev (North-Holland, Amsterdam, 1984) p. 451.
[138] I.B. Bernstein, E.A. Frieman, M.D. Kruskal and R.M. Kulsrud, Proc. Roy. Soc. A 244 (1958) 17;
I.B. Bernstein: The variational principle for problems of ideal magnetohydrodynamic stability, in: Handbook of Plasma Physics, Vol. 1, eds M.N. Rosenbluth and R.Z. Sagdeev (North-Holland, Amsterdam, 1984) p. 421.
[139] W.A. Newcomb, Phys. Fluids 26 (1983) 3246.
[140] A. Skumanich, Ap. J. 121 (1955) 408.
[141] L. Baker, Phys. Fluids 26 (1983) 950.
[142] I.B. Bernstein and D.L. Book, Phys. Fluids 26 (1983) 453.
[143] A.M. Lezzi and A. Prosperetti, Phys. Fluids A 1 (1989) 1784.
[144] M.S. Plesset and A. Prosperetti, Phys. Fluids 25 (1982) 911.
[145] A.J. Scannapieco, Phys. Fluids 24 (1981) 1699.
[146] D.L. Book, Phys. Rev. Lett. 41 (1978) 1552; J. Fluid Mech. 95 (1979) 779.
[147] D.L. Book and I.B. Bernstein, Phys. Fluids 22 (1979) 79; Ap. J. 225 (1978) 633; J. Plasma Phys. 23 (1980) 521.
[148] S.J. Han, Phys. Fluids 25 (1982) 1723.
[149] R.D. Richtmyer, Principles of Advanced Mathematical Physics, Vol. 1 (Springer, Berlin, 1978) pp. 131–132.
[150] S.I. Braginskii, Rev. Plasma Phys. 1 (1965) 215.
[151] H. Takabe, L. Montierth and R.L. Morse, Phys. Fluids 26 (1983) 2299;
H. Takabe and K. Mima, Phys. Fluids 28 (1985) 3676.
[152] J. Buckmaster, Physica D 12 (1984) 173.
[153] E.A. Spiegel: Convection in stars, in: Ann. Rev. Astron. Astrophys., eds L. Goldberg, D. Layzer and J.G. Philips (Annual Reviews Inc., Palo Alto, 1971) p. 323.
[154] J. Nuckolls, L. Woods, A. Thiessen and G. Zimmerman, Nature 239 (1972) 139.
[155] P.J. Catto, Phys. Fluids 21 (1978) 30.
[156] H. Takabe and K. Mima, Phys. Soc. Japan 48 (1980) 1793.
[157] L. Baker, Phys. Fluids 21 (1978) 295; 26 (1983) 627.
[158] D.Y. Hsieh, Phys. Fluids 21 (1978) 745; 22 (1979) 1435;
D.Y. Hsieh and S.P. Ho, Phys. Fluids 24 (1981) 202.
[159] W.M. Manheimer and D.G. Colombant, Phys. Fluids 27 (1984) 983.
[160] D.G. Colombant and W.M. Manheimer, Phys. Fluids 26 (1983) 3127.
[161] J.N. Shiau, E.B. Goldman and C.I. Weng, Phys. Rev. Lett. 32 (1974) 352.
[162] D.B. Henderson, R.L. McCrory and R.L. Morse, Phys. Rev. Lett. 33 (1974) 205.
[163] K.A. Brueckner, S. Jorna and R. Janda, Phys. Fluids 17 (1974) 1554; 22 (1979) 1841 (erratum).
[164] M.H. Emery and J.H. Gardner, Phys. Rev. Lett. 57 (1986) 703; 62 (1989) 694 (erratum);
M.H. Emery, J.P. Dahlburg, and J.H. Gardner, Phys. Fluids 31 (1988) 1007; B1 (1989) 964 (erratum).
[165] M. Tabak, D.H. Munro and J.D. Lindl, Phys. Fluids B2 (1990) 1007.
[166] K.O. Mikaelian, Phys. Rev. A 42 (1990) 4944.
[167] S. Atzeni, A. Caruso and V. Pais, Phys. Lett. A 120 (1987) 343.
[168] J.D. Lindl, Introduction to the physics of ICF capsules, in: Inertial Confinement Fusion, Proc. of the Course and Workshop held at Varenna, Italy, 1988, eds A. Caruso and E. Sindoni (Società Italiana di Fisica, Editrice Compositori, Bologna, Italy, 1989) p. 595.